Title
The South Pole Telescope bolometer array and the measurement of secondary Cosmic Microwave Background anisotropy at small angular scales

Permalink
https://escholarship.org/uc/item/2z74c4rc

Author
Shirokoff, Erik D.

Publication Date
2011

Peer reviewed|Thesis/dissertation

The South Pole Telescope bolometer array and the measurement of secondary Cosmic Microwave Background anisotropy at small angular scales

by

Erik D. Shirokoff

A dissertation submitted in partial satisfaction of the
requirements for the degree of
Doctor of Philosophy

in

Physics

in the

Graduate Division

of the

University of California, Berkeley

Committee in charge:

Professor William Holzapfel, Chair
Professor Bernard Sadoulet
Professor Chung-Pei Ma

Fall 2011

The South Pole Telescope bolometer array and the measurement of secondary Cosmic Microwave Background anisotropy at small angular scales

Abstract

The South Pole Telescope bolometer array and the measurement of secondary Cosmic Microwave Background anisotropy at small angular scales

by

Erik D. Shirokoff

Doctor of Philosophy in Physics

University of California, Berkeley

Professor William Holzapfel, Chair

The South Pole Telescope (SPT) is a dedicated 10-meter diameter telescope optimized for mm-wavelength surveys of the Cosmic Microwave Background (CMB) with arcminute resolution. The first instrument deployed at SPT features a 960 element array of horn-coupled bolometers. These devices consist of fully lithographed spider-web absorbers and aluminum-titanium bilayer transition edge sensors fabricated on adhesive-bonded silicon wafers with embedded metal backplanes. The focal plane is cooled using a closed cycle pulse-tube refrigerator, and read-out using Frequency Domain Multiplexed Superconducting Quantum Interference Devices (SQUIDs.) Design features were chosen to optimize sensitivy in the atmospheric observing bands available from the ground, and for stability with the frequency domain multiplexed readout system employed at SPT, and performance was verified with a combination of laboratory tests and field observations.

In 2008 the SPT surveyed 200 square-degrees at 150 and 220 GHz. These data have been analyzed using a cross-spectrum analysis and multi-band Markov Chain Monte Carlo parameter fitting using a model that includes lensed primary CMB anisotropy, secondary thermal (tSZ) and kinetic (kSZ) Sunyaev-Zel'dovich anisotropies, unclustered synchrotron point sources, and clustered dusty point sources. In addition to measuring the power spectrum of dusty galaxies at high signal-to-noise, the data primarily constrain a linear combination of the kSZ and tSZ anisotropy contributions (at $150\,\text{GHz}$ and $\ell = 3000$): $D_{3000}^{tSZ} + 0.5\,D_{3000}^{kSZ} = 4.5 \pm 1.0\,\mu\text{K}^2$, and place the lowest limits yet measured on secondary anisotropy power.

To Dennis

who taught me how to solder
and introduced me to the world of ideas.

Contents

List of Figures

List of Tables

Acknowledgments

Few graduate students have the fortune to play a key role in an experiment as ambitious and exciting as the South Pole Telescope. Fewer still do so with the guidance of an adviser as capable as Bill Holzapfel, whose encouragement, sound criticism, and technical savvy have been invaluable both to the project and to my own graduate career. I am also fortunate to have have the chance to work with Adrian Lee and Paul Richards, and the large and diverse group they've assembled here at Berkeley, as well as John Clarke and Helmuth Spieler.

I've also been fortunate to work with a number of talented post-doctoral researchers in our group. In particular, I am grateful to Sherry (Hsiao-Mei) Cho and Christian Reichardt. Sherry's industry and precision set the standard for our group's fabrication efforts, and it is a rare day in the lab that I do not directly benefit from her advice and experience. Without Christian's tireless work, the power spectrum analysis here (and several other SPT analysis projects) would have taken many more years to complete; his efficiency and analytic intuition are an inspiration. There are many others who played a vital role in the design and deployment of the SPT receiver, as well as the group's related projects. Among them, Brad Benson, who lead the SPT receiver design, and Matt Dobbs, who oversaw the fMUX readout development, are a large part of what made our group successful. Nils Halverson and Huan Tran both played a major role in making the lab run and overseeing hardware development in the group as a whole.

Among the former graduate students in the Berkeley group who have contributed substantially to the project are Jared Mehl (who, in addition to making major contributions to the APEX and SPT detector design, trained me in the microlab), Martin Lueker, who worked on all aspects of the receiver and fMUX development and developed much of the device characterization techniques which are used in this thesis, Tom Plagge, who worked primarily the SPT receiver hardware and software, and Trevor Lanting, who pioneered the analog fMUX readout system used in SPT. In recent years Elizabeth George, Nicholas Harrington, and Edward Young have each made significant contributions to device testing and system charterization.

Of course, the work described here wouldn't have been possible without the dedicated effort of the the entire SPT collaboration. It has been a pleasure to work with John Carlstrom, Ken Aird, Lindsey Bleem, Abigail Crites, Tijmen de Haan, John Dudley, Gil Holder, Dana Hrubes, Ryan Keisler, Lloyd Knox, Erik Leitch, Daniel Luong-Van, Marius Millea, Jeff McMahon, Steve Meyer, Tom Montroy, Steve Padin, Clem Pryke, John Ruhl, Laurie Shaw, Zak Staniszewski, Tony Stark, Kyle Story, Keith Vanderlinde, Oliver Zahn, and many others. I suspect that Tom Crawford and Kathryn Schaffer had a lot to do with setting the tone for the collaboration as a whole; their willingness to volunteer for the least personally rewarding but necessary data analysis and administrative tasks deserves celebration, as does their unwavering generosity when students and collaborators ask for help. In addition, I'm particularly grateful to Joaquin Vieira and Clarence Chang, who set aside their own work in order to help in the lab with device testing; their assistance made our second season

deployment possible.

Both SPT, and my own work, have benefited from the exchange of knowledge and resources with the Polarbear and APEX-SZ collaborations. Thanks go to Dan Schwan, Zigmund Kermish, Roger O'Brient, Erin Quealy, Bryan Steinbach, Daniel Ferrusca, Brad Johnson, Ben Westbrook, and Aritoki Suzuki. In particular, I want to thank Kam Arnold, whose insight and perspective proved invaluable in surmounting many a fabrication challenge, and who graciously volunteered his own time to help out SPT repeatedly while we struggled to meet deployment deadlines.

Finally, I would like to thank the Microlab staff and fellow users whose efforts made the array fabrication possible. There are too many to mention; however, I am particularly grateful to Bob Hamilton and Marilyn Kushner, who both volunteered to work through well-earned vacation hours to help us meet our second season deployment deadline. In addition, I am grateful to Xiao Fan Meng, whose work was essential to the SPT fabrication effort.

The SPT receiver was largely fabricated in the UC Berkeley machine shop, under the expert hands of Marco Ambrosini, Pete Thuesen, Abel Gonzales, Dave Nguyen, and the rest of the shop team, with additional machining and lab support from from Michael Solarz. For their work on the telescope design and construction, I thank by S. Busetti, E. Chauvin, T. Hughes, P. Huntley, and E. Nichols and his team of iron workers. Thanks also go to the crew of the South Pole Station, and in particular the 2009 winter population: fellow SPT winterover Ross Williamson, expert machinist Steele Diggles, and the entire crew who made the station run and kept us warm, fed, and entertained during the long months of winter. I am also personally grateful to the UC Berkeley physics department staff who make the department run and keep the grad students out of trouble: especially Anne Takizawa, Donna Sakima, Claudia Trujillo, Anthony Vitan, and Eleanor Crump.

I would also like to thank my undergraduate research advisers, George Smoot and Carl Heiles. My efforts as an undergrad did little to advance human knowledge, but *I* learned a great deal from each, and everything I've done since has benefited from the skills and knowledge I acquired under their patient guidance.

Much of the material which appears in Section 6 has been accepted for publication in the Astrophysical Journal. (Shirokoff et al., 2011) Selected portions of chapters 4 and 5 may be included in series instrument paper which the SPT collaboration expects to submit this year.

Part I

Introduction and scientific motivation

Chapter 1

Concordance cosmology & large scale structure

1.1 Introduction

When combined with other observations, precision measurements of the Cosmic Microwave Background (CMB) have provided us with a robust, quantitative standard model for the evolution of the universe from the first few seconds to the phenomenologically rich environment we observe today. This elegant model describes the observable data with only a hand full of parameters; however, it includes several astonishing features: dark matter, dark energy, and inflation. This last topic is indirectly tested by measuring the spectrum of the primordial perturbations which give rise to the primary CMB anisotropies and formed the seeds of the structure observed today. More direct tests based upon the measurement of the CMB polarization signature arising from primordial gravitational waves are underway.

Evidence for dark matter and dark energy can be found in the large scale structure of the universe today, and its recent evolution. The range of times over which the effects of dark energy are most significant (roughly $1 < z < 10$) are precisely those which are hardest to constrain: late enough that non-linear effects dominate the distribution of matter on all but the very largest scales, yet early enough that statistically meaningful optical observations are expensive and the evolution of common observables with redshift is poorly understood. One of the primary goals of modern observational cosmology today is thus to describe the large scale structure of the universe. This is interesting as an end onto itself, as it includes a rich set of phenomena which are as yet poorly understood: How did reionization, the transition from a neutral to an almost completely ionized intergalactic medium at a redshift of ~ 10 occur? How do galaxies form, and what governs their morphology and distribution? (And why are they so very different from both larger and smaller structures?) It also has the potential to provide a robust framework within which to test our understanding of dark matter, dark energy, and the role they play in the formation of the universe we observe

today.

In this chapter, I provide a short summary of several aspects of modern cosmology, with an eye toward the questions which can be addressed by measurements of the SZ power spectrum. This statistical detection of power due to the Compton scattering of CMB photons from the plasma in unresolved galaxy clusters and groups spanning a range of redshifts and masses has the potential to constrain the amplitude of the matter power spectrum today, the detailed gas physics of small and high-redshift groups which are particularly hard to observe directly, and, in principle, the duration and character of reionization.

In Chapter 2, I briefly review the overall design of the South Pole Telescope (SPT), and the receiver and frequency domain multiplexed readout. Chapter 3 introduces the Transition Edge Sensor (TES) bolometer, and derives the basic properties which govern the design of these devices, with specific examples and results appropriate to SPT. Chapter 4 discusses the design and fabrication of the SPT array. Chapter 5 characterizes the performance of the SPT array, with an emphasis on the final season configuration and performance in the field. Chapter 6 returns to the subject of the SZ power spectrum, and presents new results of an analysis of the complete 2008 SPT data set, including bandpowers at $2000 \leq \ell \leq 10000$ and multi-frequency Markov Chain Monte Carlo (MCMC) fits to various models which include SZ power and foregrounds.

1.2 Concordance cosmology

1.2.1 The ΛCDM world model

The concordance model of modern cosmology is described in numerous review papers and textbooks. The following includes just a few major points, following the elegant summary presented in Nakamura et al. (2010) but with the notation conventions used in Dodelson (2003) and elsewhere. According to this model (and all observational evidence to date), our universe is homogeneous and isotropic at the largest scales. Its global properties are therefore described by the equations of general relativity and the maximally symmetric Friedmann–Lemaître–Robertson–Walker (FLRW) metric, defined by

$$ds^2 = dt^2 - a^2(t)\left(\frac{dr^2}{1 - kr^2} + r^2 d\Omega^2\right) \tag{1.1}$$

where $a(t)$ is a dimensionless scale factor defined to be $a(t_0) = 1$ at the present epoch, and r is the so-called co-moving distance, and $d\Omega$ is an element of solid angle. The constant, k, is discrete and equal to (-1,0,1) corresponding to geometry with a (negative, flat, positive) curvature, or in the usual terminology, a universe which is (open, flat, closed).

With this metric, Einstein's equations reduce to the FriedmannLematre equations of motion,

$$H(t)^2 \equiv \left(\frac{\dot{a}}{a} \right) = \frac{8\pi G}{3} \rho - \frac{k}{a^2} + \frac{\Lambda}{3} \tag{1.2}$$

$$\frac{\ddot{a}}{a} = -\frac{4\pi}{3} G \left(\rho + 3p \right) + \frac{\Lambda}{3} \tag{1.3}$$

where $H(t) \equiv \dot{a}/a$ is the (time varying) Hubble constant, ρ and p are the energy density and pressure of the (averaged) material in the universe, G is the usual gravitational constant, and Λ is the so called cosmological constant. From these equations, or from energy conservation, one can also derive

$$\dot{\rho} = -3H(t) \left(\rho + p \right) \tag{1.4}$$

In general, the density and pressure can be expressed as a sum of contributions from various components: matter, radiation, and a cosmological constant or vacuum energy. It is convenient to describe each according to its equation of state, $w_i = p_i/\rho_i$. Matter is assumed to be pressure-less on cosmological scales, and thus $w_m = 0$, while for radiation $w_r = 1/3$. A cosmological constant can be expressed as $\rho_\Lambda = \Lambda/8\pi G$ with an equation of state $w = -1$, which can also be readily generalized to a more general dark energy with an unspecified negative (and possibly time dependent) value of w.

It is convenient to define a critical density parameter, $\rho_c = 3H_0^2/8\pi G$, and express the density of component i as $\Omega_i \equiv \rho_i/\rho_c$. For a universe composed of matter, radiation, and a cosmological constant, the total density is then $\Omega_0 = \Omega_m + \Omega_r + \Omega_\Lambda$. From the equations above, then,

$$\frac{k}{H^2 a^2} = \frac{k}{H_0^2} = (\Omega_0 - 1) \tag{1.5}$$

from which it is clear that Ω_0 determines whether the universe is open, flat, or closed.

Equations 1.4 can be immediately integrated to solve for $\rho(a)$, with the result

$$\rho_i \propto a^{-3(w+1)} \tag{1.6}$$

which describe the evolution of the energy density of each component *independent* of what drives the evolution of $a(t)$. In the case where the universe is dominated by a component with a single equation of state (or, instantaneously, for a composite universe with an effective equation of state), equations 1.2 and 1.3, can be solved for $a(t)$. Whenever the universe is close to flat – which is universally true at early times even for non-flat models – the k/a^2 term can be ignored and a particularly simple analytic solution exists. In this case, and assuming w does not depend on time, the result is

$$a(t) = \begin{cases} t^2/\left[3(w+1)\right] & \text{if } w \neq -1 \\ \exp\left[\Lambda/3t\right] & \text{if } w = -1 \end{cases} \tag{1.7}$$

It is useful to consider three extreme cases. For the very early universe dominated entirely by radiation, $\rho_r \propto a^{-4}$, $a \propto t^{1/2}$, and $H(t) = 1/2t$. In the case that matter dominates, which is a reasonably accurate description of the real universe at intermediate times, $\rho \propto a^{-3}$, $a \propto t^{2/3}$. The solution for a cosmological constant is explicitly given above, while a generic vacuum energy with $w < 0$ will result in a solution with $a(t)$ larger than the matter case. For models which are significantly non-flat, an exact parametric solution exists for each of these cases.

For a realistic model where each component is known, $a(t)$ can be easily calculated numerically. To a large extent, our ability to constrain fundamental cosmology with observations of the late universe can be reduced to measurements of $a(t)$. It is worth noting a few common results which make that comparison possible.

Using the fact that $ds^2 = 0$ for photons and the equation for the metric above, one can immediately derive the relationship between redshift and scale factor: $a = (1 + z)^{-1}$. Hubble's constant is just $H(t_0) = \dot{a}(t_0)$. Additional useful quantities include the deceleration parameter,

$$q_0 = -\frac{a\ddot{a}}{H_0^2} = \frac{1}{2}\Omega_m + \Omega_r + \frac{(1 + 3w)}{2}\Omega_\Lambda \tag{1.8}$$

where w is measured at t_0, which clearly allows for solution with positive acceleration provided that $w < -1/3$.

Two other quantities of note are the angular diameter distance and the luminosity distance. The first is defined as $d_A \equiv l/\theta$ for an object of physical length l observed to subtend an angle θ. From the equations above, this is given by

$$d_A = \begin{cases} a \sinh\left[\sqrt{\Omega_k}H_0\chi\right] / \left(H_0\sqrt{(\Omega_k)}\right) & \text{closed} \\ a\chi & \text{flat} \\ a \sin\left[\sqrt{-\Omega_k}H_0\chi\right] / \left(H_0\sqrt{(\Omega_k)}\right) & \text{open} \end{cases} \tag{1.9}$$

where $\Omega_k \equiv 1 - \Omega_0$ and χ is the co-moving distance to an object at scale factor a, given by

$$\chi(a) = \int_a^1 \frac{da'}{a'^2 H(a')} \tag{1.10}$$

The luminosity distance, defined using the observed flux, F, from a source which emits luminosity L (integrated over all wavelengths), is given by

$$d_L \equiv \left(\frac{L}{4\pi F}\right)^{1/2} = \frac{\chi}{a} \tag{1.11}$$

where χ is given above and a is the scale factor at the source.

Here, in brief, are all the tools needed to relate observations of the late universe to fundamental cosmological parameters. Given a standard candle - an object of known luminosity which can be observed at different redshifts - one can measure $d_L(a)$ and thus $H(a)$, q_0, etc. Given a standard ruler - an object, or statistical distribution of objects of known size - one can measure $d_A(a)$, independently contraining Ω and $\chi(a)$. Given a sufficiently precise model for the initial state of the universe and the process by which structure forms, one can relate the observed large scale structure today to $a(t)$, the densities of each component, and potentially the characteristics of dark energy.

1.2.2 Cosmological parameters

By combining the location of the CMB acoustic peaks and damping tail with measurements of Hubble's constant (H_0), we know that the curvature of the universe is flat to within a few percent, and thus the ratio of the total energy density to the critical energy density is $\Omega_0 = 1$. Models which start out very slightly different from $\Omega_0 = 1$ diverge from that value over time, thus it's reasonable to infer that the equality is nearly exact. What are the components which make up this energy density?

The radiation density of the early universe is extremely well constrained by the precision measurements of the spectrum of the CMB by the FIRAS instrument, which show it to be essentially a perfect blackbody with temperature today of $2.728 \pm 0.004\,\mathrm{K}$ (95% CL) (Fixsen et al., 1996). Neutrinos, which are highly relativistic at the time they freeze out of equilibrium in the early universe, add an additional radiation-like term to the energy density.

The amount of baryonic matter in the universe can be estimated in a number of ways, although two largely independent measurements now provide similar (and nearly consistent) constraints. From the relative heights of the CMB peaks, as well as the assumption of a power law initial spectrum, the total baryon density can be inferred. The most recent constraint is $\Omega_b h^2 = 0.0225 \pm 0.005$ for a ΛCDM model. (Komatsu et al., 2011) Models of nucleogenesis can be used to relate the ratio of light elements to the (unchanging) baryon to photon ratio, which, given the precision with which the CMB spectrum is known, can be used to measure the baryon density. This measurement is complicated by processing of matter at later times, and results vary depending on the data set used, with a general range of $0.019 \leq \Omega_b h^2 \leq 0.024$. (Steigman, 2007) Recent measurements of the most metal poor, and thus nearly primordial samples of the IGM appear to agree with the CMB data. (Pettini et al., 2008)

Numerous independent measurements suggest that the total matter density must be much larger than can be accounted for by baryonic matter alone. The dynamics of virialized, gravitationally bound structures on scales ranging from galaxies to massive clusters of galaxies, masses inferred from strong gravitational lensing, and the existence of significant small-scale power in the late universe matter density distribution all point to a dark matter component which is several times Ω_b. From the total height of the CMB peaks, along with H_0 constraints, $\Omega_m = .272 \pm 0.017$. (Komatsu et al., 2011) Hot dark matter, which remains

relativisitic during non-linear colapse and galaxy formation, will free stream out of dense regions and exponentially damp perturbations on small angular scales. The amplitude of large scale structure power in the late universe therefore requires that most of the dark matter be cold dark matter, which was non-relativistic at the time of galaxy formation. Many candidates for dark matter particles have been proposed, however no direct detections have been confirmed yet. Nakamura et al. (2010) includes a concise review of the subject.

The remaining density required to achieve a flat universe appears to be dark energy, a rather mysterious property of the universe evolves as though it were a substance with a negative equation of state. The case $w = -1$ corresponds to a cosmological constant in Einstein's equations, and therefore a constant vacuum energy density. The cosmological constant case has aesthetic appeal, though in general w could take on any value, or even vary with $a(t)$.

There are now several lines of observational evidence for dark energy. The first observations pointing toward a significant cosmological constant were based on comparisons of the amplitude of the matter power spectrum observed in galaxy cluster distributions compared to expectations for a CDM universe with $\Omega_m \sim 0.2$ inferred from the Cosmic Background Explorer satellite (COBE) results. (White et al., 1993) A more precise, though still indirect, argument can be made from the constraint on Ω_k and Ω_m from the CMB and H_0 measurements, though the constraint on the equation of state of the missing material is limited. (Hanany et al., 2000; Melchiorri et al., 2000) A similar but partially independent result can be obtained by comparing the inferred value of Ω_b/Ω_m from observations of rich galaxy clusters to the value of $\Omega_b h^2$ inferred from primordial nucleosynthesis, yielding a constraint on $\Omega_m = 0.28 \pm 0.06$. (Allen et al., 2007)

Direct measurements of the dark energy density, and its equation of state, all depend upon the behavior of $a(t)$ at late times. The first direct measurement of dark energy was made by two independent groups using Type 1a supernovae (SN1a) as standard candles to measure the deceleration parameter, q_0. Both detected a nonzero Ω_m at greater than 3σ. (Riess et al., 1998; Perlmutter et al., 1999) Recent results from SN1a and baryon acoustic oscillation (BAO) catalogs find $w - 1 = .013 \pm 0.07$ if w is assumed constant, and are beginning to place meaningful limits on the time evolution of w. (Hicken et al., 2009)

The components discussed above govern the evolution of the universe from the earliest times, provided one knows the initial statistical distribution of density and temperature at the beginning. There is now considerable observational support for models which begin with Gaussian, adiabatic density fluctuations with a power-law initial power spectrum, as will be discussed in more detail in 1.4.

1.3   The Cosmic Microwave Background

According to this model, this initial state includes density fluctuations which are adiabatic, Gaussian, and have a scale invariant (or nearly scale invariant) amplitude. The initial am-
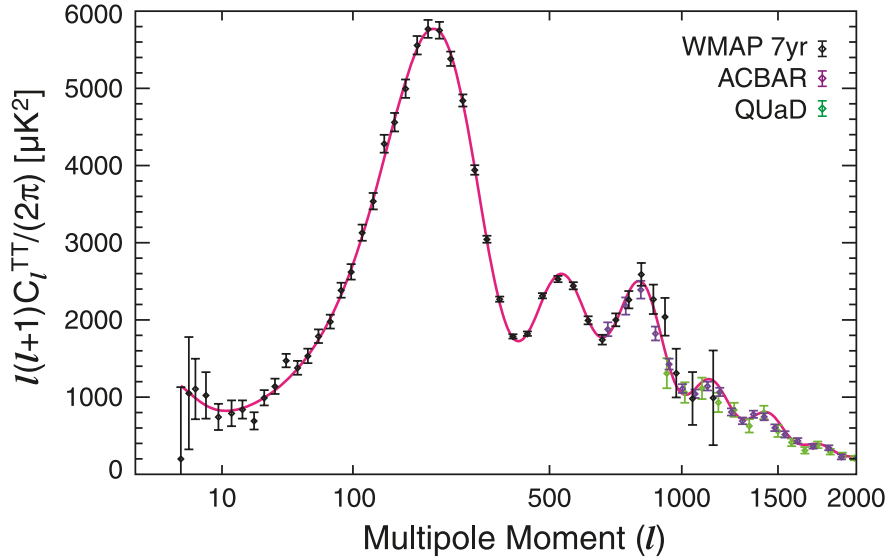
Figure 1.1 Primary anisotropy in the CMB temperature power spectrum. A best fit ΛCDM theory spectrum is shown, as well as data from the WMAP 7-year data release (WMAP7), and the Arcminute Cosmology Bolometer Array Receiver (ACBAR) and QUEST at DASI (QUaD) ground based instruments. Figure from Komatsu et al. (2011).

plitude is small, such that $\delta\rho/\rho \ll 1$. As the universe expands and cools, the reaction rates for the creation and annihilation of stable particles drop. Neutrinos, electrons, dark matter particles, nucleons, and finally light nuclei freeze out of equilibrium and the numbers of each are thereafter conserved.

After a few tens of minutes, the universe contains only a small number of components whose energy densities evolve in the classical way: photons, baryonic matter in the form of plasma composed mostly of ionized hydrogen (with some Helium and trace amount of other nuclei), neutrinos, and dark matter. Dark energy, which becomes significant at later times, make an infinitesimal contribution at these early times. The neutrinos are entirely decoupled from the other components, and have little impact on the evolution of the early universe, provided their contribution to the total energy density is small. Thompson scattering couples the baryonic matter to photons, and forms a single dynamic fluid with an equation of state that begins fully relativistic and later evolves. Dark matter interacts with the plasma only gravitationally, and to first order its only effect on the dynamics of the early universe are through its contribution to the total matter density, Ω_m and thus the dependence of the temperature and scale factor on time once the energy density ceases to be dominated by radiation.

At a redshift of roughly $z \sim 1000$, the plasma (re)combines to form neutral hydrogen. Over a length of time short compared to the age of the universe, the opacity drops by orders of magnitude and the universe becomes largely transparent. The pattern of temperature

anisotropy at this surface of last scattering gives rise to power fluctuations in the radiation field. Those photons travel with minimal interactions through the expanding universe. At a redshift of $z \sim 10$, the first stars and quasars begin emitting UV photons which reionize the intergalactic medium.

At the largest angular scales, the CMB power spectrum is dominated by the Sachs Wolfe effect, which is the gravitational redshift of photons traversing the potential wells of primordial density perturbations. Its amplitude and spectral shape are determined solely by the CMB temperature and the initial matter power spectrum. The most prominent feature of the CMB power spectrum is a pronounced peak at approximately $\ell \sim 200$, and a series of harmonic peaks of varying amplitude. (Where ℓ is the order of a spherical harmonic expansion, equivalent to wave-vector k for small regions of sky.) These acoustic peaks correspond to oscillating modes which complete an integer number of half-cycles at the time of recombination, and therefore scales as the angular diameter distance of the sound horizon at the time last scattering. Except for a weak dependence on the baryon density[1] the physical scale of the first peak is fully determined, and it can therefore serve as a standard ruler. The angular scale of the peaks can therefore be used to place strong constraints on Ωh^2 and weaker constraints on Ω_Λ. (Komatsu et al., 2011; Larson et al., 2011; Reichardt et al., 2009a)

The amplitude of the first peak, and the relative amplitudes of the first few harmonics are sensitive to the amplitude of the primordial spectrum, as well as Ω_m and Ω_b, through dynamic damping and driving terms in the equation of motion of the plasma. Beyond the first few peaks, the amplitude of the primary CMB fluctuations are exponentially suppressed due to two effects. The first, Silk damping, occurs for length scales which are comparable to diffusion length for photons interacting via Thompson scattering in the plasma.(Silk, 1968) Perturbations smaller than this scale are exponentially damped. The second effect is purely geometric: at scales small compared to the the sound speed multiplied by the timescale over which recombination occurred, the observer's line of sight will traverse multiple perturbations with intermediate optical depth, and their spectra will add incoherently. (Some authors also refer to this as Silk damping.) For concordance values, the length scale of both effects is approximately $10Mpc$, and thus the amplitude of the primary CMB spectrum decreases exponentially with increasing ℓ beyond about 1000.

At even smaller angular scales, the spectrum is dominated by secondary anisotropies and foregrounds. These secondary effects include the gravitational lensing of the primary CMB spectrum by intervening matter, and the thermal and kinetic Sunyaev Zel'dovich effects (the tSZ and kSZ). These effects occur when CMB photons are inverse Compton scattered from energetic electrons in the plasma of groups and clusters of galaxies, leading to a signal in the CMB spectrum at angular scales corresponding to the distribution of matter in the late universe. As a result, they can be used to probe the large scale structure of the universe. In

---

[1]The fractional baryon density modifies the relative amplitude of the second and third harmonic peaks of the CMB power spectrum, and can be independently constrained by multivariable fits to the power spectrum. Promordial nucleosynthesis provides even tighter constraints.

section 1.5 the SZ effects are introduced and a summary of their expected amplitudes and cosmological scaling are briefly discussed. In chapter 6, the result of measurement of the power spectrum for $2000 < \ell < 9500$ using the SPT 2008 data set is presented.

1.4 Large scale structure

1.4.1 Growth of perturbations

Observations of the CMB show that the energy density of the universe at the time of recombination was homogeneous to one part in 10^4 at all observable scales. The late universe, on the other hand, is obviously inhomogeneous, with density peaks that are order of magnitude larger than the mean density on the scale of clusters of galaxies, and larger still for smaller objects. The origin of this density contrast is no surprise: gravity will cause over-dense regions to collapse over time. However, developing a model that explains the evolution of structure - and the observables which can be used to measure it - is a challenge. In the last 40 years, a consistent and predictive quantitative description of the process of structure formation has emerged. Although there are still poorly understood phenomena, especially on the scale of individual galaxies and sub-halos, at large scales it has proven remarkably predictive.

This model begins with an initial spectrum of fluctuations in the early universe. These fluctuations are adiabatic, (temperature and density are related through the usual equation of state and in phase), Gaussian (drawn from a random distribution with no correlations between phases at different scales), and small compared to the mean energy density ($\delta\rho/\rho \sim 1 \times 10^{-4}$). The amplitude of the (three dimensional) matter density power spectrum with wavelength $\lambda = 2\pi/|\mathbf{k}|$ is generally assumed to be a power law of the form

$$P(\mathbf{k}) \equiv |\Delta_k|^2 \equiv \delta_\rho/\rho \propto k^n \tag{1.12}$$

The observed matter distribution at large scales appears to be consistant with an initial spectrum close to the scale-free spectrum proposed independently by Harrison and Zel'dovich, in which $n = 1$. (Harrison, 1970; Zeldovich, 1972) CMB results so far appear to be consistent with a power law, and find $n \equiv n_s = 0.969 \pm .012$.(Komatsu et al., 2011). These results are consistant with inflationary models, in which primordial fluctuations naturally produce a scale-invariant spectrum of density perterbations.

One of the principle endeavors of extragalactic astronomy in the last forty years has been to relate the spectrum of these primordial fluctuations to both the matter density distribution in the late universe and the observable baryonic matter which traces that distribution. The nature of the distribution can be specified in several ways, all of which are essentially equivalent, but can facilitate particular analysis. If the real-space matter distribution at $\mathbf{x}$ includes a density contrast, $\Delta(\mathbf{x}) = \delta\rho/\rho$, the two-point correlation function is given by

$$\xi(r) = \langle \Delta(\mathbf{x})\Delta(\mathbf{x}+\mathbf{r}) \rangle \tag{1.13}$$

For a power-law matter density power spectrum of the form given by 1.12, $\xi(r)$ will be

$$\xi(r) = \frac{V}{(2\pi)^2} \int P(k) e^{i\mathbf{k}\cdot\mathbf{r}} d^3 k$$

$$\propto \int \frac{\sin kr}{kr} k^{n+2} dk \tag{1.14}$$

$$\propto r^{-(n+3)}$$

where a finite maximum radial scale is assumed to insure convergence in deriving the third line. This can be recast in terms of the mass enclosed within an over-density at scale r, through the volume averaged over-density,

$$\bar{\xi} \equiv \frac{3}{r^3} \int_0^r \xi(r')\, r'^2 dr'. \tag{1.15}$$

For the specific case of a power-law, $\bar{\xi} \propto \xi(r) \propto r^{-(n-3)}$. (The general solution for $\bar{\xi}(r)$ corresponding to an arbitrary $P(k)$ is presented in Peacock & Dodds (1994a).) As mass enclosed within a sphere of radius r scales as $M(r) \propto \rho r^3$, the RMS over density as a function of mass, Δ_M, is given by

$$\Delta_M = \bar{\xi}^{1/2} \propto M^{-(n+3)/6} \tag{1.16}$$

The subsequent evolution of this initial spectrum into the matter distribution observed today can be roughly broken into three regimes: early processing prior to recombination, linear evolution in the matter-dominated era, and non-linear collapse.

Prior to recombination, fluctuations on scales larger than the sound horizon at the epoch of matter-radiation equality retain their initial power spectrum. These fluctuations grow as the scale-independent $\Delta \propto a^2(t)$ throughout the pre-recombination era.

At smaller scales, perturbations enter the sound horizon during the radiation dominated era. These modes are dynamically coupled to the dominant energy density, the plasma, and pressure support stops their evolution. The spectrum is then frozen at a value of $\Delta \propto a_H^2 \Delta_i$, where a_H is the scale factor at which a perturbation with mass M enters the horizon. Such a perturbation will enter the horizon as $M \propto \rho_{\mathrm{DM}}(ct)^3$. During the radiation dominated era, $a(t) \propto t^{1/2}$, while the dark matter density varies as $\rho_{\mathrm{DM}} \propto a^{-3}$. Thus the scale factor at which growth is suspended varies as $a_H \propto M^{-2/3}$. The final spectrum is therefore modified from $\Delta_i = M^{-(n+3)/6}$ to a final value of $\Delta = M^{-(n-1)/6}$. In terms of the power spectrum, $P(k) \propto k$ is transformed into $P(k) \propto k^{n-4}$. (Longair, 2008)

Once the universe becomes matter dominated, the dark matter decouples from the plasma and begins to collapse, with a spectrum that grows as $\Delta \propto a^{-2}$ once again. Silk damping (which becomes significant at cosmologically interesting scales only near recombination, as the opacity of the plasma decreases) suppresses the baryonic oscillations at small scales. However, assuming $\Omega_m \gg \Omega_b$, the dark matter is largely unaffected, and emerges with the modified power spectrum intact. The baryons later collapse into the potential wells of the dark matter distribution, giving rise to the observed large scale structure.

The reprocessed Harrison-Zel'dovich spectrum therefore appears as $P(k) \propto k$ at large scales and as $P(k) \propto k^{-3}$ at small scales. The exact shape can numerically calculated for a given set of cosmological parameters, with a transitional length scale that depends on the acoustic horizon at matter radiation equality, which scales as $(\Omega_m h^2 T^2_{\text{cmb}})^{-1}$ (Davis et al., 1985). It is therefore quite well known, given current constraints on cosmological parameters, and can be calculated exactly for a a model cosmology. In the limit of a pure cold dark matter universe and an $n = 1$ primordial spectrum, the reprocessed spectrum depends solely on Ωh and the amplitude of the initial perturbations. The actual result includes second order corrections due to baryon damping and the uncertainty on n. (Peacock & Dodds, 1994b) In general, reprocessing due to horizon crossing can be encapsulated in the transfer function, $T(k)$, such that $P(k) = P_0(k)T(k)^2$. $T(k)$ can be numerically evaluated using publicly available Einstein-Boltzmann code.[2]

After matter-radiation equality, the dark matter perturbations grow through gravitational collapse. For small perturbations, the result can be described by linear theory. These perturbations increase in amplitude by a factor which is independent of k and depends only on the evolution of the scale factor, $a(t)$. The $\Omega_m = 0$ result is $\xi \propto P \propto a^2$. The growth of perturbation in terms of *observable variables* therefore depends on the expansion history of the universe, and thus Ω_Λ, w, etc. With a generalized linear growth function, defined as $D(t) = \delta\rho(t_0)/\delta\rho(t)$, the final linear power spectrum at late times can be written

$$P(k,t) = P_0(k)T^2(k)\left(\frac{D(t)}{D(0)}\right)^2 \tag{1.17}$$

Particularly when extrapolating from the present matter power spectrum to that at an earlier time, it's common to use a slightly different definition of the growth function which has the a dependence removed. Thus,

$$P(k,z) = \left(\frac{1}{1+z}\frac{G(z)}{G(0)}\right)^2 P(k,0) \tag{1.18}$$

where analytic approximations for G can be calculated explicitly for various choices of Ω_Λ, w, α, etc. (Carroll et al., 1992; Linder & Jenkins, 2003)

The linear theory of structure formation is reasonably accurate for $\delta\rho/\rho \lesssim 1$, beyond which nonlinear effects become important. Initially over-dense regions will decelerate, begin

---

[2]eg. CMBFAST (Seljak & Zaldarriaga, 1996), CAMB (Lewis & Bridle, 2002), etc.

to collapse, and eventually become bound, virialized systems. After collapse, these regions will cease to participate in the global expansion of the universe, and the local two point correlation function scales simply as the inverse of the decreasing background density, thus $\xi \propto a^3$. The intermediate regime between linear evolution, $\xi \propto a^2$, and stable systems with $\xi \propto a^3$, is in general analytically intractable. Hamilton et al. (1991) demonstrated a semi-analytic fitting formula which accurately reproduces numerical models of nonlinear collapse (in an $\Omega = 1$ universe) by assuming a universal function of the form $\xi_{\mathrm{NL}} = f\left(a^2 \xi_{\mathrm{L}}\left(r_0\right)\right)$, relating the nonlinear over-density ξ_{NL} to the linear density ξ_{L}. Peacock & Dodds (1994a) extend this to alternative cosmologies and translate it to a set of coupled algebraic equations for the power spectrum, obtaining results which are accurate at the $\sim 10\%$ level. In practice, these analytic form is rarely used in fits to actual data. That's presumably due to the success and simplicity of the *halo model* approach discussed below, which connects the distribution of collapsed objects directly with the linear matter power spectrum in a manner which can be easily broken into discrete scales that are tractable either analytically or through simulation.

The brief outline above includes all the machinery required to translate between a primordial power spectrum, $P_0(k) = Ak^n$, and the matter power spectrum at late redshifts following nonlinear gravitational collapse, $P(k)$ (or equivalently, $\xi(r)$). The initial spectrum is obviously interesting in its own right, and as a probe of models of inflation, while the linear growth function's dependence on $a(t)$ can in principle probe the nature of dark energy.

1.4.2 Normalization and σ_8

Finally, its worth explicitly mentioning the power spectrum normalization convention. To fully characterize the power spectrum, its necessary to specify both its shape and its amplitude. In the notation of CMB experiments, the primordial spectrum is generally specified as $\Delta^2 = \Delta_R^2(k/k_0)^{n_s}$, where k_0 is a scale chosen to be well sampled and n_s is the same as n above. Fits to the primary CMB provide tight constraints on both n_s and Δ_R, with the accuracy of the later limited by the measurement of τ, the optical depth to re-ionization. The WMAP 7-year results constrain Δ_R at the 5% level, with $k_0 = .002\mathrm{Mpc}^{-1}$, for a standard ΛCDM cosmology.

For historical reasons, the matter power spectrum is conventionally normalized through the definition of σ_8, the linear RMS matter power fluctuation within an $8\,h^{-1}\mathrm{Mpc}$ radius spherical volume at $z = 0$. (A scale chosen to correspond roughly to the scale where $\sigma_m \sim 1$, introduced in Davis & Peebles (1983)) In terms of the correlation function and the power spectrum,

$$\sigma_r^2 = \xi\left(r\, h^{-2}\mathrm{Mpc}\right) \tag{1.19}$$

$$\sigma_r = \int \frac{d^3k}{(2\pi)^3} P(k) W_\sigma^2(kr) \tag{1.20}$$

where $W_\sigma(kr)$ is the Fourier Transform of a 3D top hat function of r,
$W_\sigma(x) = 3x^{-3}(\sin x - x\cos x)$. A succinct discussion of the extrapolation from Δ_R to σ_8, as well as approximate parameter scaling for realistic cosmologies can be found in the appendix of Hu & Jain (2004). In order to extract a measure of σ_8 from observation, its necesisary to extrapolate from the observed non-linear spectrum to the equivalent linear spectrum.

1.4.3 The mass function

For a given cosmology and primordial spectrum, the distribution of the dark matter in the late universe is well known. Measuring that distribution can therefore, in principle, be used to constrain cosmological parameters. In practice, this procedure is complicated by the fact that we observe not the matter distribution, nor even the baryon distribution, but rather individual structures - galaxies, cluster of galaxies - which form only in the most dense regions of the baryon distribution.

Instead of measuring the spatial distribution of objects, one can instead count the total number which exceed some observable threshold as a function of redshift. This is particularly relevant in studies of massive clusters, where Poisson noise dominates any signature that could be obtained from positional information. The general approach is to relate both the observable and cosmological parameter to a mass function, which is the number density of bound dark matter halos within a given mass and redshift range. It is also a critical component in the halo-model description discussed later, in which the spectrum (or spatial distribution) of objects is separated into a Poisson term with an amplitude determined by the integrated mass function and a one-halo term that describes the form of a single bound region.

The canonical approach to extrapolating from linear theory results the obtain the mass function, the number densities of collapsed dark matter halos as a function of time, was introduced by Press & Schechter (1974), and was reformulated and extended by Lacey & Cole (1993). Additional corrections by Sheth & Tormen (1999) and others allow for more realistic collapse geometries. This approach assumes that any density perturbation will grow according to the linear theory until it reaches a critical density contrast, Δ_c, at which point the object decouples from expansion and collapses until it is virialized by violent relaxation into a stable, bound halo. The value of Δ_c will depend on the shape of the over-dense region, traditionally treated as a uniform density sphere. (Provided an appropriate smoothing kernel is applied to the power spectrum, the results are insensitive to the detailed shape of a spherically symmetric region.) For the simple top hat model, $\Delta_c(t) = 1.686$. Throughout the linear regime, the background density evolution is determined entirely by $a(t)$, eg $\Delta \propto a \propto t^{2/3}$ for an $\Omega_m = 1$ Einstein-de Sitter universe, and thus any flat universe before dark energy becomes significant.

Assuming the mass distribution is Gaussian and described by an effective power spectrum $P(k) \propto k_{\text{eff}}^n$, the distribution of spherically symmetric objects of mass M with over-density Δ will be given by $P(M) \propto \exp[-\Delta^2/(2\sigma^2(M))]$, where $\sigma(M) = \bar{\xi}(M)^{-1/2} \propto M^{-(n_{\text{eff}}+3)/6}$

from 1.14. The result, given in Lacey & Cole (1993), is

$$\frac{dn(M,t)}{dM} = \left(\frac{2}{\pi}\right)^{1/2} \frac{\rho_0}{M^2} \frac{\Delta_c(t)}{\sigma(M)} \left|\frac{d\ln\sigma}{d\ln M}\right| \exp\left(-\frac{\Delta_c^2(t)}{2\sigma^2(M)}\right). \qquad (1.21)$$

The integral of this probability over all densities from $\Delta_c(t)$ to infinity gives the total probability at time t that an over-density of mass M will have formed a bound object. The total mass fraction in halos greater than M is then given by the simple form

$$P(> M, t) = \text{erfc}\left(\frac{\Delta_c(t)}{\sqrt{2}\sigma(M)}\right) \qquad (1.22)$$

Rather than explicitly defining Δ_c, it's conventional to define M^* such that $\Delta_c = \sigma(M^*)$. Note that M^* is therefore a function of time, and encapsulated the evolution of the mass function.

In practice, the Press-Schechter mass function provides a reasonably good fit to the distribution of masses in the vicinity of M^*, and as such serves as a useful fitting function when evaluating numerical results. For precision analysis and the extraction of cosmological parameters, however, detailed results from numerical modeling are more useful. Tinker et al. (2008), for example, have reported mass functions for a number of N-body, collisionless dark matter simulations for various ΛCDM parameter choices, producing a universal fitting function with a Press-Schechter like form.

One of the principle science goals of large scale cluster surveys is the determination of the mass function as a way to constrain large scale structure. The mass function of massive clusters, which form last and thus are sensitive to dark energy, can provide strong and independent constraints on the dark energy parameters and σ_8. At present, the tightest constraints using this method are from Vikhlinin et al. (2009), who use two sample of (37,49) x-ray identified clusters with a mean redshift of (0.55, 0.05) to constrain parameters. Using just the cluster sample, they constrain a combination of $\sigma_8\Omega_m^{0.47}$; with the addition of CMB and H_0 prior on Ω_m (as well as the weak WMAP CMB prior on σ_8), they find $\sigma_8 = 0.786 \pm 0.011$. Constraints on dark energy parameters offer a significant improvement over the CMB+SN+BAO constraint; assuming flat ΛCDM and a constant equation of state, they find $w = -0.991 \pm 0.045(\text{stat}) \pm 0.039(\text{sys})$, as well as providing small improvements in the constraint on an evolving w. Recent results from an SPT survey of 21 SZ-selected clusters find consistent but weaker constraints: $\sigma_8 = 0.81 \pm 0.09$ and $w = 1.07 \pm 0.29$ when combined with WMAP results. (Vanderlinde et al., 2010) The dominant source of error is due to uncertainty in the cluster mass scaling relation, and we therefore expect significant improvements with additional X-ray observations of SPT cluster candidates.

1.4.4 Baryons and large scale structure

Given the distribution of matter in dark halos as a function of redshift, all that remains in order to connect observations to cosmology is to describe the distribution of baryons within those halos. This turns out to be a more difficult task than one might naively imagine.

When considering numerous objects, such as individual galaxies or quasars, a fruitful strategy is to extract statistical information from their spatial distribution. This can be done in three dimensions, using the discrete two-point correlation function, ξ_{gal}, defined such that the number of galaxies within a volume element a distance r from another galaxy is given by

$$dN(r) = N_0 \left[1 + \xi_{\text{gal}}(\mathbf{r}) \right] dV \tag{1.23}$$

The total number of galaxies within the volume element is then an integral over r. This formulation has the advantage that it is computationally straightforward to apply to discrete data sets, provided one has reliable redshifts for the objects in a survey. This obviously requires either spectroscopic data, or well calibrated photometric redshifts for the entire sample. Empirically, the result is well described by a power-law of the form

$$\xi_{\text{gal}}(r) = \left(\frac{r}{r_0} \right)^{-\gamma} \tag{1.24}$$

where $r_0 \sim 5 h^{-1}\,\text{Mpc}$ and $\gamma \sim 1.8$ (Davis & Peebles, 1983)

An alternative is the projection of ξ onto the two-dimensional sphere to produce the two-point correlation function, defined such that

$$N(\theta)d\Omega = n_g \left[1 + w(\theta) \right] d\Omega \tag{1.25}$$

where, assuming no evolution with redshift and a power law as above, the corresponding result would be $w(\theta) = \theta^{-(\gamma-1)}$. Finally, one can instead directly measure the power-spectrum of the distribution of objects, which connects to ξ exactly as in the matter distribution discussed above.

Naively, one might imagine that the likelihood of finding a galaxy in a given location scales linearly with the dark matter density in that location, in which case $\xi_{\text{gal}} = \xi$. In practice, this is a spectacularly poor description. A better model allows for the likelihood for galaxy formation is itself density dependent. This makes intuitive sense - if galaxies tend to form in only the densest regions, then they will preferentially form in regions which are maxima at multiple k-vectors, and will therefore be more clustered at all scales than the matter distribution itself. (The famous analogy by Kolb and Turner is that the highest mountains in the world are clustered in the Himalayan plateau.)

Historically, a common approach is to introduce a single bias parameter, such that $P_{\text{gal}}(k) = b^2 P(k)$ and $\xi_{\text{gal}} = b^2 \xi_{\text{gal}}$. (Kaiser, 1984) In practice, in addition to varying widely depending on which class of objects is chosen (including luminosity cuts), b is also strongly scale dependent. An approach which provides accurate fits with few parameters over a wide

range of physical scales, both in simulations and observed data, is the so called "halo model." (The language of which is implicit in much of the discussion above.)

1.4.5   The Halo Model

The halo model assumes that essentially all of the matter in the universe is in the form of collapsed, virialized dark matter halos, and that baryonic features are formed in a way that depend only on the properties of the individual halo in which they occur. (Peacock & Smith, 2000; Seljak, 2000; Cooray & Sheth, 2002)

The power spectrum of any observable can then be written to first order as a sum of a two components, a one halo term and a two-halo term, corresponding to the correlations between objects within a single dark matter halo and the correlation between individual halos, respectively. The total power spectrum can then be schematically written as

$$\Delta^2\left(k\right) \equiv \frac{V}{2\pi^2} k^3 P\left(k\right) = {}_{1h}\Delta^2 + {}_{2h}\Delta^2 \tag{1.26}$$

$$\Delta^2_{\text{gal}}\left(k\right) = B^2(k, M)\Delta^2 = {}_{1h}\Delta^2_{\text{gal}} + {}_{2h}\Delta^2_{\text{gal}} \tag{1.27}$$

Here ${}_{1h}\Delta^2$ depends only on the halo mass profile (which in general may be a function of M) and the halo number density. ${}_{1h}\Delta^2$ is the usual linear matter power spectrum multiplied by a function which includes the halo profile, halo number density, and a halo bias parameter, $b(M, k)$. For the case of galaxy clusters, which will be discussed later, the two-halo term is fully determined by assuming a Poisson distribution of sources with a given mass function. (Discussed in more detail in section 1.6.1 for more detail.)

The two galaxy terms are similar, except that both include the Halo Occupation Distribution (HOD). The simplest HOD assumes that all halos above some mass threshold M_{min} will form a single central galaxy, and a number of satellite galaxies which scale as M/M_{sat} to some power and distributed according to the halo mass profile. The relative contribution of the 1 and 2-halo terms in the galaxy power spectrum depends on the HOD of the particular sample, leading to complicated bias term. At the largest scales, where the halo mass profile is insigificant, this can be expanded to a two-parameter form, with a scale and mass-independent bias term, as $\Delta^2_{\text{gal}}\left(k\right) \sim b^2\delta_{\text{L}}^2 + (k/k_1)^3$. (Schulz & White, 2006) More complicated halo functions are possible, and any number of choices lead to few-parameter semi-analytic models which can be fitted to survey data, as in figure 1.2

If one assumes the goal of large scale structure observations is to test cosmological models, the need to fully specify the halo density profile and HOD are disheartening. Martinez & Saar (2002) lists the usual assumptions employed in halo model calculations. In addition to the assumption about virialized collapsed halos and an initial power spectrum of Gaussian fluctuations, it's generally assumed that halos have a universal density profile (eg. Nevaro, Frenk & White (NFW)) with a core radius that depends only on mass, a well defined mass function (eg. extended Press-Schechter) and calculable halo bias term ($b(k, M)$).
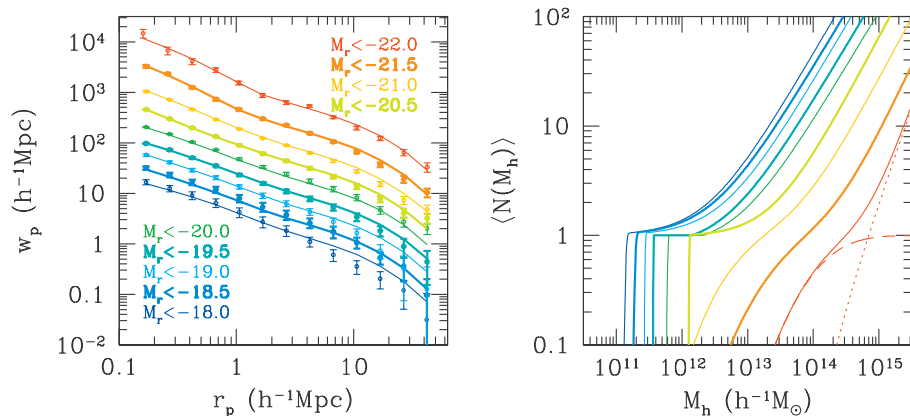
Figure 1.2 Angular correlation function and a fitted HOD model for various luminosity thresholds for a sample of 700000 galaxies from the Sloan Digital Sky Survey (SDSS) Seventh Data Release (DR7). The left panel shows data and best-fit 3-parameter HOD model, assuming ΛCDM cosmology with $ns = 0.95$ and $\sigma_8 = 0.8$. Individual data sets are staggered in amplitude for plotting. The right panel shows the fitted halo occupation functions. Dashed and dotted curves on the far right show the central and satellite galaxy contribution to the right-most total curve. Figure from (Zehavi et al., 2010)

Given all of these ingredients, one can attempt to relate the universe today to fundamental cosmological parameters. In practice, that procedure is extremely complicated at the mass scale of galaxies, where merger histories are complicated and feedback from astrophysical processes can dominate the dark matter dynamics. For very massive objects (clusters and groups with $M \gtrsim \times 10^{13} M_\odot$) distributed at scales of tens of Mpc, though, the picture is less bleak. By employing observables other than galaxy counts (or, in addition to galaxy counts), it is possible to avoid confronting one of the least accessible aspects of halo model calculations, the relationship between the dark matter distribution and galaxy populations.

1.4.6   Galaxy cluster halo profiles

Except at the very largest scales (eg. BAO observations), the one-halo term contributes significantly to the observable matter power spectrum, and understanding the form of halos and their observable tracers is required in order to extract physical information from measurements of that power spectrum. In general, a parametric model based on simple analytic arguments or dark matter simulations is used to describe the dark matter profile, which is assumed to be a universal function of halo mass. Some prescription is then required to map the distribution of observables (eg. density and temperature of gas, in the case of SZ science) onto that dark matter distribution.

One of the first treatments of halo profiles is the β model, originally derived by assuming

an isothermal distribution. The result is a density profile that scales as $(1 + r^2/r_{\text{core}}^2)^{-3\beta/2}$. (Cavaliere & Fusco-Femiano, 1976) This profile reproduces the uniform central density and power-law fall off at intermediate radii observed in real clusters, and its has obvious analytic appeal, however it does a poor job at fitting the regions of clusters beyond about R_{2500}. (Vikhlinin et al., 2005; Piffaretti et al., 2005).

A contemporary, widely used halo dark matter distribution model is the Navarro Frenk and White (NFW) profile. (Navarro et al., 1996, 1997) Simulations of collisionless cold dark matter are fit with a universal profile of the form

$$\frac{\rho(r)}{\rho_{\text{crit}}} = \frac{\delta_c}{(r/r_s)(1 + r/r_s)^2} \qquad (1.28)$$

where the scale radius, r_s, is defined as R_{200}/c, and the characteristic over-density, δ_c, is related to the dimensionless constant c by the requirement that the total mass within R_{200} be 200 times ρ_{crit}, thus

$$\delta_c = \frac{200}{3} \frac{c^3}{(\ln(1 + c) - c/(1 + c))}. \qquad (1.29)$$

The NFW profile thus includes only a single free parameter, c (or, equivalently r_s or δ_C), which depends on halo mass through the mass dependence of the formation time of bound objects. In general, the mass in large halos is less concentrated than in small halos. The authors find this profile provides a reasonable fit to simulated halos over four orders of magnitude from large clusters to small galaxies, although other simulation results disagree.

More generally, extended parametric versions of the NFW profile can be used to fit to observed to halos. For example, the addition of one free parameter, α, such that

$$\frac{\rho(r)}{\rho_{\text{crit}}} = \frac{\delta_c}{(r/r_s)^\alpha(1 + r/r_s)^{3-\alpha}} \qquad (1.30)$$

reduces to the NFW result when $\alpha = 1$, and can be adjusted to reproduce the steeper results reported by Moore et al. (1998), Jing & Suto (2000), and others. (Komatsu & Seljak, 2001).

An even more general approach by Nagai et al. (2007) includes two additional free parameters to independently adjust the slope at the innermost and outermost regions of the halo in order to fit to X-ray luminosity profiles of a catalog of nearby clusters. The resulting Generalized NFW (GNFW) profile, parametrized in terms of pressure and R_{500} (a radius well sampled by x-ray observations) is given by

$$P = \frac{P_0}{(r/r_s)^\gamma(1 + (r/r_s)^\alpha)^{(\beta-\gamma)/\alpha}} \qquad (1.31)$$

where r_s has been redefined as R_{500}/C_{500} and C_{500} is an adjustable constant as before.

To compare dark matter profiles to observation (except in the case of lensing, which is dominated by the dark matter distribution itself), its necessary to connect the matter

distribution to the pressure and density of the intracluster gas. Komatsu & Seljak (2001) begin with the modified NFW profile of equation 1.30, assume the equation of state of the gas can be represented by a polytrope with a single index within the core, $P = \rho T = \rho^\gamma$, and require that the gas density trace the dark matter density in the outermost regions of the halo. The resulting temperature and pressure profile can then be compared to hydrodynamic simulations, and to either X-ray or SZ maps of individual clusters. Arnaud et al. (2009) start with the generalized NSF profile of equation 1.31, and calibrate the results against a combination of observed X-ray clusters and simulation results to derive constraints on α, β, and γ. (β, which becomes significant only at the largest radii, is determined solely from simulations. The other parameters are constrained by the REXCESS sample of nearby clusters.) The authors then use the results to generate predictions for the SZ profile and integrated Y_{SZ} amplitude as a function of cluster mass.

1.4.7   Other observables

One strategy for deriving cosmologically useful constraints from large scale structure is to probe the matter distribution with something other than galaxy counts. Several observables have been considered. In addition to constraints from X-ray and SZ observations of clusters, which will be discussed later, these include the large scale velocity fields of galaxies, weak gravitational lensing, Lyman-alpha forest measurements, and 21-cm observations.

One of the earliest methods employed to measure the mass distribution itself is to measure the proper motion of galaxies. By assuming that any primordial proper motions will be damped by expansion, and that any remaining large scale motions result from the linear evolution of gravitational potential wells at the largest scales, one can directly relate the velocity flows to the matter distribution. Of course, in order to do so it is necessary to obtain independent redshift and velocity measurements for large sample of galaxies. The only realistic candidate for suitable tracer of velocity is is the proper motions derived using the Tully-Fisher velocity-luminosity relation for spectroscopically observed spiral galaxies. The resulting velocity field can either be correlated with number-density counts in order to measure the effective bias parameter, as in Nusser & Davis (1995), or for a sufficiently large data set, used independently to derive a bias-free estimate of the mass distribution. Nusser & Davis (2011) analyze 3000 galaxies from the SFI++ data set and conclude that the results are consistent with WMAP7 best fit ΛCDM parameters. Relaxing the prior only on σ_8, they find $\sigma_8 = 0.86 \pm 0.11$, consistent with other measurements but an order of magnitude less precise than can be obtained from cluster counts.

An alternative approach is to measure the matter power spectrum through lensing, the deflection of light from a source due to the gravitational influence of intervening matter. Lensing has the advantage that it is sensitive to the total matter distribution, and one doesn't need to account for galaxy bias or model gas distributions. (Alternatively, one can measure bias through galaxy lens-map correlations.) Weak lensing studies, in which perturbations to the distribution of background sources (or their shapes) are measured over

large surveys are, in principle, a sensitive and direct probe of the matter distribution at late times. However, massive surveys are required in order to achieve interesting signal-to-noise. (Kaiser, 1998) When combined with lensing source redshift information, as from massive photometric surveys, they can also potentially constrain dark energy parameters in a way nearly independent of other methods. (Hu & Jain, 2004) In principle, stacked lensing maps of individual clusters can also be used to test simulation-based halo mass profiles and mass-richness relations. (Johnston et al., 2007)

The best current constraints on σ_8 from weak lensing measurements is from the Canada-France-Hawaii Telescope Legacy Survey (CFHTLS) data. Lensing amplitude, just like mass function results from cluster counts, constrains a combination of σ_8 and Ω_m. Combined with WMAP3 constraints on Ω_m, the current best constraint is $\sigma_8 = 0.771 \pm 0.029$, which is consistent with but weaker than recent cluster survey results, but offers a significant improvement over the WMAP-only constraint. (Hoekstra et al., 2006; Fu et al., 2008)

Another potentially powerful probe of large scale structure is the Lyman α (Lyα) forest. UV photons emitted from Quasars at high redshift are absorbed by the 1216 ÅLyα line in neutral hydrogen along the line of sight. By measuring the depth and redshift of absorption lines, the distribution of material along the line of sight can be inferred. (Rauch, 1998) By probing the least dense structures in the Inter-Galactic Medium (IGM), Lyα measurements can, in principle, recover the matter power spectrum at scales smaller than 10 Mpc where galaxy counts are complicated by nonlinear effects. (Croft et al., 1998) With sufficient number of high resolution spectra, combined with simulations, one can in principle obtain constraints on σ_8 and a combination of Ω_m and w from the redshift distribution of features; however, in practice, uncertain gass physics and particularly complications due to feedback from nearby galaxies complicate the analysis.(Zaldarriaga et al., 2001; Weinberg et al., 2003) Given spectra for very large numbers of objects, one can also include spatial information in the analysis, mapping out lines of sight through the local 3D volume, and potentially measuring both the matter power distribution at 100 Mpc scales and resolving the BAO feature. Results from the Baryon Oscillation Spectroscopic Survey (BOSS)/SDSS survey, which will eventually include 160000 quasar spectra, are expected soon. (Ho et al., 2010; Aihara et al., 2011; Schlegel et al., 2009).

Finally, there is the 21 cm wavelength spin-flip transition in neutral hydrogen, which has long been the most powerful probe of gas density in our own galaxy and other nearby galaxies. High redshift 21-cm line observations which aim to constrain the onset and duration of reionization are underway, though no cosmologically interesting results have been published yet.(Bowman et al., 2006) At lower redshifts, experiments have been proposed which employ the 21 cm signal to measure the BAO feature as a function of redshift, using the correlation between netural hydrogen density and total density to produce a (biased) 3D map of the gas density. In essence, the result is a weighted average of galaxy counts and the distribution of structures which contribute to the Lyα forest. Several instruments currently in design or under construction expect to significantly constrain the BAO at redshifts beyond optical

surveys, including The Canadian Hydrogen Intensity Mapping Experiment (CHIME)[3] and the The Cylindrical Radio Telescope (CRT). (Seo et al., 2010)

1.5 The SZ effects

The scattering of CMB photons from free electrons in the plasma of the intergalactic medium can be seperated into two processes, the thermal Sunyaev-Zel'dovich (tSZ) and the kinetic Sunyaev-Zel'dovich (kSZ) effects. The thermal Sunyaev-Zel'dovich (SZ) Effect (tSZ), is the inverse Compton scatting of CMB photons from the energetic electrons in the plasma of galaxy clusters and groups, first described by Sunyaev & Zeldovich (1972, 1970). Individual photons are blue-shifted to higher energies, which distorts the spectrum of the CMB. The kinetic SZ Effect (kSZ) is a Doppler shift imparted on CMB photons which scatter from the peculiar motion of electrons with respect to the CMB rest frame. This term includes both a contribution from the Intra-Cluster Medium (ICM) associated with clusters and groups, often called the non-linear part, and a contribution from large scale flows on linear scales, the Ostriker Vishniac (OV) effect. (Ostriker & Vishniac, 1986; Vishniac, 1987).

The sum of the SZ effects can be expressed as a fractional change in power (in CMB Temperature units) along a particular line of sight as

$$\frac{\Delta T}{T_{\text{CMB}}} = \left(\frac{\Delta T}{T_{\text{CMB}}} \right)_{\text{tsz}} + \left(\frac{\Delta T}{T_{\text{CMB}}} \right)_{\text{ksz}} = f_\nu y - b. \tag{1.32}$$

The first term, the tSZ, can be separated into two parts, one which depends on the integrated electron pressure along the line of sight, the other which accounts for the frequency dependence.

The first of these, the dimensionless Compton y parameter, is given by

$$y \equiv \frac{k_B \sigma_T}{m_e c^2} \int n_e T_e dl = \int \theta_e d\tau \tag{1.33}$$

where

$$\theta_e \equiv \frac{k_{\text{B}} T_e}{m_e c^2} = 1.96 \times 10^{-3} \left(\frac{k_{\text{B}} T_e}{\text{keV}} \right) \tag{1.34}$$

is a dimensionless temperature parameter and the optical path along the path dl is given by

$$d\tau \equiv \sigma_{\text{T}} n_e dl = 2.05 \times 10^{-3} \left(\frac{n_e}{10^{-3} \text{ cm}^3} \right) \left(\frac{dl}{\text{Mpc}} \right). \tag{1.35}$$

The tSZ frequency dependence is given by

$$f_\nu \equiv x_\nu \coth(x_\nu/2) - 4, \quad x_\nu \equiv h\nu/(k_{\text{B}} T_{\text{CMB}}). \tag{1.36}$$

---

[3]http://www.phas.ubc.ca/chime/

For a CMB spectrum, there is a null at $\nu = 218\,\mathrm{GHz}$ associated with blueshifting photons across the peak of the Planck curve. The tSZ appears as a decrement at lower frequencies and an increment at higher frequencies. There are additional, small corrections due to relativistic effects. For even the largest galaxy clusters, these corrections amount to a few percent of the SZ signal except very near the null. (Itoh et al., 1998)

The kSZ effect has no frequency dependence, and an amplitude which depends on the integrated line-of-sight velocity, expressed as a dimensionless velocity parameter b, where

$$b \equiv \frac{\sigma_{\mathrm{T}}}{c} \int n_e v_{\mathrm{los}} dl = \int \beta_{\mathrm{los}} d\tau, \tag{1.37}$$

$$\beta_{\mathrm{los}} \equiv \frac{v_{\mathrm{los}}}{c} = 3.34 \times 10^{-4} \left(\frac{v_{\mathrm{los}}}{100 \text{ km/s}} \right). \tag{1.38}$$

Before moving on to consider the contribution of SZ power from unresolved sources to the high-ℓ spectrum of the CMB, its worth noting a few significant features of the SZ equations.

First, for a typical galaxy cluster, the tSZ amplitude is expected to be an order of magnitude larger than the kSZ, and can be several hundred μK_{CMB} for the centers of large clusters, where gas temperatures reach $T \sim 10\,\mathrm{keV}$. Carlstrom et al. (2002). The unique frequency signature makes distinguishing between SZ signal and foregrounds straightforward. (Discrete astrophysical sources which produce a point-like power decrement would be surprising.) As the kSZ has the same spectrum as the CMB, it can only be distinguished from primordial CMB fluctuations by its spatial scale, making detection of the kSZ contribution from individual objects harder still. Figure 1.3 shows a map and radial profile of a massive cluster observed with SPT.

Second, there is no redshift dependence in the SZ amplitudes, unlike, say, X-ray luminosity or the optical and IR luminosities of galaxies in clusters. A resolved cluster will have exactly the same amplitude at any redshift, which makes the SZ an attractive technique for obtaining uniform surveys of high redshift clusters. The only role distance plays in detection with an SZ survey is through the changing angular diameter distance of clusters, which scales with cosmology as in equation 1.9. Over the range of redshifts over which galaxy cluster surveys are cosmologically interesting, the angular size of clusters changes by only a small amount.

Third, the pressure and density scaling of the tSZ and kSZ are worth noting. The tSZ amplitude scales as $\int n_e T d\updownarrow$, which is the integrated gas pressure along the line of sight, and this is sensitive to the largest and most dense objects: large clusters at redshift $z \lesssim 1$ or so. Further, because the SZ has a different scaling from the X-ray luminosity, which is proportional to $\int n_e^2 \Lambda_{eH} d\updownarrow$ (where Λ_{eH} is the cooling function), the two observations can in principle be combined to constrain cluster properties. The kSZ, on the other hand, scales only as $\int n_e v$. Its amplitude is therefore much more sensitive to populations of low-mass groups, and in particular to correlation between density and velocity in the field. As a result,
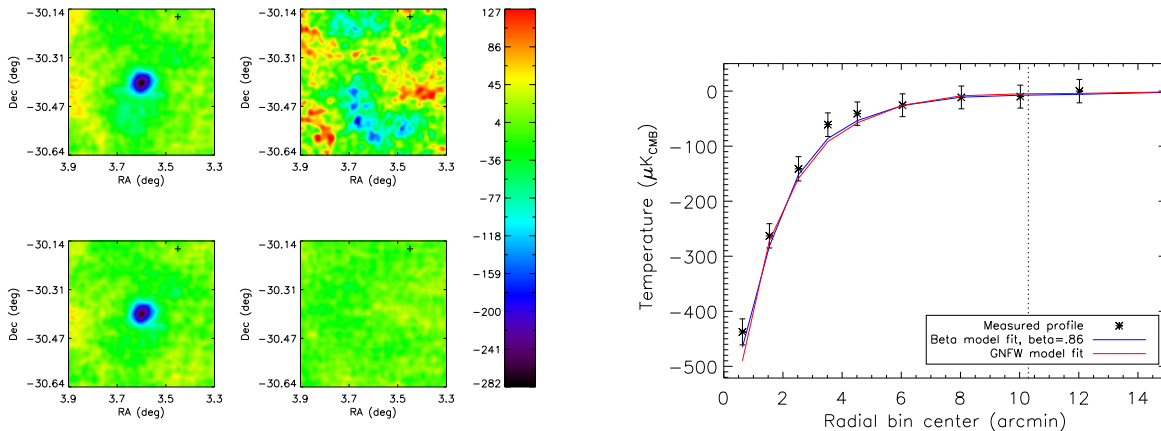
Figure 1.3 SPT observations for cluster A 2744. The four maps are 150 GHz (upper left), 220 GHz (upper right), band subtracted maps (lower left), and a scan-based jackknife map (lower right). Units are μK_{CMB}. Figure from Plagge et al. (2010)

the kSZ has the potential to constrain the high redshift universe, from reionization through the present.

1.6   SZ contributions to the CMB power spectrum

1.6.1   Early SZ results

Now, we turn our attention from the SZ signal arising from a discrete galaxy cluster to the statistical detection of SZ power due to an ensemble of unresolved sources. As in most fields, there has been significant feedback between theoretical modeling and experimental results in quest to measure, and extract cosmologically useful information from, the SZ power spectrum. The last decade has seen exponential growth in both the sensitivity with which measurements of the high-ℓ CMB spectrum constrain the SZ power and the detail and breadth of astrophysics included in models for the SZ spectrum.

In principle, the SZ power spectrum derived using a halo model approach includes both a one-halo term and a two-halo term, just as in the case of galaxy counts. However, the two-halo term, also called the "clustering component", contributes at most a few percent of the total tSZ power at $\ell \geq 2000$ and can therefore be neglected. (The comparably large amplitude of the primary CMB anisotropy at low-ℓ, where the clustering term would otherwise become significant, means that only the one-halo term need be considered for any realistic experiment.) (Komatsu & Kitayama, 1999)

Komatsu & Seljak (2002) provided an early, well motivated analytic prediction for the SZ power spectrum at high-ℓ as well as analytic scaling relations for various cosmological parameters. Using a halo model approach and keeping only the one-halo term, the tSZ power can be written in a rather straightforward way as a Poisson power term due to the number density of halos, multiplied by the transform of a single halo, and integrated over mass and redshift. Thus,

$$C_\ell = g_\nu^2 \int_0^{z_{\max}} dz \frac{dV}{dz} \int_{M_{\min}}^{M_{\max}} dM \frac{dn(M,z)}{dM} |\tilde{y}_\ell(M,z)|^2 \qquad (1.39)$$

where g_ν is the spectral SZ term, V is the co-moving volume at redshift z, and $\frac{dn(M,z)}{dM}$ is the co-moving halo mass function, and $\tilde{y}_\ell(M,z)$ is the 2D Fourier transform of the projected Compton y-parameter for a single halo. For a given set of cosmological parameters, and on the mass scales of groups and clusters which contribute significantly to the total power, everything except the last term is well understood. The term, $\tilde{y}_\ell$, however, is much less well constrained. Schematically, the procedure is straightforward: if a cluster of a given mass at a given redshift has a known gas pressure profile, the Compton y-parameter is fully defined, and can simply be projected into 2D and converted into its Fourier space equivalent. In practice, the gas pressure profile is poorly constrained, especially when it comes to low-mass cluster and group scale and high redshifts, where deep X-ray observations are sparse.

Komatsu & Seljak (2002) employed an analytic universal pressure profile based upon an NFW density profile and assuming hydrostatic equilibrium and a universal polytropic equation of state for the gas. With a few additional assumptions, the authors derive a prediction for the tSZ spectrum, and show that the power spectrum amplitude scales roughly as $C_\ell \propto \sigma_8^7 (\Omega_b h)^2$ for a flat universe with $\Omega_m \lesssim 0.4$ and $\sigma_8 \sim 1$. The strong dependence on σ_8 lead the authors to conclude that the SZ amplitude could provide leading constraints on that parameter, compared to results obtained from cluster counts and weak lensing.

Because they made the (at the time reasonable) assumption that $\sigma_8 \sim 1$, the authors predicted a much larger value of the tSZ amplitude than has been observed. None the less, their principal results remain valid, and are worth noting. In addition to the strong scaling of the tSZ amplitude with σ_8, weaker scaling with $\Omega_b h^2$, and comparably slight variation with other parameters, there are several important points. First, the majority of the tSZ power originates at between 0.2 and 0.4 times the virial radius of the halo, and is therefore expected to be less sensitive to the details of dense cluster cores, which are hard to model, and the gas distribution in the outermost regions of clusters, which are hard to calibrate due to the paucity of X-ray photons from these regions. Second, at $\ell = 3000$, the tSZ power peaks at roughly $z \sim 1$, with around half the power coming from halos at higher redshift. Third, roughly half of the tSZ power is due to halos with $M < 2 \times 10^{14} M_\odot$. (And, in general, higher ℓ power is associated with halos at higher redshift and lower mass.) These last two points indicate that a large part of the tSZ contribution comes from objects for which statistically convincing X-ray observations do not exist, and thus predictions depend

critically on simulations or analytic treatments which extrapolate from low-redshift and high-mass catalogs. To derive meaningful cosmological constraints from the tSZ spectrum is therefore a significant challenge. (It is worth noting that Komatsu and Seljak draw quite the opposite conclusion: that the significant contribution from nearby large clusters and steep σ_8 scaling make the tSZ power spectrum a prime candidate for constraining σ_8. It's only due a combination of the dramatically improved constraints on σ_8 from low-redshift cluster catalogs combined with CMB and H_0 parameters, and the relatively low value of σ_8 which decreases tSZ signal-to-noise in the presence of point sources and the primary CMB, that the prospect seems less likely.)
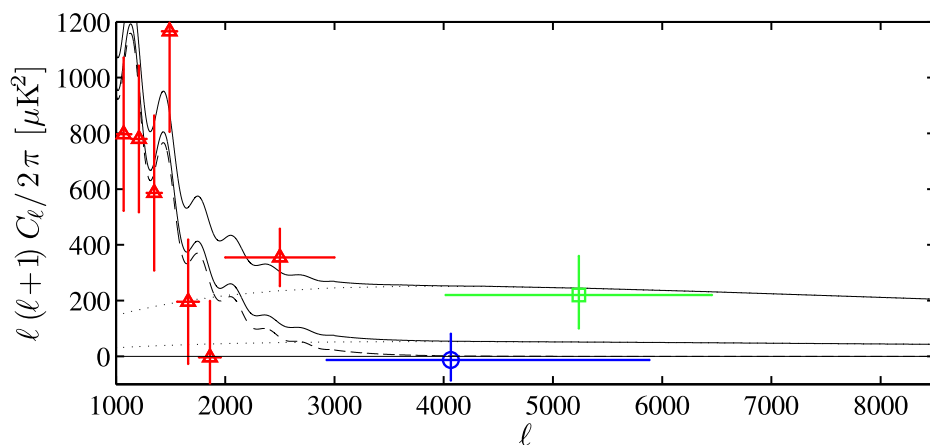
Figure 1.4 Recent measurements of the power at $\ell > 2000$ from three interferometers operating at $30\,GHz$ after point source subtraction. Blue circle is from Sunyaev-Zel'dovich Array (SZA), green square is from the Berkeley-Illinois-Maryland Association interferometer (BIMA), red triangles are from Cosmic Background Imager (CBI). Error bars report the 68% confidence level assuming Gaussian sample variance, which significantly under-estimates the true variance. Dashed black line is the WMAP 5-year data release (WMAP5) spectrum and upper and lower solid lines are the sum of the primary and modeled tSZ spectrum for $\sigma_8 = 0.8$ and $\sigma_8 = 1.0$, respectively. For comparison to the $150\,GHz$ plots in section 6, the tSZ component should be scaled by $f_\nu(150\,\mathrm{GHz})/f_\nu(30\,\mathrm{GHz}) = 0.49$. Figure from Sharp et al. (2010).

Early measurements of the high-ℓ power spectrum at $30\,\mathrm{GHz}$ by the CBI experiment reported a $(3.1\,\sigma)$ detection of power greater than the CMB primary spectrum at $2000 \leq \ell \leq 3500$. The reported amplitude was a factor of 2-3 larger than models predict for $\sigma_8 = 0.8$, with a maximum likelihood value of $\sigma_8 = 1$. (Mason et al., 2003; Bond et al., 2005) Observations at smaller scales with the BIMA, also at $30\,\mathrm{GHz}$, found a consistent result at $\ell_{\mathrm{eff}} \sim 6800$ Dawson et al. (2002). A combined analysis of the two results using the Komatsu and Seljack analytic power spectrum placed a 95% confidence limit $\sigma_8(\Omega_b h/.035)^{0.29} = 1.04 \pm 0.12$, in significant tension with recent constriants on σ_8. The most recent results from CBI

include a joint analysis of the CMB primary spectrum find a best fit template scaling of 3.5 ± 1.3 times the KS value for $\sigma_8 = 0.8$, resulting in a limit of $\sigma_8 = 0.922 \pm 0.047$ at 68% confidence.(Sievers et al., 2009) The final results from the BIMA survey find an excess of $220^{+140}_{-120} \, \mu\text{K}^2$ at $\ell_{\text{eff}} = 5237$, though because of the small survey area sample variance allows for values of σ_8 which are consistant with both the CBI and other data, $\sigma_8 = 1.03^{+0.20}_{-0.29}$.(Dawson et al., 2006) More recently, the SZA, also operating at $30 \, GHz$, has published an upper limit of $155\mu\text{K}^2$ at 95% confidence at $\ell_{\text{eff}} = 4066$, consistant with BIMA and in slight tension with the CBI result. The authors find the result largely consistant with $\sigma_8 = 0.8$, but also report significant differences between sets of maps generated using four different simulations which are larger than the statistical error in any given set.(Sharp et al., 2010) Figure 1.4 shows the final published data points for these experiments.

1.6.2   Recent SZ results

At higher frequencies, several experiments have measured the power spectrum at $\ell \geq 2000$ in recent years. Operating at $150 \, \text{GHz}$, the ACBAR (Reichardt et al., 2009a) and QUaD (Friedman et al., 2009) experiments have measured the damping tail of the primary CMB spectrum at $\ell \leq 3000$. Both results are consistent with any realistic model of SZ power, as well as with a model that includes only the primary CMB power. At smaller scales, $150 \, \text{GHz}$ measurements with Bolocam (Sayers et al., 2009) and The Atacama Pathfinder Experiment SZ Camera (APEX-SZ) (Reichardt et al., 2009b) constrain power beyond the primary CMB to less than 1080 and 105 μK^2, respectively, in a large band at $3000 \leq \ell \leq 10000$. Errors on σ_8 from the APEX result are dominated by non-Gaussian sample variance due to the relatively small sky coverage, (~ 1 square degree), and the final value constraint of $\sigma_8 < 1.18$, provides little constraint when compared to other data sets, such as those derived from cluster counts.

In anticipation of the deployment of the The Atacama Cosmology Telescope (ACT) and SPT instruments, Sehgal et al. (2010) produced a new, detailed model for the expected SZ power spectrum. The SZ component of this model begins with an unlensed WMAP5 map to which has been added a Gaussian realization of the best-fit WMAP5 power spectrum at small angular scales. To model the intervening structure, the authors begin with an N-body dark matter simulation in an $L = 1000 \, h^{-1}\text{Mpc}$ box. The box is replicated 8 times to create a full-sky simulation. Simulation parameters are chosen to match WMAP5, with $\sigma_8 = 0.8$ and $\Omega_b = 0.044$, and assuming a cosmological baryon fraction in all halos. Using a smoothed representation of the particle distribution at an appropriate radius in each time-step of the simulation, the model lensing potential is calculated and used to generate a lensing correction to the CMB maps. The SZ signals are modeled in three different ways. For halos with $M > 2 \times 10^{13} M_\odot$ and $z < 3$, dark matter halos are identified in the simulation and converted to a pressure and momentum profile by applying the gas physics model from Bode et al. (2009). This model assumes a polytropic equations of state ($\Gamma \equiv d \ln P / d \ln \rho = 1.2$), hydrostatic equilibrium, and allows for variable star formation and non-thermal pressure support with values calibrated against the X-ray catalogs of observed low-redshift clusters

and groups from Vikhlinin et al. (2006) and Sun et al. (2009). For smaller halos at $z < 3$, which are less well sampled by the particle mesh, an alternative approach is used. Assuming virial equilibrium, the velocity distribution of dark matter particles is directly mapped to a pressure and momentum field. For halos at $z > 3$, the gas is assumed to trace the dark matter distribution with a uniform value of $T_e = 10^4$ K. Reionization is assumed to occur instantaneously, and the so-called patchy contribution due to the correlations between the momentum field and ionization during a finite width reionization is not included.

By tracing rays through this ensemble gas distribution, the authors produce simulated maps and power spectra for both the tSZ and kSZ, as well as modeled estimates for various foregrounds. Scaled to the SPT 150 GHz band, this model predicts the tSZ power will be $D_{3000}^{tSZ} = 7.5 \, \mu\text{K}^2$ at $\ell = 3000$, with very broad D_ℓ dependence over the range from $1000 \leq \ell \leq 10000$. The predicted kSZ power is $D_{3000}^{kSZ} = 2.05 \, \mu\text{K}^2$. The prediction for both tSZ and kSZ are shown, along with several other templates discussed later, in figure 6.5. The tSZ result is comparable to the older Kamatsu & Seljak (KS) model, except that it predicts slightly less power at low ℓ. (A difference of $< 15\%$ over $1000 < \ell < 5000$).
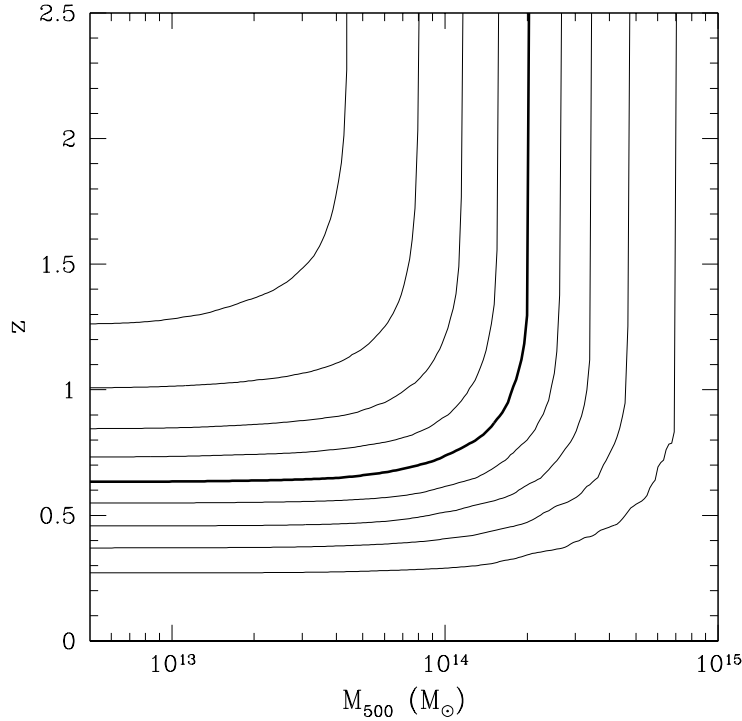
Figure 1.5 The fraction of the tSZ power at $\ell = 3000$ as a function of minimum mass and maximum redshift for the Sehgal et al. (2010) (S10) model. From bottom to top, the curves are for $PDF(> M_{500}, < z) = [0.1, 0.9]$ in increments of 0.1. Figure from Trac et al. (2011).

Following the publication of this model, both the SPT and ACT collaborations gave

published observations of the high-ℓ power spectrum. The first SPT power spectrum results were published in Lueker et al. (2010) (L10) and Hall et al. (2010), using observation at 150 and $220\,$GHz of $100\,$deg^2 in the southern sky. After combining the two bands to remove dusty foregrounds, the result is a constrain on the linear combination of tSZ and ksZ power. In units of $D_\ell = C_\ell\,\ell(\ell+1)/2\pi)$ at a multipole of $\ell = 3000$, the result is $D_{3000}^{tSZ} + 0.46 D_{3000}^{kSZ} = 4.2 \pm 1.5\,\mu\text{K}^2$. The result is consistent with all the experimental results mentioned above, except for the CBI measurement, with which it disagrees at 2.6σ. It is also in significant tension with the S10 and KS models for values of σ_8 allowed from cluster counts. Expressed as a constraint on A_{sz}, the ratio of the observed value of the SZ power to the model prediction for $\sigma_8 = 0.8$, the result is 0.42 ± 0.21.

Following the publication of L10, the ACT collaboration published the power spectrum at $600 \le \ell \le 8000$ using observations of $228\,$deg^2 at $148\,GHz$. Their result is a constraint on $A_{sz} < 1.63$ at 95% confidence, corresponding to $\sigma_8 < 0.86$, consistant with both the SPT results and with $A_{sz} = 1$.

The departure of the L10 result form prediction suggests that either σ_8 is significantly lower than required by cluster counts and other large scale structure constraints, or that models are over-estimating the amount of power in the tSZ spectrum. One intriguing possibility is that the S10 model over-predicts the pressure of the gas in the clusters and groups which contribute to the tSZ effect. The cluster model used is calibrated against X-ray observations, however the sample size is small, and the redshift range cover only a small portion of the total range which contributes to the tSZ power: 13 clusters with a maximum redshift of 0.23 for the high mass sample, and 43 groups with a maximum redshift of 0.12 for the low mass sample, respectively, with the majority of objects located at much lower redshifts. The lower-than-expected tSZ power may indicate significantly more non-thermal pressure support or other effects present in the low-mass, high-redshift clusters which make up the bulk of the tSZ power spectrum.

Soon after the SPT and ACT power spectra were published, several new models have been introduced which consider effects that reduce the total amount of SZ power, including three which are briefly discussed here. The first is by Trac et al. (2011), and is based upon the same dark matter simulations as the S10 model, but with several variations on the cluster gas formulation. These variations include a simple adiabatic model, with no star formation or energetic feedback, the model from S10, a model with twice as much star formation and feedback, and the "Nonthermal20" model, which includes 20% nonthermal pressure support in addition to added start formation and reduced feedback. These last two models each predict significantly less tSZ power than either the S10 or KS models. The nonthermal20 model provides the lowest tSZ power result, and predicts only 60% of the S10 model result for the tSZ power at $\ell = 3000$. This template is included in the new analysis of SPT data in section 6. In addition to the new templates, the authors also explore the scaling of the SZ power with cosmological parameters and model choices. In general, they find that increased star formation, increased energetic feedback, and increased non-thermal pressure support all decrease the tSZ power.

The second recent model, by Battaglia et al. (2010), is the first to generate SZ templates entirely with smoothed particle hydrodynamic (SPH) simulations which incorporate feedback and cooling terms. Their simulation includes two components: large periodic $(100 - 330\,h^{-1}\mathrm{Mpc})$ boxes to obtain sufficient statistics, and a "zoomed" simulation including multiple realizations of a single cluster with high resolution ($m_{\mathrm{gas}} = 1.7 \times 10^{-8}h^{-1}M_\odot$, $m_{\mathrm{DM}} = 1.7 \times 10^{-8}h^{-1}M_\odot$). Three models are included: an adiabatic case, a version with star formation, SN Feedback, and cosmic rays from structure formation shocks, and a version with radiative cooling, star formation, and AGN feedback. The AGN feedback is represented in simulation by assuming a fixed relation between star formation and AGN accretion rate. Both of the non-adiabatic models predict significantly less tSZ power than S10, and both show a somewhat different shape, with relatively less power at lower-ℓ. In particular, the authors find that the effective adiabatic index of the cluster gas increases from $\Gamma \sim 1.2$ in the dense region of a cluster to $\Gamma \sim 5/3$ by around $2R_{200}$, consistent with a departure from the S10 and KS shape at $\ell \lesssim 2000$. In the fits to SPT data described later, the AGN feedback model template is used, with a nominal prediction of $D_{3000}^{\mathrm{tSZ}} = 5.6\,\mu\mathrm{K}^2$ in the SPT $150\,\mathrm{GHz}$ band.

The third recent model is an analytic treatment by Shaw et al. (2010), which calculate the Poisson (one-halo) term obtained using the mass function from Tinker et al. (2008) with a simulation-calibrated NFW cluster profile and derive a pressure profile by starting with a constant adiabatic relation ($\Gamma = 1.2$) and include a series of parametrized extensions. These extension include a model for star formation (which removes gas), dynamic heating of the ICM via energy transfer in major mergers, feedback heating of the ICM via AGN and supernova (modeled as a function of the total stellar mass and calibrated against low-redshift observations), and non-thermal pressure support due to the turbulent motion associated with infalling and merging sub-structures. The authors produce a model for the tSZ spectrum based upon best-available estimates of each parameter; the result is nearly identical to the nonthermal20 model of Trac et al. (2011) in both shape and amplitude. (This is the final model used as a template in fits to the SPT spectrum in section 6.) The authors also use the analytic model to derive scaling relations for the tSZ power as a function of each extension, and demonstrate that they can very nearly reproduce several other simulation-based results by fixing the appropriate parameters in their model, as shown in figure 1.6. In general, they find that increasing feedback decreases power at high-ℓ, increasing non-thermal pressure support decreases power at low-ℓ, and that failing to include reasonably contributions from non-thermal pressure support leads to an over-estimate of the power at $\ell \sim 3000$ by as much as 50%.

In late 2010, the ACT collaboration published a new power spectrum, including data at both 148 and $218\,\mathrm{GHz}$ covering $300\,\mathrm{deg}^2$ and $\ell < 10000$. In addition to measuring the primary CMB damping tail, the result includes an improved constraint on SZ power. By assuming a homogeneous kSZ and requiring both the kSZ and tSZ to scale by a single amplitude parameter, they obtain a constraint of $D_\ell^{tSZ} + D_\ell^{kSZ} = 6.8 \pm 2.9\,\mu\mathrm{K}^2$, which corresponds to $A_{tSZ} = 0.62 \pm 0.26$ assuming the S10 template and increases to $A_{tSZ} = 0.96 \pm 0.43$ when
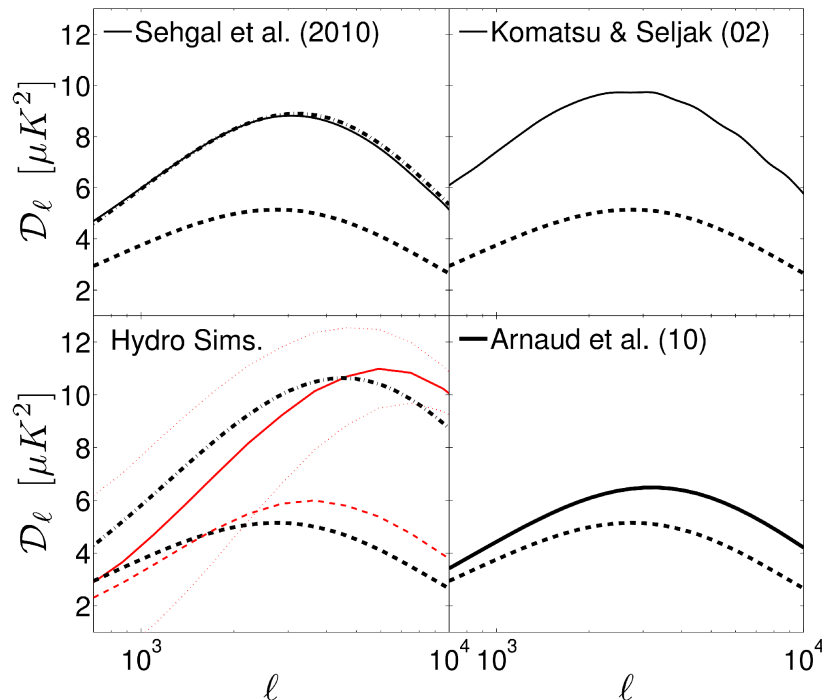
Figure 1.6 The analytic model for the tSZ spectrum from Shaw et al. (2010) is compared to simulations. In all cases, the (lowest) black dotted line is the fiducial model from Shaw et al., and the black dot-dash line is the analytic model with parameters modified to match the cluster physics included in each comparison simulation. In the top left, the solid line is the non-feedback, N-body result from S10. The top right shows the analytic KS model. The bottom right shows the Battaglia et al. (2010) adiabatic model (solid red) and the AGN feedback model (dashed red). All results are for 147 GHz with $\sigma_8 = 0.8$. Figure from Shaw et al. (2010)

using the nonthermal20 template from Trac et al. (2011). The authors also place significant constraints on foregrounds, including a clustering Dusty Star Forming Galaxy (DSFG) term. (Das et al., 2011; Dunkley et al., 2011) The result is consistent with both $A_{sz} = 1$ and $\sigma_8 = 0.8$, and with the result from Lueker et al. (2010).

In section 6, the result of a new analysis of the complete 2008 SPT data will be presented, including band powers at high-ℓ and multi-frequency MCMC fits to a model that includes foregrounds and the various templates for the tSZ and kSZ power discussed here. The result is entirely consistent with the Lueker et al. (2010) constraints, but with significantly smaller error bars. If one assumes perfect knowledge of the model, this allows for a determination of σ_8 which is a factor of two more precise than one finds using only primary CMB results.

However, given the wide range of model predictions discussed here, and the precision with which σ_8 is constrained by cluster counts, it is more sensible to view the result as a constraint on cluster model parameters.

Chapter 2

The South Pole Telescope

2.1 The Telescope

The South Pole Telescope is a dedicated, 10-meter diameter telescope optimized for mm-wavelength observations of the CMB with arc-minute resolution and a degree field of view. The optical design is described in detail in Padin et al. (2008), and the mechanical properties of the telescope and secondary cryostat are described in Carlstrom et al. (2011). The following includes only a cursory summary of the material presented there.

The telescope is located at the Amundsen-Scott South Pole Station, run by the United States National Science Foundation. The site is exceptionally well suited for mm-wavelength astronomy, with a median percipital water vapor during winter of roughly $0.25\,\mathrm{mm}$. At $150\,\mathrm{GHz}$, a corresponding opacity at zenith is 3%, and the median brightness fluctuation power is $31\,\mathrm{mK}^2_{\mathrm{CMB}}\mathrm{rad}^{-5/3}$. (Chamberlin, 2001; Lane, 1998; Bussmann et al., 2005)

The SPT is an offset Gregorian design, consisting of two mirrors and a weak HDPE lens. The primary is 10 in diameter, with a $7\,\mathrm{m}$ focal length. The front surface consists of 218 lightweighted aluminum panels, each approximately $1/2\,\mathrm{m}^2$. These panels are mounted on a composite (aluminum and carbon fiber) backing structure, and adjusted using five manual positional screws per panel. After adjustment, the surface accuracy of a single panel is typically $5-10\mu\mathrm{m}$ rms. Following iterative adjustments and holography, the total average surface accuracy (including the metal spacers which bridge the gap between panels) is measured to be $23\,\mu\mathrm{m}$ rms, with an additional expected deflection under gravity of roughly $10\,\mu\mathrm{m}$ rms over the range of observing elevations. The optics design is shown in figure 2.1.

To control the illumination of the primary and avoid unnecessary optical loading, a cold stop is essential. Because the optical design does not include an image between the secondary and receiver, this is accomplished by placing the secondary mirror in a large cryostat. Cold ($10\,\mathrm{K}$) absorber forms an aperture in front of the secondary, illuminating the central $7.5\,\mathrm{m}$ of the primary. The secondary mirror is $1\,\mathrm{m}$ diameter machined aluminum structure with a cold surface accuracy of roughly $50\mu\mathrm{m}$. The lens is made from machined
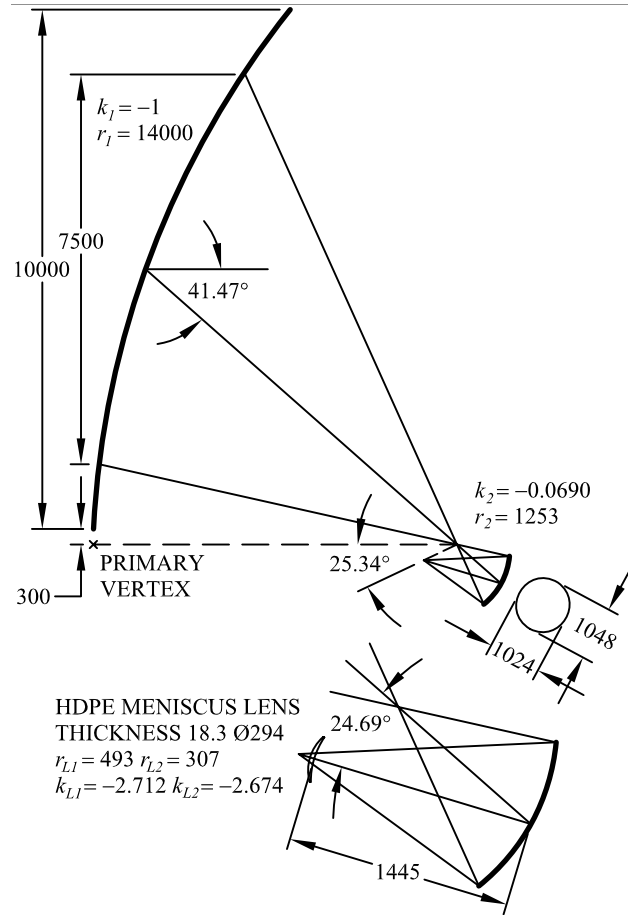
Figure 2.1 Optical design of the South Pole Telescope. The top image shows the basic offset Gregorian design; the bottom figure is a detail for the optical design as presently configured, with an additional meniscus lens following the secondary mirror. The secondary mirror, lens, and a cold stop (now shown) are all cooled to $10\,K$. Dimensions in mm of the radius of curvature, r, and conic constant k for each surface are shown. Figure from Padin et al. (2008)

High Density Poly-Ethelene, and includes an anti-reflection treatment consisting of azimuthal grooves to minimize reflections It is introduced to make the focus telecentric and more uniformly illuminates the secondary mirror. The secondary cryostat consists of a cylindrical aluminum vacuum shell, with a window made from 100 mm thick expanded polypropylene foam (Zotefoam PPA30), and two concentric cryogenic Shields which are cooled to $10\,$K and $70\,$K with a closed cycle, helium, pulse tube refrigerator. (Cryomech Inc., model PT410.) The entire inner surface of the $10\,$K space is blackened with microwave absorber (Emmerson Cumming HR-10) to absorb stray reflections. A series of 9-12 Inverse cm (ICM) heat blocking metal mesh filters and IR Shaders are located at the 70, 10, and 4 K stages. The secondary
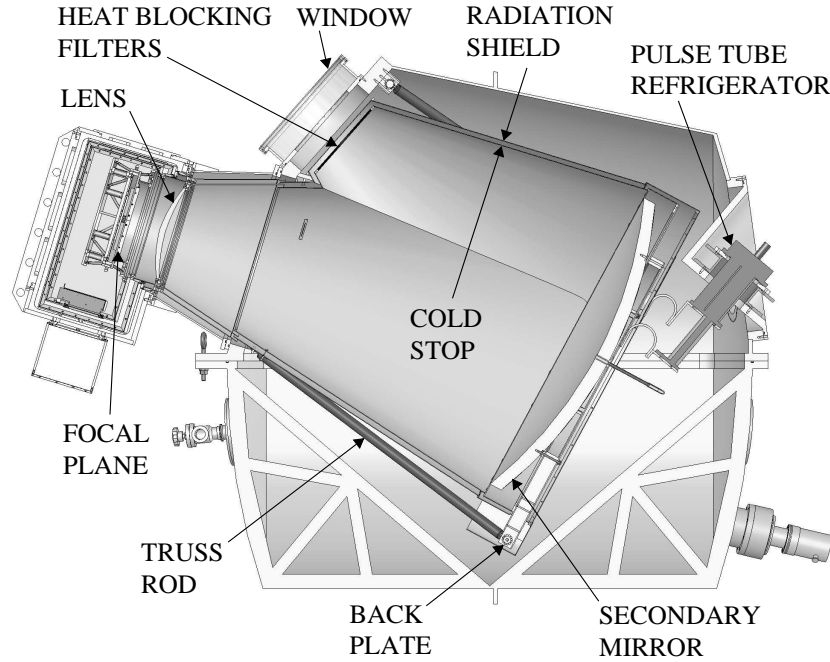
Figure 2.2 A cross sectional view of the SPT secondary cryostat and receiver. Incoming mm-wavelength radiation passes through heat blocking filters followed by a cold aperture stop, then to a a 1.25 m diameter secondary mirror. Radiation then passes through a weak lens, and into the receiver cryostat, where it passes through harmonic blocking filters and then reaches the focal plane, which is described later. The cold stop consists of HR-10 absorber adhered to an aluminum shroud which surrounds the beam. The cold stop, as well as the secondary mirror are cooled to approximately 10 K. Figure from Carlstrom et al. (2011)

cryostat is shown in cross section in figure 2.2

2.2   The Receiver

2.2.1   Optical and Mechanical Design

After passing through the lens located at the exit of the secondary cryostat, radiation enters the receiver cryostat. The receiver shares a vacuum space with the secondary but includes independent cryogenic cooling. The focal plane consists of six triangular wedges arrange as pie-slices. Each of these wedges includes metal mesh filters which define the upper edge of the observing band, conical smooth walled feed horns coupled to cylindrical waveguide which sets the lower band edge, and the array of transition edge sensor bolometers. The wedge modules and detectors are discussed in detail in section 3.

Aluminized mylar sheets bridge the gap between the cryogenic shells of the receiver cryostat, forming an RF shield which fully encloses the detectors and cold readout electronics. Cryogenic shells at approximately 70 and 4 K are cooled by a second pulse tube cooler. (Cryomech Inc., model PT415). The SQUIDs and associated cold readout electronics are located on the 4K stage, which also serves as the mounting point for the sub-K refrigerator. A three-stage (^{4}He, ^{3}He, ^{3}He) helium sorption refrigerator (Chase Research Cryogenics Ltd., model CRC10) cools the focal plane to approximately 250 mK. This refrigerator is cycled roughly once every 36 hours, which requires roughly eight hours during which observations must cease. (Roughly 3/4 of this time is required to cycle the refrigerator and wait for the focal plane to reach its operating temperature, the rest is spent tuning SQUIDs and biasing bolometers.)

The final configuration is designed for a beam with focal ratio $F = 1.3$. For a single horn, optical coupling is maximized when coupling to a smooth walled conical feedhorn of aperture diameter $2F\lambda$. For SPT, we use the same feedhorn diameter, 4.5 mm for all three observing bands. This provides a significant benefit, as it allows for interchangable mask sets and machine tooling, but is not optimal. After accounting for a fixed focal plane area and a maximum number of readout channels, and assuming detector sensitivity is re-optimized to account for changes in loading, mapping speed efficiency is degraded by approximately 20% at 90 GHz compared to the optimal configuration, and by only a few percent in the other bands.

End-to-end simulations of the optical efficiency and loading due to both absorption and scattering of each of the optical elements have been carried out, and are described in Benson et al (in prep.) Using observations of RCW38, a bright, southern HII region for which extensive calibrated measurements exist, one can directly measure the total end-to-end optical efficiency for a single detector. For a compact source,

$$\eta_{\text{tot}} = \frac{P_{\text{meas}} * \Omega}{F \Delta\nu \lambda^2} \tag{2.1}$$

where P_{meas} is the peak measured power in watts, Ω is the effective solid angle, F is the known source flux, and $\Delta\nu$ and λ are the effective bandwidth and observing wavelength. In 2009, average measured values are 0.1, 0.209, and 0.247 in the 90, 150, and 220 GHz bands, respectively.

This efficiency includes losses in all of the optical elements and from diffusive scattering from the primary, as well as the detector efficiency. The largest term is due to beam spillover at the cold stop past the secondary mirror, which is expected to contribute a factor of 0.50, 0.80, and 0.93 in the three bands. The expected band-averaged bolometer efficiency, defined as the total fraction of the power present in the waveguide portion of the bolometer which is detected as optical power in the readout system, is expected to be roughly 60% in all bands, based on simulations of the bolometer cavity and absorber. The array average measured values are consistent with this, to within the ten percent uncertainty with which the emissivity of the cold optical elements are known.

2.2.2 Frequency Domain Multiplexing

In order to reduce thermal loading and wiring complexity, SPT employs the Frequency Domain Multiplexing (fMUX) system developed at U.C. Berkeley, Lawrence Berkeley National Lab, and McGill University. (Lanting et al., 2005, 2006) The bias circuit for each TES sensor includes a discrete inductor and capacitor which determines the resonant frequency for a channel. Groups of 7 channels are then connected in parallel. Each channel is biased with an AC carrier at its resonant frequency, and the comb of AC currents is then read out using a single Superconducting Quantum Interference Device (SQUID) ammeter. This consists of a series SQUID array developed by The National Institute of Standards and Technology (NIST) in Boulder and a warm feedback amplifier with negative feedback. To reduce the total dynamic range of the current passing through the SQUID (and thus the requirements on the amplifier feedback loop necessary to achieve a linear response), a nulling signal is introduced, which destructively interferes with the unchanging part of the current from each channel. A diagram of the bias circuit is shown in figure 2.3, and the system and implications for TES operation and characterization are discussed in more detail in sections 3 and 4.
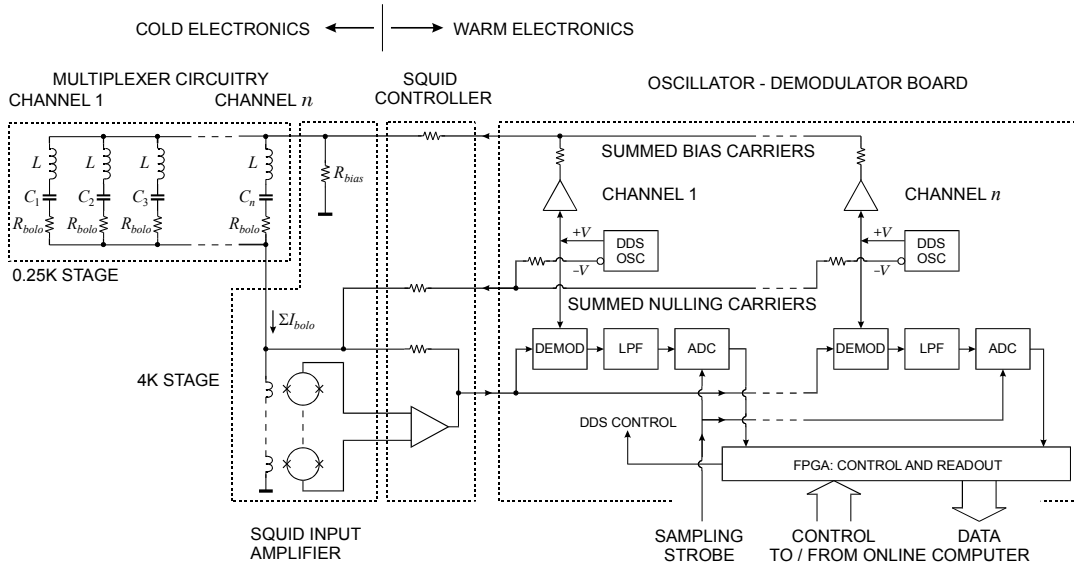
Figure 2.3 The Fourier domain multiplexed (fMUX) readout system as implemented in SPT. Figure from Dobbs et al. (in prep)

2.2.3 Focal plane modifications

Since first-light in Feb 2007, the receiver has been modified several times. The entire focal plane was upgraded with new detectors prior to Austral winter 2008 in order to take

advantage of improvements in detector fabrication. This season 2 focal plane included two wedges at $220\,\mathrm{GHz}$, three wedges at 150 GHz, and was used to map approximately 200 square degrees to observation depth ($\sim 18\,\mu\mathrm{K}^2$) at $150\,\mathrm{GHz}$, as well as to make several observations of pointed clusters. The result of a power spectrum analysis of these 2008 fields is presented in chapter 6. This season 2 focal plane also included a final wedge at $90\,\mathrm{GHz}$ with disappointing yield and low sensitivity, which has not been used in analysis. Prior to austral winter 2009, the focal plane was again upgraded. Three wedges were replaced, and minor changes to the filter configuration were made. This season 3 focal plane is the principle focus of the instrument portions of this document, and the final configuration and performance are discussed in section 5. Prior to the 2010 season, a final minor modification was made to the receiver, blackening several parts of the focal plane and filter holders in order to reduce reflections, leading to minor improvements in sensitivity. The same receiver configuration was installed with no changes in 2011, which is expected to be the final year of observation before a new instrument is deployed at the telescope.

Part II

The South Pole Telescope SZ Camera Detectors

Chapter 3

Transition Edge Sensor bolometers

3.1 Introduction

In this chapter, I review the behavior of a transition edge sensor bolometer. Section 3.2 introduces the basic behavior of a simple voltage biased TES sensor. Section 3.3 summarizes the behavior of a TES sensor modified to include a large, well-coupled thermal mass (called BLING), as in the SPT design. In section 3.4, this model is extended to include a second, poorly coupled excess heat capacity; this extended model provides a much better fit to the low loop-gain behavior of real SPT bolometers, while reducing to the previous case in the limit of moderate loop gain. Section 3.5 summarizes the contributions to the expected noise performance of the SPT detectors. Section 3.6.1 discusses device optimization for realistic devices with composite thermal links and fixed optical loading. Finally, Section 3.7 summarizes the important results for a voltage biased TES sensor operating at intermediate loop-gain.

Any radiation detector used in astronomy must couple to photons from the sky and produce a signal which can be recorded and analyzed, while adding as little noise to the signal as possible. One such devices is the bolometer.

A bolometer consists of a radiation absorber attached to a temperature-dependent resistor that is weakly coupled to a low temperature thermal bath. A combination of Joule heating and incident optical power raises the temperature of the device above that of the bath, and change in optical power are read-out by amplifying and recording changes in the current (or voltage) of the device. A number of materials have been implemented as bolometer thermistors. (Richards, 1994) Two contemporary choices which have been used for background limited astronomical instruments include Neutron Transmutation Doped germanium resistors (NTDs) and superconducting transition edge sensors. The former are high-resistivity materials which exhibit a negative $\partial R/\partial T$ at cryogenic temperatures, and are generally biased with constant current sources and read out using cooled semiconductor voltage preamplifiers, such as Junction Gate Field-Effect Transistors (JFETs). Quite a

number of successful astronomical instruments based upon this technology have been fielded in the last two decades. (Holland et al., 1999; Runyan et al., 2003; Haig et al., 2004; Yoon et al., 2006; Planck HFI Core Team et al., 2011)

The later make use of the steep $R(T)$ curve of a superconductor in its transition. When biased with a constant voltage, negative eletrothermal feedback causes these devices to remain at the same operating point despite changing in optical loading. Optical power leads to a change in the current passing through the device, which which can be read out using a low impedance current transducer, such as a SQUID ammeter. Since the first laboratory demonstrations of voltage biased TES sensors in the mid 1990s, a number of successful TES based astronomical instruments have been fielded, with more on the way. (Lee et al., 1996; Lee et al., 2003; Schwan et al., 2003; Ogburn et al., 2010; Sheehy et al., 2010; Crill et al., 2008)

For any phase-insensitive radiation detector, shot noise arising from the discrete nature of photons sets an ultimate lower limit to the signal to noise in a measurement. It's customary to compare noise in terms of the Noise Equivalent Power (NEP), or the equivalent amount of power required to generate a signal equal to the noise, with units of power per $\sqrt{\mathrm{Hz}}$. When mapping an extended source with detectors whose properties are fixed, the time required to reach a given map depth in units of ΔT^2 scales as NEP^2/N, where N is the number of detectors. In the limit of an incoherent radiation source, photon noise sets a limit of $\mathrm{NEP}_{\mathrm{opt}}^2 = 2h\nu P_{\mathrm{opt}}$ where P_{opt} is the total optical power reaching the detector at frequency ν.

The total noise in the detected signal will be the quadrature sum of the photon noise, the intrinsic noise of the detector itself, and any contributions from second stage readout electronics, thus $\mathrm{NEP}^2 = \mathrm{NEP}_{\mathrm{opt}}^2 + \mathrm{NEP}_{\mathrm{det}}^2 + \mathrm{NEP}_{\mathrm{ro}}^2$. Assuming the readout term can be made small, this sets a design limit for any efficient detector technology. To be competitive, a single detector should achieve $\mathrm{NEP}_{\mathrm{det}} < \mathrm{NEP}_{\mathrm{opt}}$.

The fundamental noise limit of a bolometer is set by fluctuations in the transport of thermal carriers which connect the sensor to the heat bath. As discussed in more detail in §3.6.2, it is given by $\mathrm{NEP}_g^2 = 4\gamma k_B T^2 G$, where γ is a material dependent factor, generally around 0.5, T is the temperature of the sensor, and G is thermal conductivity of the heat link. Up to a numeric factor of order unity, $TG \sim P_{\mathrm{opt}}$. The optimal choice of T will vary with material properties, but is generally not far from twice the stage temperature. After optimization, the final result is roughly $\mathrm{NEP}_g^2 \sim 20 K_B T_c P_{\mathrm{opt}}$, where the numeric factor is inexact, but provides a reasonable estimate over a range of realistic materials.[1]

The ratio of $NEP_{\mathrm{det}}/NEP_{\mathrm{opt}}$ therefore scales roughly as $10\sqrt{k_B T/h\nu}$. When using a helium sorption refrigerator, stage temperatures are generally limit to roughly $T_b \sim 250\,mK$, and the optimal value of T is roughly $500\,\mathrm{mK}$. In that case, a bolometer becomes photon noise dominated at $\nu \gtrsim 100\,\mathrm{GHz}$, and in general out-performs the other candidate technologies which have yet been demonstrated at mm-wavelengths.

---

[1]I am grateful to Kent Irwin for pointing out this surprisingly predictive numerical rule of thumb.

Once a detector approaches the photon noise limit, it becomes impossible to improve the sensitivity of a single device. In order to increase the sensitivity and mapping speed of the instrument as a whole, it is therefore necessary to develop arrays of pixels. TESes are a particularly attractive candidate for multiplexed arrays. Superconducting materials with an appropriate range of transition temperatures are regularly used in lithographic, thin-film fabrication, which allows for scaling to large arrays of devices. Voltage biased TESes have other advantages over older bolometers as well. First, in the superconducting transition, the resistance is a very steep function of temperature, and can be orders of magnitude larger than the equivalent curves for NTD bolometers. This steep $R(T)$ curve makes it possible to operate in eletrothermal feedback at high loop gain, in which case the response of the detector is a linear function of power. Second, the comparatively low impedance of TESes makes them relatively insensitive to acoustic vibrations and RF interference. These benefits come with a cost: readout requires a low noise, low impedance, current transducer, such as a SQUID ammeter.

In addition to requiring the fabrication of large numbers of detectors, scaling to large arrays also requires dramatic increases in the number of readout channels required. In order to achieve reasonable cryogenic loads, and to reduce the cost and complexity of cold electronics wiring, readout multiplexing is essential for kilopixels arrays. A number of schemes have been proposed, and are in various stages of implementation. Among the leading candidates are active Time Division Multiplexing (TDM), largely developed at NIST and The University of British Columbia. (Chervenak et al., 1999; Reintsema et al., 2003; Irwin, 2002; Battistelli et al., 2008) In recent implementation, each TES in an array is coupled to an individual first stage SQUID. The first stage SQUIDS are then turned on and read out sequentially at a rate faster than the intrinsic time constant of each pixel. A number of recent experiments make use of TDM. In addition to calorimeters used for particle and high-energy photon detection, TDM has been used on a number of fielded astronomical instruments, including ACT (Swetz et al., 2010), BICEP2 (Ogburn et al., 2010) and KECK Array (Sheehy et al., 2010), and several new instruments are currently being developed.

The other mature multiplexing scheme is the Frequency Domain Multiplexing (fMUX) system developed primarily by UC Berkeley, Lawrence Berkeley National Lab, and McGill University. (Lanting et al., 2005, 2006) The bias circuit for each TES sensor includes a discrete inductor and capacitor which determines the resonant frequency for a channel. As implemented in SPT, groups of 7 channels are then connected in parallel, and each channel is biased with an AC carrier at its resonant frequency. The comb of AC currents is then read out using a single SQUID ammeter, which consists of a series SQUID array developed by NIST in Boulder and a warm feedback amplifier with negative feedback. A schematic of the fMUX system used in SPT is showin in figure 2.3. Similar implementations have now been succesfully deployed in APEX-SZ Schwan et al. (2010) and EBEX (Aubin et al., 2010), in addition to SPT, and development is underway for several future instruments including SPTPol (McMahon et al., 2009). For device characterization, the MUX readout system is significant only in so far as it imposes a narrower eletrothermal feedback bandwidth than

a typical DC single channel system. This imposes additional requirements on the intrinsic time-constants of detectors which can be stably operated, as discussed in Section 3.3.

3.2 A review of TES bolometer properties

3.2.1 A simple model of a TES bolometer
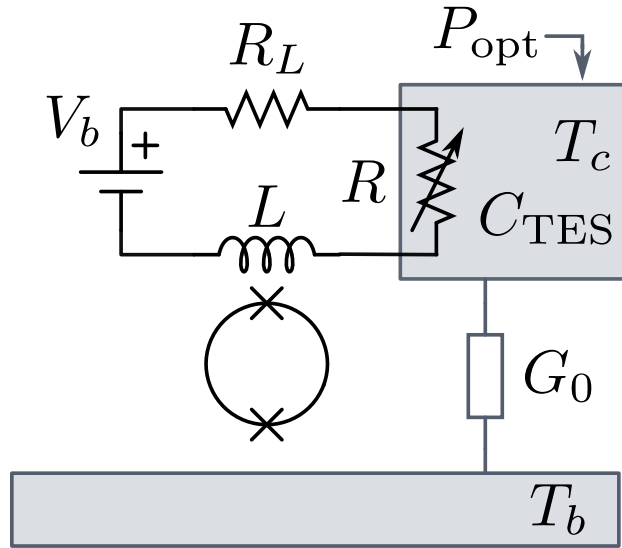
Figure 3.1 This model illustrates the properties of a simple TES bolometer. The TES, with heat capacity C_{TES} is connected via a thermal link, G_0, to a heat bath at temperature T_b. A fixed bias voltage, V_b is supplied via a circuit with series resistance R_L to the TES with resistance, R, that is a steep function of temperature and may also depend on current. A combination of optical power, P_{opt} and Joule heating keeps the TES at its transition temperature, T_c. The current through the TES is then read out using a SQUID ammeter with inductance L, followed by additional amplification (not shown.) In practice, the voltage bias is generally provided by current-biasing a small ($\ll R$) bias resistor. For most mm-wavelength devices, the optical power will actually couple to the TES through an antenna or absorber, such as the gold spiderweb in an SPT device.

Consider the simplified model of a DC voltage biased TES bolometer in figure 3.1. Optical power couples to the absorber, and electrical power is dissipated in the TES. The TES acts a lumped thermal element with heat capacity C_0 and electrical resistance $R(T, I)$, which is assumed to be a steep function of T near the superconducting transition temperature T_c.

The TES is connected via a heat link (also called a G-link) with a total thermal conductance $\overline{G}(T_c, T_b)$, which has units of power per Kelvin and in general will be a smooth

function of both the TES temperature and the bath temperature. The total power incident on the TES can be written $P_{\text{tot}} = \overline{G}(T_c - T_b) = \overline{G}\Delta T$. The change in that power in response to a small perturbation is given by $G \equiv \partial P/\partial T$, from which it follows that $G = (T_c - T_b)\partial\overline{G}/\partial T_c + \overline{G}$. (Numerical values for $\overline{G}$ and G for the case of thermal conductivities with power-law temperature dependence is discussed in section 3.6.2.) In the limit as T_c approaches T_b, these two terms are equivalent, and some authors fail to distinguish between them.

The TES itself behaves as a resistor whose value is, in general, a function of both temperature and current. (In later sections we will assume that the current dependence is negligible, as a generally true for high resistance devices such as used in SPT.) For small excursions about a particular bias point, we define the logarithmic derivatives of the TES resistance R(T,I) as

$$\alpha = \frac{\partial \log R}{\partial \log T} \tag{3.1}$$

$$\beta = \frac{\partial \log R}{\partial \log I} \tag{3.2}$$

An example plot of $R(T)$ and α are shown in figure 4.5, for a candidate SPT device. As will be discussed later, near optimal noise properties can be obtained for devices with a range of both T_c and α.

3.2.2   The equations of motion of a simple TES bolometer

For this simple model of a TES, the electrical and thermal response to a stimulus can be solved analytically. Though it has been treated by numerous authors, the following summary follows the detailed review by Irwin & Hilton (2005), with notation taken from Lindeman (2000), as well as extensions for a slightly more complicated model which were introduced in Lueker (2010).

For small signals, we can expand the bias power, bias current, bias voltage, and TES resistance about their DC values as $P_{bias} = P_0 + \delta P$, $I = I_0 + \delta I$, $V = V_0 + \delta V$, and $R = R_0 + \delta R$. To first order, the resistance of the TES is given by

$$\frac{\delta R}{R} = \alpha\frac{\delta T}{T} + \beta\frac{\delta I}{I_0} \tag{3.3}$$

The total power incident on the bolometer, P_{tot}, is the sum of Joule heating of the resistor, P, and optical radiation incident on the absorber, P_{opt}. (Note that in other parts of this document, the notation P_{bias} is used instead to refer to the bias power in order to avoid confusion. In all cases, the other two labels are unchanged.)

Expanding this to first order and assuming a fixed bias voltage,

$$\delta P = \delta(I^2 R) = (2 + \beta)I_0 R_0 \delta I + \mathcal{L}G\delta T \tag{3.4}$$

where $\mathcal{L}$ is at present an arbitrarily defined function. It will turn out to be the loop gain of the eletrothermal feedback circuit, and is given by

$$\mathcal{L} \equiv \frac{\alpha P_{\text{bias}}}{G T_0} \tag{3.5}$$

Expanding the total power flowing through the thermal link, using the definitions of $\overline{G}$ and G as defined above and again keeping only first order terms,

$$\delta(\overline{G}(T - T_b)) = \overline{G}(T_0 - T_b) + G\delta T \tag{3.6}$$

To derive the equations of motion of this system, we write down Ohm's law and the conversation of energy,

$$L\frac{d}{dt}I = V - IR - IR_L \tag{3.7}$$

$$C\frac{d}{dt}T = -\overline{G}(T - T_{\text{bath}}) + P_{\text{bias}} + P_{\text{opt}} \tag{3.8}$$

Expanding these equations and keeping only first order terms in δI, δP, and δT, the result is a pair of linear differential equations

$$L\frac{d}{dt}\delta I = \delta V - (1 + \frac{R_L}{R_0} - \beta)R_0\delta I - \frac{G\mathcal{L}}{I_0}\delta T \tag{3.9}$$

$$C\frac{d}{dt}\delta T = (\mathcal{L} - 1)G\delta T + (2 + \beta)I_0 R_0 \delta I \tag{3.10}$$

This set of coupled equations governs the response of the TES to small perturbations in bias and optical power. These equations can be made more intuitive by introducing two time-constants, the TES intrinsic time constant τ_0, and an electrical time constant equivalent to the inverse of the bias circuit bandwidth, τ_e. Further, define two arbitrary parameters for notational convenience, the bias stiffness parameter, ε, and ζ, defined by

$$\varepsilon \equiv R_L/R_0 \tag{3.11}$$

$$\tau_0 = C/G \tag{3.12}$$

$$\tau_e \equiv \frac{L}{R_0(1 + \beta + \varepsilon)} \tag{3.13}$$

$$\zeta \equiv \frac{2 + \beta}{2(1 + \beta + \varepsilon)} \tag{3.14}$$

For all the devices which will be considered here, both β and ε are close to zero, in which case $\zeta \to 1$. The pair of differential equations can be conveniently written in matrix form as

$$\frac{d}{dt}\begin{pmatrix} LI_0\delta I \\ C\delta T \end{pmatrix} = \begin{pmatrix} -\tau_e^{-1} & -\mathcal{L}\tau_0^{-1} \\ 2\zeta\tau_e^{-1} & (\mathcal{L}-1)\tau_0^{-1} \end{pmatrix}\begin{pmatrix} LI_0\delta I \\ C\delta T \end{pmatrix} + \begin{pmatrix} I_0\delta V \\ \delta P_{\mathrm{opt}} \end{pmatrix} \tag{3.15}$$

The matrix equation above can be written in compact form by defining $\mathbf{v}$, $\mathbf{A}$ and $\mathbf{p}$ such that

$$\frac{d}{dt}\mathbf{v} = \mathbf{A}\mathbf{v} + \mathbf{p} \tag{3.16}$$

The solution to the homogeneous form of this equation (with the right term set to zero) can be found by assuming a solution of the form $\mathbf{f}_\pm = f_\pm(t)\mathbf{u}_\pm$, where $\mathbf{u}_\pm$ are the eigenvectors of $\mathbf{A}$ with eigenvalues $\lambda_\pm \equiv -1/\tau_\pm$, satisfying

$$\mathbf{A}\mathbf{v}_\pm = \lambda_\pm \mathbf{v}_\pm \tag{3.17}$$

The solution can then be found by direct integration. (For an explicit derivation of this result, see Irwin & Hilton (2005). The result is

$$\begin{pmatrix} \delta I \\ \delta T \end{pmatrix} = A_+ e^{-t/\tau_+}\mathbf{u}_+ + A_- e^{-t/\tau_-}\mathbf{u}_- \tag{3.18}$$

where $A_\pm$ are adjustable constants and $\mathbf{u}_\pm$ are the eigenvectors given by

$$\mathbf{u}_\pm = \begin{pmatrix} \frac{-\tau_e}{2\zeta\tau_0}\left(\mathcal{L}-1-\frac{\tau_0}{\tau_\pm}\right) \\ 1 \end{pmatrix} \tag{3.19}$$

and $\tau_\pm$ are the negative inverse of the eigenvalues, $\tau_\pm = -\lambda_\pm$. Here $\lambda_\pm$ are eigenvalues of equation 3.18, given by

$$\lambda_\pm = \frac{\mathrm{Tr}(\mathbf{A})}{2} \pm \frac{1}{2}\sqrt{\mathrm{Tr}(\mathbf{A})^2 - 4\,\mathrm{Det}(\mathbf{A})} \tag{3.20}$$

Writing this out explicitly for the equation above, the effective time constants of the system are given by

$$\frac{1}{\tau_\pm} = \frac{\mathcal{L}-1}{2\tau_0} - \frac{1}{2\tau_e} \pm \frac{\sqrt{\tau_0^2 - 2([4\zeta+1]\mathcal{L}+1)\tau_0\tau_e + (\mathcal{L}-1)^2\tau_0^2}}{2\tau_0\tau_e} \tag{3.21}$$

Equation 3.16 fully determines the response of the TES to changes in either bias voltage or optical loading. With the addition of appropriate boundary conditions and a specific solution as required for any driving terms, equation 3.18 describes the behavior of the system. Irwin & Hilton (2005) provide exact solutions for two important cases: an impulse applied to the optical power, and a sinusoidal excitation. More generally, this equation can be integrated numerically to derive the response of the bolometer to an arbitrary signal. Alternatively, one can explore a few specific interesting limits appropriate for the case of SPT-like devices, and derive the basic behavior of a TES sensor under voltage bias.

First, consider the case where the the loop gain of the device approaches zero, appropriate for the response of a bolometer which is heated to a temperature above its transition. In this case, the equations of motion become decoupled, and the bolometer behavior can be solved through direct integration. Alternatively, we can simply take the limit $\mathcal{L} \to 0$ of the above solution. The result is

$$\lim_{\mathcal{L} \to 0} \tau_+ = \tau_e = \frac{L}{R_0(1 + \beta + \varepsilon)} \tag{3.22}$$

$$\lim_{\mathcal{L} \to 0} \tau_- = \tau_0 = \frac{C}{G} \tag{3.23}$$

In the low loop gain limit, the response of the TES is governed by two independent time constants: an electrical time constant, appropriately labeled τ_e, which determines the response of the current to a change in voltage through the bias circuit, and an intrinsic thermal time constant, τ_0, which governs the change in the temperature of the TES in the absence of eletrothermal feedback. (Thus justifying the choice of notation for these two time constants above.)

A second useful limit to consider is the case where the electrical and thermal time-constants are well separated. This is an accurate description of an SPT detector in a test cryostat read out with a commercial DC SQUID, or a device in the field at intermediate loop gains. (Neglecting the slight complications associated with the AC bias circuit, which will be discussed below.) The most straightforward approach is to expand the eigenvalues above as a power series in τ_e/τ_0 about zero. Keeping only terms to first order, the result is

$$\frac{1}{\tau_+} \approx \frac{[2\zeta - 1]\mathcal{L} + 1}{\tau_0} - \frac{2\mathcal{L}\zeta\left([2\zeta - 1]\mathcal{L} + 1\right)}{\tau_0}\left(\frac{\tau_e}{\tau_0}\right) \tag{3.24}$$

$$\tau_- \approx \tau_e \tag{3.25}$$

Here, τ_+ is the effective thermal time constant of the device under feedback; its label will be shortened to τ throughout the rest of this document. Discarding all but the first term,

$$\tau \approx \frac{\tau_0}{(2\zeta - 1)\mathcal{L} + 1} = \frac{\tau_0}{\left(\frac{1-\varepsilon}{1+\varepsilon+\beta}\right)\mathcal{L} + 1} \tag{3.26}$$

In the usual limit of stiff voltage bias and a superconducting transition which is independent of current, $\zeta \to 1$, and this reduces to the classic result for a voltage biased TES under eletrothermal feedback. Under these conditions, the device responds to power perturbations with a time constant given by $\tau \approx \tau_0/(\mathcal{L} + 1)$.

Hence, the (heretofore arbitrary) definition of $\mathcal{L}$ is appropriate, and the TES under eletrothermal feedback behaves much as a closed loop amplifier circuit with strong negative electrical feedback: its response time speeds up by a factor of $\mathcal{L}+1$. A second time constant, τ_e describes the response of the current to a sudden change in bias voltage, as expected.

This result also can provide some intuition about the degree to which the usual zeroth order result is a reasonable choice when interpreting results in the laboratory: the inferred time constant based upon the simplified model will be wrong by a factor which is approximately $2\mathcal{L}\tau_e/\tau_0$. In the limit of high loop gain, this is roughly $2\tau_e/\tau$. Thus, for an SPT pixel with $\tau_0 \approx 30\,\mathrm{ms}$, read out using the AC biased system with $\tau_e \approx 40\,\mu\mathrm{s}$, the actual behavior of the device departs from the model by roughly 10% at $\mathcal{L} \sim 37$. For the moderate loop gains that we tend to use in the field, it is therefore perfectly reasonable to use the simple, approximate result.

The results in both of these limits are common knowledge, and could have been derived more easily without the formalism above. However, this method naturally extends to devices with more complicated thermal structures. This also serves as a cross-check that the linearized equations of motions reproduce our intuition.

3.2.3 Response of a TES bolometer to sinusoidal variations

Given the solutions above, once can calculate the response of a simple TES to a sinusoidal signal at a single frequency. The first order equations of motion in equations 3.15 are linear, and we can decompose any input signal and output signal into components which oscillate frequency ω. Given perturbations of the form,

$$\delta V = V_\omega e^{i\omega t} \tag{3.27}$$

$$\delta P_{\mathrm{opt}} = P_\omega e^{i\omega t} \tag{3.28}$$

the solution to equation 3.15 includes terms of the form $\delta I(\omega) = I_\omega e^{i\omega t}$ and $\delta T(\omega) = T_\omega e^{i\omega t}$. Note that all of the subscripted terms here, eg V_ω, are complex constants, allowing for arbitrary phase and amplitude matching. The solution to 3.15 can now be found either by making use of equation 3.18 and solving for $A_\pm$ to express the $I(\omega)$ in terms of the eigenvectors of $\mathbf{A}$, as Irwin & Hilton (2005) do, or by solving the (now algebraic) equation directly. Substituting the $\delta I(\omega)$ and $\delta T(\omega)$ into the equation of motion, one can write

$$(\mathbf{A} - i\omega)\mathbf{v} + \mathbf{p} = 0 \tag{3.29}$$

$$\mathbf{v} = (i\omega - \mathbf{A})^{-1}\mathbf{p} \tag{3.30}$$

The current responsivity to a change in optical power, $s_i = I_\omega/P_\omega$ is then given by the top right field of $(i\omega - \mathbf{A})^{-1}$. This quantity is usually referred to simply as the responsivity, and determines the response of the bolometer to an optical signal. The top left field, on the other hand, determines the bolometer response to a change in bias voltage, which is useful for laboratory diagnostics.

The result is (Irwin & Hilton, 2005)

$$s_i(\omega) = -\frac{L}{I_0}\left(\frac{\tau_e}{2\zeta}\right)\left(\frac{1+(\mathcal{L}-1)\,\tau_+/\tau_0)}{1+i\omega\tau_+}\right)\left(\frac{1+(\mathcal{L}-1)\,\tau_-/\tau_0)}{1+i\omega\tau_-}\right) \tag{3.31}$$

In the usual limit of moderate loop gain, where $\tau_e \ll \tau$, we can use equations 3.24 and 3.25 to write this in a simpler form. Dropping terms of order τ_e/τ_0, this simplifies to

$$s_i(\omega) = -\frac{\tau_e L}{I_0}\frac{\mathcal{L}}{(2\zeta-1)\,\mathcal{L}+1}\left(\frac{1}{1+i\omega\tau}\right)\left(\frac{1}{1+i\omega\tau_e}\right) \tag{3.32}$$

which can be rewritten in terms of R_0 and bias corrections as

$$s_i(\omega) = \frac{1}{R_0 I_0}\frac{\mathcal{L}}{(1-\varepsilon)\,\mathcal{L}+1+\beta+\varepsilon}\left(\frac{1}{1+i\omega\tau}\right)\left(\frac{1}{1+i\omega\tau_e}\right) \tag{3.33}$$

The response of the TES in this limit looks like a simple filter with two widely separated poles, whose at frequencies that correspond exactly to the rise and fall times of the homogeneous solution above. In the usual limit of $\zeta \to 1$, in which case it also follows that $V_{\text{bias}} = I_0 R_0$, this reduces to the usual form

$$s_i(\omega) = \frac{1}{v_{\text{bias}}}\frac{\mathcal{L}}{\mathcal{L}+1}\left(\frac{1+(\mathcal{L}-1)\,\tau_+/\tau_0)}{1+i\omega\tau_+}\right)\left(\frac{1+(\mathcal{L}-1)\,\tau_-/\tau_0)}{1+i\omega\tau_-}\right) \tag{3.34}$$

At high loop gain, and still in the limit of stiff bias and wide readout bandwidth, the DC responsivity is given by the inverse of the bias voltage. In that case, the change in total power in response to a change in optical power is given by

$$\delta P_{\text{tot}} = \delta P_{\text{bias}} + \delta P_{\text{opt}} = V_{\text{bias}}\,s_i\,\delta P_{\text{opt}} \approx \text{constant} \tag{3.35}$$

In the limit of large loop gain, the total power, and thus the bias point of the device itself remains constant. At low loop gain, the ratio of $\delta P_{\text{bias}}/\delta P_{\text{opt}}$ is weakened by a factor of $\mathcal{L}/(\mathcal{L}+1)$, leading to a loading-dependent change in the TES response. Consider the case where V_{bias} is fixed, and the optical power changes by an amount which is small compared to the total. Making use of equation 3.5, and assuming the change in T_0 is small compared to T_0, and keeping only terms which are first order, we can solve for the change in s_i as follows

$$\delta s_i = \frac{\partial s_i}{\partial P\text{opt}} = \frac{\partial s_i}{\partial \mathcal{L}}\frac{\partial \mathcal{L}}{\partial P_{\text{opt}}}\delta P_{\text{opt}} \tag{3.36}$$

$$\frac{\delta s_i}{s_i} \approx \frac{1}{(\mathcal{L}+1)^2}\frac{\delta P_{\text{opt}}}{P_{\text{opt}}} \tag{3.37}$$

Under these approximations, the response of the TES to changes in optical power will depart from the linear result as $1/(\mathcal{L}+1)^2$. In practice, whenever this term is too large

to ignore, it will significantly complicate the analysis of time-stream data. It is practical, therefore, to demand that the fractional change in s_i is small in each of the three various observing scenarios.

The first constraint is the maximum expected change in loading due to weather variation in a single observation. Although in principle the variation with weather can be quite large - up to a few pW out of a total of 12 pW for the 150 GHz band in bad weather - in practice, it is almost certainly uncorrelated with position on the observed field. Because we always average over hundreds of individual observations, the impact of gain non-linearity due to weather is dramatically reduced.

The second constraint comes from the change in loading associated with elevation when observing a single field. This artifact will add coherently across the field, and therefore become the most significant factor in deciding on a minimum loop gain. For a planar atmosphere with uniform temperature and opacity (on average), the column density and thus the atmospheric loading scales as $\csc(\theta)$ where θ is the angle away from the zenith. Taking as the limiting case a 10 degree field centered at -45 degrees declination, the atmospheric loading will change by 25% from the bottom to the top of the field. Assuming that the entire loading is due to atmosphere, which is a significant over-estimate, even at modest loop gains of $\mathcal{L} \geq 4$, the resulting change in responsivity is less than 1%.

A third constraint is that the relative gain calibration between fields, and between fields and astronomical calibration sources must be small. Allowing for a generous slew of 60 degrees from the zenith, the total atmospheric loading changes by a factor of 1 at most. Even in this extreme scenario, only a modest loop gain of $\mathcal{L} \geq 9$ is required in order to reduce the variation of s_i to 1% between fields. (At extremely low elevations, as required for beam mapping with planets, more care will obviously be necessary.) In all cases, therefore, a TES bolometer which is stable and can be operated at loop gains of $\mathcal{L} \sim 10$ will behave as a linear detector with a constant responsivity for any reasonably observing strategy. In practice, other effects can easily cause similar changes in response and should be considered. For example, variation of the stage temperature due to the orientation of the refrigerator vessels with respect to gravity must be measured.

3.2.4   Stability of a TES bolometer.

To be useful as a detector, a TES must be stable under eletrothermal feedback. From the solution to the equation of motion of the simple TES model, 3.18, and the general form of the eigenvalues in 3.20, we can determine the conditions under which stable bias is possible.

First, we require that both $\tau_\pm$ must be positive, or equivalently,$\lambda_\pm = -1/\tau_\pm < 0$) Should either $\tau_\pm$ become negative, the solution will diverge until the device either reaches another bias point or latches in the superconducting state. A minimum condition for stability is therefore $\lambda_\pm < 0$, or $\mathrm{Tr}(A) > 0$. From equation 3.15, this requirement can be written

$$\mathcal{L} \leq \frac{\tau_e}{\tau_0} + 1 \tag{3.38}$$

This result makes intuitive sense. In order to provide negative eletrothermal feedback, the bias circuit must have a bandwidth $\Delta f / 2\pi = L/R = 1/\tau_e$ wide enough that the circuit can respond to perturbative excursions of the TES, which are limited to the effective time constant of the device, $\tau \approx \tau_0/(\mathcal{L}+1)$. Once the device becomes too fast for the readout, an unstable runaway occurs.

A more stringent stability condition is the requirement that the device not only be stable against growing modes, but also that it be over-damped, returning to equilibrium without oscillations. This is equivalent to requiring that both τ_0 must be entirely real valued, and thus the argument of the square root in equation 3.20 must be greater than zero:

$$\mathrm{Tr}(\mathbf{A})^2 - 4\,\mathrm{Det}(\mathbf{A}) \geq 0 \tag{3.39}$$

Taking the limit where $\zeta \approx 1$, expanding this in powers of τ_e/τ, and keeping only the leading terms, this can be written

$$\mathcal{L} < \left(3 - 2\sqrt{2}\right)\frac{\tau_0}{\tau_e} + 1 - \sqrt{2} + \frac{1}{2\sqrt{2}}\frac{\tau_e}{\tau_0} \tag{3.40}$$

In the limit of high loop-gain and slow intrinsic time constant, $\mathcal{L} \gg 1$ and $\tau \gg \tau_0$, this gives a limit on the effective loop gain beyond which a device becomes under-damped, first derived in Irwin et al. (1998)

$$\mathcal{L} \leq (3 - 2\sqrt{2})\frac{\tau_0}{\tau_e} \approx \frac{\tau_0}{5.8\tau_e} \tag{3.41}$$

Thus, for stable, over-damped operation, the effective time constant $\tau \approx \tau_0/(\mathcal{L}+1)$ of the bolometer must be larger than $5.8\tau_e$.

The extension of this method to the case of an AC biased channel is straightforward. Lueker (2010) shows in detail that for an on-resonance channel demodulated using the maximum signal phase, the results are identical to the DC bolometer case, except that the readout time-constant defined in equation 3.13 needs to be modified to take into account both sidebands, and is therefore given by

$$\tau_e = \frac{2L}{R_0(1 + \beta + \varepsilon)} \tag{3.42}$$

For the SPT readout, $\mathcal{L} = 16\,\mu\mathrm{H}$, and $R_0 \approx 1\,\Omega$. The LRC filter bandwidth is thus 5 KHz for a $1\,\Omega$ device, and $\tau_e = 32\mu\mathrm{s}$ high in the transition. If we require that the device be over-damped down to $0.5\,\Omega$, the detectors must satisfy $\tau_0/(\mathcal{L}+1) \gtrsim 400\,\mu\mathrm{S}$ when operating at sufficiently high loop gain.

The first prototype spiderweb bolometers designed for the APEX-SZ camera had intrinsic time constants of roughly $200\,\mu\mathrm{s}$. Though suitable for laboratory testing using a DC SQUID,

they could not be run under AC bias except at the very top of the transition. In order to slow the detectors and make it possible to run them with the fMUX system at moderate loop gain, it was necessary to add a large additional heat capacity. In collaboration with Jared Mehl and Sherry Cho, several prototype APEX-SZ and SPT devices with large gold features were designed and tested. The most successful of these included a 32μm wide, 200μm outer diameter, 3μm thick ring of evaporated gold at the center of the spiderweb, connected to the gold G-link of the TES. Although a number of wedges were successfully fielded using this design, the extremely thick gold layer proved challenging to fabricate using available techniques, and the relatively poor thermal coupling between the BLING and TES lead to instability at high loop gain, as will be discussed in the next section. These early devices, as well as the improvements associated with the new design, are discussed in Schwan et al. (2010) and Westbrook et al. (2009).

3.3 Model TES with additional thermal mass (BLING)

In order to meet the stability criterion for the SPT detectors at sufficiently high loop gain, a large additional heat capacity is added to the center of the spiderweb and thermally coupled to the TES. This additional thermal mass, called BLING (and given the reverse acronym Bandwidth Limiting Interface Normally made of Gold in Lueker et al. (2009)), dominates the heat capacity of the bolometer, slowing τ_0 from C_{TES}/G to C_0/G, where C_0 is the heat capacity of the BLING material. Provided that the BLING is sufficiently thermally conductive that it thermalizes much faster than τ and that it is well thermally connected to the TES itself, the composite device will behave exactly as if it were the simple model discussed above, but with a much larger time constant.

In practice, the finite thermal connection between the TES and the BLING become significant at high loop gain, and a more complicated thermal model is required. For a detailed derivation of this model, as well as the extension to a more general lumped thermal circuit, consult appendix A in Lueker (2010). The result is an equation of motion similar to the one presented above.

The thermal model shown in figure 3.2 includes several new terms. For notational convenience, we define the ratio of thermal conductances to be $\gamma \equiv G_{\text{int}}/G$, where G_{int} connects the TES to the BLING and G_0 is the usual heat link which now connects the BLING to the thermal bath. In general, we will be interested in the limit where $G_{\text{int}} \gg G_0$ and γ will be large.

In general, it is important to specify exactly how G_{int} is defined, as a thermal link which spans a significant temperature gradient will in general respond with a different small signal G depending on which side of the link is being perturbed. For the sake of definiteness, we can choose $G_{\text{int}} = \partial P/\partial/T_{\text{TES}}$. However, in the limit of large γ, the temperature difference across the G_{int} link will be small compared to T_c, and we can safely use the equilibrium approximation. In that case,
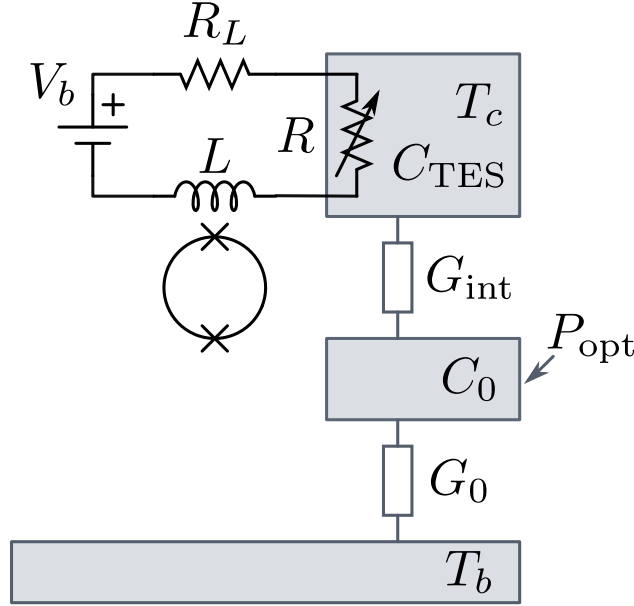
Figure 3.2 This model illustrates the properties of a TES bolometer with BLING, additional heat capacity designed to slow the device. All properties retain the same meaning as in figure 3.1, except for the addition of a the BLING with heat capacity C_0, which is connected to the TES by an internal thermal link, D_{int}. Here, $C_{\text{TES}} \equiv C_0/\eta \ll C_0$, and $G_{\text{int}} \equiv \gamma G_0 \gg G_0$.

$$G_{\text{int}} = \frac{\partial P_1}{\partial T_{\text{TES}}} \approx \frac{\partial P_1}{\partial T_0} \approx \frac{P_1}{T_{\text{TES}} - T_0} \tag{3.43}$$

where P_1 is the power flowing from the TES into the BLING across the internal heat link. (It is particularly convenient that we can make this approximation, as the details of the thermal interface between the TES and BLING are difficult to model with any certainty.)

For notational convenience, retain G_0 as the small signal thermal conductance of the primary heat link, and define an effective G, G_{eff}, as the small signal conductance at the TES due to both the heat link to the bath and the heat link to the BLING. Thus,

$$G_{\text{eff}} = \frac{\gamma}{\gamma + 1} G_0 \tag{3.44}$$

Further, define the ratio of heat capacities to be $\eta = C_0/C_{\text{TES}}$, which will ordinarily be much larger than one. With these definitions, and the topology shown in figure 3.2, the equation of motion can be written in a manner analogous to 3.15.

$$\frac{d}{dt} \mathbf{v} = \mathbf{A}\mathbf{v} + \mathbf{p} \tag{3.45}$$

where the matrix elements are given by

$$\mathbf{v} \equiv \begin{pmatrix} LI_0\delta I \\ \frac{C_0}{\eta}\delta T_{\text{TES}} \\ C_0\delta T_0 \end{pmatrix} \quad , \quad \mathbf{p} \equiv \begin{pmatrix} I_0\delta I \\ \delta P_{\text{TES}} \\ \delta P_0 \end{pmatrix} \tag{3.46}$$

$$\mathbf{A} \equiv \begin{pmatrix} -\tau_e^{-1} & -\eta\frac{\gamma}{\gamma+1}\mathcal{L}\tau_0^{-1} & 0 \\ 2\zeta\tau_e^{-1} & \eta\left(\frac{\gamma}{\gamma+1}\mathcal{L} - \gamma\right)\tau_0^{-1} & \gamma\tau_0^{-1} \\ 0 & \eta\gamma\tau_0^{-1} & -(\gamma+1)\tau_0^{-1} \end{pmatrix} \tag{3.47}$$

As in the simple model case, this set of linear differential equations can be solved explicitly, and the response of the device to small excursions about its bias point is fully determined by a set of three eigenvectors and three complex eigenvalues. However, the analytic result isn't terribly informative. Instead, it's more useful to jump directly to the stability criteria after applying several simplifying assumptions. First, we make the usual assumption of small stray resistance and $\beta \approx 0$, thus $\zeta \to 1$. Second, we assume that the BLING is much better coupled to the TES than the bath, and $\gamma \gg 1$. Third, we assume the heat capacity of the BLING dominates the bolometer, and thus $\eta \gg 1$. Finally, we assume that the composite device is slow compared to the readout time constant, $\tau \gg \tau_e$.

The solution in the absence of any of these assumptions can be readily explored numerically; however, obtaining sufficiently accurate estimates of the required parameters for a physical device in order to make realistic predictions is generally no simpler than fabricating and testing entire devices. We therefore seek an rough approximate solution to guide design decisions, rather than a fully predictive, quantitative model.

As discussed in the simplified case, a sufficient condition for the device to be stable (where stable can mean under-damped) is that $\text{Tr}(\mathbf{A}) \leq 0$. Using equation 3.47 and keeping only first order terms in $1/\eta$ and τ_e/τ_0, this condition can be written

$$\begin{aligned} \mathcal{L} &< \gamma + 1 + \frac{1+\gamma}{\gamma}\frac{\tau}{\eta\tau_e} \\ &< \gamma + 1 + \frac{C_{\text{TES}}}{G_{\text{eff}}\tau_e} \end{aligned} \tag{3.48}$$

The last term is equivalent to the time-constant of the TES itself when thermally decoupled from the BLING divided by τ_e, which reproduces the usual stability criterion for the simple TES model explored previously.

In general, therefore, a TES with this geometry can be stably operated provided that $\mathcal{L} < \gamma + 1$, and in order a device with a discrete BLING to operate at high loop gain, the thermal interface between the TES and BLING should be maximized.

In addition to requiring stability, a second condition is that the device not be under-damped. The requirement becomes $\text{Tr}(A)^2 - 4\text{Det}(\mathbf{A}) \geq 0$. As all the elements of $\mathbf{A}$ are real-valued, the first term is always positive. With no assumptions except that $\zeta - > 1$,

$$\text{Det } \mathbf{A} = -\frac{(\mathcal{L}+1)\gamma\eta}{\tau^2 \tau_e} \tag{3.49}$$

which is always negative. As a result, there is no under-damped solution given this geometry, assuming stiff voltage bias and a current-independent superconducting transition, and any solution which is stable will also be overdamped.

Given the equation of motion above, it is straightforward to derive the responsivity of the bolometer to perturbations in optical power and voltage bias. The result, in the limit of $\zeta \to 1$, is Lueker (2010)

$$s_i(\omega) = \frac{\mathcal{L}}{I_0 R_0} \left(\frac{G(\omega)}{G_{\text{eff}}} (1 + i\omega\tau_e) + \mathcal{L}(1 - i\omega\tau_e) \right)^{-1} \tag{3.50}$$

where $G(\omega)$ is the zero loop gain limit of the power response to a small temperature perturbation, given by

$$G(\omega) \equiv \lim_{\mathcal{L} \to 0} \frac{\delta P(\omega)}{\delta T(\omega)} = \lim_{\mathcal{L} \to 0} \frac{1}{s_T(\omega)} \tag{3.51}$$

As in the case of the simple device, s_T can be found by solving equation 3.45 when driven by a perturbation of the form $\delta P_{\text{TES}} = P_\omega e^{i\omega t}$. The solution can be read off immediately from the center field of $(i\omega - \mathbf{A})^{-1}$. With $\mathcal{L} \to 0$, and under the assumptions $\eta \gg 1$ and $\zeta \approx 1$,

$$G(\omega) = G_0 \frac{\gamma}{\gamma + 1} \left(\frac{1 + i\omega\frac{C}{G_0}}{1 + i\omega\frac{C}{(\gamma+1)G_0}} \right) \tag{3.52}$$

In the usual limit that $\gamma \gg 1$ and $\tau \gg \tau_e$, these reduce to the equivalent solutions for the simple idealized bolometer, except that the effective heat capacity is now given by C_0 of the BLING rather than C_{TES}. In this case $G(\omega)$ reduces to $G(\omega) \approx G_0 + i\omega C$, and the responsivity is identical to equation 3.33, where $\tau \approx \tau_0/(\mathcal{L}+1)$ and τ_0 is given by the total heat capacity and effective conductance, both of which are dominated by the BLING values, $\tau_0 = C_{\text{tot}}/G\_\text{eff} \approx C_0/G_0$.

3.4   A TES model with three thermal masses

The eletrothermal response of fielded SPT devices under observing conditions is well fit by the TES & BLING model described in the preceding section. However, at low loop gain and low frequencies, we find that the SPT device response to a bias perturbation rolls off with

frequency more slowly than the single-pole filter response predicted by this model. A more complicated model is therefore necessary.

In principle, the number of models which can fit a set of response curves is unlimited; our strategy is therefore to choose the simplest model which is consistent with both design expectations and adequately explains the data.
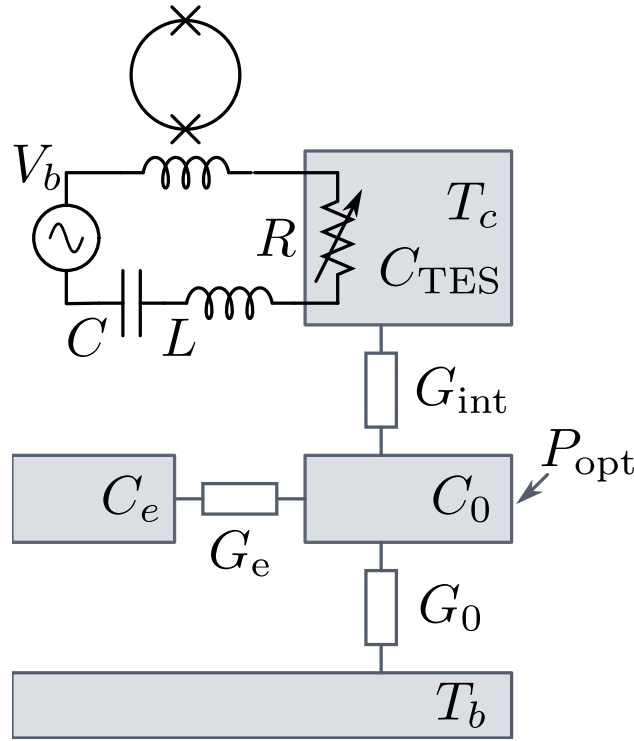
Figure 3.3 A model for the electrical (black) and thermal (gray) circuit which is used to fit the thermal response of the SPT devices to bias perturbations. The TES, with heat capacity C_{TES} is connected via an internal thermal link, G_{int} to the BLING with much larger heat capacity C_0. The BLING is connected via a weak thermal link, G_0, to the stage at temperature T_b, and to an excess heat capacity, C_e, via thermal link G_e. A fixed ac bias voltage, V_b, is applied to the TES at the resonant frequency of the filter composed of an inductor, L, and a capacitor, C, in series with the TES resistor. The current through the TES is then measured using a SQUID ammeter, followed by additional amplification (not shown.) A combination of optical power, P_{opt} and Joule heating keeps the TES at its transition temperature, T_c.

The addition of single additional thermal mass, C_e connected via a thermal link G_e to the device provides a much better fit to the response of all the season 3 SPT devices. This model is shown in figure 3.3. Other simple models which can produce similar low loop gain behavior - for example, a large heat capacity in the TES itself combined with a significant

secondary coupling from the TES to the heat bath - are dismissed as physically unlikely. The addition to the simple model of either a non-zero current dependence in the R(T) curve, $\beta = d \log P / d \log I > 0$, or a bias circuit series resistance compatible with limits determined by measuring the LRC pass band of superconducting detectors ($R_L \leq 0.005\Omega$) does not improve the fits. (A non-zero β actually steepens the low frequency response beyond a single pole filter.)

The equations of motion for this TES model are only slightly modified from the TES & BLING model described earlier, applying the general strategy discussed in Lueker (2010). We introduce a new heat capacity, $C_e = \eta_e C_{\text{TES}}$, which is connected only to the BLING by $G_e = \gamma G_0$. The electrical part of the solution is unchanged, except for replacing the explicit formula for G_{eff} in the second row and column with a variable which can be solved for later. Writing the equivalent of the matrix form of the equations of motion in equation 3.47, this system is described by

$$\frac{d}{dt}\mathbf{v} = \mathbf{A}\mathbf{v} + \mathbf{p} \tag{3.53}$$

where the matrix elements are given by

$$\mathbf{v} \equiv \begin{pmatrix} LI_0\delta I \\ \frac{C_0}{\eta}\delta T_{\text{TES}} \\ C_0\delta T_0 \\ C_e\delta T_e \end{pmatrix} \quad , \quad \mathbf{p} \equiv \begin{pmatrix} I_0\delta I \\ \delta P_{\text{TES}} \\ \delta P_0 \\ \delta P_e \end{pmatrix} \tag{3.54}$$

$$\mathbf{A} \equiv \begin{pmatrix} -\tau_e^{-1} & -\eta\frac{\gamma}{\gamma+1}\mathcal{L}\tau_0^{-1} & 0 & 0 \\ 2\zeta\tau_e^{-1} & \left(\frac{\mathcal{L}G_{\text{eff}}}{G_0} - \gamma G_0\right)\tau_0^{-1} & \gamma\tau_0^{-1} & 0 \\ 0 & \eta\gamma\tau_0^{-1} & -(\gamma+1)\tau_0^{-1} & \frac{\eta\gamma_e}{\eta_e}\tau_0^{-1} \\ 0 & 0 & \gamma_e\tau_0^{-1} & \frac{\eta\gamma_e}{\eta_e}\tau_0^{-1} \end{pmatrix} \tag{3.55}$$

where all other symbols retain their meaning from section 3.3. The analytic solution to this matrix isn't particularly compact or illuminating; however, its numerical solution can be easily fitted to laboratory data in order to extract physical parameters from response curves.

As before, the effective thermal conductance is given by the top left element of the inverse of the A matrix at zero loop gain,

$$G_{\text{eff}} = -C_{\text{TES}} / \left(\mathbf{A}[\mathcal{L} = 0]^{-1}\right)_{11} \tag{3.56}$$

which reduces to the familiar $G_{\text{eff}} = \gamma/(\gamma + 1)G_0$ and $G \approx G_0$ for $G_e \ll \gamma G_0$ and $\gamma \gg 1$, respectively. For the SPT devices, both these conditions are satisfied.

The responsivity to a perturbation in optical power, at a frequency ω, for a device at loop gain $\mathcal{L}$ is once again given by the top left element of the inverse of $(i\omega - \mathbf{A})$,

$$s_i(\omega) = \frac{dI(\omega)}{dP(\omega)} = \frac{(i\omega - \mathbf{A})_{11}^{-1}}{LI_0} \tag{3.57}$$

In the limit of moderate loop gain such that $C_e/G_e \ll \tau = \tau_0/(\mathcal{L} + 1)$ and $\mathcal{L} < \gamma$, the additional heat capacity C_e will decouple from the thermal circuit, and the device will behave exactly as the simplified model described previously. Thus, measuring C_e and G_e is only really essential in order to accurately characterize C_0 and γ and thus predict the behavior of the device at higher loop gain, and the scaling of thermal properties with fabrication changes.

Section 5.3 discusses model fits to the response curves for fielded SPT devices, and the resulting device parameter constraints. In general, there is excellent agreement between the data and a model with a large $(C_e \sim 0.5C_0)$and weakly coupled $(G_e \sim 2G_0)$ excess heat capacity. At high loop gain, where we actually operate, this excess term decouples, and the device behaves as described by the model discussed in section 3.3.

3.5 TES Sensitivity

3.5.1 Noise Equivalent Power

Sources of noise in bolometer, and in voltage biased transition edge sensors in general, have been thoroughly presented in the literature. The following brief review lists the major noise contributions for an SPT device, and the assumptions that are required in their derivation.

The Noise Equivalent Power (NEP) is the power spectral density referred to an equivalent amount of power incident on the detector. It determines the sensitivity of the detector, and (along with a measure of optical efficiency), the ultimate Noise Equivalent Temperature (NET) and mapping speed on the sky. A fully general description of the thermal state and noise sources in a TES is complicated, and is in general not analytically tractable. Generally accurate, though not formally rigorous, results can be derived under the linear equilibrium anzats (LEA). This framework, introduced for the case of bolometers by Mather (1982) and explored in detail for the case of TES sensors by Irwin & Hilton (2005), assumes that predictions based upon the fluctuation-dissipation theorem applied to an equivalent system at equilibrium hold for the real system, and that the small signal behavior of all elements is linear with respect to both temperature and current changes.

For noise sources which appear as heat on the TES, such as thermal carrier noise, the NEP is simply the power spectral density of the noise source itself. Sources of current noise appear in timestreams as an equivalent power noise after being scaled by the responsivity of the detector S_i. In general, a distinction must be made between current sources generated

on the TES (or thermally well coupled to the TES) and therefore participating in eletrothermal feedback), and those generated elsewhere in the readout system. The former includes Johnson noise in the TES, as well as current noise present in resistive heaters on the device. These terms will be suppressed by eletrothermal feedback, and scale as the loop gain of the detector, $\mathcal{L}$. The later include Johnson noise from the Bias resistor, readout noise associated with the SQUID itself, and noise from the first stage readout amplifier. Noise present on the voltage bias itself, such as digitization noise in the DAC generating the bias signal, should generally be included and converted to power as $\mathrm{d}P/\mathrm{d}V_{\mathrm{bias}}$; however, in all cases considered here voltage sources are negligible.

The total NEP of an optical device is given by

$$\mathrm{NEP}^2 \equiv S_{\mathrm{tot}} = S_{\mathrm{opt}} + S_G + S_J + S_{\mathrm{readout}} \tag{3.58}$$

where the terms are, from left to right, the total measured NEP (in units of power per root Hz), the optical noise due to the total optical power incident on the device (including astronomical signals, sky loading, and cryostat loading), thermal carrier noise, Johnson noise present in the TES itself, and readout noise. The last term includes contributions from Johnson noise in the bias resistor, noise from the SQUID ammeter itself, and noise in the warm electronics, essentially all due to the first stage amplifier. Sources of current noise are multiplied by the responsivity, $s_i = \partial i/\partial P_{\mathrm{bias}} \approx 1/v_b$ to convert them to equivalent power.

3.5.2 Photon noise

The photon noise, S_opt, sets a fundamental limit to the sensitivity of any device and a noise target required to build an efficient focal plane. It includes two terms,

$$S_{\mathrm{opt}} = 2h\nu P_{\mathrm{opt}} + \frac{\xi P_{\mathrm{opt}}^2}{\delta \nu} \tag{3.59}$$

where ν is the band center of the observed radiation, P_{opt} is the total optical power, $\delta\nu$ is the effective bandwidth defined by $P\Delta\nu = \int P_\nu \nu d\nu$, and ξ varies between 0 and 1 as discussed below.

The first term is due to photon shot noise, derived by counting the number of photons of energy $h\nu$ incident per unit time in an optical signal with total power $P_{\mathrm{opt}} = nh\nu$ and assuming no correlations between photon arrival. (Formally one needs to average over the bands and the radiation of the incoming spectrum. In practice, uncertainty in the second term, and in the accuracy with which optical elements are characterized will generally dominates the error introduced by using any reasonably defined band center.)

The second is the so-called photon bunching term, which comes from applying Bose statistics to the incoming radiation. For the case of a single-moded horn measuring radiation from a single blackbody source in the diffraction limit, $S\Omega \approx \lambda^2$ for an antenna surface area S and solid angle Ω, the result is $\xi = 1$. In the opposite limit, $\xi = 0$. For an actual

experiment, where the loading is dominated by coupling to a layered atmosphere and also includes significant contributions from internal loading due to warm optical elements and scattered light, a detailed calculation of ξ is infeasible. We therefore adopt the standard practice of leaving ξ as an undetermined parameter and allow it to vary between 0 and 1. In the example numerical calculations later, $\xi = 0.3$ will be adopted unless otherwise specified.

For the SPT 150 GHz band, $\nu = 150 GHz$, $\Delta nu = 38 GHz$, and $P_{\text{opt}} \approx 11 pW$. We therefore expect an NEP given by

$$S_{\text{opt}} = \begin{cases} 48 aW/\sqrt{Hz} & \text{for } \xi = 0 \\ 57 aW/\sqrt{Hz} & \text{for } \xi = 0.3 \\ 75 aW/\sqrt{Hz} & \text{for } \xi = 1 \end{cases} \qquad (3.60)$$

Plots of measured NEP for a single SPT optical channel, as well as the distribution of NEP for the full season 3 focal plane are shown in chapter 5. Typically, we see more noise in optical channels than would be expected if $\xi = 0$, and values for the NEP at several Hz (beyond the low-frequency noise from the atmosphere) which is consistent with values of $0.3 \lesssim \xi \lesssim 0.6$ for most channels; however, there are a number of uncertain terms in the calibration of the readout system which make it difficult to attribute this measured excess noise to a particular source.

3.5.3 Thermal carrier noise

The dominant source of noise in an optimized TES sensor will be thermal carrier noise, associated with heat transport from the device to the thermal bath along the thermal link. Given that this is by nature a non-equilibrium system, an exact solution isn't generally possible; however, the LEA approximation produces reasonable results for a wide class of devices. The solution was explicitly described for the case of bolometers by Mather (1982), and is carefully derived (and extended to the $\beta \neq 0$ case, which will not be considered here) in Irwin & Hilton (2005). The power noise due to thermal fluctuations in the heat link is approximately

$$S_G = 4\gamma_{\text{NE}} k_B T_c^2 G \qquad (3.61)$$

where $G = \partial P/\partial T$ is the usual small-signal term and γ_{NE} is a numerical factor which depends on the material properties of the heat link and T_b and T_c. This factor, which is of order 1 for realistic cases, encapsulates the difference between an isothermal equilibrium model and a device in which the thermal conductivity of the heat link depends on temperature. For a G-link material with thermal conductivity that depends only on T, the result is Mather (1982)

$$\gamma_{\text{NE}} = \frac{\int_{T_b}^{T_c} \left[\frac{T k(T)}{T_c k(T_c)} \right]^2 dT}{\int_{T_b}^{T_c} \frac{k(T)}{k(T_c)} dT} \qquad (3.62)$$

In the case where the thermal conductivity is a power law, of the form $k \propto T^{\beta}$, the exact solution is

$$\gamma_{\text{NE}} = \frac{\beta + 1}{2\beta + 3} \frac{1 - (T_c/T_b)^{-2\beta-2}}{1 - (T_c/T_b)^{-\beta-1}} \tag{3.63}$$

The result is plotted in figure 3.5.3. In the limit $T_c/T_b \to 1$, $\gamma_{\text{NE}} \approx 1$. (This is the classic equilibrium result.) For a realistic device operating near a noise optimum with a heat link that lies somewhere between these two extrema, a range of values are possible. For the example SPT device considered below, $\beta \sim 1.7$, and thus $\gamma_{\text{NE}} = 0.5$.
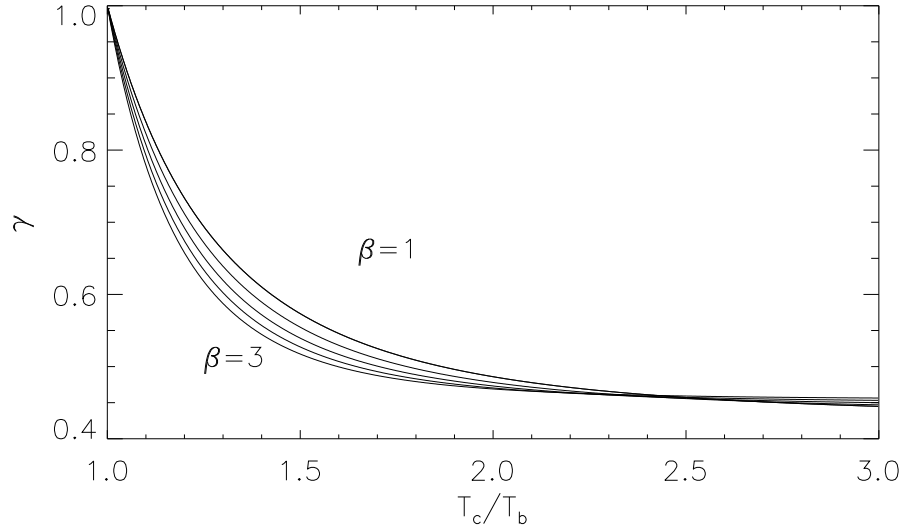
Figure 3.4 The non-equilibrium factor, γ_{NE}, associated with thermal carrier noise for a heat link with power law thermal conductivity $k \propto T^{\beta}$ and values of $\beta = 1$, 1.5, 2, 2.5, 3. The values of 1 and 3 correspond to normal metal and a dielectric heat link, respectively.

3.5.4   Bolometer Johnson Noise

The expected signal from Johnson noise from the TES itself is derived in detail for a DC-biased device in Irwin & Hilton (2005). Lueker (2010) shows that when the bias frequency and readout phase are chosen to maximize signal to noise, the result for the AC biased system and Tayloe demodulator used in SPT is identical, and is given by

$$S_J = 4k_B T_c R \frac{I_{\text{bias}}^2}{|s_i|^2} \mathcal{L}^{-2}(1 + \omega^2\tau^2) \tag{3.64}$$

where I_{bias} is the (large signal) bias current flowing through a device with resistance R, and $s_i = \partial i/\partial P_{\text{bias}} \approx (1/v_b)\,\mathcal{L}/(\mathcal{L}+1)$ is the responsivity used to convert from a current noise source to an equivalent power noise. In terms of bias power rather than current and responsivity,

$$S_J = 4k_B T_c P_{\text{bias}} \frac{(\mathcal{L}+1)^2}{\mathcal{L}^4}(1+\omega^2\tau^2) \tag{3.65}$$

where P_{bias} is the total bias power on the device, ω is the frequency at which the noise is measured, and τ is the effective time-constant of the bolometer. In the limit of high loop gain, the factor of $\mathcal{L}^{-2}$ makes this term negligible for both a DC biased system and the AC biased system as it is usually configured. At very low loop gain, when reading out the opposite phase quadrature, or if the bias frequency is chosen to be far from the LRC resonance, this term can become significant.

3.5.5   Readout noise

The last significant contribution to the total noise budget of a TES device is readout noise, an umbrella term which includes every source of current-like noise attributable to the readout electronics. Assuming an optimally choice of bias frequency and readout phase, this is dominated by three terms in the case of SPT: Johnson noise from the bias resistor (with a small contribution from any real stray impedance in the bias circuit), intrinsic SQUID noise, and noise from the warm first stage amplifier. A detailed discussion of these terms is beyond the scope of this document, and can be found in (Lanting, 2006), and in Dobbs et al. (in prep).

Unlike Johnson noise present in the TES itself, Johnson noise from the bias resistor is not reduced by eletrothermal feedback. In order to minimize the number of wires and heat load between the 4K stage and the cold stage, the bias resistors are located on the SQUID mounting cards at 4K. The NEP^2 due to Johnson noise is then given by

$$S_J, \text{bias} = 4k_B T_c I^2 R_{\text{bias}} \frac{(\mathcal{L}+1)^2}{\mathcal{L}^2}(1+\omega^2\tau^2) \tag{3.66}$$

where I is the DC bias current, and $I^2 = P_{\text{bias}}/R_{\text{TES}}$. In the low-frequency, moderate loop-gain limit, and assuming a $30\,m\Omega$ bias resistor at 4K, this gives:

$$\text{NEP}_{J,\text{bias}} = 9\text{aW}/\sqrt{Hz}\,(\frac{P_{\text{bias}}}{12pW})^{1/2}(\frac{R_{\text{TES}}}{1\Omega})^{-1/2} \tag{3.67}$$

This significant, though sub-dominant noise term could be made negligibly small either by moving the bias resistor to the mK stage, or by replacing the resistor with a dissipation-less inductor. The first strategy requires doubling the number of wires to our cold load. The second introduces a large frequency-dependence into the bias circuit and significantly complicate the hardware biasing and testing procedure. Some improvement could be achieved

by lowering the value of the bias resistor; however, the requirement that the bias resistor be large compared to stray impedance in series with the bias circuit, which are of order a few $m\Omega$ and tens of mH leaves little room to adjust this value.

In addition to the bias resistor Johnson noise, there is a contribution to the total noise budget arising from the SQUID ammeter itself. A significant advantage of series-array SQUIDs is that the voltage from the individual SQUIDs will add coherently, while the noise is uncorrelated and adds incoherently. The signal-to-noise for a given input current can be arbitrarily improved (as $1/sqrt(N)$) by building a larger array. For the 100-element NIST SQUID arrays used in SPT, the post-demodulation NEP is given by

$$\text{NEP}_{\text{SQUID}} = 2.8 \text{pA}/\sqrt{Hz} v_{\text{bias}} = 10 \text{aW}/\sqrt{Hz}\, (\frac{P_{\text{bias}}}{12pW})^{1/2}(\frac{R_{\text{TES}}}{1\Omega})^{-1/2} \tag{3.68}$$

Finally, there is a contribution from the warm electronics in the readout system, generally dominated by the first stage amplifier following the SQUID. For the components used in SPT, the white noise post-demodulation NEP due to all the warm electronics is approximately

$$\text{NEP}_{\text{electronics}} = 4.1 \text{pA}/\sqrt{Hz} v_{\text{bias}} = 14 \text{aW}/\sqrt{Hz}\, (\frac{P_{\text{bias}}}{12pW})^{1/2}(\frac{R_{\text{TES}}}{1\Omega})^{-1/2} \tag{3.69}$$

The readout contributions all add in quadrature, and contribute a total of

$$\text{NEP}_{\text{readout}} = 20 \text{pW}/\sqrt{Hz}\, (\frac{P_{\text{bias}}}{12pW})^{1/2}(\frac{R_{\text{TES}}}{1\Omega})^{-1/2} \tag{3.70}$$

to the total measured noise in the system. In SPT (as in any efficient system), the total from all these sources is sub-dominant compared to both the photon noise and the thermal carrier noise in the detectors.

3.5.6 Low frequency noise

Low frequency noise from the readout system is significant, and dominates measurements of the low frequency performance of dark bolometers. Low frequency noise sources in the readout in include contributions from gain drift in the transistors used in the DAC output, thermal variation in the digital potentiometers used in the bias circuit, and DAC clock drift, as well as the (comparably small) $1/f$ noise in the first stage amplifier. The DAC clock drift is suppressed because the same DAC output becomes the reference for the demodulator, and the DAC output transistors contribute the most to the total.

Measurements of individual components show that the low frequency sideband noise from the warm electronics which generate the bias signal is proportional to carrier amplitude and measured to have a $1/f$ spectrum and an amplitude of $\lesssim 10^{-5}\sqrt{Hz}$ times the carrier amplitude at $1\,\text{Hz}$ from the carrier. For the example optical device discussed above with $P_{\text{bias}} = 12pW$ and a total white NEP $\approx 70 \text{aW}/\sqrt{Hz}$, this leads to a $1/f$ knee of $1.7\,Hz$.

Precision measurements of the low frequency noise inherent to the SPT detectors themselves are time consuming and have only been carried out for a very small sample of individual devices. The best available data for season-3 style detectors is from a measurement made using the fMUX system, in which a single detector was biased and then read out using two independent demodulators. By differencing the time-streams and assuming the two channels have independent readout noise with the same spectrum in addition to a common bolometer signal, one can correct the observed spectrum to remove an estimate of the readout contribution. That result includes every contribution that is correlated between two channels on the same SQUID (eg. stage temp drifts, any common gain variations, etc), and thus should be an upper limit on the noise intrinsic to the device itself. With this technique, we've placed an upper limit on the intrinsic $1/f$ knee for one device at just below 0.3 Hz.

When observing, low frequency noise from atmospheric fluctuations dominates instrumental noise at low frequencies. Raw data shows a strong $1/f^\alpha$ component and a white-noise knee of between 1.5 and 3 Hz, though there is significant variation in the noise properties on day timescales. Removing an instantaneous common signal from each wedge in the array reduces the low frequency noise significantly, and has been incorporated into the SPT data analysis pipeline and used in all subsequent analysis projects.

3.5.7 Excess noise

A number of research groups have reported excess noise in transition edge sensors in recent years. Although a complete and unified explanation has so far proven illusive, the observations have converged on several phenomenological points. In most cases the excess noise appears as a rise above the expected white noise level at high frequencies, of order the roll-off frequency of the sensor. For a given set of films and basic geometries, it appears to be well correlated with α, the steepness of the transition, and is improved by several physically very different α-mitigation techniques, including the addition of normal-metal structures to soften the transition, choosing alternative bias points, and exposing the device to large magnetic fields. (Ullom et al., 2004; Jethava et al., 2009) There is anecdotal mention of TES layer edge treatments and the presence of localized regions with depressed T_c may be significant, although published data is sparse.

In SPT, and the related devices employed by APEX-SZ and EBEX, there is no evidence for excess noise of this type. Whether this is an inherent property of the Al-Ti bilayers and fabrication process is unclear, however. We also operate in a significantly different regime from most of the experiments which have reported significant excess noise: in particular, at moderately low loop gains ($\mathcal{L} \sim 10$), and with a data band that spans only a few decades of frequency, all well below the intrinsic thermal crossing time of the TES itself.

In addition to unexplained excess noise, there is a thoroughly understood, but none the less non-standard noise contribution that arises in a TES bolometer whenever the heat capacity of the thermal link to the heat bath becomes significant compared to the TES itself.

Gildemeister et al. (2001) presents a complete treatment of this noise term.[2] For the case of SPT devices, the peak of this noise term occurs at several kHz for the most conservative estimates of material properties, and thus can be safely ignored.

3.6 Optimizing thermal properties of real devices

3.6.1 Multi component thermal links

Consider a bolometer biased at temperature T_c and connected to a heat bath at temperature T_b by a thermal link which has thermal conductivity per unit length given by $k(T)$. The total power traveling through the heat link, from both bias voltage heating the TES and optical loading is defined by the saturation power of the device, P_{sat}, though the subscript will be dropped in cases where there is no confusion.

For bulk materials where thermal conduction is limited by diffusion of thermal carriers, $k(T)$ will obviously scale as the cross sectional area of the material, though in the limit of thin films the geometric scaling is less clear. Assuming that the thermal diffusion length is short compared to the length of the thermal link, the power flowing through the heat link at every point is given by

$$P = k(T)\frac{dT}{dx} \tag{3.71}$$

In general one can assume a power law dependence of the form $k(T) = k_0 T^\beta$. For conduction associated with electrons in normal metals at low temperatures, $\beta \approx 1$. For semiconductors and superconducting materials, $\beta \approx 3$. For thin films such as those used in SPT bolometers, specular reflection and surface features are significant, and a range of values are possible.

Integrating over the entire heat link,

$$P \int_0^x dx = k_0 A \int_{T_b}^{T(x)} T^\beta dT \tag{3.72}$$

$$x(T) = \frac{Ak_0}{P}\frac{1}{\beta+1}\left(T^{\beta+1} - T_b^{\beta+1}\right) \tag{3.73}$$

For a bolometer at temperature T_c, connected by a heat link of length l to a bath at T_b, this gives the total power:

$$P = k\frac{1}{\beta+1}\left(T_c^{\beta+1} - T_b^{\beta+1}\right) = k\frac{1}{n}\left(T_c^n - T_b^n\right) \tag{3.74}$$

---

[2]Note that there is a minor typesetting error in equation 7 of that work. The final index on the last term in equation 7 should read $i+1$ rather than i. However, both the qualitative and numerical results presented are all correct.

where for notational convenience we define $n \equiv \beta + 1$ and $k = k_0/l$. (In the bulk limit for a heat link with cross sectional area A, $k = Ak/lT_{ref}$ is the usual thermal conductivity in units of dyne/cm K defined at T_{ref}.) We can immediately find values for the effective thermal conductance to the bolometer. Throughout this document, I'll use the following notation to refer to the "average G," $\overline{G}$, the "small signal G," G, defined as:

$$\overline{G} \equiv \frac{P}{\Delta T} = k \frac{1}{n} \left(\frac{T_c^n - T_b^n}{T_c - T_b} \right) \tag{3.75}$$

$$G \equiv \frac{\partial P}{\partial T_c} = (T_c - T_b) \frac{\partial \overline{G}}{\partial T_c} + \overline{G} = kT^{n-1} \tag{3.76}$$

$\overline{G}$ is the quantity that determines how the detectors will respond to DC optical loading, and sets the dynamic range of an operating detector. For SPT, the design goal is a detector for which the saturation power, P_{sat}, is equal to twice the expected optical loading in the field. This insures we can achieve reasonably high loop-gains and thus detectors which respond linearly to the range of loading present within a standard CMB field, and provides some margin against scatter in fabrication parameters.

The small signal value, G, describes the response of bolometer to a small change in power in the absence of electrothermal feedback. The detector responsivity and response to thermal carrier noise are determined by this value. (Mather, 1982)

Finally, one can consider the "stage differential G", $G_{SD} = -\partial P/\partial T_b$, which is useful primarily in characterizing detectors in a dark cryostat, and is trivially given by kT_b^n.

In general, the actual thermal link for a real bolometer will include a more complicated network of components. For the SPT devices (and, indeed, for most devices in which interface transmission is a small factor and the length scale of thermal links are long compared to the mean free path of thermal carriers), there are two cases to consider. The first is a network of disconnected parallel conductive leads which all extend from T_c to T_b ; the second is the case where two leads made from different material are physically proximate and are well coupled to each other along their length. Both cases lead to an identical $T(x)$ solution (under the assumptions discussed above), which is a trivial extension of the previous equation, and the same carrier noise (to first order.) With the additional assumption that all thermal conductivities obey a power law with respect to temperature,

$$P = \sum_i P_i = \sum_i k_i \frac{1}{n_i} \left(T_c^{n_i} - T_b^{n_i} \right) \tag{3.77}$$

where i refers to each individual thermal link. It's common practice to describe this composite thermal circuit as though it were a single material with an intermediate power-law index, n, thus

$$P \equiv k_{\text{eff}} \frac{1}{n} \left(T_c^n - T_b^n \right) = \sum_i k_i \frac{1}{n_i} \left(T_c^{n_i} - T_b^{n_i} \right) \tag{3.78}$$

However, it's worth noting that the naive application of this approach can lead to results which are significantly incorrect. In particular, the effective index of the composite link becomes a function not only of the geometry and material properties of the link, but also of both T_b and T_c, and must not be treated as an intrinsic property of the device. Measurements of the same TES in cryostats with different stage temperatures will disagree on the value of n! Provided this distinction is kept in mind, it is true that the device with composite leads will have thermal and noise properties identical to the simplified equivalent.

The effective composite thermal properties are then given by

$$\overline{G} \equiv \frac{P}{\Delta T_c} = \sum_i k_i \frac{1}{n_i} \left(\frac{T_c^{n_i} - T_b^{n_i}}{T_c - T_b} \right) \tag{3.79}$$

$$G \equiv \partial P / \partial T_c = \sum_i k_i T^{n_i - 1} \tag{3.80}$$

The effective power law index, n, can be calculated in a straightforward way starting with n_T, the differential index in response to changes in T_c, via a pair of algebraic equations,

$$n_T = \frac{\partial \log P}{\partial \log T_c} = \frac{T_c}{P} G \tag{3.81}$$

$$n_T = n \frac{T_c^n}{T_c^n - T_b^n} \tag{3.82}$$

The most general analytic treatment of these equations is not particularly illuminating. The more useful approach is to include several assumptions appropriate for SPT devices and evaluate the result numerically.

3.6.2 T_c **Optimization**

Given the above discussion of the properties of composite G links and the noise results discussed previous, one can explore the range of T_c which leads to optimal performance.

First, we assume that the bolometer is connected to the stage through parallel links which have only two possible thermal indices. First, there is a dielectric term which is governed by conduction within the Low Stress Nitride legs of the bolometer and the superconducting leads. Assuming diffusive (bulk-like) scaling, $k = kT^\beta$ where $\beta = 3$ and $n = 1 + \beta = 4$. Further, assume that the mechanical properties of this material are fixed for a given device, and have been minimized to the extent that process reliability and focal plane layout will allow. Second, there is a metal term - the gold G-link - which scales as $n = 1 + \beta = 2$. Assume that the thickness of this metal link can be arbitrarily changed, and that we've chosen to modify its thickness in order to achieve the target value of P_{sat} required to match the expected optical load on the detector. (Obviously at very high temperatures the nitride

alone will reach values of $\overline{G}$ larger than this target, at which point we realistically assume no gold is deposited and that P_{sat} increases with T_c.)

For the specific case of a third season SPT detector operating at 150 GHz, we expect $P_{\mathrm{opt}} = 12 \pm 2pW$, and thus require $P_{\mathrm{sat}} = 24pW$. The noise optimum occurs at the lowest achievable stage temperature, which in this case is approximately $275mK$. The result of this calculation is show in figure 3.5. Above roughly $Tc = 700mK$ the dielectric conductivity exceeds the target saturation power, the metal link thickness is reduced to zero, and P_{turn} increases with T_c.

There are several significant features to note. First, the value of n varies smoothly from the normal metal value at low temperatures to that of a pure dielectric at high temperatures, as one would expect. When considering fabrication reliability, if T_c is less reliably constrained than the thermal conductance of the metal G-link, it is advantageous to choose higher values of T_c, since $g = \partial P_{\mathrm{sat}} / \partial T_c$ is lower. This is somewhat counter-intuitive - one might imagine that maximizing r and thus minimizing n would universally lead to relaxed fabrication constraints. It's certainly true that maximizing r for a fixed T_c is universally optimal, both for fabrication reliability and noise properties; however, in the limit of a fixed nitride contribution, the fact that all the power law indices are greater than unity means that the decrease in G while increasing T_c wins out over the increase in n.

Second, the thermal carrier noise, NEP_g, does have an optimum value; however, the feature is extremely broad. In this specific case, NEP_g is minimized for $T_c = 480\,\mathrm{mK}$. The range of T_c over which the NEP is different from its optimal value by less than 10% extends from 390 to 600 mK. This is comparable to the precision, generally around 20%, with which a given value of $\overline{G}$ and P_{sat} can be achieved in fabrication, and in practice we therefore gain little by attempting to achieve a more precise optimum. This range of T_c values also encompasses the range of values observed using our standard bilayer fabrication recipe over the course of many years. The strategy adopted by SPT has therefore largely been to allow T_c to vary, measure it using witness samples from each deposition, and then adjust the gold link properties to achieve a specific value of P_{sat}.

3.7   A summary of TES results

The preceding sections discuss the basic dynamic properties of both the simple point-mass TES and a slightly more complicated model which includes extra heat capacity in the form of a discrete BLING, and the design drivers for adjustable parameters. The major results can be summarized as follows.

Given a telescope and receiver optical design which couples radiation from the sky to a fixed number of detectors on a focal plane, maximum signal-to-noise is achieved when the bandwidth of each detector is maximized and internal loading from optical elements in the receiver is minimized. (The global problem of optimizing the entire system is complicated and dominated by detailed hardware costs and mechanical constraints, and is beyond the
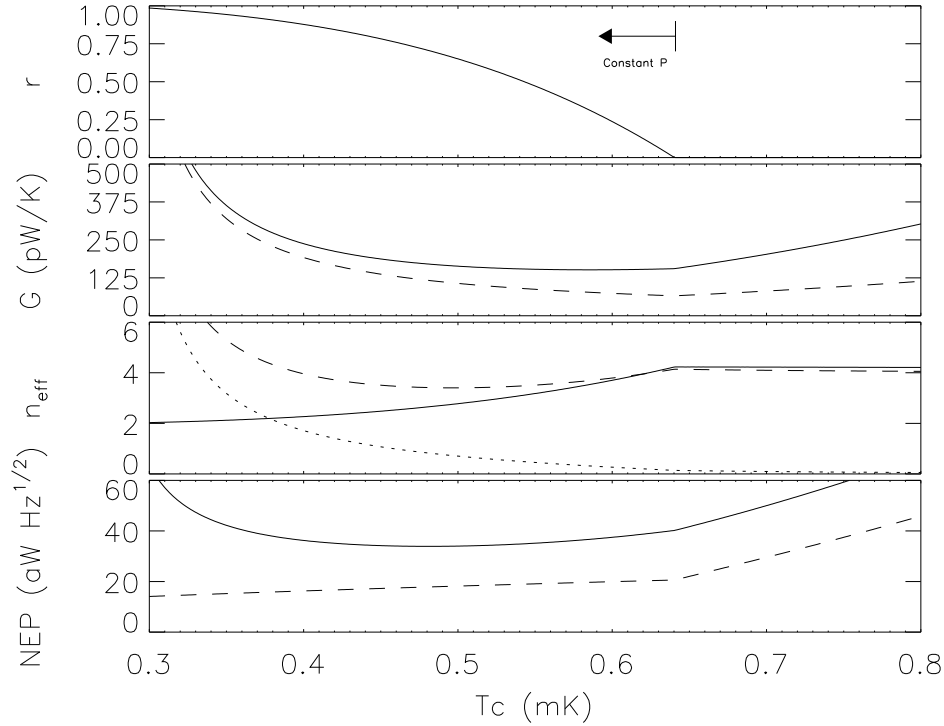
Figure 3.5 Variation of thermal properties and intrinsic NEP with Tc for a model bolometer with a composite thermal link, as described in §3.6.2.

Top: Fraction of the total power which is transported along the metal link.

Second: Thermal conductance of the thermal link. The solid line is the small signal $G = \partial P / \partial T_C$. The dashed line is $\overline{G} = P_{sat}/\Delta T$.

Third: The solid line shows the effective power law index of the thermal conductance of the composite link, where $n = \beta_{\mathrm{eff}} + 1$ and $k \propto T^{\beta_{\mathrm{eff}}}$. As T_c increases, n changes from metal-like to dielectric-like. Also shown are predictions for the differential index one would measure by modulating either T_b or T_c; the dashed and dotted lines show values for $\mathrm{d}\log P_{sat}/\mathrm{d}\log T_c$ and $\mathrm{d}\log P_{\mathrm{sat}}/\mathrm{d}\log T_b$, respectively.

Fourth: Intrinsic NEP for this device. The solid line shows the predicted thermal carrier noise. Note the broad optimum; NEP varies by only 10% over 235 mK. The dashed line indicates the predicted Johnson noise for a $1\,\Omega$ TES *at low loop gain* ($\mathcal{L} = 1$). In normal operation, this term will be suppressed by $1/\mathcal{L}$, and can generally be ignored. Readout current noise is not plotted; the NEP of these sources will depend only on P_{sat}.

scope of the discussion here.) Atmospheric lines place strong constraints on the observation bands available from the ground. Within a given observing atmospheric window, one should maximize optical coupling to the detectors and the passband of filter elements. Horn cou-

pled spiderweb detectors with metal mesh filters are a reliable and well tested method of transforming optical power into thermal energy. The thermal crossing time of the spiderweb dominates the temporal response of such detectors, and the details of the optical cavity and backplane determine overall optical efficiency.

In SPT, we use frequency domain multiplexed, voltage-biased Transition Edge Sensors to measure the power incident on a spiderweb absorber. Changes in power lead to changes in the current through the device, which are read out using a SQUID ammeter. The thermal and electrical properties of the TES bolometer are constrained by several considerations.

The total large-signal heat conductance to the bath, $\overline{G} = \delta P_{\text{tot}}/(T_c - T_{\text{bath}})$, must be chosen such that P_{tot} is larger than the expected optical loading in the field, P_{opt}. Higher values of P_{tot} give rise to noisier detectors. Lower values of P_{tot} lead to reduced loop gain and non-linear behavior of the TES itself, since loop gain scales as $\mathcal{L} \propto P_{\text{tot}}/P_{\text{bias}}$. A reasonable choice that allows for some safety margin in dynamic range, electrical noise sub-dominant to photon noise, and loop gain of many tens for realistic film properties is $P_{\text{tot}} \gtrsim 2P_{\text{bias}}$.

The small-signal conductance, $G = \partial P_{\text{tot}}/\partial T_c$ depends both on $\overline{G}$ and on the material constraints of the device. For a device where the heat link consists of both dielectric and normal metal parts, noise performance improved by minimizing the dielectric contribution. When the dielectric contribution is fixed by mechanical constraints, and the bath temperature is fixed, T_c can be chosen for optimal noise. For the SPT detectors, there is a very broad optimum in T_c centered near 500 mK.

A detector with a given value of G, a heat capacity C, and a superconducting transition such that $\alpha = \partial \log R \partial \log T$ at an operating resistance R_0 will have an intrinsic time constant given by $tau_0 = C/G$, and an effective time constant given approximately by $\tau = \tau_0/(\mathcal{L}+1)$, where the loop gain is $\mathcal{L} = \alpha P_{\text{bias}}/G T_c$. In general, α increases as one moves from the normal to the superconducting state, and the operating loop gain can be selected by biasing to a particular depth in the transition.

The responsivity of the bolometer to incoming power, $s_i = \delta i/\delta P_{\text{opt}}$, is given by 3.33. At low frequencies, it scales as $1/\left(v_{\text{bias}}\left(\mathcal{L}+1\right)^2\right)$. For a 1% variation in responsivity over a range of 60 degrees from the zenith, we require $\mathcal{L} \gtrsim 10$. At higher frequencies, the response rolls off approximately as a one-pole filter with the effective time constant of the bolometer, τ.

If the TES is voltage biased in a circuit with no stray resistance and inductance L, the readout system will impose a time constant which is the inverse of the readout bandwidth. In a DC system, $\tau_e = L/R_0$, while in the AC biased system used in SPT, $\tau_e = 2L/R_0$. In practice, optimizing the choice of L and R_n is complicated. Frequency spacing is driven by cryogenic loads and amplifier loop phase delays associated with wire lengths within the cryostat, constraints on channel-to-channel cross talk, and the availability of warm electronics. R_n must be chosen so that it dominates the bias resistor and any stray impedances in the system, while also insuring that the Johnson noise from the TES remains small compared to other noise terms and that the thermal conductivity across the TES (governed by Weidermann-Franz electron transport) remains a sub-dominant part of the thermal cir-

cuit. For the Analog fMUX system used in SPT, $R_n \approx 1\,\Omega$ and $L = 16\,\mu\text{H}$, in which case $\tau_e \approx 32\,\text{ms}$.

For stable (over-damped) operation, it is necessary that $\tau \geq 5.8\tau_e$. This sets a limit on the maximum loop gain at which a device can be run. More generally, as τ approaches τ_e, the response of the bolometer departs from the simple approximation. In order to operate SPT devices at suitably high loop gain, it is necessary to radically increase the effective heat capacity of the device by adding a large thermal mass called BLING. At low frequencies, the device behaves as a simple TES whose time constant is dominated by the bling heat capacity, $\tau_0 = C_0/G_0$. At high frequencies, the TES will thermally decouple from the BLING and become unstable. If the BLING is coupled to the TES with a thermal link characterized by $G_{\text{bl}} = \gamma G_0$, the maximum loop gain before decoupling occurs is approximately given by $\mathcal{L} \leq \gamma + 1$. For stable operation at high loop gain, it is important to maximize the coupling between the BLING and the TES.

The response of season 3 SPT devices depart from the simple TES & BLING model at low frequencies and low loop gain. Extending the model to include on additional excess heat capacity, presumably due to material physically distributed on the web and TES island, provides a much better fit to laboratory data. At the moderate loop gains this excess heat capacity decouples from the TES thermal circuit. Thus, the simpler model adequately describes the behavior of SPT devices operated in the field.

These constraints shape the design of the SPT detectors. The challenge then is to design a fabrication process which is robust, repeatable, and high-yield, and also meets all of these design criteria, which is the subject of the next chapter.

Chapter 4

Device design and fabrication

4.1 Introduction

This chapter discusses the design choices and fabrication process for the SPT devices, including the final season-3 fabrication recipe and several earlier test results. All of the work discussed here was conducted in the Berkeley Microlab[1].

I anticipate that new students working with similar devices in the Microlab, and its successor, the Marvel Nanofabrication Facility,[2] will be among the principle readers of this document, and therefore include somewhat more detail regarding both the final fabrication recipe and process design and testing than is conventionally reported in the literature. General readers will probably be satisfied with the summary of the device design in subsection 4.2.1, and the discussion of device performance section 5.

Following initial deployment of the SPT-SZ receiver, the instrument focal plane has been reconfigured three times in order to take advantage of ongoing detector development and fabrication. This document is principally concerned with the season 3 focal plane, which was deployed during Austral winter 2009 and redeployed with minor changes to receiver hardware during Austral winter 2010. Except where otherwise specified, fabrication details refer to these devices.

4.2 The design of SPT devices

4.2.1 Design overview

The South Pole Telescope SZ-Receiver focal plane is divided into six triangular modules, each containing the following elements: a capacitive metal mesh filter which defines the upper band edge, an array of smooth walled conical horns connected to cylindrical waveguide which

---

[1]http://microlab.berkeley.edu/
[2]http://nanolab.berkeley.edu/

define the lower band edge, a printed circuit board (LC Board) which includes the resonant LC filters used for the frequency domain multiplexed detector bias circuit, and a triangular silicon detector wedge. Each SPT detector wedge is fabricated on a 100 mm composite wafer which consists of a 1/4 wavelength device layer, an reflective aluminum backplane, and a permanent adhesive bonded backing wafer.
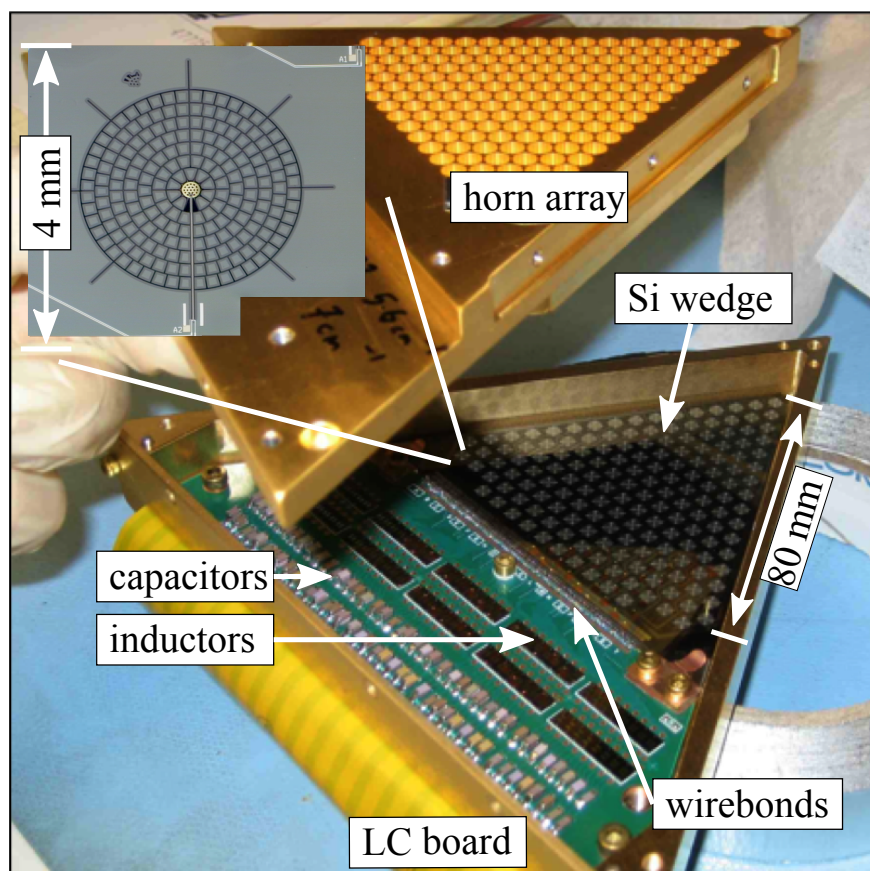
Figure 4.1 The SPT wedge module, showing the horn array, readout LC board, and silicon wedge. The wedge and LC board are mounted on an invar backing plate attached to the gold plated aluminum housing. In operation, triangular metal mesh filters are installed on top of the horn array and held in place with metal clips. The inset shows a single spiderweb bolometer. Figure from Shirokoff et al. (2009)

Each wedge includes 161 monolithic, fully lithographed spiderweb bolometers with aluminum-titanium Transition Edge Sensors (TESes), superconducting aluminum bias leads, and wirebond pads. Each bolometer consists of a 3 mm diameter gold spiderweb on a Low Stress Nitride (LSN) support structure, suspended by eight 0.5 mm long LSN legs for thermal isolation. The bolometers are arranged in a triangular grid with 4.78-mm spacing between
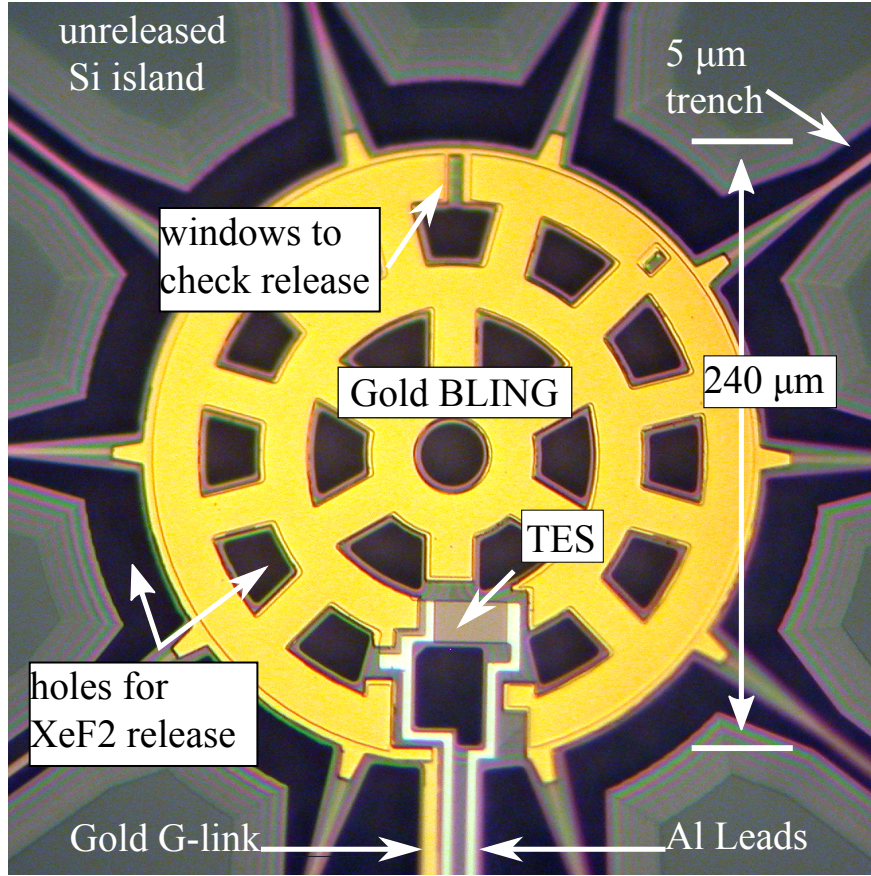
Figure 4.2 The central region of an SPT season 3 bolometer, showing the TES sensor, gold BLING, aluminum leads, gold thermal link, and gold web. The striped region around the perimeter of the LSN islands is the extent of the excavation during XeF_2 release.Figure from Shirokoff et al. (2009)

detectors. Parallel, coplanar $10\,\mu$m wide superconducting aluminum leads connect each detector to bond pads which are wirebonded to the LC board using standard aluminum wirebonds.

Each TES sensor is $31\,\mu$m long and $19\,\mu$m wide, with a normal resistance (R_n) of 1.1 Ohms and a transition temperature (T_c) of 550 mK. The transition widths, from 0.1-0.9 R_n and from 0.4-0.6 R_n are 20 mK and 2.5 mK, respectively. The value of $\alpha \equiv d\log(R)/d\log(T)$ smoothly increases with decreasing R, reaching approximately 20 at 0.7 R_n and 100 at 0.5 R_n. The thermal link between the TES and the cold bath includes a contribution due to the LSN structure and an additional gold thermal link. The thickness of this $5\,\mu$m feature which extends from the TES to the periphery of the web is tuned to achieve a target saturation power at a given transition temperature. Typical values of between 25 and 40 nm achieve saturation powers of 18 to 28 pW, with a stage temperature of 270 mK.

A large gold feature near the TES, the BLING, adds thermal mass to the device. The addition of 27000 μm^3 of gold leads to an intrinsic time constant of $\tau_0 = 30$ ms, and a device which can be stably biased with a 5 kHz readout bandwidth at moderate loop gain ($\mathcal{L} \gtrsim 10$).

The absorber consists of a grid of 2 μm wide gold traces with a 200 μm pitch. An approximately 200 nm thick gold layer produces an average sheet resistance of between 200 and 250 $\Omega/\square$, suitable for both efficient absorption and reliable fabrication. The array is constructed on an adhesive-bonded composite silicon wafer with an embedded Aluminum back-plane located $\lambda/4$ behind the spiderweb. Numerical modeling of the web, backplane, and feed-horn geometry was used to optimize the absorber cavity design.

The gold absorber is supported by a 1.2 μm thick LSN membrane, with 6μm wide features. After etching trenches in the LSN layer, the substrate immediately beneath the released membrane web is removed with a XeF$_2$ dry gas etch. Each segment of the LSN spiderweb is surrounded by a 5 μm wide silicon trench, and the region between segments consists of an island of LSN which remains unreleased, capping a silicon pillar which remains after XeF$_2$ spiderweb release. These islands minimize the amount of exposed Si surface area during the XeF$_2$ release, reducing the amount of LSN which is lost during release. Additional 20 μm scale apertures in the center island allow the XeF$_2$ gas to reach the area at the center of the web.

Table 4.1 SPT Fabrication layers

layer	mat.	thickness	Deposition	Etch
Substrate	Si	$105 - 250\,\mu$m	–	XeF$_2$ dry gas
Backplane	Al	$1.5\,\mu$m	DC Sputter	–
Membrane	LSN	$1.2\,\mu$m	LPCVD	CF$_4$ RIE
Leads / TES	Al	40 nm	DC Sputter	Cl$_2$ RIE
TES	Ti	80 nm	DC Sputter	SF$_6$ RIE
Absorber	Au	20 nm	Thermal Evaporation	Resist liftoff
Thermal link	Au	30 nm	Thermal Evaporation	Resist liftoff
BLING	Au	700 nm	Thermal Evaporation	Resist liftoff

Note. — All instances of Al are from a sputter target which includes 2% Si. A single Al layer forms the leads and the low T_c component of the bilayer; the Ti portion of the bilayer is deposited in the same vacuum step. All gold layers include a thermall evaporated 2.5 nm Ti adhesion layer. A brief Ar sputter etch occurs prior to the Absorber deposition. Acryonyms used include Low pressure Chemical Vapour Deposition (LPCVD) and parallel plate Reactive Ion Etch (RIE). Cl$_2$ RIE is a multi-gas Aluminum etch described in the text. SF$_6$ RIE includes 10% O_2.

4.2.2 Reflective back-plane position and wafer bonding

In order to efficiently couple radiation to the detectors, a reflective backplane is placed behind the absorber. The case of an idealized geometry, in which a plane-wave is incident on a uniform sheet resistance suspended above an air-gap, a uniform sheet of silicon dielectric, and a fully reflective back plane is described in detail in Appendix A of Gildenmeister (2000). Perfect absorption occurs for a sheet resistance matched to the impedance of free space, $R_\square = Z_0 = 377\Omega$, which is placed at the anti-node of a standing wave reflecting from the backplane. Neglecting the air-gap, this occurs at $n\lambda/4$ for $n = 1, 3, 5\ldots$, where λ is the wavelength in the substrate. The width of the absorption band decreases linearly with increasing order, n, as one would expect.

Though useful for building intuition, the plane wave model fails to take into account a number of important features of real devices. The final SPT design made use of detailed numerical simulations of the bolometer cavity using the commercial software package HFSS, a finite element Maxwell's equation solver. This work was primarily undertaken by Jared Mehl, and complete details can be found in Mehl (2009). The basic model includes the waveguide and launching opening, a vacuum gap, a spider-web absorber represented as a disc of constant surface resistivity, a circular slab of dielectric material, and an infinitely conductive back-plane. A dielectric constant of $\epsilon = 11.66$ is assumed for the silicon. (Afsar & Chi, 1994) A 3 mm diameter, $25\,\mu m$ thick disc with reduced dielectric constant $\epsilon = 7.13$ is placed directly behind the spiderweb. This structure approximate the bulk properties of the region from which material has been removed during the XeF_2 spiderweb release, based upon the measured dimensions of released devices and the approximate formula from Grann et al. (1994).

As expected from the plane-wave model, maximal coupling occurs with a backplane distance of $\lambda/4$, where λ is the wavelength of the band center in Silicon. The power radiated sideways into the silicon substrate, which can lead to optical cross-talk between pixels, is largest at the lower end of the band. In order to minimize cross talk, we've chosen wafer thicknesses which are slightly higher (by 5-10%) than the maximal absorption choice.

At 150 GHz, this corresponds to only $145\,\mu$m. Processing such thin wafers in the U.C. Berkeley Microlab proved impossible. Not only were such thin wafers fragile and prone to damage during transport and processing, but the optical lithography system lacked sufficient throw to focus on the top surface of wafers outside of the standard range of roughly 350 to $650\,\mu$m . (Adjusting the optical stack to move the focal plane is possible, but would have been incompatible with other users' processes.)

For the first season SPT deployment (as well as the initial APEX-SZ focal plane), time constraints drove us to accept a sub-optimal $3\lambda/4$ thickness configuration. Based on HFSS simulations using our our measured optical bands, we selected $450 \pm 5\,\mu$m thick wafers, which were compatible with all the required fabrication equipment and easily handled, but had relatively poor optical efficiency and significant cross-talk between detectors.

Following the deployment of the first SPT array in 2007, we developed a process for con-
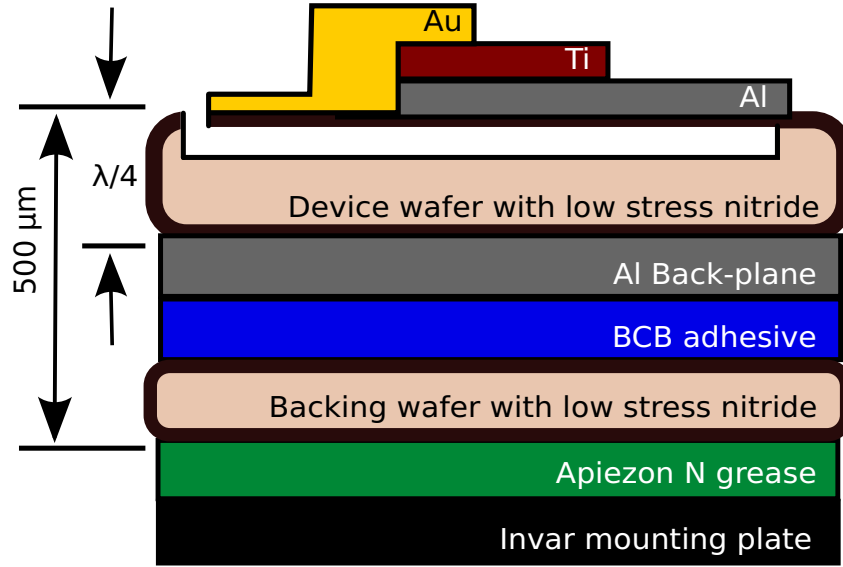
Figure 4.3 A schematic representation of a cross-section through an SPT wafer. Figure is not to scale. The device wafer, backplane, adhesive, and backing wafer are shown, as well as a cartoon of the device layers. Figure from Shirokoff et al. (2009)

structing composite wafers with a $\lambda/4$ backplane in all bands. The final wafer thickness and the detailed configuration of the waveguide were chosen by optimizing numerical simulations of the simplified model described above.

After optimizing to achieve maximum absorption in the spider-web and minimum "crosstalk" (optical power traveling parallel to the silicon wafer which can couple to other detectors), we selected wafer thicknesses of 105, 150, and $250\,\mu$ms for the 220, 150, and 95 GHz bands, respectively.

4.3   Fabrication

4.3.1   Low Stress Nitride deposition

We begin with Double Side Polished low resistivity (1-100 $\Omega-$cm) 100 cm diameter Si wafers, obtained from a commercial vendor with a specified thickness of 105, 150 and $250\,\mu$ms and a tolerance of $\pm5\,\mu$ms for the 95, 150, and 220 GHz band. After a standard chemical cleaning step, in which the wafers are immersed for 10 minutes in a bath of piranha (heated sulfuric acid and hydrogen peroxide), flushed with DI water in a Quick-Dump-Rinse (QDR) sink until they exceed a fixed resistivity ($> 10\,\mathrm{M}\Omega - $cm), and dried in a Spin-Rinse-Dry (SRD) machine, the wafers are immediately loaded into the LSN furnace.
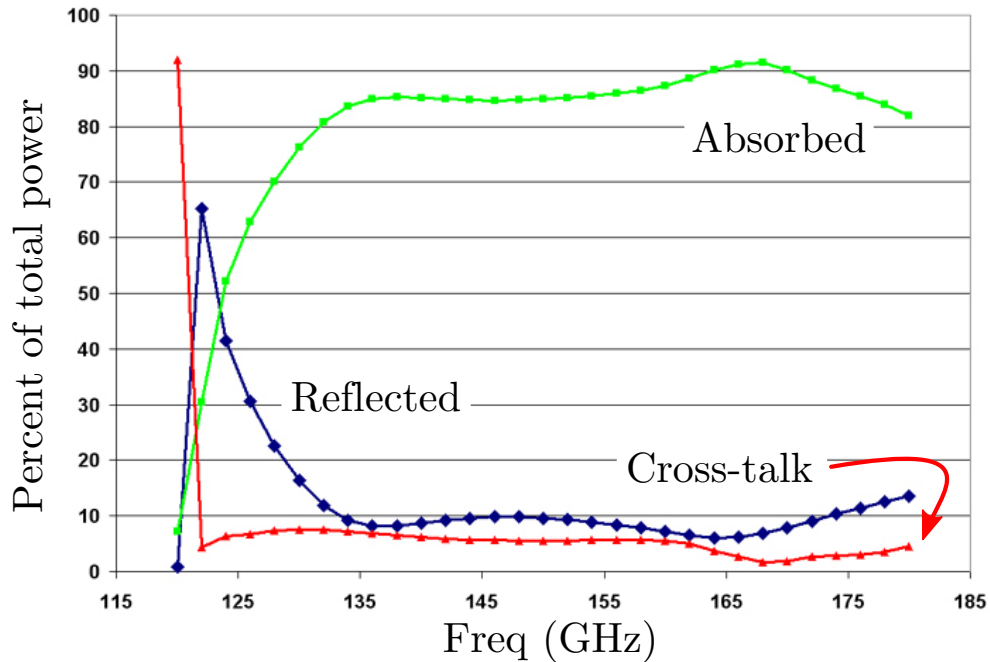
Figure 4.4 Absorption for an SPT pixel with $\lambda/4$ backshort, from simulations conducted by Jared Mehl. This design achieves high absorption, low reflection, and small power loss sideways into the dielectric (labeled "cross-talk" in the figure) throughout the 150 GHz atmospheric window

The Microlab Tystar-17 furnace to deposits Low Stress Nitride by reacting Dichlorosilane (DCS; SiH_2Cl_2) with Ammonia (NH_3 at high temperature to produce non-stoichiometric silicon nitride (LSN; Si_3N_x). Consistent results are obtained with the standard process parameters (100 SCCM DCS, 25 SCCM NH_3, 140 mTorr, 835° C) and a process time chosen based upon the lab furnished process characterization data - typically, approximately 330 minutes for a 1.2 micron layer. Because there is a significant variation in the film thickness depending on the position in the furnace, we place only 10-15 device wafers in the center of the rack, and use the remaining space for backing wafers and test dummies.

Tests of an SPT wedge in which half the bolometers were not patterned with a gold G-link measured the contribution of the LSN legs to the total G (thermal conductance) of the device. With a LSN thickness of $1.2\,\mu m$, a total power at turn-around (P_{turn}) of $10pW$ for a detector with $T_C = 530\,\text{mK}$ and $T_b = 280\,\text{mK}$. For our fielded 150 GHz detectors, LSN therefore contributes roughly 50% of the total thermal conductance.

Silicon dioxide has been selectivity in the XeF_2 release than LSN, which prompted us to try several test wafers with a thin (10 to 80 nm) thermal oxide layer beneath the LSN. The resulting films were remarkably robust in the XeF_2 release and based upon a visual inspection

of the released structures had film stress comparable to the bare LSN devices. Subsequent tests showed that the resulting thermal conductivity of the spiderweb legs increased by nearly a factor of three, making the process unusable for SPT without a significant focal plane re-design. Because of time constraints, we did not thoroughly characterize the source of this increased thermal conductivity. It is clearly much larger than the contribution due to the conductivity of the additional silicon dioxide material. Previous studies have found that the surface properties of LSN can significantly influence its thermal conductivity. We suspect, therefore, that the SiO_2 layer served to protect the LSN surface during release, leading to fewer surface features and less phonon scattering and thus increasing the conductivity of the LSN itself.

4.3.2   Back-plane deposition and wafer bonding

To produce wafers which are mechanically robust and can be processed using standard fabrication equipment, we use a composite wafer with an embedded metal back-plane. Several back-plane materials were considered. Gold would be ideal for our process, however we use several general-purpose tools in the Microlab's Very Large Scale Integration (VLSI) device area, where gold is forbidden because of the danger it will contaminate semiconductor processes. Sputtered copper and niobium were considered, and one wafer was processed to completion with a $1\,\mu m$ thick RF sputtered Cu layer, deposited on LSN following a $20\,nm$ DC sputtered Ti adhesion layer. Both materials were abandoned due to the labor-intensive deposition options available at the time at our facility.

For the backplane, a 1.0 to 1.5micron thick layer of Aluminum (2% Silicon) is deposited on the back side of the device wafer via DC sputtering. (Using the CPA 9900 track sputtering system, manufacturer by Circuits Processing Apparatus Inc, a base pressure of $5\times10^{-7}\,Torr$, $6\,mTorr$ Argon process pressure, $1\,KW$ DC magnetron power with a $15\,inch$ target.) Our observation frequencies exceed the frequency associated with the superconducting energy gap of the Aluminum, so it is necessary to deposit a layer of material equivalent to several skin-depths at the expected resistivity of our Aluminum films measured above the transition temperature. In cryogenic tests of thinner aluminum films from the same system, we've measured a resistivity of approximately $2\,\mu\Omega cm$ at 2.3 K, which is consistent with both our TES resistance and literature values for the bulk properties of room temperature Aluminum, and is likely to be an upper limit on the low temperature resistivity of thicker films. At 75 GHz (the bottom of our lowest frequency observing band), the skin depth is therefore $\delta = \sqrt{2\rho/\omega\mu} \approx 0.25\,\mu m$. Thus, we expect the $1\,\mu m$ thick films to efficiently reflect radiation in our observation bands.

A backing wafer chosen for a final composite wafer thickness of between 450 and 500 μm is prepared with a 1.0 μm thick layer of LSN, which will protect the wafer during our final release step. (We considered using a thin layer of silicon dioxide, which should provide better selectivity in the XeF_2 release step; however, LSN grown via LPCVD in the same furnace batch as device wafers was successful and saved a processing step.) Both back-side-etched

and double side polished wafers were successfully used as backing wafers, though there is anecdotal evidence that the DSP wafers are more robust to handling.

The bond is made using the commercial adhesive benzocyclobutene (BCB). BCB is a spin-on low-K dielectric polymer used in a number of commercial applications, including the manufacture of flat panel displays. The material is mechanically and chemically robust, and cures at relatively low temperature without evolve gasses, which makes it ideal for our application. In recent years several research groups have used BCB in bonding patterned MEMs devices, for example, Hwang et al. (2004), and Niklaus et al. (2001) found that it compared favorably with other candidates for whole wafer adhesive bonding.

Using a manual photoresist spinner, a 3.0 μm layer of benzocyclobutene adhesive (BCB, Dow Cyclotene 3022-46) is deposited on the backing wafer following the manufacturer's guidelines. The back side of the wafer is covered with temporary-adhesive dicing tape to protect it from stray BCB splash. An adhesion promoter (Dow AP 3000) is deposited on the LSN surface and spun-dry prior to deposition. and the edge bead and outer 1.5 cm rings of BCB is then removed by hand with a foam applicator dipped in Dow T1100 solvent. The backing wafer is then soft baked at 90 C for 12 minutes, after which it can be stored at room temperature in air for many days before use with no ill effects.

No special preparation is required for the device wafer, and we obtain very strong permanent bonds between the BCB and the untreated Aluminum surface of the backing wafer. The backing wafer and device wafer are aligned by hand and sandwiched between two clean standard-thickness silicon dummy wafers. These provide additional mechanical support and prevent particle contamination from contact with the wafer chuck. The wafer are then loaded into a commercial wafer bonder, the Karl Suss SB6 with Unitool head. The bonding chamber is repeatedly purged with alternating dry nitrogen and vacuum and then evacuated to a pressure of $\leq \times 10^{-5}$ Torr. The wafers are compressed at 3000 KPa, and then heated with a 90 minute linear temperature ramp to 300 degrees Celcius. After eight hours at 300C, they are cooled to less than 80C in approximately 45 minutes, after which the chamber is pressurized to one atmosphere and the wafers removed.

Following bonding, the dummy wafers are removed and the bonded wafer is visually inspected to check for fractures, dimples, and surface irregularities. Occasionally a small amount of excess BCB material is present around the edges of the wafer, and this is manually removed with a razor blade. The composite wafer is then cleaned for several minutes in an acetone sonic bath, rinsed in acetone, isopropyl, and DI-water, and finally passed through a commercial Spin-Rinse-Dry (SRD) machine. Following cleaning, the wafers are transferred to the Al-Ti bilayer deposition process.

4.3.3 Alternate bonding techniques

A number of alternative bonding techniques were attempted, and ultimately discarded. Among the three varieties considered were: permanent thermocompression bonds, generally involving the backplane metal itself with the bonding process placed either before or

after the bilayer deposition; permanent adhesive bonds, and temporary bonds which are broken and re-applied before every lithography step. The requirements are stringent: permanent bonds must be compatible with all our processing steps, including high vacuum at elevated temperatures, brief excursions to 300C or more, submersion in acetone, exposure to XeF_2 and various plasmas, mechanical dicing, and cryogenic cycling.

Several attempts at thermocompression bonds were made. There is considerable literature on the use of gold-gold bonds, both for die and whole wafers. Because we make use of several machines in the VLSI area of the Microlab, where the contamination risk posed by gold prevents its use, even in unexposed circumstances, the only option that allowed for gold bonds required wafer bonding following bilayer deposition. Several tests were conducted to see whether our bilayer material would be degraded at the temperatures and pressures reported for existing gold bonds in the literature. After one hour at 450C in dry nitrogen, visible degradation of the bilayer films occurred. At higher temperatures, even less time was required. We determined that no existing recipes for gold thermocompression bonds could be used after bilayer deposition. Despite a few promising experiments with evaporated Tin-Tin and Tin-Lead thermocompression bonds on small dies, we eventually abandoned that line of research because of the danger that the low melting point of those metals would be incompatible with later etch and deposition steps.

In collaboration with Miguel Daal, we attempted to replicate the Titanium-Silicon thermocompression bonds reported by Yu et al. (2006, 2007), in which a specially prepared Ti and bare Si surface are compressed at 450 C, forming a permanent $TiSi_x$ bonding layer. Despite replicating the author's preparation, we were unable to achieve reliable bonds in several attempts; wafers would initially stick together, but could be easily pried apart with a razor, revealing large voids and a small number of bonded regions across a wafer surface.

A number of permanent adhesive (and intermediary bonding material) approaches were attempted. Sodium silicate spin-on-glass, deposited on an oxide-capped-metal layer was considered, and some successful initial experiments on unmetalized wafers were carried out. However, the amount extra processing required and sensitivity to particle contamination and surface quality reported in the literature made it unattractive.(Puers & Cozma, 1997) The negative photoresist epoxy, SU-8, (SU-8 2007, manufactured by Microchem) was tested. There is extensive literature on the use of SU-8 for bonding, most commonly for the bonding of patterned glass wafers with curing UV exposure through the wafer. In private correspondence, other Microlab users report having successfully used uncured SU-8 for wafer bonding; however, we found that no reasonable amount of time or heat would turn unexposed SU-8 into a reliable bonding medium. Experiments on surface preparations to enable bonding with post-cured SU-8 were abandoned following successful tests of BCB.

Several novel adhesives were also tried. Among these, vacuum-degassed Stycast 2850FT (a two part epoxy manufactured by Emmerson Cumming, widely used in cryogenic hardware) applied with rollers proved difficult to handle, prone to void formation, and became visibly degraded following brief temperature excursions to 300C. Eccobond 24 (a two part epoxy manufactured by Emmerson Cumming) was successfully used for several completed

wafers, two of which underwent full cryogenic cycling and electrical characterization. The epoxy was manually mixed, degassed for several minutes in a vacuum belljar attached to the house vacuum system, then applied with a manual photoresist spinner to a backing wafer. The device wafer, upon which the Al/Ti bilayer had already been deposited was then manually aligned with the backing wafer, and the two were compressed using metal weights in room air overnight. Although several of our processing steps exceed the recommended maximum temperature supplied by the manufacturer, we saw no mechanical failures or visible degradation of the adhesive.

Attempts at temporary bonds included commercial Cyanoacrylate glue and standard I-line negative photoresist. In this process, the thin device wafer would be bonded to a handle wafer prior to lithography, remain bonded during the etch process, removed in acetone or other solvents along with the process resist, and then re-bonded for the next layer. Cyanoacrylate was unreliable at even slightly elevated temperatures, and photoresist turned out to be difficult to remove cleanly, tending to form bonds which were too robust to be readily dissolved in acetone and yet fragile enough that gaps and voids formed during each resist-removal step, makings it unsuitable as a permanent adhesive.

One extreme version of temporary bond proved successful. After spin-coating photoresist on the device wafer, it was placed flat against a clean backing wafer, and small dots of commercial rubber cement were applied to several places around the wafer perimeter. The completed stack could then be exposed using the standard wafer stepper. Following exposure, the backing wafer and rubber cement residue was removed by hand, and the wafer then processed as a thin wafer. Although several complete SPT arrays were fabricated in this fashion during our 2007 season, the process was both time consuming and failed to protect against the fragility of thin wafers during processing.

4.3.4   TES bilayer

Following wafer bonding and cleaning, a superconducting bilayer consisting of approximately 40 nm Al (2% Si) beneath 80 nm Ti is deposited by DC sputtering in a single vacuum step. (Using the CPA 9900 track sputtering system, manufacturer by Circuits Processing Apparatus Inc, a base pressure of 5×10^{-7} Torr, 6 mTorr Argon process pressure, 1 and 1.5 KW DC magnetron power for the Al and Ti layer, respectively, with a 15 inch target.) The layer thicknesses are adjusted to achieve a superconducting transition temperature of approximately 550 mK, with a typical resistivity of approximately 0.65 Ohms per square when normal.

In principle, the transition temperature of a bilayer is calculable when various conditions are satisfied, and there exists a significant body of literature comparing experimental data with theory. (Werthamer, 1963; Clarke, 1968; Duzer & Turner, 1999) In practice, it is generally easier to determine an appropriate material thickness by fabricating and testing films with varying properties, making use only of the most basic constraints on the functional form of the expected behavior, which can be separated into three qualitatively distinct regimes.
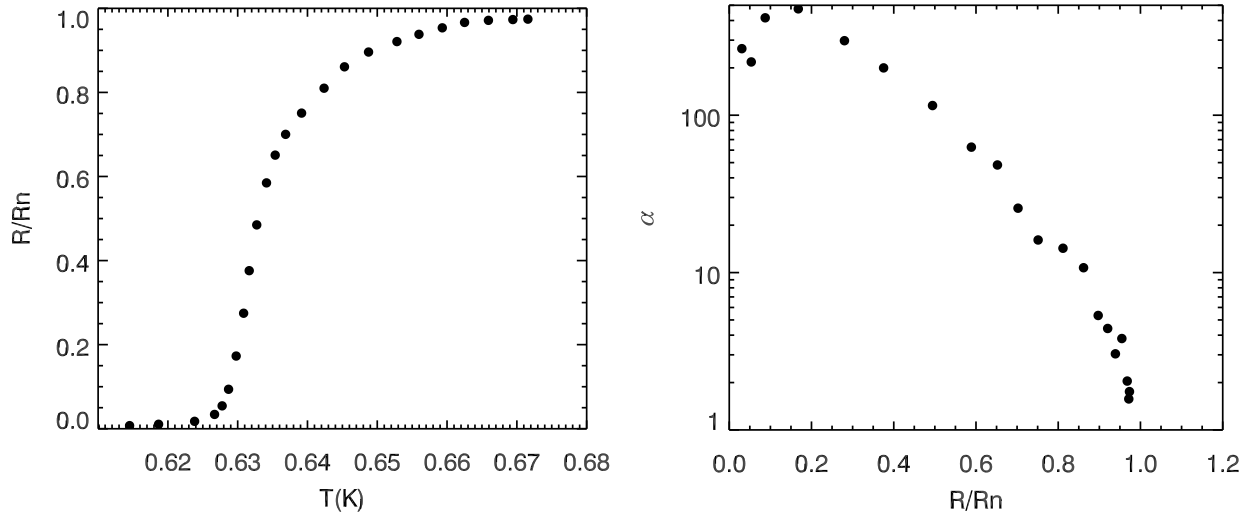
Figure 4.5 R(T) and $\alpha \equiv \partial \log R / \partial \log T$ for an SPT TES. Data were taken for an early season 3 witness pixel, which shows a higher transition temperature than fielded devices. R(T) was measured by applying a small modulated voltage bias (corresponding to $< 1\,\text{aW}$ at $0.5\,R_n$) and measuring the current with a DC SQUID and feedback amplifier manufactured by Quantum Design. α is extrapolated from piecewise linear fits to the data.

In the first regime, where the thickness of the superconducting layer is large compared to an intrinsic scale length ξ_s (typically several tens of nm), T_c approaches the superconductor value. In the second regime, where neither layer is much larger than its respective scale length, the resulting temperature depends on the thickness of both films. In the third regime, where the thickness of the normal layer is large compared to ξ_n but the superconducting layer thickness is not much larger than ξ_s, T_c will depend only on the thickness of the superconducting layer. To minimize sensitivity to variable material properties, its advantageous to operate TES detectors in this third regime. The resulting Tc will be intermediate between the native transition temperatures of the superconducting and the "normal" metals, and will monotonically increase with the thickness of the superconducting layer.

Using starting values determined from previous fabrication efforts with the group, we tested several combinations of film thicknesses. Figure 4.6 shows Tc vs. superconducting film thickness for samples taken over the course of several years and under varying conditions.

Two complications hindered the fabrication of SPT bilayers. The first is variability in the measured Tc for films produced under the same conditions at different time, presumably due to variation in machine parameters and or contamination of the deposition chamber. Between subsequent depositions - even those separated by only days - we often measured variations in Tc of up to 100 mK for identical deposition parameters. Further, we observed significant variation of transition temperature with the amount of time between layer depositions, which suggests that either the presence of small amount of oxygen in the chamber leads to the
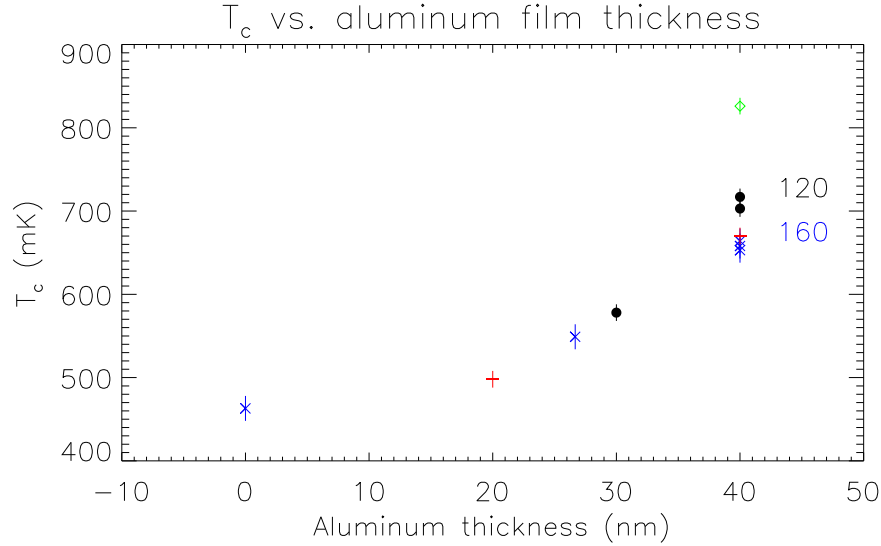
Figure 4.6 T_c vs. aluminum film thickness for bare Al-Ti bilayers deposited over the course of several years. Ti layers are all 80 nm thick except where indicated by text, where callouts refer to layer thickness in nm. The 160 and 120 nm films are associated with the higher valued blue cross and filled circle, respectively. *Black circles* indicate films processed on 2008/11/01, with the time between layer depositions minimized. The *green diamond* is data from the same deposition, but with an approximately 10 minute pause between layer depositions. *Red dashes* indicate films processed on 2007/10/01. *Blue crosses* indicate films processed on 2005-08-07.

formation of intermediate oxide layers on films, or that there is an unexpectedly steep film property dependence on the temperature of the substrate during deposition.

In order to compensate for this variability, we adopted a policy of including test wafers in each fabrication run. A witness wafer, consisting of a standard thickness test grade Si wafer with a LSN film grown in the same furnace batch as production wafers, is included in every bilayer pallet. Immediately following bilayer deposition, the witness wafer is diced into small samples and Tc and an the cryogenic sheet resistance are measured using a four point resistance measurement in a lab cryostat. The measured value of the final expected Tc is then used in determining an appropriate gold G-link thickness, or, in the case of rare and extreme excursions (usually associated with unusually high base pressure in the CPA or recent target changes), the entire batch of wafers is stripped of bilayer (in an SF_6 + 10% O_2 parallel plate etch followed by a standard aluminum wet-etch) and re-processed.

Throughout the SPT fabrication effort, we've consistently seen a change in bilayer Tc between test films and completed bolometers. Time and resource constraints prevent the careful investigation of this phenomena, and we have not attempted a quantitative model to

explain it. We note that the magnitude of the drop can be significantly different between the single-pixel witness samples for a wedge and devices on the wedge itself. Because these devices participate in the same fabrication steps except for the XeF_2 release and subsequent O_2 resist ash, we infer that some part of these last steps is significant in causing the T_c drop. Heating, leading either to an annealing of the bilayer metal or to the diffusion of oxygen beyond the film surfaces is the most likely candidate, although experiments to reproduce the effect under controlled conditions have proven inconclusive.

In practice, we assume a change in Tc of approximately 100 mK from the bare film value for the first wafer in a bilayer batch, and adjust the G-link gold thickness accordingly. Iterating on subsequent wafers in a single batch and processing recipe allows for Tc values which are consistent to within a few 10s of mK, which is comparable to the accuracy with which we can control the thermal conductivity of the G-link.

The Al layer used for the TES bilayer also forms the superconducting leads and bond pads. This insures electrical contact between the TES and leads without the need for a pre-deposition sputter etch, and simplifies fabrication. We consistently find the aluminum layer superconducting transition between 1.3 and 1.4 K, consistent with measurements in the literature for thin aluminum films.

4.3.5 TES and lead fabrication

Using standard photo-lithography techniques the TES sensors are patterned in a 10X reduction wafer stepper. After a dehydration bake (30 minutes at 120C in the VWR convection oven, followed by the vapor deposition of an HDMS to promote adhesion), an automated resist coater track is used to deposit $1.1\,\mu m$ of OiR 10i (I-Line) photoresist, followed by a 60 second bake at 90C.

Using the GCA 6200 wafer stepper, dies with alignment keys are exposed on the silicon wafer outside of the region used for the SPT array. Using an automated developer track, OPD HPRD 4262 developer is used to develop the exposed dies. No post-exposure bake occurs prior to the developer step, and the unexposed resist covering the rest of the wafer is unchanged and can be exposed and developed as usual. The alignment keys, which consist solely of photoresist on Ti, are then used to align the first layer. By checking the alignment of each subsequent layer using patterned dummy wafers, its is generally possible to achieve regular alignment to better than $0.5\mu m$, although the SPT mask layout can accommodate a shift of up to $1.5\mu m$ without problems. (This constraint is principally driven by the desire to minimize the size of the superconducting aluminum strip which separates the TES from the BLING. The spiderweb to LSN web alignment constraint is comparable.)

The same wafer stepper is used to define the Ti regions of the TES sensors and to remove Ti from the regions which will later form the superconducting leads. Bilayer material is also left beneath the bling, providing additional heat capacity and increased thermal coupling between the bling and TES. A standard post-exposure bake (1 minute at 120C on hotplate) and a pass through the track developer completes the Ti lithography.

The Titanium is then etched with Sulfer Hexaflouride (SF_6 +10% O_2) in a parallel-plate Reactive Ion Etch (RIE), which stops at the Aluminum layer. A standard photoresist removal using acetone, followed by manual cleaning with acetone, Iospropyl, and DI-wafer and a hand-dry is used to remove photoresist. The wafers are then baked and primed with HDMS and coated with resist as described above. (This step, as well as the acetone resist removal, will be ommited from subsequent discussion.)

Aluminum electrical leads and bond pads are patterned in a two-step process which uses both the wafer stepper and a contact printer. The aluminum leads within each pixel are defined using the stepper. Visual alignment checks are performed on bilayer-coated dummy wafers before each exposure. Without an intervening develop step, a 1:1 contact printeter is then used to expose the bond pads and the array scale leads which connect them to each pixel. Dark regions mask the central region of each pixel, which are exposed on the wafer stepper. In the Berkeley Microlab, there is a systematic alignment offset between the two lithography systems, due to an offset between the microscope reticle position and the center of the mask when properly aligned with the optical column. A small ruler feature on the alignment key is used to measure and correct for this offset, which is of order $12\,\mu$ms and is stable over year timescales.

The first season SPT wafers suffered from significant damage due to dust and resist debris present on the contact mask. Dark regions created superconducting aluminum bridges between leads, shorting devices and rendering them unusable. Several approaches were tried to improve yield, including the use of a second exposure with a slightly enlarged contact mask, designed to take advantage of the small likelihood of particle contamination in the same place on both masks. Ultimately, we found that a thorough mask cleaning procedure, in which the contact mask is vigorously scrubbed with an acetone-soaked foam brush, then rinsed and blown dry under a flow hood immediately before each exposure dramatically reduced losses due to mask debris.

Following a standard post exposure bake and develop step, the resist is then hard-baked for 6 hours at 120C in air. The Aluminum layer is then etched in a multi-gas RIE parallel plate etcher, the Microlab *lam3* machine, a Lam Research AutoEtch Plasma Etch System which has been optimized for Aluminum processing. (The etch consists of the standard Cl_2 based plasma etch, followed by a $CF_4 + O_2$ plasma passivisation temp. A 25-40 second etch is used, with a time-based end-point chosen after examining dummy wafers.)

The same etch step removes $2\,\mu$ms of titanium along the edge of the TES parallel to the direction of current flow, which decreases our susceptibility to alignment shifts. Following the Al etch step, O_2 plasma in a parallel plate etcher is used to ash the hard-baked photoresist. Lab tests were used to confirm that the O_2 ash step does not significantly change the electrical properties of either the TES or Al leads.

4.3.6 Gold deposition

After the TES and leads are complete, three successive layers of gold are deposited using photoresist lift-off in a thermal evaporator. The gold spider-web made from $2\,\mu m$ wide gold lanes spaced at $200\,\mu m$s is deposited first. Numerical simulations indicate that a web resistivity of approximately 250 Ohms per square provides adequate coupling, and this value is reliably achieved using 12.5 nm gold with a 2.5 nm Ti adhesion layer.(Mehl, 2009) In principle, one could achieve slightly better coupling to free space with a more resistive web; however, we are limited both by the scale of the smallest possible lithography and the thickness of layers which we can reliably deposit. This limit is machine specific, but in general we find that for films thinner than a few tens of nm thermally evaporated gold tends to pool into a collection of disconnected μm-scale islands rather than a continuous film.

In addition to forming the spider-web, this thin gold layer is deposited over the Ti layer in the bling region, and forms the thermal interface between the bilayer material and thick gold layers. Prior to deposition, a brief Ar plasma is used to remove oxide from the Ti layer in this overlap region. Following standard photoresist patterning with no hard bake, a brief O_2 plasma descum is used to clean the wafer. (Microlab Ptherm parallel plate etcher, 50 Watts at 13.56 MHz with a 12-inch diameter plate, 100 sccm O_2 at roughly 40 mTorr, 1.5 minutes.) Following several repeated chamber purges with nitrogen followed by argon, the oxide layer is removed using an etch in argon. (Microlab Ptherm parallel plate etcher configured as above, 100 Watts, 50 sccm Ar, P=21 mTorr, 3 minutes.) Note that the process pressure used in this argon sputter etch is much higher than is generally used in standard ion-milling applications, which makes redeposition significantly more likely. SEM images of the thin gold films deposited following this step, as well as cryogenic four-point-measurements of the interface resistivity between the Ti layer and the gold film indicate that we are able to achieve robust electrical contact while maintaining surfaces that are smooth on the scale of our gold film thicknesses. Note that the active TES region is entirely covered with photoresist throughout this step, and only the region which will be covered with gold web material is exposed.

Immediately following the argon clean step, the wafer is transferred manually to a thermal evaporator. (Either the Microlab Veeco V401 or the NRC machines.) These machines both feature two sample stations, a DC current source, target shutters, and a resonating crystal film thickness monitor. After achieving a base pressure of at least 2×10^{-6}, a 2.5 nm thick adhesion layer of titanium is deposited from a high purity Ti rod over the course of approximately 4 minutes. Following a twenty minute cooling period, the target is switched to a tungsten boat containing gold wire (99.995% pure). Approximately 20 nm of gold is deposited at a rate of 1.5 nm/s. Witness pixels which contain a sample of the actual web geometry as well as wirebond pads are used for cryogenic four-point-measurements to verify web resistivity. In general, resistivity appears to be quit consistent for films deposited under similar conditions over several years, except in pathological cases where webs are obviously damaged. (In late 2008, a series of wedges were produced which showed significant damage

to the gold web, which had pooled and formed disconnected, pillow-like structures rather than a single film. No conclusive explanation was found, and subsequent wafers did not show this problem.)

Following the web deposition, we find the photoresist is significantly hardened and liftoff using a standard acetone bath is ineffective. Reliable liftoff is achieved with an 8 hour soak in SVC-14 photoresist stripper (manufacturer by Shipley) heated to 75C, followed by brief sonic agitation in the same vessel and a standard rinse and dry procedure.

Following gold web deposition and liftoff, two more gold layers are deposited via thermal evaporation. A 2 mm long, 5 μm wide gold thermal link extends from the edge of the TES to the unreleased edge of the bolometer. The total thermal conductivity to the bath is then tuned by adjusting the thickness of this gold link. Roughly 30 nm of gold, deposited at 1.5 nm/s in the same thermal evaporator, (in addition to a 4 nm Ti adhesion layer) adds roughly 45 pW/K to the 25 pW/K conductivity measured for the LSN structure alone. In this step, only the brief O_2 descum is performed, and there is no argon clean step. The thermal link is made between the new metal layers and a clean gold surface at the device side, and a thick LSN layer at the far side, thus oxide removal is not required.

A 240 μm diameter perforated disc of 700 nm thick gold is then deposited at the center of the spiderweb. This BLING adds thermal mass to the device, slowing its intrinsic time constant and allowing it to be stably biased by frequency domain multiplexed readout channel with $\tau_e \sim 32\,\mu$s. The thermal crossing time of the BLING itself is expected to be insignificant compared to other device time-constants; however, the BLING is made as small as fabrication will allow in order to avoid compromised absorption due to the low-impedance surface of the BLING interacting with incoming radiation. HFSS simulations suggest the current design modified the total absorption by at most a few percent compered to a device with no bling.

4.3.7 LSN Spiderweb

In a final lithography step, the suspended LSN spiderweb is patterned. The spiderweb is a circular mesh with 5 μm thick segments aligned to the gold web. Eight radial supporting legs extending to a diameter of 4 mm. One of these supporting legs is widened to accommodate the Al electrical leads and the gold thermal G-link which extend to the center of the web. In the center of the device, perforations in the LSN island allow XeF_2 gas to etch the back side of the suspended structure. This is essential to successfully releasing features with such a large ratio of LSN thickness to width of Silicon undercut.

The LSN spiderweb is then etched in a CF4 RIE gas etch. In the past, we've used an SF_6 + 10% O_2 gas etch; however the high etch rate of substrate Si in the SF_6 etch makes it difficult to avoid damaging the edge devices while over-etching to accommodate non-uniformity across our wafer surface. The addition of a small fraction of O_2 to the CF4 etch increases the rate of photoresist removal without providing any observable improvement in uniformity or repeatability of the etch.

Following the LSN etch, the silicon wedge is cut from the wafer with a dicing saw. Dies

containing optical test pixels and resistivity samples are removed and processed independently for laboratory testing. Following dicing, a brief sonic clean in DI water is used to remove dicing debris, and a thin layer of photoresist is painted by hand onto the exposed silicon edges of the wedge to protect it during release. After a brief bake at 90C and several pump and purge cycles with dry nitrogen to remove moisture, a cyclic XeF_2 dry etch is used to excavate silicon from behind the suspended LSN spiderweb.

4.3.8 Release of suspended structures

The XeF_2 gas cycle was carefully tuned in order to fully release devices across the 80-mm diameter active area of the wafer without damaging the structural LSN of the devices at the wafer edge. Our best results were obtained using a cycle consisting of a nine second exposure to XeF_2 at a pressure of 2 Torr, followed by a Nitrogen purge to many tens of Torr and a subsequent chamber evacuation. (A process which requires the use of "special etch mode 1" in the Microlab X-Etch machine.) Given the observed etch rate and exposed surface area, we deplete only a few percent of the XeF_2 gas in the chamber during each cycle.

Significant process development was required in order to achieve reliable release across the entire SPT wedge. Initial tests of single pixels, and the experience fabricating the APEX-SZ array lead us to imagine that the XeF_2 release would be straightforward, with more than adequate selectivity against the etching of LSN. In practice, the release of a full array proved much more difficult, testing the limits of the aspect ratios that can be achieved. In the process, several surprising features of the release have been observed, although time constraints prevented us from fully investigating and quantifying these features.

First, the local density of exposed Si dramatically alters the excavation rate, on scales which range from tens of μm appropriate to feature distributions on a single detector to the cm scales over which detectors are distribution on a wedge. The time required to release the central island of the spiderweb, which is surrounded by exposed trenches, is as much as a factor of two larger than the time required to release a test structure with the same dimensions located far from the spiderweb. Thus, calibration and estimates obtained for test dies are at best a rough guide for process design, and wafer-scale tests are necessary whenever a change is made. For the SPT array, the Si etch rate at the tips to the triangular is significantly larger than at the center of the array. Full release generally requires 18 μm of lateral excavation for the center-most pixel, at which point the outermost pixels exhibit an average of 35μm of undercut. The requirements for LSN selectivity are therefore roughly a factor of two larger than one would infer from the geometry of a single pixel.

Second, the selectivity of the Si etch with respect to LSN varies considerably with both process parameters and sample geometry. In general, it appears that the relative LSN etch rate increases dramatically with the amount of time spent on each gas cycle in the etch chamber. Even more surprising, the LSN etch rate appears to increase with the total amount of Si in the chamber such that it scales faster with surface area than the total etch time. Multiple tests involving identical structures from single-pixels, full SPT arrays, and

test dies have confirmed that the presence of exposed Si on physically isolated substrate increases the relative rate at which LSN is etched compared to Si. For example, a set of four SPT single pixels placed along in the chamber can be over-etched by a factor of four, using process parameters identical to those which destroy the webs on a full array long before release. These pixels emerge with fully intact nitride, despite having a larger ratio of exposed Si/LSN than a wedge.

Although far from definitive, these results suggest that a product of the Si-XeF$_2$ inter-action may play a significant role in determining LSN selectivity. Alternative explanations include presence of water vapor in the chamber, perhaps due to a small room air leak, leading to the formation of HF on substrates, and the possibility that reaction heating of the substrate and or the chamber gas may alter the relative etch rates. The first cannot readily explain the change in relative selectivity with nearby exposed Si. The second appears to be inconsistent with the small observed change in etch rates with chamber temperatures, which is observed to be $\leq 10\%$ for for a $2\,°$C temperature change at $35\,°$C, combined with the single pixel results, where local substrate heating should be even larger.

Third, we find that the presence of exposed gold causes a very large and local increase in the etch rate of both LSN and Si in regions which are located mm from the gold. The gold itself appears to be undamaged, and the etch rates return to normal for devices located several mm away. During the fabrication of first-season detectors, for which the thickness of the bling structure approached the limits of what could be covered with standard photoresist, incompletely capped gold lead to many failures.

These features drove the design of the SPT fabrication process in several ways. First, a release recipe was developed to minimize the length of exposure during each gas cycle as much as possible. Second, the pixels were designed to minimize the amount of exposed silicon. Instead of large open regions between spiderweb elements, the space between is filled with LSN capped Si islands, with only narrow trenches surrounding each element.

The rate at which Si is excavated near a trench is a non-linear function of the dimensions of the aperture. When designing the web and openings in the central island of the SPT devices, a series of test dies were produced to measure the rate of release around trenches and rectangular features of varying dimensions. An example of the result is shown in Figure 4.7. For large features ($\gtrsim 40\,\mu$m for a $15\,\mu$m excavation) the excavation rate approaches a constant, governed by the rate of surface interactions on the exposed Si. For smaller features, the rate is approximately linear with the log of the trench dimensions. In the limit of very large excavations, the break in the curve moves toward larger dimensions. For efficient release, one should choose features which are near the break in the release curves for a given total excavation depth. By placing release trenches of varying dimensions near released structures with varying aspect ratios, one can gain some improvement in the range of scales which can be successfully released. In the case of SPT, the spiderweb elements are surrounded by $5\,\mu$m trenches, intended to slow the excavation rate and this preserve nitride for these narrow features. The central island is surrounded by a $20\,\mu$m trench, designed for maximum efficiency. The release holes in the central island are roughly $20\,\mu$m square, which

is roughly 20% less efficient than maximum, but is a reasonable compromise between total bling area and release rate.
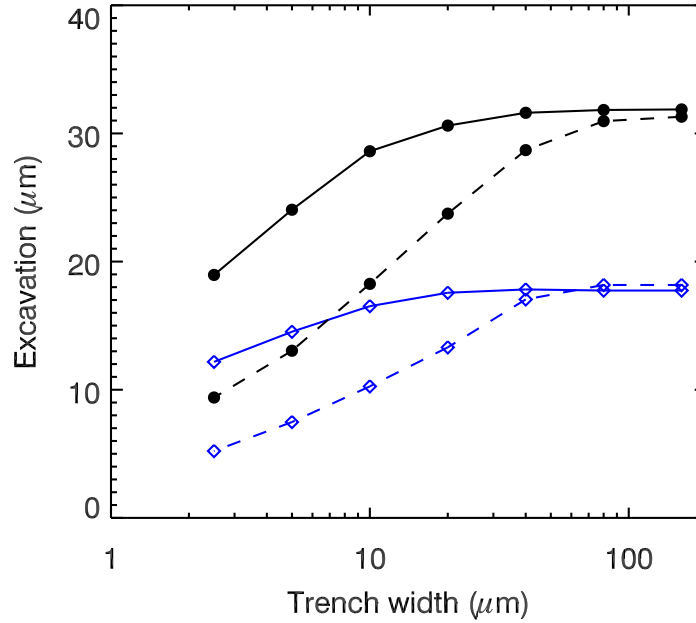
Figure 4.7 Extent of excavation during XeF_2 release for structures of varying dimensions on a sparse test die using the standard recipe in the UC Berkeley Microlab Xetch machine. Black circles show the extent of lateral undercutting for a 10-cycle release. Blue diamonds show the same for a 20-cycle release. Solid lines are 1 mm long trenches of width given by the x-axis. Dashed lines are square features of side length given by the x-axis.

4.3.9   Final photoresist ash and inspection

The end point of the XeF_2 release is verified by visual inspection. Several observation windows are included in the central island, chosen to be among the last parts of the device to be released. These small regions contain no layers except LSN. By inspection, one can see whether there remains a Si pillar beneath the LSN island in order to check for release. In practice, it was discovered that the slight displacement from the wafer plane is a more reliable indicator of release. The central regions of SPT pixels "pop" out of the Si plane by between 2 and 4 μm upon release, which can easily be seen in an optical microscope with minimized depth of field.

After release, photoresist is then removed using an oxygen plasma in a parallel plate etcher. Initial experiments indicated that the relatively high-power, high pressure standard

ash in the Microlab Ptherm parallel plate etcher caused significant damage to our thin gold webs, presumably due to mechanical abrasion. 20 minutes in the Ptherm, using 50 Watts at 13.56 MHz with a 12-inch diameter plate, 100 sccm O_2 at roughly 40 mTorr completely removed the thin gold web, from which we inferred that the 5-8 minute ash required to remove resist with the same parameters would be likely to significantly degrade our webs. A lower-power photoresist ash in the SEMI machine (30 mTorr O2, 100W, 80 minutes) was found to remove all the remaining resist without any observable damage to the gold web, verified by comparing ashed samples to solvent-cleaned samples in cryogenic DC four point measurements

Following the final photoresist ash, a detailed visual inspection of every device and trace on the wedge is carried out under a microscope. Potential problem devices are noted, and candidates are selected for removal from the array in order to accommodate the 7/8 channel readout restriction. Superconducting electrical shorts and large thermal shorts between the suspended island and the substrate both lead to devices which cannot be biased normal or nulled, rendering entire MUX combs unusable. We have therefore chosen to be very conservative in excising devices which appear to fall into either of these categories.

4.4 Mechanical housing and readout electronics

Following inspection, the wedge is mounted on an invar backing plate using a thin layer of Apiezon-N vacuum grease. This mounting method eliminates vibration of the silicon wedge when cold, while allowing the wedge to be easily removed from the support structure. Metal spring clips and rubber cement insure that the wedge remains in place during room-temperature handling.

Manual wirebonds attach the wedge to an LC-Board, a printed circuit board containing the resonant filters of the Frequency Domain Multiplexed (fMUX) readout system. After mounting, the room-temperature DC resistance across each device is measured and compared to a standard wedge in order to check for electrical shorts and opens in the leads.

The LC boards are fabricated using standard printed circuit board techniques at a commercial manufacturing facility. They consist of two sections of rigid printed circuit board connected by a flexible section. The flexible section becomes an internal layer in the rigid board. The copper on all six layers are treated with super-conducting White Immersion Tin, except for small regions of bare copper which allow for wirebonding.

Each resonant LC filter is composed of a 16 uH inductor and a surface mount capacitor. The capacitors are hand sorted and the boards populated to achieve a staggered frequency schedule that maximizes the separation between physically adjacent multiplexed groups. The inductors are superconducting Niobium devices fabricated by either Northrop Grumman or NIST in Boulder, Co and delivered as dies consisting of 8 inductors. The dies are mounted on the LC board with rubber cement and wirebonded to the LC board.

Chapter 5

Detector Performance

5.1   Introduction

In this chapter, I review the properties and performance of the fielded season 3 SPT detectors. Section 5.2 summarizes the thermal and electrical properties of the array. Section 5.3 discusses the measurement of the eletrothermal response of the devices, using the model described in Section 3.4. Section 5.4 summarizes the optical response and optical time constants of the fielded array. Section 5.5 summarizes the yield and uniformity of the array as a whole. The final array sensitivity and NEP are discussed in section 5.6.

5.2   Device parameters

The properties which govern the electrical and thermal behavior of a TES bolometer are discussed in chapters 3 and 4. For the SPT season 3 array, typical values are shown in table 5.1, and listed in more detail later in this chapter. The three parameters which drive the design and fabrication constraints are optical efficiency, stability under eletrothermal feedback, and appropriate saturation power.

Assuming a properly optimized waveguide and backshort, the optical efficiency of the device is governed primarily by the sheet resistance (and electrical continuity) of the gold spiderweb. Regular cryogenic, DC, four-point resistance measurements of specially prepared web samples with contact pads are carried out during fabrication to check web resistivity, and wafer-scale samples demonstrate that resistivity values typically vary by 15% across the active area of an SPT wedge, with most of that variation occurring in the outermost 1/4 of the wafer radius. In several instances, specific wedges have been observed to have unusually low optical efficiency. Scanning Electron Microscope images have shown that in those cases the gold web appears damaged, with material arranged in irregular disconnected μm scale regions. In general, the gold web films appear continuous and smooth for most of the SPT devices.

Table 5.1 Typical device parameters.

Description	Symbol	Value
Absorber resistivity	R_{web}	$250\,\Omega/\square$
Optical time constant	τ_{opt}	$20\,\mathrm{ms}$
Transition temperature	T_c	$530 - 570\,\mathrm{mK}$
Transition width $(T(0.9R_n) - T(.1R_n))$	δT	$20\ \mathrm{mK}$
Normal resistance	R_n	$1.1\,\Omega$
Operating point	R/R_n	0.7
Stage temperature	T_b	$275\,\mathrm{mK}$
Dark saturation power	P_{sat}	$15 - 30\,\mathrm{pW}$
Optical load	P_{opt}	$7 - 17\,\mathrm{pW}$
Thermal conductivity index $(k \propto T^{\beta})$	β	$2 - 2.5$
Non-equilibrium carrier noise factor	γ_{NE}	0.48
Differential conductivity (dP/dT_c)	G	$120 - 175\ \mathrm{pW/K}$
Intrinsic time constant (C_0/G)	τ_0	$30\,\mathrm{ms}$
BLING heat capacity	C_0	$4\ \mathrm{pJ/K}$
BLING coupling factor (G_{int}/G)	γ	45
Typical operating loop gain	$\mathcal{L}$	10
Readout time-constant	τ_e	$32\,\mathrm{ms}$
Bias resistor	R_b	$0.03\,\Omega$
Bias carrier frequency	F_b	$0.3 - 1.0\,\mathrm{MHz}$
Bias series inductance	L	$16\,\mu\mathrm{H}$

Note. — Typical parameters for the season 3 SPT focal plane. A range of values indicates substantial differences between wedges or bands; these values are reported for individual wedges later in the text.

Stability under eletrothermal feedback is discussed in detail in chapter 3. For an SPT-like device, where the heat capacity of the TES is negligible compared to the BLING, operating in a bias circuit such that $\tau = \tau_0/(\mathcal{L}+1) < 5.8\tau_e$, the condition for stability is that the loop gain is smaller than the ratio of the thermal coupling between the TES and the BLING to the thermal coupling between the BLING and the stage, $\mathcal{L} < \gamma$. As the loop gain becomes comparable to $\gamma = G_{\mathrm{int}}/G_0$, the BLING decoupled from the TES and the effective time constant of the device drops much faster than $1/(\mathcal{L}+1)$, almost immediately violating the readout stability criterion. Achieving adequately large values of γ is therefore essential. The season 3 SPT detectors include several improvements over earlier devices designed to achieve this goal, as discussed in chapter 4, and all of the devices tested demonstrate values of γ between 40 and 60, suitable for operation at moderate loop gains of 10 or more.

To produce devices which exhibit linear response to power and near-optimal sensitivity,
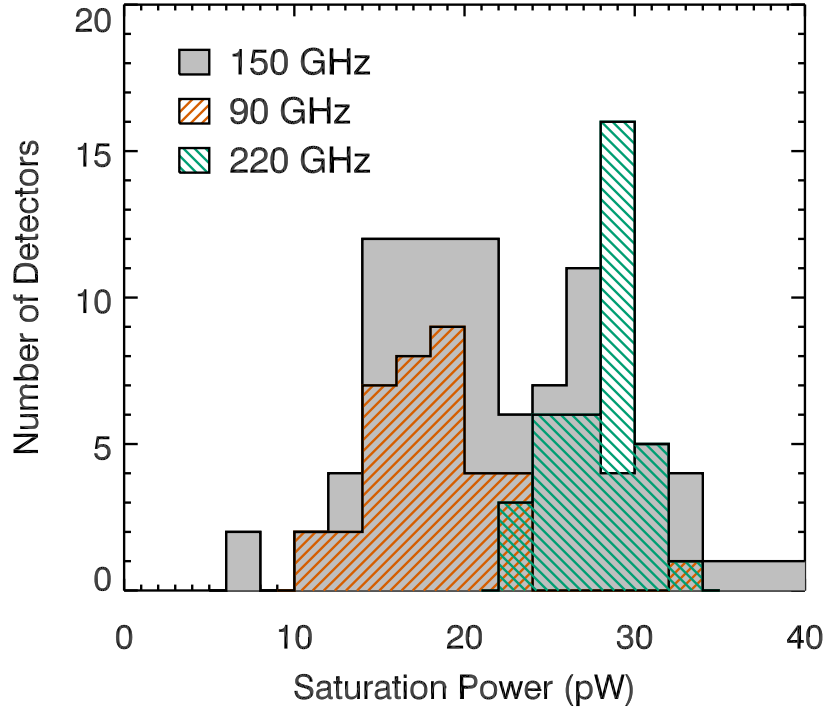
Figure 5.1 A histogram showing the typical saturation power (at turn-around) for dark detectors. These data represent a subset of the season 3 SPT focal plane which includes approximately 1/3 each of the 90 GHz wedge, the 220 GHz wedge, and three of the four 150 GHz wedges. These data include an expected 20% variation in readout system calibration between channels.

achieving an accurate target saturation power, P_{sat} is vital. Too low a saturation power, and the devices will be saturated when looking at the sky. Too high, and the Noise Equivalent Power (NEP) and integration will grow. For SPT, we chose to a target for the dark saturation power of twice the expected optical load for observing bands which cover as much of the relevant atmospheric windows as possible. For the 150, 90, and 220 GHz bands, these targets were 22, 20, and 25 pW, respectively. In practice, reliably achieving these targets as well as high yield and high optical efficiency proved a challenge, largely due to the day to day variation in both the conductivity of evaporated gold films and the T_c of our TES bilayers after processing, combined with an aggressive deployment schedule. In the final season 3 array, four wedges roughly met the P_{sat} targets. Two the 150 GHz wedges which were otherwise ideal candidates for deployment had slightly low values of P_{sat}. To compensate and insure the devices could be achieve adequate loop gain in the field, these two wedges

were outfitted with a horn array and filter stack designed for a slightly smaller pass-band, reducing the expected optical loading by $\sim 10\%$.

5.3 Electrothermal response

In general the thermal properties of TES sensors will depend in detail on fabrication conditions and are difficult to predict from discrete measurements with sufficient accuracy. In order to fully characterize the devices and allow for design iteration, laboratory characterization of complete detectors is essential.

One such characterization is a measurement of the TES current response to a small sinusoidal voltage applied at a frequency offset from the carrier by $\delta\nu$. By applying the perturbative signal in one carrier sideband, and reading out the TES response in the other sideband, it is possible to avoid the complication of having to accurately measure the complex impedance of the device under eletrothermal feedback. This measurement, described in detail in Lueker et al. (2009), is equivalent to measuring the responsivity of the device to a sinusoidal power deposited at the TES itself. The resulting response curve, in units of inferred power vs. offset frequency, can then be fit to a parametric thermal model.

The simplest model which is consistent with expectations and adequately explains the data is described in section 3.4. This model includes a TES with negligible heat capacity, a large additional heat capacity (BLING) with heat capacity C_0 which is weakly connected to the heat bath via G_0 and tightly coupled to the TES with $G_{\mathrm{int}} = \gamma G_0$, and an additional excess heat capacity, C_e, which is comparable to C_0 and weakly connected to the BLING with heat link G_e.

Typically, the result of fits to SPT devices include a C_{exc} which is roughly $1/2$ of the BLING heat capacity, C_0, although in a few wedges that value can be larger by as much as a factor of two. G_{exc} is a factor of 2 or 3 times G_0, leading to a thermalization time constant, $\tau_{\mathrm{exc}} = C_{\mathrm{exc}}/G_{\mathrm{exc}}$ which comparable to the intrinsic time constant of the bolometer, tau_0.

Because the thermalization time constant for this additional material is not sped up by eletrothermal feedback, it effectively decouples from the TES once $\tau < \tau_{\mathrm{exc}}$. The response of the bolometer at moderate loop gain then reduces to the simpler TES & BLING model discussed in section 3.3, and all the response and stability results from that discussion apply here.

In reality, this additional heat capacity is likely to be a distributed thermal system, some or all of which is likely located on the web and participates in the web thermalization in response to optical power. Its detailed structure is both hard to obtain from measurements of single devices, and largely irrelevant when describing the operation of the bolometer. The eletrothermal response of the TES is fully described by the simplified model over the range of loopgains of interest. The temporal response of the bolometer to an optical signal, which is obviously sensitive to the presence of additional heat capacity on the web, is extremely difficult to predict and is therefore directly measured in the field for every device with an

optical chopper.
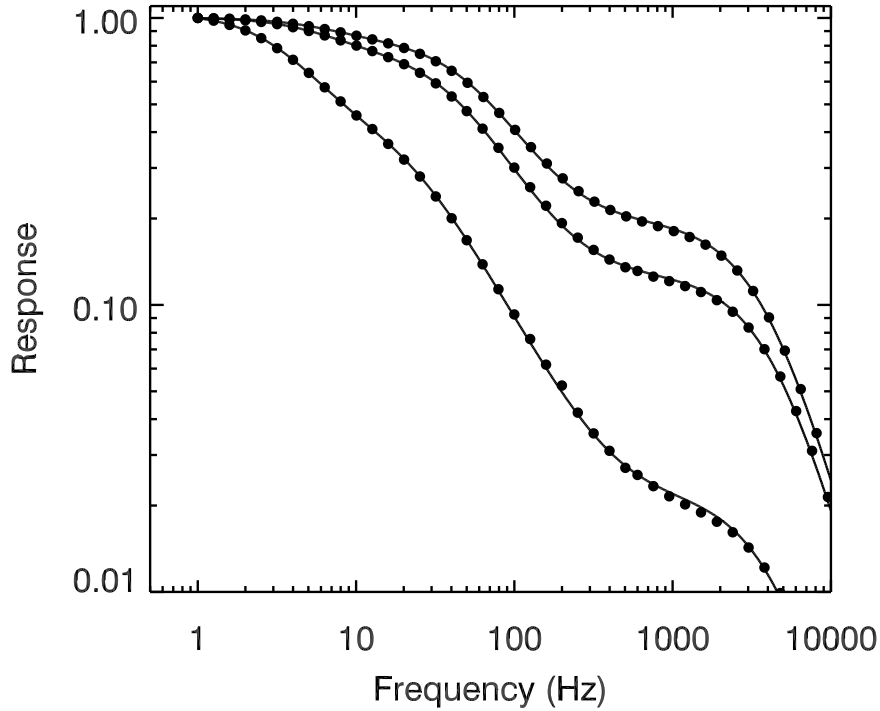
Figure 5.2 The response of an SPT TES to a small bias perturbation, when operating at several different loopgains. Points are laboratory data taken for a TES on wedge SA13, operated in a dark cryostat with a base temperature of 280 mK. Lines are fits to the model described in the text. From left to right, the curves correspond to loopgains of 1, 6, and 10. The model corresponds to a device with an intrinsic time-constant of $\tau_0 = 35ms$ which can be stably operated at loop gains of $\mathcal{L} \leq 45$

Figure 5.2 shows the response of a single device on one of the fielded SPT wedges, SA12, at three different positions in the transition. This wedge is unique, as it appears to include the largest excess heat capacity of any fielded SPT wedge. Also plotted are composite fits to the model shown in 3.3. The $\mathcal{L} = 1$ point is easily specified in the lab, as it coincides with the point where $\delta I/\delta V = 0$ in a standard IV curve. From a fit to the left-most curve, with $\mathcal{L}$ fixed, values of all parameters except γ and τ_e are derived. Those parameters are then fixed, and the remaining curves are fit with a model in which only γ, τ_e, and $\mathcal{L}$ are allowed to vary. In principle, τ_e can be independently constrained by measuring the bolometer resistance and inductor value. In practice, the fits from these data are more precise than the calibration of the readout electronics for an arbitrary channel in the presence of stray impedance. The

resulting values of τ_{eff} are consistent with expectations, and fixing them to an artificially offset value changes the other parameters by only a negligible amount.

The model fits include a negligible TES heat capacity, but a significant excess heat capacity, C_{exc} which is equal to the BLING heat capacity but poorly coupled to the rest of the thermal circuit. At low frequencies and low loopgains, the device responds with $\tau sim(C_{\text{bl}} + C)\text{exc}/G = 2.0\tau_0$. At moderate loop gains, the excess heat capacity decouples, and the TES responds with $\tau_0 = 37\,\text{ms}$. The fit to the last curve indicates that the ratio of the BLING-TES coupling to the thermal conductivity to the heat bath is given by $\gamma = 46$, which sets the upper limit to the loop gain at which the device can be stably operated. The other wedges in the the SPT focal plane which have been characterized in this manner all exhibit smaller values of C_{exc}, and are well fit by models with $C_{\text{exc}} \lesssim 0.5 C_{\text{bl}}$.

Figure 5.3 shows a similar fit to a test device. On an otherwise typical SPT wedge, half the gold G-links were dropped out during patterning, in order to measure the LSN contribution to thermal conductivity. The gold devices on this wedge typically show $P_{\text{sat}} = 30 pW$, while the LSN only devices are generally close to $10\,\text{pW}$, for $T_c = 530\,\text{mK}$ and $T_b = 280\,\text{mK}$. The best fits model includes $C_e/C_0 = 0.50$ at all loop gains and for both devices. G_e/G_0 is allowed to vary in each fit; for the high-G device, both fits result in a value of 1.40 ± 0.02, while the best fit value for the low-G device varies from 2.5 to 1.7 for the low and high loop gain curve, respectively. The readout time-constant is poorly constrained by these fits.

These data indicate that SPT devices can be stable operated at loop gains of up to 40 or so, although in practice we achieve suitably linear response and stable operation at $\mathcal{L} \sim 10$ in the field. At moderate loop gain, the device response to optical or bias power changes will behave as a single-pole filter with a time constant given by $\tau_0/(\mathcal{L}+1)$ where τ_0 is approximately $30\,\text{ms}$, although at very low or very high loop gain, the response will depart from this simple model.

5.4 Optical Response

The response of a spiderweb bolometer operated at moderate to high loopgain is dominated by the thermalization time of the the spiderweb itself, and is to first order independent of the properties of the TES. At low loop gain, when the effective eletrothermal time constant of the device becomes comparable to the web thermalization time, this approximation breaks down and care must be taken to account for changing time constants with bias and loading.

In the SPT, both the optical time constants and responsivity of every bolometer are measured using a chopped thermal load. This calibrator consists of a $\sim 1000\,\text{K}$ heated filament behind a chopper wheel, connected by a light pipe to a hole in the center of the secondary mirror. The chopped wheel can be set to frequencies of between 4 and 100 Hz. Several times throughout the season a detailed sweep at frequencies between 4 and 24 Hz is carried out to measure the time-constants of the array. Weekly checks at 6, 14, and 22 Hz at a range of elevations spanning the SPT fields test for loading-dependent changes. Brief
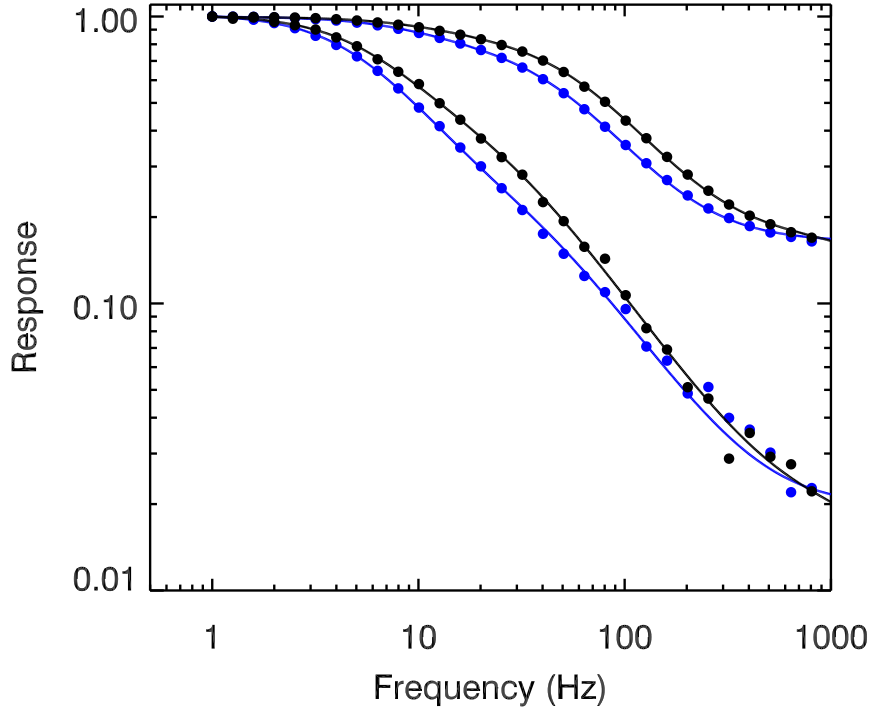
Figure 5.3 Response of two detectors from an SPT wedge. The black curve is a typical, if slightly high-G device, the blue curve is an identical device except that the gold thermal link was not deposited during fabrication. Points are laboratory data for devices operated in a dark cryostat with a base temperature of 280 mK. Lines are fits to the model described in the text. From left to right, the curves correspond to loopgains of approximately 1 and 10. The black model corresponds to a device with an intrinsic time-constant of $\tau_0 = 30ms$ which can be stably operated at loop gains of $\mathcal{L} \leq 50$. The addition of a gold link increases $\overline{G}$ by a factor of 2.25, while only slightly increasing τ_0 and G.

responsivity checks at 6 Hz are carried out many times a day throughout the usual observing schedule, and are used to reference the responsivity of the full array to periodic calibration maps of HII regions made using a subset of the array. Because the range of calibrator frequencies doesn't fully span our science data, which corresponds to approximately 0-7 Hz for the present SPT scan strategy, several additional cross checks are performed. Comparison with the signal from small elevation nods and with periodic full-array maps of HII regions verify the amplitude calibration. The time constant response is checked by looking for artifacts in maps which have been deconvolved using the measured value, both in the left-right going scan difference maps of individual bright sources and with the use of left-right

jack-knife tests on large fields.
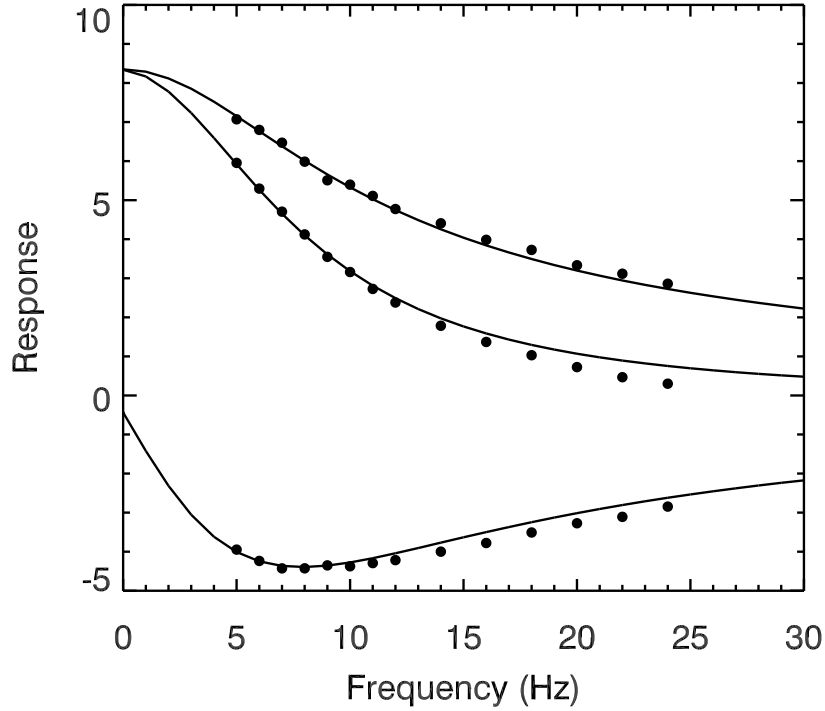
Figure 5.4 Measured optical response to the calibrator for a typical channel on $150\,GHz$ wedge X16 during a single calibration sweep. Curves from bottom to top are the (negative) in-phase, quadrature-phase, and total response. Points are measured data, lines are the best fit single-pole filter model in the region between 5 and 10 Hz, with a time constant of $19\,ms$. Evidence for the departure from a single-pole filter response can be seen at frequencies above 10 Hz.

For frequencies below 10 Hz, covering the SPT data band, the response of all of the optical detectors in the array is well fit by a single pole filter with a time constant of approximately 20 ms. At higher frequencies, there is evidence for a slight departure from single-pole behavior for a large fraction of the array. The response of these channels rolls off more slowly than the single pole model would predict. This can be seen in figure 5.4, where there is a visible phase shift and a slight discrepancy in the total power between the model and the data at frequencies above 10 Hz. We see no evidence for additional departures from single pole behavior at very low frequencies, either in the analysis of maps with minimal high pass filtering or in tests where a shutter is used to measure the response of the devices to a step function in power.
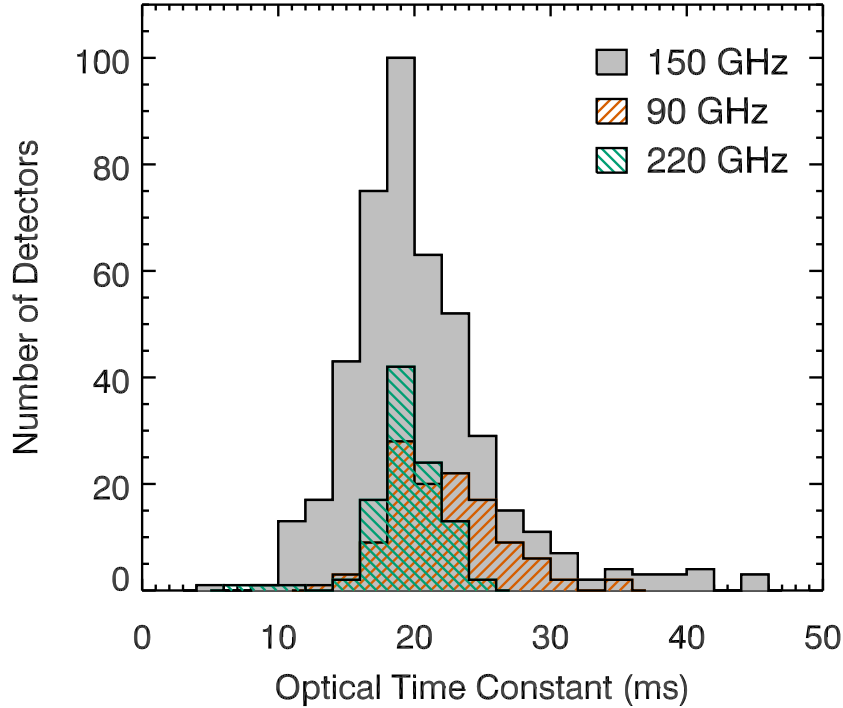
Figure 5.5 Measured optical time constants for the SPT season3 array. During a typical observing day, the phase and response of each detector to a calibrator signal in the range $5 - 10\,\mathrm{Hz}$ is fit with a single pole response function. Median values are listed in table 5.3

5.5   Yield

In addition to fabricating detectors with suitable properties, an efficient focal plane requires that the devices be produced with high yield. The most common types of damage which impact yield are shorts and opens in the Aluminum leads of individual channels. These are often caused by dust or particle contamination in the Al lithography step or air bubbles in subsequent photoresist layers which allow developer to react with the Aluminum. Manual cleaning of the contact printer mask prior to each exposure dramatically improved our yield; however several channels are typically damaged on any given wedge. Because superconducting shorts render a multiplexed comb useless, we have adopted a conservative strategy of excising any channels which appear to be potentially compromised based upon a visual inspection of the wedge.

Each wedge in the SPT focal plane contains 161 detectors, of which 140 can be operated by our fMUX readout system as presently configured. Additional channels are removed due

to damage in processing. The selection of which channels are not connected to the read out system occurs during wirebonding. Judicious selection of drop-out channels based on visual inspection data allows for partial overlap between the readout loss factor and the damage losses. Our 2009 focal plane configuration includes readout connections to 132, 540, and 126 out of a possible 140, 560, and 140 channels in the 90, 150, and 220 GHz bands respectively, for a total of 798 active channels. For diagnostic purposes we've placed metal tape over 27 of these pixels at the entrance of the feed horn. These sere serve as dark reference bolometers. Six additional thin film resistors are mounted on the LC-boards and used for readout system diagnostics.

At the start of every 36 hour observing cycle, all SQUIDS and bolometers are biased up and operated, and a series of calibration observations are performed. The number of detectors which pass noise and optical response cuts and are used in our analysis varies by a small amount daily. During the 2009 winter season, a total of 707 channels passed all our optical response and noise cuts at least once. The median and maximum number of channels which passed all our optical response and noise cuts on any single day during winter 2009 were 695 and 677, respectively.

5.6   Sensitivity and Noise Equivalent Power

Table 5.2 Observing bands and photon noise estimates for season 3 focal plane.

Wedge ID	Horn cutoff (GHz)	Filter (cm^{-1})	ν_0 (Hz)	$\Delta\nu$ (Hz)	P_{opt} (pW)	NEP$_{\mathrm{opt}}^{\mathrm{shot}}$	NEP$_{\mathrm{opt}}^{\mathrm{Bose}}$	NEP$_{\mathrm{opt}}^{\mathrm{tot}}$
X16	130	5.6	155.0	35.0	7.5 ± 0.5	43	$48\sqrt{\bar{\xi}}$	50
X13	130	5.6	155.0	35.0	9.0 ± 0.5	39	$40\sqrt{\bar{\xi}}$	45
X12	123.5	5.6	153.0	39.0	11.5 ± 0.5	48	$58\sqrt{\bar{\xi}}$	58
X15	123.5	5.6	153.0	39.0	11.5 ± 0.5	48	$58\sqrt{\bar{\xi}}$	58
SA12	78	8.4	97.6	31.3	7.3 ± 0.2	31	$41\sqrt{\bar{\xi}}$	38
X6	192	3.7	219.8	49.1	17 ± 1.0	70	$77\sqrt{\bar{\xi}}$	82

Note. — Observing bands for the season-3 focal plane. Horn cutoff and filter values are the design specifications for the horn array waveguide cutoff and band-defining metal mesh filter low pass cutoff, respectively. All NEP values are in units of $aW/\sqrt{Hz}$. Fourier Transform Spectroscopy (FTS) measurements of the bands are used to calculate the center frequency and effective (top hat) bandwidth, ν_0 and $\Delta\nu$. This measurement is described in Bleem et al. (in prep.)

The expected sensitivity of a TES sensor is discussed in detail in section 3.5. The principle result is that the total expected NEP for an SPT detector with saturation power P_{sat} and

Table 5.3 Saturation powers and noise estimates for season 3 focal plane.

Band	ID	P_{sat} (pW)	G (pW/K)	$\text{NEP}^{\text{car}}_{\text{est}}$	$\text{NEP}^{\text{ro}}_{\text{est}}$	$\text{NEP}^{\text{tot}}_{\text{est}}$	NEP_{meas}
150	X13	18 ± 4	125	32	16	56–73	66 ± 10
150	X16	17 ± 4	120	33	19	54–67	67 ± 11
150	X12	24 ± 5	154	36	20	63–86	81 ± 10
150	X15	27 ± 6	170	38	23	65–87	91 ± 11
95	SA12	18 ± 4	125	31	19	47–63	66 ± 11
220	X6	28 ± 2	175	38	19	82–112	94 ± 10

Note. — Here, P_{sat} is the power measured at turn-around ($\mathcal{L} = 1$) estimated from dark measurements of a subset of the array. For all devices, $T_{\text{bath}} = 275\,\text{mK}$ and $T_c = 550 \pm 30\,\text{mK}$. $G = \partial P/\partial T_c$. NEP values, in units of $\text{aW}/\sqrt{\text{Hz}}$, are the expected contribution from thermal carrier noise, $\text{NEP}^{\text{car}}_{\text{est}}$, the total arising from the readout system and bolometer Johnson noise, $\text{NEP}^{\text{car}}_{\text{est}}$, and the total which includes both photon shot noise and a Bose term for a correction factor of $\xi = 0 - 1$, $\text{NEP}^{\text{tot}}_{\text{est}}$. Measured noise is the average NEP in a frequency band from $3 - 5\,\text{Hz}$ during a single 10 minute observation in good weather in August 2009. A single common mode has been removed from each wedge at every time step to remove a portion of the atmospheric low frequency noise.

optical power P_{opt} will be

$$
\begin{aligned}
\text{NEP}^2 = & \left(2h\nu_0 P_{\text{opt}} + \frac{\xi P_{\text{opt}}^2}{\Delta\nu} \right) \cdot \left(1 + \frac{f^2}{(2\pi\tau_{\text{opt}})^2} \right) \\
& + 4\gamma_{\text{NE}} k_B T_c^2 G \\
& + 4k_B T_c P_{\text{bias}} \frac{(\mathcal{L}+1)^2}{\mathcal{L}^4} \\
& + v_b \frac{(\mathcal{L}+1)^2}{\mathcal{L}^2} \cdot \left(9.8\text{pA}/\sqrt{Hz} \right)
\end{aligned}
\tag{5.1}
$$

The first line is the noise associated with photon arrival, which includes a shot-noise component and a Bose correlation component with a correlation factor ξ. Here h is Planck's constant, ν_0 is the observation band center, and $\Delta\nu$ is the observation bandwidth. This term includes the filter response of the spiderweb optical time constant, τ_{opt}, at measured frequency f. The second line is the thermal carrier noise, where γ_{NE} is the non-equilibrium correction factor, k_B is Boltzmann's constant, T_c is the transition temperature, and G is the differential thermal conductivity. The third line is the Johnson noise from the TES itself. For an on-resonance channel at moderate loop gain, this term is suppressed by a factor of $\mathcal{L}^4$. The fourth line is the contribution from all current-like sources of noise in the readout system, including Johnson noise from the $30\,\text{m}\Omega$ bias resistor (at 3.8 K), SQUID noise, and first

stage amplifier noise. In converting to NEP, these current sources are divided by the current responsivity, which reduces to v_b at high loop gain. Additional frequency dependent terms that account for the bolometer response have been omitted, as these terms do not become significant until well outside of both the SPT data bandwidth and the digital anti-aliasing filter applied prior to re-sampling to a 100 Hz data rate.
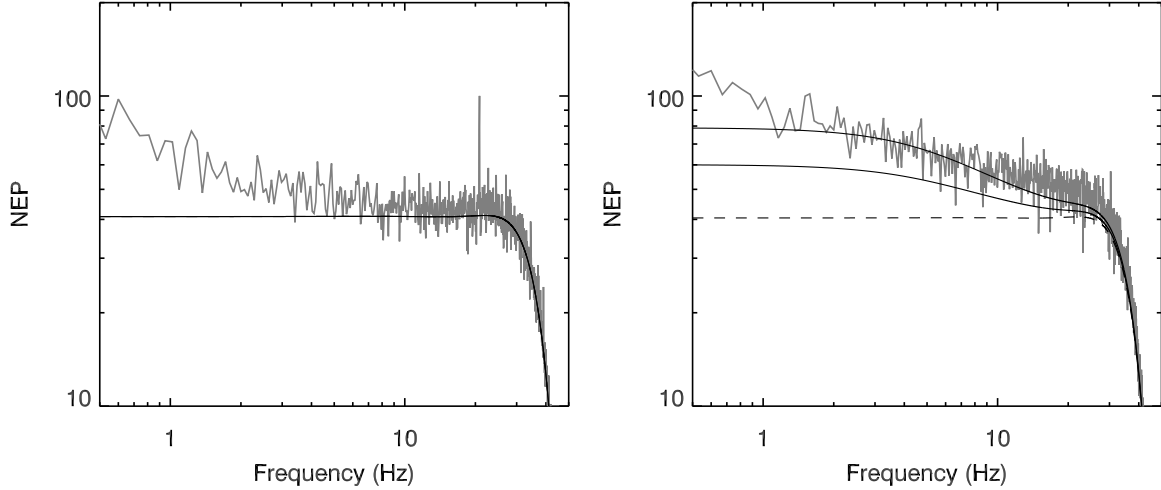
Figure 5.6 Measured NEP for individual detectors in the season 3 focal plane. Data from a single 10 minute stationary observation in August 2009 is shown in gray. Predictions based on model parameters are in black. On the left, a dark bolometer from wedge SA12, with $P_{\mathrm{sat}} = 15\,\mathrm{pW}$, and a plot of the predicted NEP with no optical loading. On the right, an optical device from wedge X16, with $P_{\mathrm{sat}} = 24\,\mathrm{pW}$, $P_{\mathrm{opt}} = 10.5\,\mathrm{pW}$, and $\tau_{\mathrm{opt}} = 25\,\mathrm{ms}$. The dashed line includes predicted NEP for all non-photon contributions. Lower and upper solid lines are the total noise for Bose factor $\xi = 0$ and $\xi = 1$, respectively. In all cases, the response of the digital anti-aliasing filter has been applied to predicted curves.

The measured bands, measured optical loading, and resulting predicted optical NEP for the SPT season 3 focal plane is listed in table 5.2. Device and bias parameters and dark noise contributions from both carrier noise and readout noise, as well as the total expected NEP are listed in table 5.3. The measured NEP during a 10 minute noise stare in good weather in November 2009 is also listed. In general, the agreement between predicted and measured NEP is reasonably close, especially considering that there is likely to be residual contamination from changing atmosphere as well as additional low frequency noise from the readout system. (Note that in practice, the atmospheric contribution dominates the low frequency readout system contribution during actual observations.)

A plot of the measured NEP for a single 10 minute stationary observation in good weather is shown in figure 5.6, for two individual detectors. One channel is optical, and pointed at the sky. The other channel is dark; metal tape is used to cover the feed horn. Figure 5.7
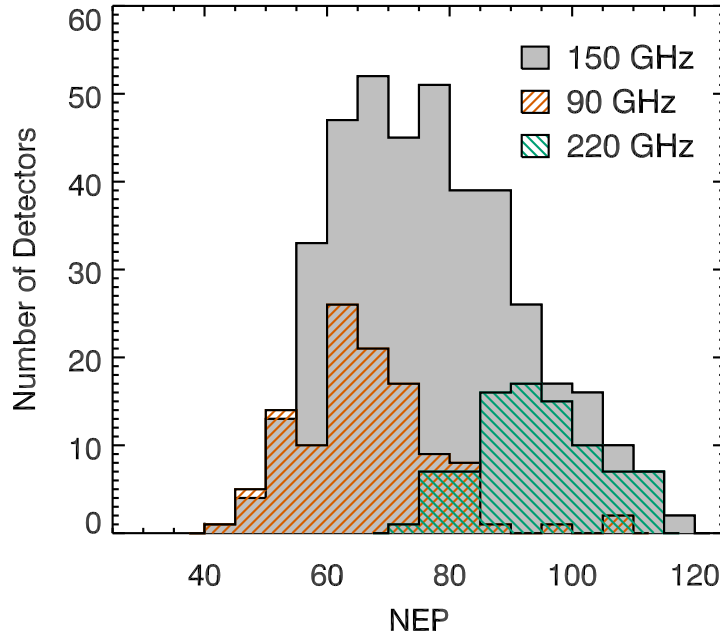
Figure 5.7 Measured NEP for the season 3 array, showing the average NEP in a frequency band from $3 - 5$ Hz for every optical channel during a single 10 minute observation in good weather in August 2009. A single common mode has been removed from each wedge at every time step.

shows a histogram of the measured NEP during a similar noise stare for all the live, optical channels on a typical observing day in 2009.

5.7   Discussion

In the preceding two chapters, the basic properties of voltage biased TES bolometers are discussed, and the design and fabrication techniques specific to the SPT array and related spiderweb-coupled TES sensors developed at UC Berkeley were described. Despite a number of implementation challenges, the final season 3 array described in this chapter has achieved remarkable sensitivity, with nearly 700 live pixels in three atmospheric observing bands, most of which exhibit NEPs that are within a factor of $\sqrt{2}$ of the photon-noise limit.

Today, SPT has surveyed more than 1700 square degrees to survey depth ($18\,\mu\mathrm{K}^2$ at 150 GHz), and plans to complete a survey of 2500 square degrees by the time the instrument is replaced in December 2011. Although analysis is still ongoing, a number of science results have been published. Among these, the first detection of previously unknown clusters in an

SZ survey, and several catalogs of clusters from the partial survey.(Staniszewski et al., 2009; Vanderlinde et al., 2010; Williamson et al., 2011) Power spectrum results include constraints on the SZ effect and the power due to Dusty Star Forming Galaxies at high-*ell* presented in Lueker et al. (2010) and Hall et al. (2010), the measurement of the primary CMB at intermediate-ℓ presented in Keisler et al. (2011), and the results presented in the following chapter.

Part III

Secondary CMB anisotropies measured with SPT

Chapter 6

Improved constraints on cosmic microwave background secondary anisotropies from the complete 2008 South Pole Telescope data

6.1 Introduction

As discussed in Chapter 1, measurements of temperature anisotropy in the cosmic microwave background (CMB) have proven to be some of the most powerful and robust tests of cosmological theory. (Komatsu et al., 2011; Larson et al., 2011; Reichardt et al., 2009a; Dunkley et al., 2011) The large- and intermediate-scale anisotropy is dominated by the signal from the primary anisotropy of the CMB. On smaller scales, the primary anisotropy is exponentially suppressed by Silk damping (Silk, 1968); fluctuations on these scales are dominated by foregrounds and secondary anisotropies. The largest of these secondary anisotropies is expected to be the Sunyaev-Zel'dovich (SZ) effect (Sunyaev & Zel'dovich, 1972), which consists of two components: the thermal SZ (tSZ) and kinetic SZ (kSZ) effects.

The first SPT power spectrum results were recently reported by Lueker et al. (2010, hereafter L10). The SPT 150 GHz bandpowers were used by Hall et al. (2010, hereafter H10) to set a 95% CL upper limit of $13 \, \mu\text{K}^2$ on the kSZ power at $\ell = 3000$. Those results, independent limits on SZ power reported by the Atacama Cosmology Telescope (ACT), and several recently published models for the expected SZ power are discussed in Section 1.6.2.

In addition to the tSZ and kSZ signal, the measured power at these frequencies and angular scales includes contributions from several significant foregrounds. The power from dusty star-forming galaxies (DSFGs) has both a Poisson and clustered component, with distinct angular scale dependencies. Measurements of DSFG power at multiple millimeter wavelengths can be combined to constrain the DSFG spectral index. H10 constrained the

spectral index of the Poisson term to be $\alpha_p = 3.86 \pm 0.23$ and the index of the clustered term to be $\alpha_c = 3.8 \pm 1.3$ using fits to the L10 single-frequency bandpowers. H10 also interpret the implications of the spectral index constraint on the dust temperature and redshift distribution of the dusty galaxies. Dunkley et al. (2011) also detect significant power attributed to clustered DSFGs in the ACT data. They find a preferred spectral index of 3.69 ± 0.14, consistent with the H10 result.

In this work, we make two key improvements upon the first SPT power spectrum release (L10 and H10). First, we include both fields observed by SPT in 2008, doubling the sky coverage and reducing the bandpower uncertainties by 30%. Second, we test cosmological models with a true multi-frequency analysis of the bandpowers, properly accounting for the multi-frequency covariance matrix and frequency dependence of each component to estimate cosmological parameters. Including the additional frequency information in the parameter estimation leads to improved model constraints. We present the minimal model required to explain the data, and then explore a number of extensions to this minimal model such as the possibility of the tSZ signal being correlated with dust emission. None of these extensions significantly improve the fits or change the general conclusions concerning the amplitudes of the kSZ and tSZ power.

We describe the instrument, observations, beams, and calibration strategy in Section 6.2. The time-ordered data filtering and map-making algorithm is outlined in Section 6.3, along with the procedure to derive bandpowers from maps. The results of tests for systematic errors applied to the SPT data are discussed in Section 6.4. The bandpowers are given in Section 6.5, and the model is presented in Section 6.6. The fitted parameters and their cosmological interpretation are given in Section 6.7 and Section 6.8, respectively. We summarize our conclusions in Section 6.9.

6.2   Instrument and Observations

The SPT it briefly discussed in Chapter 2, and is described in more detail in Ruhl et al. (2004), Padin et al. (2008), and Carlstrom et al. (2011). The receiver and detectors are described in Chapters 3, 4, and 5.

In this analysis, we use data at 150 and 220 GHz from two $\sim$100 deg^2 fields observed by SPT in the 2008 austral winter. The fields are centered at right ascension (RA) 5^h30^m, declination (decl.) $-55°$ (J2000) (henceforth the 5^h30^m field) and RA 23^h30^m, decl. $-55°$ (the 23^h30^m field). The locations of the fields were chosen for overlap with the optical Blanco Cosmology Survey (BCS)[1] and low dust emission observed by IRAS at $100\,\mu$m (Schlegel et al., 1998). After data quality cuts, a total of 1100 hours of observations are used in this analysis. The final map noise is $18\,\mu$K-arcmin^2 at 150 GHz and $40\,\mu$K-arcmin at 220 GHz. These data

---

[1]http://cosmology.illinois.edu/BCS

[2]Throughout this work, the unit K refers to equivalent fluctuations in the CMB temperature, i.e., the temperature fluctuation of a 2.73 K blackbody that would be required to produce the same power fluctuation.

include the majority of the sky area observed in 2008. In 2009 and 2010, the SPT has been used to survey an additional 1300 deg^2 to the same depth at 150 GHz.

The fields were observed with two different scan strategies. The 5^h30^m scan strategy involves constant-elevation scans across the 10° wide field. After each scan back and forth in azimuth across the field, the telescope executes a 0.125° step in elevation. A complete set of scans covering the entire field takes approximately two hours, and we refer to each complete set as an observation.

The 23^h30^m field was observed using a lead-trail scan strategy. Two consecutive observations each map approximately half the field. Due to the Earth's rotation, both halves of the field are observed at the same range of azimuth angle. This would allow the removal of ground-synchronous signals if detected; however, we see no evidence for such a signal at the angular scales of interest. A complete observation of one half-field takes approximately 40 minutes. The two halves are generally observed directly after one another, though for this analysis we also include a small number of lead trail pairs (31 out of 480) which were not observed sequentially, due to poor weather or other interruptions. The requirement that both halves of the 23^h30^m field are observed at the same azimuth leads to a larger elevation step (0.268°) and therefore less uniform coverage across the map. We ameliorate this non-uniform coverage in the cross-spectrum analysis by combining two lead-trail map pairs into one 'observation' unit. The lead-trail pairs are chosen to to maximize coverage uniformity in the resulting map and minimize temporal offsets.

6.2.1 Beam Functions

The power spectrum analysis presented here depends on an accurate measurement of the beam function, which is the azimuthally averaged Fourier transform of the beam map. Due to the limited dynamic range of the detectors, the SPT beams for the 2008 observing season were measured by combining maps of three sources: Jupiter, Venus, and the brightest point source in each field. Maps of Venus are used to stitch together the outer and inner beam maps from Jupiter and the point source, respectively. Maps of Jupiter at radii > 4′ are used to constrain a diffuse, low-level sidelobe that accounts for roughly 15% of the total beam solid angle. The beam within a radius of 4′ is measured on the brightest point source in the field. The effective beam is slightly enlarged by the effect of random errors in the pointing reconstruction. We include this effect by measuring the main beam from a source in the final map. The main-lobe beam is approximately fit by 2D Gaussians with full width at half-maximum (FWHM) equal to 1.15′ at 150 GHz and 1.05′ at 220 GHz. We have verified that the measured beam is independent of the point source used, although the signal-to-noise drops for the other (dimmer) sources in either field. The beam measurement is similar to that described in L10, although the radii over which each source contributes to the beam map have changed. However, the estimation of beam uncertainties has changed. We now

---

The conversion factor is given by the derivative of the blackbody spectrum, $\frac{dB}{dT}$, evaluated at 2.73 K.

determine the top three eigenvectors of the covariance matrix for the beam function at each frequency, and include these as beam errors in the parameter fitting. These three modes account for $> 99\%$ of the beam covariance power. The beam functions and the quadrature sum of the three beam uncertainty parameters are shown in Figure 6.1.
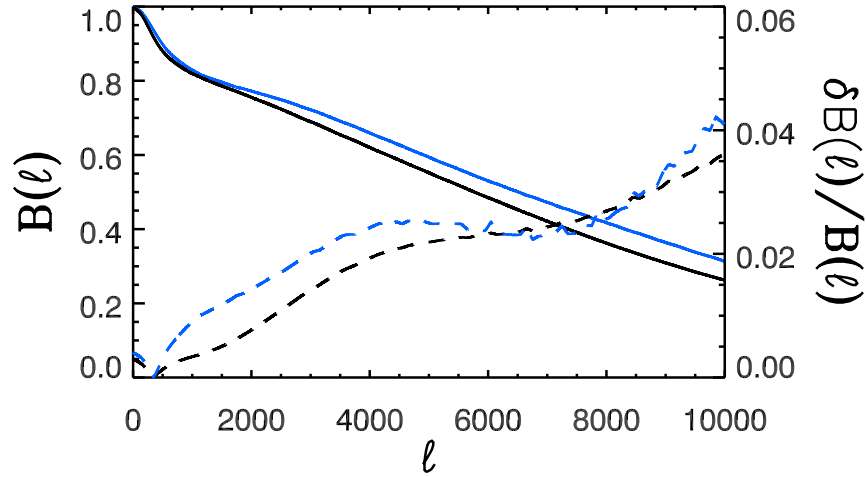
Figure 6.1 *Left axis:* The measured SPT beam functions at $150\,\mathrm{GHz}$ (**black line**) and $220\,\mathrm{GHz}$ (**blue line**). *Right axis:* The fractional beam uncertainties at $150\,\mathrm{GHz}$ (**black dashed line**) and $220\,\mathrm{GHz}$ (**blue dashed line**). The beam uncertainty is parametrized by a three component model, the quadrature sum of which is plotted here.

6.2.2 Calibration

The absolute calibration of the SPT data is based on a comparison of the CMB power at degree scales in the WMAP 5-year maps with dedicated SPT calibration maps. These calibration maps cover four large fields totaling $1250\,\mathrm{deg}^2$ which were observed to shallow depth during the 2008 season. Details of the cross-calibration with WMAP are given in L10, and remain essentially unchanged in this work. Although the beam functions changed slightly at $\ell > 1000$ as a result of the improved beam measurement described in Section 6.2.1, this change had a negligible effect at the angular scales used in the WMAP calibration. The calibration factors are therefore unchanged from L10; however as discussed above, we have slightly changed the treatment of beam and calibration errors, and are no longer folding part of the beam uncertainty into a calibration uncertainty.

We estimate the uncertainty of the temperature calibration factor to be 3.5%, which is slightly smaller than the value of 3.6% presented in L10. We applied this calibration to the $220\,\mathrm{GHz}$ band by comparing $150\,\mathrm{GHz}$ and $220\,\mathrm{GHz}$ estimates of CMB anisotropy in the survey regions. This internal cross-calibration for $220\,\mathrm{GHz}$ is more precise than, but consistent with, a direct absolute calibration using observations of RCW38. We estimate the

220 GHz temperature calibration uncertainty to be 7.1%. Because the 220 GHz calibration is derived from the 150 GHz calibration to WMAP, the calibration uncertainties in the two bands are correlated with a correlation coefficient of approximately 0.5.

As discussed in Section 6.7.1, our MCMC chains also include two parameters to adjust the overall temperature calibration in each SPT band. The resulting calibration factors are listed in the Table 6.1 comments.

6.3   Analysis

In this section, we present an overview of the pipeline used to process the time-ordered data (TOD) to bandpowers. The method closely follows the approach used by L10, and we refer the reader to L10 for complete details of the method. We highlight any differences between this analysis and that work.

Given the small field sizes, we use the flat-sky approximation. We generate maps using the oblique Lambert equal-area azimuthal projection and analyze these maps using Fourier transforms. Thus, the discussion of filtering and data-processing techniques refer to particular modes by their corresponding angular wavenumber $\mathbf{k}$ in radians with $|\mathbf{k}| = \ell$.

6.3.1   TODs to Maps

Each detector in the focal plane measures the CMB brightness temperature plus noise, and records this measurement as the TOD. Noise in the TOD contains contributions from the instrument and atmosphere. The instrumental noise is largely uncorrelated between detectors. Conversely, the atmospheric contribution is highly correlated across the focal plane, because the beams of individual detectors overlap significantly as they pass through turbulent layers in the atmosphere.

We bandpass filter the TOD to remove noise outside the signal band. The TOD are low-pass filtered at 12.5 Hz ($\ell \sim 18000$) to remove noise above the Nyquist frequency of the map pixelation. The TOD are effectively high-pass filtered by the removal of a Legendre polynomial from the TOD of each detector on a by-scan basis. The order of the polynomial is chosen to have the same number of degrees of freedom (dof) per unit angular distance ($\sim$1.7 dof per degree). The polynomial fit removes low frequency noise contributions from the instrument and atmosphere.

Correlated atmospheric signals remain in the TOD after the bandpass filtering. We remove the correlated signal by subtracting the mean signal over each bolometer wedge[3] at each time sample. This filtering scheme is slightly different from that used by L10, although nearly identical in effect at 150 GHz. L10 subtracted a plane from all wedges at a given

---

[3]The SPT array consists of 6 pie shaped bolometer wedges of 160 detectors, of which five wedges are used in this analysis. Wedges are configured with a set of filters that determine their observing frequency (e.g. 150 or 220 GHz).

observing frequency at each time sample. Since SPT had two wedges of 220 GHz bolometers and three wedges of 150 GHz bolometers in 2008, the L10 scheme filters the 220 GHz data more strongly than the 150 GHz data. The wedge-based common mode removal implemented in this work results in more consistent filtering between the two observing bands.

The data from each bolometer is inverse noise weighted based on the calibrated, pre-filtering detector power spectral density. We bin the data into map pixels based on pointing information, and in the case of the $23^{\rm h}30^{\rm m}$ field, combine two pairs of lead and trail maps to form individual observations as discussed in Section 6.2. A total of 300 and 240 individual observation units are used in the subsequent analysis of the $5^{\rm h}30^{\rm m}$ and $23^{\rm h}30^{\rm m}$ fields, respectively.

6.3.2 Maps to Bandpowers

We use a pseudo-C_ℓ method to estimate the bandpowers. In pseudo-C_ℓ methods, bandpowers are estimated directly from the Fourier transform of the map after correcting for effects such as TOD filtering, beams, and finite sky coverage. We process the data using a cross spectrum based analysis (Polenta et al., 2005; Tristram et al., 2005) in order to eliminate noise bias. Beam and filtering effects are corrected for according to the formalism in the MASTER algorithm (Hivon et al., 2002). We report the bandpowers in terms of $\mathcal{D}_\ell$, where

$$\mathcal{D}_\ell = \frac{\ell(\ell+1)}{2\pi} C_\ell . \tag{6.1}$$

The first step in the analysis is to calculate the Fourier transform $\tilde{m}^{(\nu_i, A)}$ of the map for each frequency ν_i and observation A. All maps of the same field are apodized by a single window that is chosen to mask out detected point sources and avoid sharp edges at the map borders. After windowing, the effective sky area used in this analysis is $210\,\mathrm{deg}^2$. Cross-spectra are then calculated for each map-pair on the same field; a total of 44850 and 28680 pairs are used in the $5^{\rm h}30^{\rm m}$ and $23^{\rm h}30^{\rm m}$ fields, respectively. We take a weighted average of the cross-spectra within an ℓ-bin, b,

$$D_b^{\nu_i \times \nu_j, AB} \equiv \left\langle \frac{\mathrm{k}(\mathrm{k}+1)}{2\pi} \tilde{m}_{\mathbf{k}}^{(\nu_i, A)} \tilde{m}_{\mathbf{k}}^{(\nu_j, B)*} \right\rangle_{k \in b} . \tag{6.2}$$

As in L10, we find a simple, uniform selection of modes at $k_x > 1200$ is close to the optimal mode-weighting. With the adopted flat-sky approximation, $\ell = k$.

The bandpowers above are band-averaged pseudo-C_ℓs that can be related to the true astronomical power spectrum $\widehat{D}$ by

$$\widehat{D}_b^{\nu_i \times \nu_j, AB} \equiv \left(K^{-1}\right)_{bb'} D_{b'}^{\nu_i \times \nu_j, AB} . \tag{6.3}$$

The K matrix accounts for the effects of timestream filtering, windowing, and band-averaging. This matrix can be expanded as

$$K_{bb'}^{\nu_i \times \nu_j} = P_{bk} \left(M_{kk'}[\mathbf{W}] F_{k'}^{\nu_i \times \nu_j} B_{k'}^{\nu_i} B_{k'}^{\nu_j} \right) Q_{k'b'} . \tag{6.4}$$

Here Q_{kb} and P_{bk} are the binning and re-binning operators (Hivon et al., 2002). $B_k^{\nu_i}$ is the beam function for frequency ν_i, and $F_k^{\nu_i \times \nu_j}$ is the k-dependent transfer function which accounts for the filtering and map-making procedure. The mode-mixing due to observing a finite portion of the sky is represented by $M_{kk'}[\mathbf{W}]$, which is calculated analytically from the known window $\mathbf{W}$.

Transfer Function

We calculate a transfer function for each field and observing frequency. The transfer functions are calculated from simulated observations of 300 sky realizations that have been smoothed by the appropriate beam. Each sky realization is a Gaussian realization of the best-fit lensed WMAP7 ΛCDM model plus a Poisson point source contribution. The Poisson contribution is selected to be consistent with the results of H10, and includes radio source and DSFG populations. The amplitude of the radio source term is set by the de Zotti et al. (2005) model source counts at 150 GHz with an assumed spectral index of $\alpha_r = -0.5$. The DSFG term has an assumed spectral index of 3.8. The effective point source powers are $C_\ell^{150\text{x}150} = 7.5\times10^{-6} \, \mu\text{K}^2$, $C_\ell^{150\text{x}220} = 2.3\times10^{-5} \, \mu\text{K}^2$, and $C_\ell^{220\text{x}220} = 7.8\times10^{-5} \, \mu\text{K}^2$. The sky realizations are sampled using the SPT pointing information, filtered identically to the real data, and processed into maps. The power spectrum of the simulated maps is compared to the known input spectrum, $C^{\nu,\text{theory}}$, to calculate the effective transfer function (Hivon et al., 2002) in an iterative scheme,

$$F_k^{\nu,(i+1)} = F_k^{\nu,(i)} + \frac{\langle D_k^\nu \rangle_{\text{MC}} - M_{kk'} F_{k'}^{\nu,(i)} B_{k'}^{\nu\,2} C_{k'}^{\nu,\text{theory}}}{B_k^{\nu\,2} C_k^{\nu,\text{theory}} w_2}. \tag{6.5}$$

Here $w_2 = \int dx \mathbf{W}^2$ is a normalization factor for the area of the window. We find that the transfer function estimate converges after the first iteration and use the fifth iteration. For both fields and both bands, the result is a slowly varying function of ℓ with values that range from a minimum of 0.6 at $\ell = 2000$ to a broad peak near $\ell = 5000$ of 0.8.

Bandpower Covariance Matrix

The bandpower covariance matrix includes two terms: variance of the signal in the field (cosmic variance), and instrumental noise variance. The signal-only Monte Carlo bandpowers are used to estimate the cosmic variance contribution. The instrumental noise variance is calculated from the distribution of the cross-spectrum bandpowers $D_b^{\nu_i \times \nu_j, AB}$ between observations A and B, as described in L10. We expect some statistical uncertainty of the form

$$\left\langle (\mathbf{c}_{ij} - \langle \mathbf{c}_{ij} \rangle)^2 \right\rangle = \frac{\mathbf{c}_{ij}^2 + \mathbf{c}_{ii}\mathbf{c}_{jj}}{n_{obs}} \tag{6.6}$$

in the estimated bandpower covariance matrix. Here, n_{obs} is the number of observations that go into the covariance estimate. This uncertainty on the covariance is significantly higher

than the true covariance for almost all off-diagonal terms due to the dependence of the uncertainty on the (large) diagonal covariances. We reduce the impact of this uncertainty by "conditioning" the covariance matrix.

How we condition the covariance matrix is determined by the form we expect it to assume. The covariance matrix can be viewed as a set of nine square blocks, with the three on-diagonal blocks corresponding to the covariances of a 150×150, 150×220, or 220×220 GHz spectrum. Since the bandpowers reported in Tables 6.1 and 6.4 are obtained by first computing power spectra and covariance matrices for bins of width $\Delta \ell = 100$ with a total of 80 initial ℓ-bins, each of these blocks is an 80×80 matrix. The shape of the correlation matrix in each of these blocks is expected to be the same, as it is set by the apodization window. As a first step to conditioning the covariance matrix, we calculate the correlation matrices for the three on-diagonal blocks and average all off-diagonal elements at a fixed separation from the diagonal in each block,

$$\mathbf{c}'_{kk'} = \frac{\sum_{k_1 - k_2 = k - k'} \frac{\widehat{\mathbf{c}}_{k_1 k_2}}{\sqrt{\widehat{\mathbf{c}}_{k_1 k_1} \widehat{\mathbf{c}}_{k_2 k_2}}}}{\sum_{k_1 - k_2 = k - k'} 1}. \tag{6.7}$$

This averaged correlation matrix is then applied to all nine blocks.

The covariance matrix generally includes an estimate of both signal and noise variance. However, the covariance between the 150×150 and 220×220 bandpowers is a special case: since we neither expect nor observe correlated noise between the two frequencies in the signal band, we include only the signal variance in the two blocks describing their covariance.

Combining the Fields

We have two sets of bandpowers and covariances—one per field—which must be combined to find the best estimate of the true power spectrum. We calculate near-optimal weightings for this combination at each frequency and ℓ-bin using the diagonal elements of the covariance matrix,

$$w_b^{\nu_i \times \nu_j} \propto 1/(C_{bb}^{(\nu_i \times \nu_j) \times (\nu_i \times \nu_j)}). \tag{6.8}$$

This produces a diagonal weight matrix, w, for which the bandpowers can be calculated:

$$\widehat{D}_b^{\nu_i \times \nu_j} = \sum_{\zeta} \left(w_{\zeta}^{\nu_i \times \nu_j} \widehat{D}_{\zeta}^{\nu_i \times \nu_j} \right)_b, \tag{6.9}$$

where ζ denotes the field. The covariance will be

$$\mathbf{c}_{bb'}^{(\nu_i \times \nu_j) \times (\nu_m \times \nu_n)} =$$

$$= \sum_{\zeta} \left(w_{\zeta}^{\nu_i \times \nu_j} \mathbf{c}_{\zeta}^{(\nu_i \times \nu_j) \times (\nu_m \times \nu_n)} w_{\zeta}^{\nu_m \times \nu_n} \right)_{bb'}. \tag{6.10}$$

After combining the two fields, we average the bandpowers and covariance matrix into the final ℓ-bins. Each initial $\Delta \ell = 100$ sub-bin gets equal weight.

6.4 Jackknife tests

We apply a set of jackknife tests to the data to search for possible systematic errors. In a jackknife test, the data set is divided into two halves based on features of the data associated with potential sources of systematic error. After differencing the two halves to remove any astronomical signal, the resulting power spectrum is compared to zero. Significant deviations from zero would indicate a systematic problem or possibly a noise misestimate. Jackknives with a cross-spectrum (as opposed to an auto-spectrum) estimator are less sensitive to small noise misestimates since there is no noise bias term to be subtracted. We implement the jackknives in the cross-spectrum framework by differencing single pairs of observations and applying the cross-spectrum estimator outlined in Section 6.3.2 to the set of differenced pairs. In total, we perform three jackknife tests based on the observing parameters: time, scan direction, and azimuthal range.

The data can be split based on the time of observation to search for variability in the calibration, beams, detector time constants, or any other potentially time variable aspect of the observations. The "first half - second half" jackknife probes variations on month time scales. Results for the "first half - second half" jackknife are shown in the top panel of Figure 6.2. We note that in the 23^h30^m field, the combination of individual field observations into four-map units, discussed in section 6.2, results in a small number of constituent maps (9 out of 960) that are grouped into the wrong side of this split. This does not affect the 5^h30^m field, where the observation unit is a single map.

The data can also be split based on the direction of the scan in a "left - right" jackknife (panel 2 of Figure 6.2). We would expect to see residual power here if the detector transfer function has been improperly de-convolved, if the telescope acceleration at turn-arounds induces a signal through sky modulation or microphonics, or if the wind direction is important.

Sidelobe pickup could potentially introduce spurious signals into the map from features on the ground. In deep coadds of unfiltered data, we observe features with scales of several degrees that are fixed with azimuth and are presumably caused by ground pickup. This ground pickup is significantly reduced by the wedge common-mode removal, but could still exist at low levels. We split the data as a function of azimuth based on the observed RMS signal on these large scales. This split is different than the choice made in L10, which was based upon the distance in azimuth between an observation and the closest building. The azimuthal jackknife is shown in the third panel of Figure 6.2.

We calculate the χ^2 with respect to zero for each jackknife over the range $\ell \in [2000, 9500]$ in bins with $\Delta\ell = 500$. The probability to exceed the measured χ^2 (PTE) for the three individual jackknives is 5%, 66%, and 15% at 150 GHz and 99%, 21%, and 98% at 220 GHz for the "first half - second half," "left - right," and "azimuth" jackknives, respectively. The combined PTE for the three jackknives is 10% for the 150 GHz data, 96% for the 220 GHz data and 55% for the combined set of both frequencies. We thus find no evidence for systematic contamination of the SPT band powers.
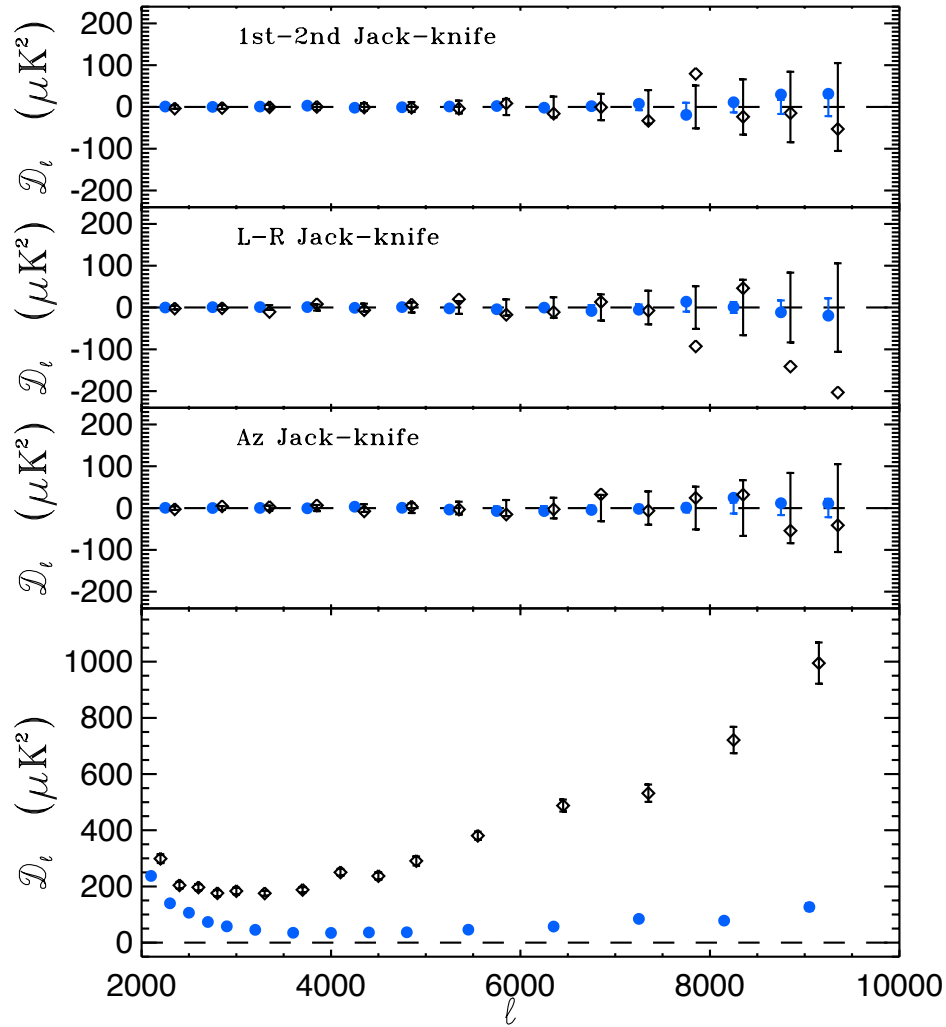
Figure 6.2 Jackknives for the SPT data set at 150 GHz (**blue circles**) and 220 GHz (**black diamonds**). For clarity, the 220 GHz jackknives have been shifted to the right by $\Delta\ell = 100$. *Top panel:* Bandpowers of the "first half - second half" jackknife compared to the expected error bars about zero signal. Disagreement with zero would indicate either a noise misestimate or a time-dependent systematic signal. *Second panel:* Power spectrum of the left-going minus right-going difference map. This test yields strong constraints on the accuracy of the detector transfer function deconvolution and on possible directional systematics. *Third panel:* Bandpowers for the difference map when the data are split based on the observed very large scale ($\ell < 100$) ground pickup as a function of azimuth. Signals fixed in azimuth, such as ground pickup on smaller scales, would produce non-zero power. We see no evidence for ground-based pickup across this ℓ-range. The cumulative probability to exceed the χ^2 observed in these three tests at 150 and 220 GHz is 55%. *Bottom panel:* The un-differenced SPT power spectra at each frequency for comparison.

6.5 Power spectra

The bandpowers presented in Table 6.1 and plotted in Figure 6.3 are the result of applying the analysis described in Section 6.3 to the 210 deg^2 observed by SPT in 2008. The errors shown in Table 6.1 are the diagonal elements of the covariance matrix. The full covariance matrix including off-diagonal elements can be found at the SPT website[4] along with the window functions describing the transformation from a theoretical spectrum to these bandpowers (Knox, 1999).

In these power spectra, we have measured the mm-wave anisotropy power at $\ell > 2000$ with the highest significance to date. Anisotropy power is detected at $92\,\sigma$ at $150\,\mathrm{GHz}$ and $74\,\sigma$ at $220\,\mathrm{GHz}$. Below $\ell \sim 3000$, the bandpowers reflect the Silk damping tail of the primary CMB anisotropy. At $\ell > 3000$, the bandpowers follow the $D_\ell \propto \ell^2$ form expected for a Poisson point source distribution. The measured spectral index ($\alpha \sim 3.6$ where $S_\nu \propto \nu^\alpha$) points to a dust-like spectrum for the point sources indicating that the DSFGs are the dominant point source population. However, the CMB and Poisson terms do not fully explain the data. Adding two free parameters representing the tSZ and effects of point source clustering improves the best-fit model likelihood, $\mathcal{L}$, by $\Delta \ln \mathcal{L} = 65$. Using a combination of the $150\,\mathrm{GHz}$ auto-spectrum, 150×220 cross-spectrum and $220\,\mathrm{GHz}$ auto-spectrum, we can separate these foregrounds and secondary anisotropies; however, substantial degeneracies remain. Future SPT data analyses will include a third frequency band, which we expect will significantly reduce these degeneracies.

6.6 Cosmological model

We fit the SPT bandpowers to a model including lensed primary CMB anisotropy, secondary tSZ and kSZ anisotropies, galactic cirrus, an unclustered population of radio sources and a clustered population of DSFGs. In total, this model has six parameters describing the primary CMB anisotropy, up to two parameters describing secondary CMB anisotropies, and up to eleven parameters describing foregrounds.

Parameter constraints are calculated using the publicly available CosmoMC[5] package (Lewis & Bridle, 2002). We have added two modules to handle the high-ℓ data; one to model the foregrounds and secondary anisotropies and one to calculate the SPT likelihood function. These extensions, with some differences in the treatment of the secondary anisotropy, are also discussed in Millea et al. (2011). These modules and instructions for compiling them are available at the SPT website.[6]

Although there are observational and theoretical reasons to expect contributions to the power spectra from each of the components outlined above, a good fit to the current SPT

---

[4]http://pole.uchicago.edu/public/data/shirokoff10/
[5]http://cosmologist.info/cosmomc
[6]http://pole.uchicago.edu/public/data/shirokoff10/

Table 6.1 Single-frequency bandpowers

ℓ range	ℓ_{eff}	150 GHz		150 × 220 GHz		220 GHz	
		$\hat{D}$ (μK^2)	σ (μK^2)	$\hat{D}$ (μK^2)	σ (μK^2)	$\hat{D}$ (μK^2)	σ (μK^2)
2001 - 2200	2056	242.1	6.7	248.8	8.3	295.9	14.9
2201 - 2400	2273	143.2	4.2	154.7	5.6	201.5	11.7
2401 - 2600	2471	109.3	3.2	122.1	4.5	193.5	11.0
2601 - 2800	2673	75.9	2.6	102.8	4.1	172.1	10.4
2801 - 3000	2892	60.2	2.3	80.4	3.7	179.3	11.1
3001 - 3400	3184	47.5	1.5	73.5	2.5	169.7	8.2
3401 - 3800	3580	36.9	1.6	69.5	2.7	180.7	9.2
3801 - 4200	3993	36.7	1.8	81.0	3.3	240.1	11.6
4201 - 4600	4401	38.5	2.2	81.5	3.9	226.6	12.6
4601 - 5000	4789	39.3	2.7	96.9	4.7	276.9	15.2
5001 - 5900	5448	49.2	2.5	122.3	4.2	361.3	13.3
5901 - 6800	6359	60.8	3.9	158.7	6.2	457.4	20.0
6801 - 7700	7256	89.1	6.0	173.9	9.5	488.8	28.4
7701 - 8600	8159	81.7	9.5	229.2	14.2	653.0	42.3
8601 - 9500	9061	131.9	14.4	309.1	21.9	895.2	66.0

Note. — Band multipole range and weighted value ℓ_{eff}, bandpower $\hat{D}$, and uncertainty σ for the 150 GHz auto-spectrum, cross-spectrum, and 220 GHz auto-spectrum of the SPT fields. The quoted uncertainties include instrumental noise and the Gaussian sample variance of the primary CMB and the point source foregrounds. The sample variance of the SZ effect, beam uncertainty, and calibration uncertainty are not included. To include the preferred calibration from the MCMC chains, these bandpowers should be multiplied by 0.92, 0.95, and 0.98 at 150 GHz, 150 × 220 GHz, and 220 GHz respectively. (See Section 6.7.1.) Beam uncertainties are shown in Figure 6.1 and calibration uncertainties are quoted in Section 6.2.2. Point sources above 6.4 mJy at 150 GHz have been masked out in this analysis. This flux cut substantially reduces the contribution of radio sources to the bandpowers, although DSFGs below this threshold contribute significantly to the bandpowers.

data can be obtained with a much simpler, four-parameter extension to the primary CMB anisotropy. This minimal model contains four free parameters: the tSZ amplitude, the Poisson and clustered DSFG amplitudes, and a single spectral index which sets the frequency dependence of both DSFG terms. All other parameters are tightly constrained by external data. A similar model was used in recent ACT analysis (Dunkley et al., 2011). We adopt this four-parameter extension as the baseline model for this work.

In this baseline model, several simplifications are made. The distributions of spectral indices are set to delta functions ($\sigma_X = 0$). The radio source spectral index is fixed to
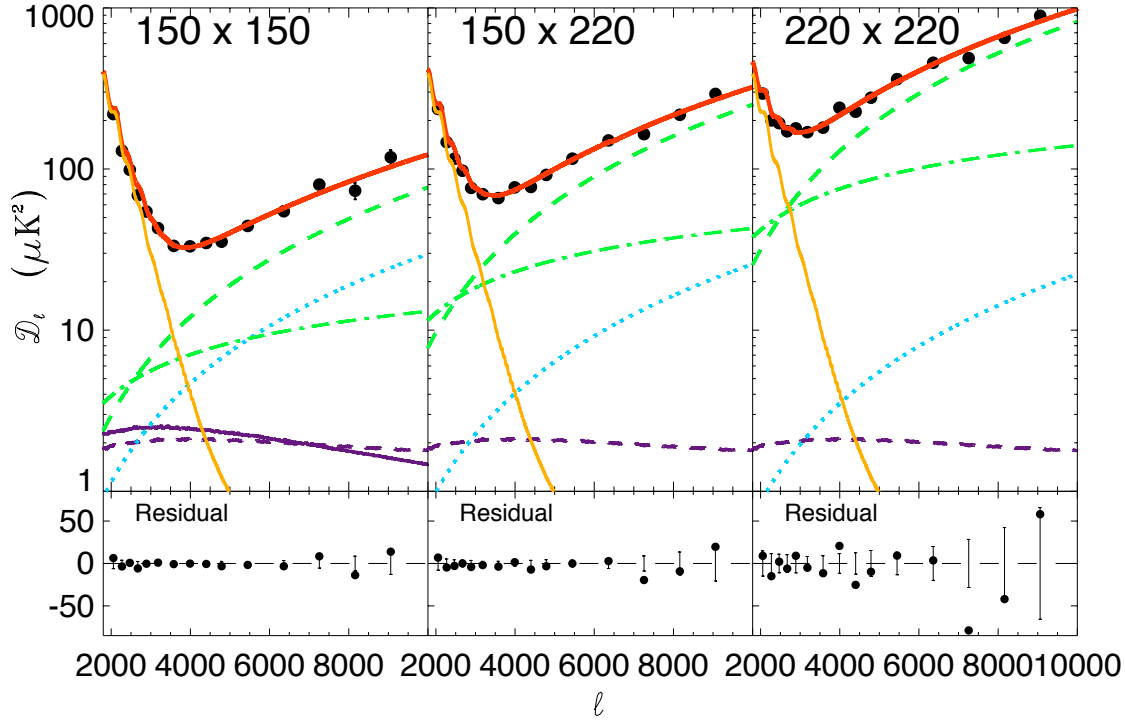
Figure 6.3 *Top panel:* From left to right, the SPT 150 GHz, 150 × 220 GHz, and 220 GHz bandpowers. Overplotted is the best-fit model (**red line**) with components shown individually. The lensed primary CMB anisotropy is marked by an **orange line**. The best-fit tSZ (**purple line**) and predicted kSZ (**purple dashed line**) power spectra are also shown. The predicted radio source term is represented by the **blue dots**. The DSFG Poisson term at each frequency is denoted by the **green dashed line** and the clustered DSFG component by the **green dot-dash line**. The damping tail of the primary CMB anisotropy is apparent below $\ell = 3000$. Above $\ell = 3000$, there is a clear excess with an angular scale dependence consistent with point sources. These sources have low flux (sources detected at $> 5\,\sigma$ at 150 GHz have been masked) and a rising frequency spectrum, consistent with expectations for DSFGs. *Bottom panel:* Plot of the residual between the measured bandpowers and best-fit spectrum.

$\alpha_r = -0.53$. The amplitudes of the kSZ, radio source, and cirrus power spectra are fixed to expected values. The tSZ-DSFG correlation is set to zero. We discuss the priors placed on these components in the following subsections.

To compare the SPT data to these cosmological models, we combine the SPT high-ℓ bandpowers with low-ℓ CMB measurements from WMAP7, ACBAR, and QUaD (Larson et al., 2011; Reichardt et al., 2009a; Brown et al., 2009). During the preparation of this paper, the ACT bandpowers were published (Das et al., 2011); however, it was not until
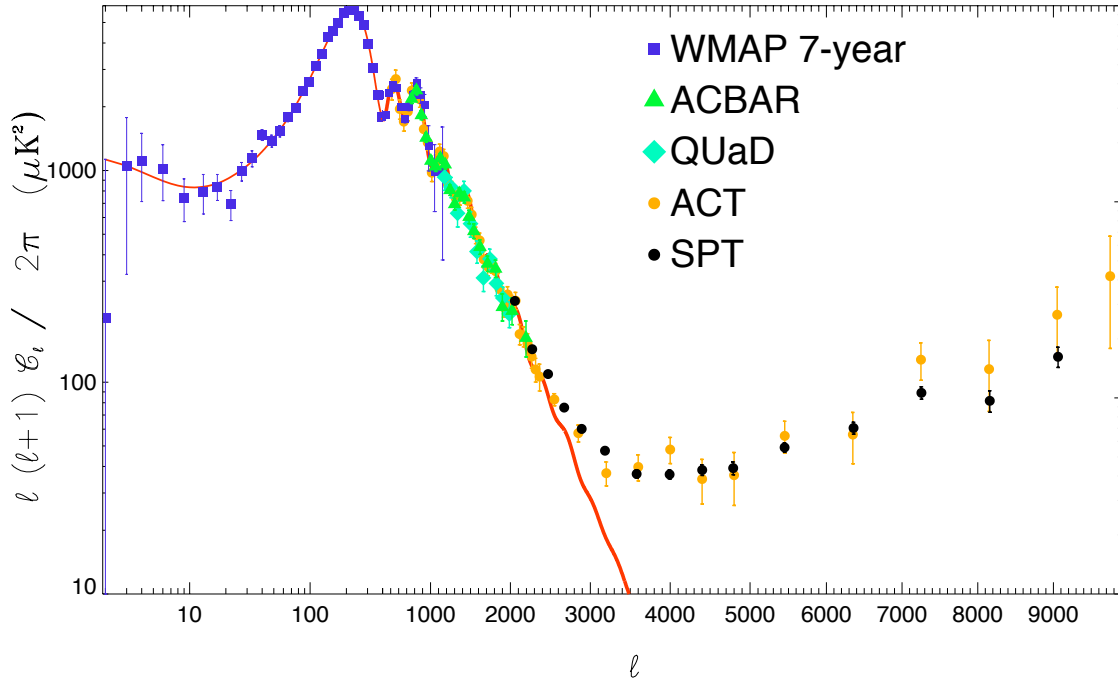
Figure 6.4 The SPT 150 GHz bandpowers (**black circles**), WMAP7 bandpowers (**purple squares**), ACBAR bandpowers (**green triangles**), QUaD bandpowers (**cyan diamonds**), and ACT 150 GHz bandpowers (**orange circles**) plotted against the best-fit lensed ΛCDM CMB spectrum. The damping tail of the primary CMB anisotropy is apparent below $\ell = 3000$. Above $\ell = 3000$, there is a clear excess due to secondary anisotropies and residual point sources that has now been measured by both SPT and ACT. Note that the source masking threshold in the SPT data (6.4 mJy) is lower than that in the ACT data, so we expect less radio source power at high ℓ. We have multiplied the SPT bandpowers by the best-fit calibration of 0.92 as determined in parameter fits.

after the model fitting runs were completed that the window functions were made available. For this reason, we do not include the ACT bandpowers in the fits although they are the best current constraints for $\ell \in [1600, 2000]$. We expect that including the ACT data would have little impact on the results. The low-ℓ CMB bandpowers tightly constrain the ΛCDM model space. We restrict the ACBAR and QUaD bandpowers to $\ell < 2100$ where the details of the secondary anisotropies and point source spectra are negligible compared to the primary CMB anisotropy. These additional components are challenging to model between experiments since they are frequency-dependent and, in the case of point sources, mask-dependent. In practice, removing this restriction does not affect the results since the SPT data dominates the constraints above $\ell = 2000$.

6.6.1 Primary CMB Anisotropy

We use the standard, six-parameter, spatially flat, lensed ΛCDM cosmological model to predict the primary CMB temperature anisotropy. The six parameters are the baryon density $\Omega_b h^2$, the density of cold dark matter $\Omega_c h^2$, the optical depth to recombination τ, the angular scale of the peaks Θ, the amplitude of the primordial density fluctuations $\ln[10^{10} A_s]$, and the scalar spectral index n_s.

Gravitational lensing of CMB anisotropy by large-scale structure tends to increase the power at small angular scales, with the potential to influence the high-ℓ model fits. The calculation of lensed CMB spectra out to $\ell = 10000$ is prohibitively expensive in computational time. Instead, we approximate the impact of lensing by adding a fixed lensing template calculated for the best-fit WMAP7 cosmology to unlensed CAMB[7] spectra. The error due to this lensing approximation is less than $0.5\,\mu\text{K}^2$ for the allowed parameter space at $\ell > 3000$. This is a factor of 20 (260) times smaller than the secondary and foreground power at 150 (220) GHz and should have an insignificant impact on the likelihood calculation. We tested this assumption by including the full lensing treatment in a single chain with the baseline model described above. As anticipated, we found no change in the resulting parameter constraints.

We find the data from SPT, WMAP7, ACBAR, and QUaD considered here prefer gravitational lensing at $\Delta\ln\mathcal{L} = -5.9$ ($3.4\,\sigma$). Most of this detection significance is the result of the low-ℓ data and not the high-ℓ SPT data presented here; without including SPT data in fits, lensing is preferred at $3.0\,\sigma$. In estimating the preference for gravitational lensing, we used the true lensing calculation instead of the lensing approximation described above.

6.6.2 Secondary CMB Anisotropy

We parametrize the secondary CMB anisotropy with two terms describing the amplitude of the tSZ and kSZ power spectra: D_{3000}^{tSZ} and D_{3000}^{kSZ}. The model for the SZ terms can be written as

$$D_{\ell,\nu_1,\nu_2}^{SZ} = D_{3000}^{tSZ} \frac{f_{\nu_1} f_{\nu_2}}{f_{\nu_0}^2} \frac{\Phi_\ell^{tSZ}}{\Phi_{3000}^{tSZ}} + D_{3000}^{kSZ} \frac{\Phi_\ell^{kSZ}}{\Phi_{3000}^{kSZ}}. \tag{6.11}$$

Here, Φ_ℓ^X denotes the theoretical model template for component X at frequency ν_0. The frequency dependence of the tSZ effect is encoded in f_ν; at the base frequency ν_0, $D_{3000,\nu_0,\nu_0}^{tSZ} = D_{3000}^{tSZ}$. The kSZ effect has the same spectrum as the primary CMB anisotropy, so its amplitude is independent of frequency. In this work, we set ν_0 to be the effective frequency of the SPT 150 GHz band (see Section 6.6.4).

---

[7]http://camb.info

tSZ Power Spectrum

We adopt four different models for the tSZ power spectrum. Following L10, we use the power spectrum predicted by S10 as the baseline model. S10 combined the semi-analytic model for the intra-cluster medium (ICM) of Bode et al. (2009) with a cosmological N-body simulation to produce simulated thermal and kinetic SZ maps from which the template power spectra were measured. The assumed cosmological parameters are $(\Omega_b, \Omega_m, \Omega_\Lambda, h, n_s, \sigma_8) = (0.044,$ 0.264, 0.736, 0.71, 0.96, 0.80). At $\ell = 3000$, this model predicts $D_{3000}^{tSZ} = 7.5 \, \mu K^2$ of tSZ power in the SPT 150 GHz band. We use this model in all chains where another model is not explicitly specified.

We also consider tSZ power spectrum models reported by Trac et al. (2011), Battaglia et al. (2010), and Shaw et al. (2010). Trac et al. (2011) followed a procedure similar to that of S10, exploring the thermal and kinetic SZ power spectra produced for different input parameters of the Bode et al. (2009) gas model. We adopt the nonthermal20 model (hereafter the Trac model) presented in that work, which differs from the S10 simulations by having increased star formation, lower energy feedback, and the inclusion of 20% non-thermal pressure support. It predicts a significantly smaller value of $D_{3000}^{\mathrm{tSZ}} = 4.5 \, \mu K^2$ when scaled to the SPT 150 GHz band. The second template we consider is that produced by Battaglia et al. (2010) from their Smoothed-Particle-Hydrodynamics simulations including radiative cooling, star formation and AGN feedback (hereafter the Battaglia model). This model predicts $D_{3000}^{\mathrm{tSZ}} = 5.6 \, \mu K^2$, intermediate between the baseline model and the Trac model, and peaks at slightly higher ℓ than either of those models. Shaw et al. (2010) investigate the impact of cluster astrophysics on the tSZ power spectrum using halo model calculations in combination with an analytic model for the ICM. We use the baseline model from that work (hereafter the Shaw model), which predicts $D_{3000}^{\mathrm{tSZ}} = 4.7 \, \mu K^2$ in the 150 GHz band. The model of Shaw et al. (2010) is also used to rescale all the model templates as a function of cosmological parameters, as described in Section 6.8.

All four tSZ models exhibit a similar angular scale dependence over the range of multipoles to which SPT is sensitive (see Figure 6.5). We allow the normalization of each model to vary in all chains, and detect similar tSZ power in all cases (see Table 6.6). However as we discuss in Section 6.8, the difference between models is critical in interpreting the detected tSZ power as a constraint on cluster physics or σ_8.

kSZ Power Spectrum

We use the S10 (homogeneous reionization) kSZ template as the baseline kSZ model. At $\ell = 3000$, this model predicts $D_{3000}^{kSZ} = 2.05 \, \mu K^2$ of kSZ power. The kSZ amplitude depends on the details of reionization, and the scaling of the kSZ power with cosmological parameters, particularly σ_8, is much weaker than the scaling of the tSZ power. We therefore choose to fix the amplitude of the kSZ signal to a model value and allow tSZ to vary independently. This treatment differs from Dunkley et al. (2011), which uses a single normalization for both
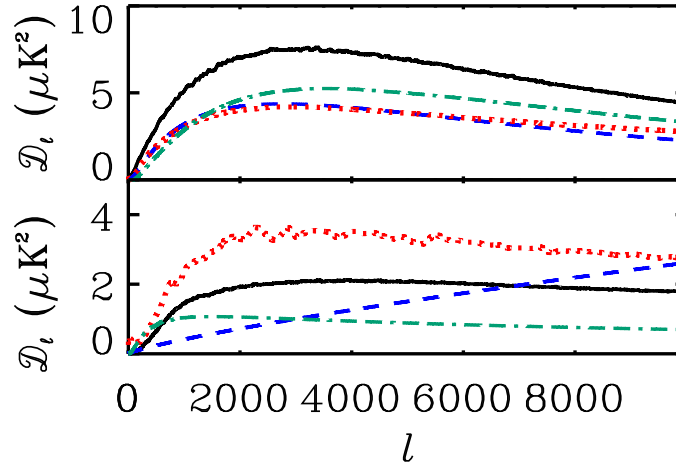
Figure 6.5 Templates used for the tSZ, kSZ, and clustered DSFG power discussed in Section 6.6. The *top plot* shows alternate tSZ templates. The **black, solid line** is the (baseline) S10 model. The **blue, dashed line** is the Shaw model. The **red, dotted line** is the Trac model. The **teal dot-dash line** is the Battaglia model. The *bottom plot* shows both kSZ and clustered DSFG templates. The **black, solid line** is the (baseline) S10 kSZ model. The **red, dotted line** is the patchy kSZ model. The **blue, dashed line** is the (baseline) power-law clustered DSFG template. The **teal, dot-dash line** is the linear-theory clustered DSFG template. The clustered DSFG templates have both been normalized to 1 μK^2 at $\ell = 3000$.

SZ components, and Millea et al. (2011) in which a fitting function is used to calculate the kSZ power as a function of cosmological parameters at each step in the MCMC chain. For the current SPT data set, where tSZ and kSZ power are largely degenerate, we expect the differences in kSZ treatment to be insignificant. This assumption was tested by importance sampling an MCMC chain with variable kSZ amplitude according to the scaling at $\ell = 3000$ described in Millea et al. (2011). As expected, we find no significant difference in fitted parameters.

In Section 6.7 we will discuss the impact of two alternate kSZ treatments in addition to the baseline model. First, we consider a kSZ template that includes the signal from patchy reionization (hereafter the patchy kSZ template). This template, which was also used in L10, is based upon the "FFRT" semi-analytic model of Zahn et al. (2011). It was calculated in a 1.5 Gpc/h cosmological column where the x- and y-axes correspond to roughly 15 degrees on a side and the z-axis corresponds to redshift, with a median redshift of 8. The inclusion of patchy reionization increases the kSZ amplitude to at most $3.3\,\mu$K^2, and changes the shape of D_ℓ^{kSZ} slightly when compared to the fiducial template (see Figure 6.5). In the second kSZ treatment, we consider the impact of allowing the overall kSZ amplitude to vary. In this

treatment, we found the small difference between the S10 and patchy kSZ template shapes had no impact on the result. We therefore use the S10 template for all variable amplitude kSZ constraints.

6.6.3 Foregrounds

At $\ell > 3000$, the measured anisotropy is dominated by astrophysical foregrounds, particularly bright radio point sources. We mask all point sources detected at $> 5\,\sigma$ (6.4 mJy at 150 GHz) when estimating the power spectrum. In order of importance after masking the brightest point sources, we expect contributions from DSFGs (including their clustering), radio sources (unclustered), and galactic cirrus. We parametrize these galactic and extragalactic foregrounds with an eleven-parameter model. Five parameters describe the component amplitudes at $\ell = 3000$: three point source amplitudes in the 150 GHz band (clustering and Poisson for DSFGs and Poisson for radio) and a galactic cirrus amplitude in each of the two observation bands. One parameter describes the correlation between the tSZ and clustered DSFG terms. Three parameters describe the effective mean spectral indices of each point source component, and the final two parameters describe the distribution about the mean spectral index for the Poisson radio source and DSFG populations.

The frequency dependencies of many of these foregrounds are naturally discussed and modeled in units of flux density (Jy) rather than CMB temperature units. This is because the flux density of these foregrounds can be modeled as a power law in frequency, $(S_\nu \propto \nu^\alpha)$. However, in order to model these foregrounds in the power spectrum, we need to determine the ratio of powers in CMB temperature units. To calculate the ratio of power in the ν_i cross ν_j cross-spectrum to the power at (the arbitrary frequency) ν_0 in units of CMB temperature squared, we multiply the ratio of flux densities by

$$\epsilon_{\nu_1,\nu_2} \equiv \frac{\frac{dB}{dT}\big|_{\nu_0}\frac{dB}{dT}\big|_{\nu_0}}{\frac{dB}{dT}\big|_{\nu_1}\frac{dB}{dT}\big|_{\nu_2}}, \tag{6.12}$$

where B is the CMB blackbody specific intensity evaluated at T_{CMB}, and ν_i and ν_j are the effective frequencies of the SPT bands. Note that ν_i may equal ν_j. The effective frequencies for each foreground calculated for the measured SPT bandpass (assuming a nominal frequency dependence) are presented in Section 6.6.4.

Poisson DSFGs

Poisson distributed point sources produce a constant C_ℓ (thus, $D_\ell \propto \ell^2$). A population of dim ($\lesssim 1$ mJy) DSFGs is expected to contribute the bulk of the millimeter wavelength point source flux. This expectation is consistent with recent observations (Lagache et al. (2007), Viero et al. (2009), H10, Dunkley et al. (2011)). Thermal emission from dust grains heated to tens of Kelvin by star light leads to a large effective spectral index ($S_\nu \propto \nu^\alpha$), where $\alpha > 2$ between 150 and 220 GHz, for two reasons (e.g. Dunne et al., 2000). First, these frequencies

are in the Rayleigh-Jeans tail of the blackbody emission for the majority of the emitting DSFGs. Second, the emissivity of the dust grains is expected to increase with frequency for dust grains smaller than the photon wavelength (2 mm for 150 GHz) (Draine & Lee, 1984; Gordon, 1995).

Assuming that each galaxy has a spectral index α drawn from a normal distribution with mean α_p and variance σ_p^2, then following Millea et al. (2011), the Poisson power spectrum of the DSFGs can be written as

$$D_{\ell,\nu_1,\nu_2}^p = D_{3000}^p \epsilon_{\nu_1,\nu_2} \eta_{\nu_1,\nu_2}^{\alpha_p+0.5\ln(\eta_{\nu_1,\nu_2})\sigma_p^2} \left(\frac{\ell}{3000}\right)^2 \tag{6.13}$$

where $\eta_{\nu_1,\nu_2} = (\nu_1\nu_2/\nu_0^2)$ is the ratio of the frequencies of the spectrum to the base frequency. D_{3000}^p is the amplitude of the Poisson DSFG power spectrum at $\ell = 3000$ and frequency ν_0.

In principle, the frequency scaling of the Poisson power depends on both α_p and σ_p. H10 combine the dust spectral energy distributions (SEDs) from Silva et al. (1998) with an assumed redshift distribution of galaxies to infer $\sigma_p \sim 0.3$ (although they conservatively adopt a prior range of $\sigma_p \in [0.2, 0.7]$). However, for $\alpha = 3.6$, the ratio of Poisson power at 220 to 150 GHz only increases by 2% for $\sigma_p = 0.3$ versus $\sigma_p = 0$, which is small compared to the constraint provided by the current data. The complete model includes six parameters describing three measured Poisson powers in two bands. In order to reduce this to a reasonable number of parameters, we set $\sigma_p = 0$ in the baseline model. The equivalent Poisson radio galaxy spectral variance, σ_r, has a negligible effect on the radio power at 220 GHz and is also set to zero.

Clustered DSFGs

Because DSFGs trace the mass distribution, they are spatially correlated. In addition to the Poisson term, this leads to a 'clustered' term in the power spectrum of these sources,

$$D_{\ell,\nu_1,\nu_2}^c = D_{3000}^c \epsilon_{\nu_1,\nu_2} \eta_{\nu_1,\nu_2}^{\alpha_c} \frac{\Phi_\ell^c}{\Phi_{3000}^c}. \tag{6.14}$$

D_{3000}^c is the amplitude of the clustering contribution to the DSFG power spectrum at $\ell = 3000$ at frequency ν_0. The model for the clustering contribution to the DSFG power spectrum is Φ_ℓ^c, which we have divided by Φ_{3000}^c to make a unitless template which is normalized at $\ell = 3000$.

We consider two different shapes for the angular power spectrum due to the clustering of the DSFGs, shown in Figure 6.5. The first is the shape of the fiducial model used in Hall et al. (2010). This spectrum was calculated assuming that light is a biased tracer of mass fluctuations calculated in linear perturbation theory. Further, the model assumes all galaxies have the same SED, that of a grey body, and the redshift distribution of the luminosity density was given by a parametrized form, with parameters adjusted to fit SPT,

BLAST, and Spitzer power spectrum measurements. Here we refer to this power spectrum shape as the "linear theory" template.

On the physical scales of relevance, galaxy correlation functions are surprisingly well-approximated by a power law. The second shape we consider is thus a phenomenologically-motivated power law with index chosen to match the correlation properties observed for Lyman-break galaxies at $z \sim 3$ (Giavalisco et al., 1998; Scott & White, 1999). We adopt this "power law" model in the baseline model, and use a template of the form $\Phi_\ell^c \propto \ell^{0.8}$ in all cases except as noted.

We also consider a linear combination of the linear-theory shape and the power-law shape. Such a combination can be thought of as a rough approximation to the two-halo and one-halo terms of a halo model. The present data set has limited power to constrain the ratio of the two terms; however, we do find a slight preference for the pure power-law model over the pure linear-theory model, as discussed in sections 6.7.3 and 6.7.3.

The spectrum of the clustered component should be closely related to the spectrum of the Poisson component since they arise from the same sources (H10). However, the clustered DSFG term is expected to be more significant at higher redshifts, where the rest-frame frequency of the SPT observing bands is shifted to higher frequencies and out of the Raleigh-Jeans approximation for a larger fraction of the galaxies. One might therefore anticipate a slightly lower spectral index for the clustered term.

We assume a single spectral index for the Poisson and clustered DSFG components in the baseline model ($\alpha_c = \alpha_p$), and explore the impact of allowing the two spectral indices to vary independently in Section 6.7.3. In general, we require $\alpha_c = \alpha_p$, except where otherwise noted.

tSZ-DSFG correlation

The tSZ signal from galaxy clusters and the clustered DSFG signal are both biased tracers of the same dark matter distribution, although the populations have different redshift distributions. Thus, it is natural to expect these two signals to be partially correlated and this correlation may evolve with redshift and halo mass. At frequencies below the tSZ null, this should result in spatially anti-correlated power. At 150 GHz, some models that attempt to associate emission with individual cluster member galaxies predict anti-correlations of up to tens of percent (S10). L10 argue against this being significant in the SPT 150 GHz band, because cluster members observed at low redshift have significantly less dust emission than field galaxies. It is, of course, possible for this emission to be significant at higher redshifts where much of the tSZ power originates. Current observations place only weak constraints on this correlation. (As we show in Section 6.7.4, the data presented here are consistent with an anti-correlation coefficient ranging from zero to tens of percent.) To the extent that the Poisson and clustered power spectra have the same spectral index, the differenced band powers discussed in Section 6.7.5 (as well as in L10) are insensitive to this correlation.

A correlation, $\gamma(\ell)$, between the tSZ and clustered DSFG signals introduces an additional

term in the model,

$$D^{tSZ-DSFG}_{\ell,\nu_1,\nu_2} = \gamma(\ell)\left(\sqrt{D^c_{\ell,\nu_1,\nu_1} D^{tSZ}_{\ell,\nu_2,\nu_2}} + \sqrt{D^c_{\ell,\nu_2,\nu_2} D^{tSZ}_{\ell,\nu_1,\nu_1}}\right).$$

(6.15)

We will assume no tSZ-DSFG correlation in all fits unless otherwise noted. In Section 6.7.4, we will investigate constraints on the degree of correlation and the impact on other parameters from allowing a DSFG-tSZ correlation.

Radio galaxies

The brightest point sources in the SPT maps are coincident with known radio sources and have spectral indices consistent with synchrotron emission (Vieira et al., 2010, hereafter V10). Much like the Poisson DSFG term, the model for the Poisson radio term can be written as

$$D^r_{\ell,\nu_1,\nu_2} = D^r_{3000}\epsilon_{\nu_1,\nu_2}\eta^{\alpha_r+0.5\ln(\eta_{\nu_1,\nu_2})\sigma_r^2}_{\nu_1,\nu_2}\left(\frac{\ell}{3000}\right)^2.$$

(6.16)

The variables have the same meanings as for the treatment of the DSFG Poisson term. Clustering of the radio galaxies is negligible.

In contrast to DSFGs, for which the number counts climb steeply towards lower flux, $S^2 dN/dS$ for synchrotron sources is fairly constant. As a result, the residual radio source power (D^r_{3000}) in the map depends approximately linearly on the flux above which discrete sources are masked. For instance, if all radio sources above a signal to noise threshold of 5σ (6.4 mJy) at 150 GHz are masked, the de Zotti et al. (2005) source count model predicts a residual radio power of $D^r_{3000} = 1.28\,\mu\text{K}^2$. For a 10σ threshold, the residual radio power would be $D^r_{3000} = 2.59\,\mu\text{K}^2$.

The de Zotti model is based on radio surveys such as NVSS extrapolated to 150 GHz using a set spectral index for each subpopulation of radio sources. Extrapolating over such a large frequency range obviously introduces significant uncertainties; however, we do have an important cross-check on the modeling from the number counts of bright radio sources detected in the SPT or ACT maps (V10, Marriage et al. (2011)). The de Zotti number counts appear to over-predict the number of very high flux radio sources reported by both experiments. We find that the de Zotti model should be multiplied by 0.67 ± 0.14 to match the number of $> 20\,\text{mJy}$ radio sources in the SPT source catalog (V10). There are relatively few radio sources at these fluxes, and V10 and Marriage et al. (2011) have partially overlapping sky coverage. The counting statistics on these relatively rare objects will be improved significantly with the full SPT survey. The discrepancy disappears for lower flux radio sources and we find that, for $6.4\,\text{mJy} < S_{150} < 20\,\text{mJy}$ 150 GHz, the best fit normalization of the de Zotti model to fit the radio sources in the V10 catalog is 1.05 ± 0.14. Throughout this work, we use the de Zotti model prediction with a 15% uncertainty as a prior for residual power from sources below 6.4 mJy. Relaxing this radio prior by expanding the 1σ amplitude

prior about the de Zotti et al. (2005) model from 15% to 50% has no significant impact on resulting parameter constraints.

We analyze the two-frequency V10 catalog to determine the radio population mean spectral index (α_r) and scatter in spectral indices (σ_r) at these frequencies. For each source, we take the full (non-Gaussian) likelihood distribution for the source spectral indices from V10. We combine all sources above $5\,\sigma$ at 150 GHz with a probability of having a synchrotron-like spectrum of at least 50% in order to calculate the likelihoods of a given α_r and σ_r. (We note that the results are unaffected by the specific choice of threshold probability for being a synchrotron source.) The best-fit mean spectral index is $\alpha_r = -0.53 \pm 0.09$ with a $2\,\sigma$ upper limit on the intrinsic scatter of $\sigma_r < 0.3$. With the present power spectrum data, both this uncertainty and intrinsic scatter are undetectable. We have checked this assumption by allowing the spectral index to vary with a uniform prior between $\alpha_r \in [-0.66, -0.21]$ instead of fixing it to the best-fit value of -0.53 for several specific cases, and found no significant difference in the resulting parameter constraints. We therefore assume $\alpha_r = -0.53$ and $\sigma_r = 0$ for all cases considered.

Galactic cirrus

In addition to the foregrounds discussed above, we include a fixed galactic cirrus term parametrized as

$$D_{\ell,\nu_1,\nu_2}^{cir} = D_{3000}^{cir,\nu_1,\nu_2} \left(\frac{\ell}{3000} \right)^{-1.5}. \tag{6.17}$$

H10 measured the Galactic cirrus contribution in the 5^h30^m field by cross-correlating the SPT map and model eight of Finkbeiner et al. (1999, hereafter FDS) for the same field. We extend that analysis to the combined data set by scaling the 5^h30^m cirrus estimate by the ratio of the auto-correlation power in the FDS map of each field. We find the 23^h30^m field has 15% of the cirrus power measured in the 5^h30^m field. As the fields are combined with equal weight, we expect the effective cirrus amplitude in the combined bandpowers to be 0.575 times the 5^h30^m amplitudes reported above. Based on this analysis, we fix the amplitude of the cirrus term, $D_\ell \propto \ell^{-1.5}$, in all parameter fits to be $(D_{3000}^{cir,150,150}, D_{3000}^{cir,150,220}, D_{3000}^{cir,220,220}) = (0.35, 0.86, 2.11)\,\mu K^2$ respectively. Note that the cirrus power has a dust-like spectrum and is effectively removed in the differenced bandpowers discussed in Section 6.7.5. We assume there is zero residual cirrus power in the DSFG-subtracted bandpower analyses. Although we include this cirrus prior in the multi-frequency fitting, it has no significant impact on results; marginalizing over the amplitudes in the two bands or setting them to either extreme (zero or the high value in the 5^h30^m field) does not change the resulting parameter values.

6.6.4 Effective frequencies of the SPT bands

Throughout this work, we refer to the SPT band center frequencies as 150 and 220 GHz. The data are calibrated to CMB temperature units, hence the effective frequency is irrelevant for

a CMB-like source. However, the effective band center will depend (weakly) on the source spectrum for other sources. The actual SPT spectral bandpasses are measured by Fourier transform spectroscopy, and the effective band center frequency is calculated for each source, assuming a nominal frequency dependence. For an $\alpha = -0.5$ (radio-like) source spectrum, we find band centers of 151.7 and 219.3 GHz. For an $\alpha = 3.8$ (dust-like) source spectrum, we find band centers of 154.2 and 221.4 GHz. The band centers in both cases drop by ~ 0.2 GHz if we reduce α by 0.3. We use these radio-like and dust-like band centers to calculate the frequency scaling between the SPT bands for the radio and DSFG terms. For a tSZ spectrum, we find band centers of 153.0 and 220.2 GHz. The 220 band center is effectively at the tSZ null; the ratio of tSZ power at 220 to 150 GHz is 0.2%.

6.7 Parameter results

6.7.1 Baseline model results

As discussed in Section 6.6, the baseline secondary anisotropy and foreground model contains four free parameters (beyond the six ΛCDM parameters): the tSZ amplitude, the Poisson DSFG amplitude, the clustered DSFG amplitude, and the DSFG spectral index. For the tSZ component, we use the S10 tSZ model scaled by a single amplitude parameter. For the clustered DSFG component, we use the power-law model presented in Section 6.6.3, again scaled by an amplitude parameter. As discussed in Section 6.7.3, the data show a slight preference for the power-law clustered point source shape model compared to the linear-theory model that was adopted in L10. We require that both the clustered and Poisson DSFG components have the same spectral index, which we model as the free parameter α_p, with no intrinsic scatter ($\sigma_p = 0$). Table 6.3 shows the improvement in the quality of the fits with the sequential introduction of free parameters to the original ΛCDM primary CMB model. Beyond this baseline model, adding additional free parameters does not improve the quality of the fits.

Table 6.2 Parameters from multi-frequency fits

model	D_{3000}^{tSZ}	D_{3000}^{kSZ}	D_{3000}^{P}	D_{3000}^{C}	α_P	α_C	$D_{3000}^{P,220}$	$D_{3000}^{C,220}$
Baseline model	3.5 ± 1.0	$[2.0]$	7.4 ± 0.6	6.1 ± 0.8	3.58 ± 0.09	$--$	70 ± 4	57 ± 8
Patchy kSZ	2.9 ± 1.0	$[3.3]$	7.4 ± 0.6	5.7 ± 0.8	3.62 ± 0.09	$--$	72 ± 4	55 ± 8
Free kSZ	3.2 ± 1.3	2.4 ± 2.0	7.4 ± 0.6	5.9 ± 1.0	3.59 ± 0.11	$--$	71 ± 5	57 ± 9
Free α_c	3.4 ± 1.0	$[2.0]$	7.9 ± 1.0	5.4 ± 1.4	3.46 ± 0.21	3.79 ± 0.37	69 ± 5	59 ± 8
Linear-theory clustering	3.5 ± 1.0	$[2.0]$	9.3 ± 0.5	4.9 ± 0.7	3.59 ± 0.09	$--$	89 ± 5	47 ± 7
Free α_c & linear theory	3.4 ± 1.0	$[2.0]$	9.2 ± 0.7	5.3 ± 1.4	3.62 ± 0.14	3.47 ± 0.34	90 ± 5	46 ± 7
tSZ-DSFG correlation	3.4 ± 1.0	$[2.0]$	9.3 ± 0.7	4.9 ± 0.8	3.60 ± 0.13	$--$	89 ± 5	46 ± 7
tSZ-DSFG cor, free kSZ	1.8 ± 1.4	5.5 ± 3.0	9.1 ± 0.7	4.4 ± 0.9	3.62 ± 0.14	$--$	89 ± 5	43 ± 8

Priors and Templates								
model	N_{pars}	Free α_c	Free D_{3000}^{kSZ}	tSZ model	kSZ model	DG clustered model	$-2\Delta\ln\mathcal{L}$	
Baseline model	10	No	No	S10	S10	power law	$-$	
Patchy kSZ	10	No	No	S10	Patchy	power law	1	
Free kSZ	11	No	Yes	S10	S10	power law	0	
Free α_c	11	Yes	No	S10	S10	power law	0	
Linear-theory clustering	10	No	No	S10	S10	linear theory	4	
Free α_c & linear theory	11	Yes	No	S10	S10	linear theory	4	
tSZ-DSFG cor	11	No	No	S10	S10	linear theory	4	
tSZ-DSFG cor, free kSZ	12	No	Yes	S10	S10	linear theory	4	

Note. — Parameter constraints from multi-frequency fits to the models described in Section 6.6. The amplitudes are $\mathcal{D}_\ell$ at $\ell = 3000$ for the $150\,\mathrm{GHz}$ band, in units of $\mu\mathrm{K}^2$. In all cases, the error specified is one half of the 68% probability width for a given parameter after marginalizing over other parameters as described in the text. Where α_c is unspecified, both the clustered and Poisson DSFG components share an identical spectral index given by α_p. The majority of the chains use a fixed kSZ spectrum; in these cases, the kSZ value appears in brackets. In addition to the model parameters described in Section 6.6, we include two derived parameters, $D_{3000}^{P,220}$ and $D_{3000}^{C,220}$, which are the amplitude of the Poisson and clustered DSFG component in the SPT 220 GHz band, respectively. We also summarize the free parameters, templates, and relative goodness of fit for each case.

The additional parameters of the model discussed in Section 6.6 are all fixed or constrained by priors. The kSZ power is fixed to the $D_{3000}^{\mathrm{kSZ}} = 2.05 \, \mu\mathrm{K}^2$ expected for the homogeneous reionization model of Sehgal et al. (2010). Radio galaxies are included with a fixed spectral index $\alpha_r = -0.53$ and zero intrinsic scatter and an amplitude $D_{3000}^{r} = 1.28 \, \mu\mathrm{K}^2$ with a 15% uncertainty. Here, and throughout this work, we also include a constant Galactic cirrus power as described in Section 6.6.3. In addition to astrophysical model components, for each band we include a term to adjust the overall temperature calibration and three terms to parametrize the uncertainty in the measurement of the beam function. This baseline model provides the most concise interpretation of the data. As will be demonstrated in subsequent sections, relaxing priors on the fixed or tightly constrained parameters in this model has minimal impact on the measured tSZ power.

Table 6.3 $\Delta\chi^2$ with the addition of model components

Variable	dof	$-2\Delta\ln\mathcal{L}$
point sources (Poisson)	2	-7821
point sources (including clustering)	1	-104
tSZ	1	-25
kSZ	0	-1

Note. — The addition of DSFG and SZ terms in the model significantly improves the quality of the maximum likelihood fit. From top to bottom, the improvement in the fit χ^2 as each term is added to a model including the primary CMB anisotropy and all the terms above it, e.g., the tSZ row shows the improvement from adding the tSZ effect with a free amplitude to a model including the CMB, and point source power, including the contribution from clustering of the DSFGs. The second column (dof), lists the number of degrees of freedom in each component. The free Poisson point source parameters are the amplitude and spectral index of the DSFGs. Note that the third Poisson component (the radio power) is constrained by an external prior rather than the data and we have marginalized over the allowed radio power. The free clustered point source parameter is the amplitude of the power-law clustered template. The spectral index of the DSFG clustering term is fixed to that of the Poisson term. The last two rows mark the addition of the S10 tSZ template with a free amplitude, and the addition of the S10 homogeneous kSZ template with a fixed amplitude. We do not find a significant improvement in the likelihood with any extension to this model, including allowing the kSZ amplitude to vary, or allowing independent spectral indices for the two DSFG components.

Parameter constraints from this baseline model are listed in Table 6.2 and Figure 6.7. For the tSZ power, we find $D_{3000}^{tSZ} = 3.5 \pm 1.0 \, \mu\mathrm{K}^2$, which is consistent with previous measurements (L10, Dunkley et al. (2011)) and significantly lower than predicted by the S10 model. We detect both the Poisson and clustered DSFG power with high significance, with amplitudes of $D_{3000}^{p} = 7.4 \pm 0.6 \, \mu\mathrm{K}^2$ and $D_{3000}^{c} = 6.1 \pm 0.8 \, \mu\mathrm{K}^2$ respectively. The shared spectral index of these components is found to be $\alpha = 3.58 \pm 0.09$, in line with both theoretical

expectations and previous work (H10, Dunkley et al. (2011)). The amplitude of the Poisson term is significantly lower than what was measured in H10; however, as we show in the following sections, this discrepancy is eliminated by adopting the linear-theory clustered DSFG template used in that work.

We explore the effect of altering this baseline model by replacing the tSZ template with the three alternatives discussed in Section 6.6.2: the Shaw, Trac, and Battaglia models. As anticipated, we find no significant difference between the models for any of the measured parameters. The resulting tSZ powers are listed in Table 6.6; they are statistically identical. The other model parameters also vary by less than 1% for all four tSZ model templates.
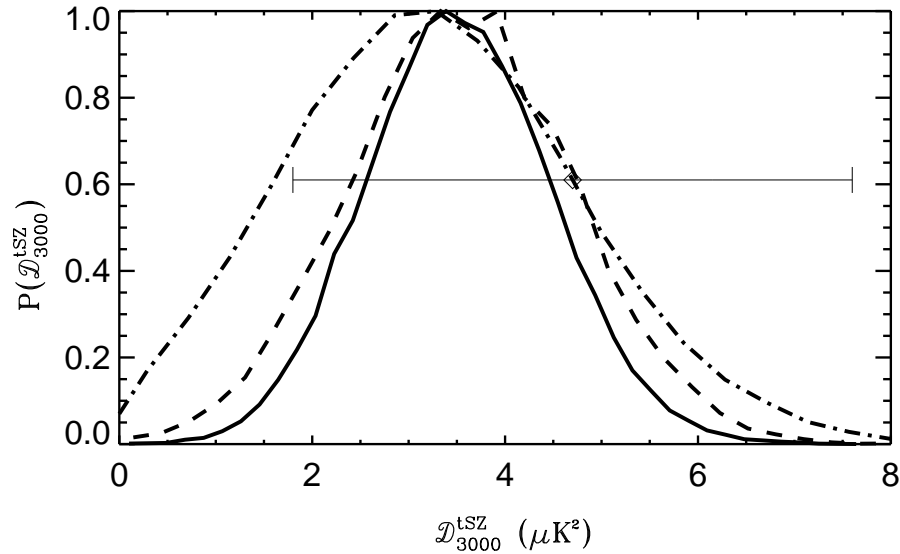

Figure 6.6 The **solid black bline** shows the 1D likelihood surface for D^{tSZ}_{3000} from the multi-frequency analysis presented in Section 6.7.1 . The baseline model with the S10 homogeneous kSZ template has been assumed. Also plotted are the equivalent results from L10 (**dot-dash line**) and the DSFG-subtracted analysis in Section 6.7.5 of this work (**dashed line**). In addition, the median value and 68% confidence region for the tSZ amplitude from Dunkley et al. (2011) is shown by the **diamond and thin horizontal line**.

6.7.2 kSZ variants

The baseline kSZ model is the homogeneous reionization model presented in S10. In this section, two alternative kSZ cases are considered. First, for the same set of model parameters, we change the (fixed) kSZ power spectrum from the baseline homogeneous reionization model to a template with additional power from patchy reionization. In the second case, we allow

the kSZ amplitude to vary in order to explore the tSZ-kSZ degeneracy and to set upper limits on the SZ terms.

We explore the effect of replacing the homogeneous kSZ template with the patchy kSZ template described in Section 6.6.2. The patchy kSZ model increases the power at $\ell = 3000$ by 50% to $D_{3000}^{kSZ} = 3.25 \, \mu\text{K}^2$, and has a slightly modified angular scale dependence with additional large-scale power. The likelihood of the best-fit model is nearly unchanged from the homogeneous kSZ case. The increase in kSZ power by $1.2 \, \mu\text{K}^2$ leads to a decrease in tSZ power by $0.6 \, \mu\text{K}^2$, as one would expect given the near-degeneracy along the tSZ + 0.5 kSZ axis which we discuss below. The kSZ spectrum shape difference has no impact on the results.

As an alternative to the fixed kSZ models discussed above, we also allow the kSZ amplitude to vary, adding one additional parameter to MCMC chains. With two frequencies, the current SPT data does not allow the separation of the tSZ, kSZ, and clustered point source components. The chains show a strong degeneracy between the components, as shown in Figure 6.8. The best-constrained eigenvector in the kSZ/tSZ plane is approximately tSZ + 0.5 kSZ, very similar to the proportionality used in the differenced bandpowers in Section 6.7.5. For this linear combination, we find $D_{3000}^{tSZ} + 0.5 \, D_{3000}^{kSZ} = 4.5 \pm 1.0 \, \mu\text{K}^2$. We note that the data show some preference for a positive tSZ power, at just under 2σ. We tested whether this preference is due to the detailed shapes of the two templates by swapping the tSZ and kSZ templates. This model swap had no significant impact on the 2d likelihood surface, indicating that the preference for positive tSZ power is driven by the unique frequency signature of the tSZ. When marginalizing over the tSZ amplitude and other parameters, we find the upper limit on the kSZ power to be $D_{3000}^{kSZ} < 6.5 \, \mu\text{K}^2$ at 95% confidence. The corresponding upper limit on tSZ power is $D_{3000}^{tSZ} < 5.3 \, \mu\text{K}^2$ at 95% confidence.

6.7.3 Clustered DSFG extensions to the baseline model

The baseline model contains DSFG sources that generate both Poisson and clustering contributions to the power spectrum. The spectral index of the Poisson power and clustering power is fixed to be the same. In this section, we examine two changes to this baseline model. First, we allow the clustered DSFG spectral index to vary independently, and second, we change the clustered template from a power-law to linear-theory model. We explore all four permutations of these two Boolean cases (one of the four is the baseline case). One dimensional likelihood curves for each case are shown in Figure 6.9 and discussed below. We also consider a mixture of the power-law and linear-theory templates, each with its own variable amplitude, again for a total of five free parameters. As we will discuss in Section 6.7.3, the SPT data slightly prefer the power-law template.
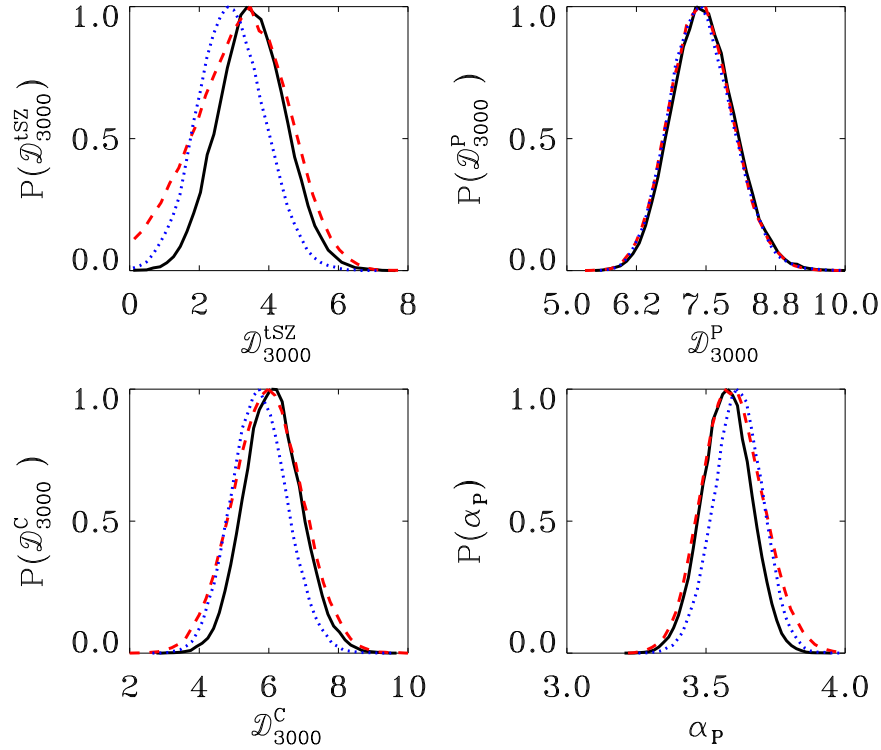
Figure 6.7 1D likelihood plots for model parameters for three different kSZ treatments. The **black, solid line** is the baseline (fixed amplitude, S10 homogeneous model) kSZ model. The **blue dotted line** is the patchy kSZ model with fixed amplitude. The **red, dashed line** is the model where the amplitude of the (default) kSZ template is free to vary. All powers are measured at $\ell = 3000$ and 150 GHz. The *top left panel* shows constraints on the tSZ power spectrum. The preferred tSZ power drops as the assumed kSZ power increases; this trade-off can be seen in more detail in Figure 6.8. The *top right panel* shows the likelihood curves for the Poisson DSFG power, and the *bottom left panel* shows the same for the clustered DSFG power. The *bottom right panel* shows the Poisson DSFG spectral index. There is a slight decrease in clustered DSFG power with the increased kSZ power expected from patchy reionization; this is accompanied by small shift to higher spectral indices, preserving the higher-frequency bandpowers.

Free α_c

As discussed in Section 6.6.3, the Poisson and clustered DSFG amplitudes are sensitive to different weightings of the DSFGs with redshift and brightness and thus we expect these components to have slightly offset spectral indices. For instance, the Righi et al. (2008) model predicts $\alpha_p - \alpha_c = 0.2$. To study this offset, we allow the two spectral indices to vary independently. The resulting spectral indices for the clustered and Poisson DSFG terms separate by approximately one σ; however, this shift is in the opposite direction
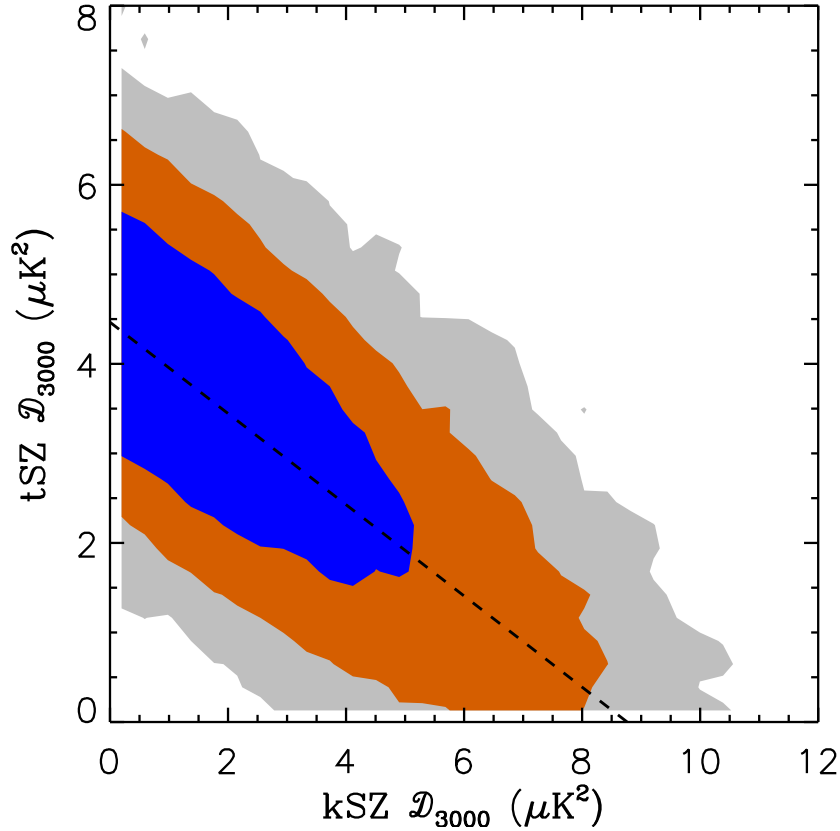
Figure 6.8 2D likelihood contours for D_{3000}^{tSZ} vs. D_{3000}^{kSZ}. The 68%, 95% and 99.7% contours are marked with blue, orange, and gray respectively. Both tSZ and kSZ model templates are from S10. As in the differenced spectrum analysis, the data primarily constrain a linear combination $D_{3000}^{tSZ} + 0.5 D_{3000}^{kSZ} = 4.5 \pm 1.0 \, \mu\mathrm{K}^2$. The dashed line shows this axis of near degeneracy. Due to this degeneracy, neither parameter is significantly detected above zero. However, 95% CL upper limits of 5.3 and $6.5 \, \mu\mathrm{K}^2$ can be placed on the tSZ and kSZ respectively.

from what the Righi et al. (2008) model predicts. With the addition of this additional free parameter, the uncertainty on the Poisson and clustered amplitudes and spectral indices increase significantly. At 220 GHz, both DSFG powers are essentially unchanged, while the 150 GHz Poisson and clustered amplitudes slightly increase and decrease, respectively.

Linear-theory model

We adopt the H10 model as the linear-theory clustered DSFG model. The angular scale dependence of this model is very similar to the tSZ template and nearly flat in D_ℓ. Swapping between the power-law and linear-theory models does not change the measured tSZ power.
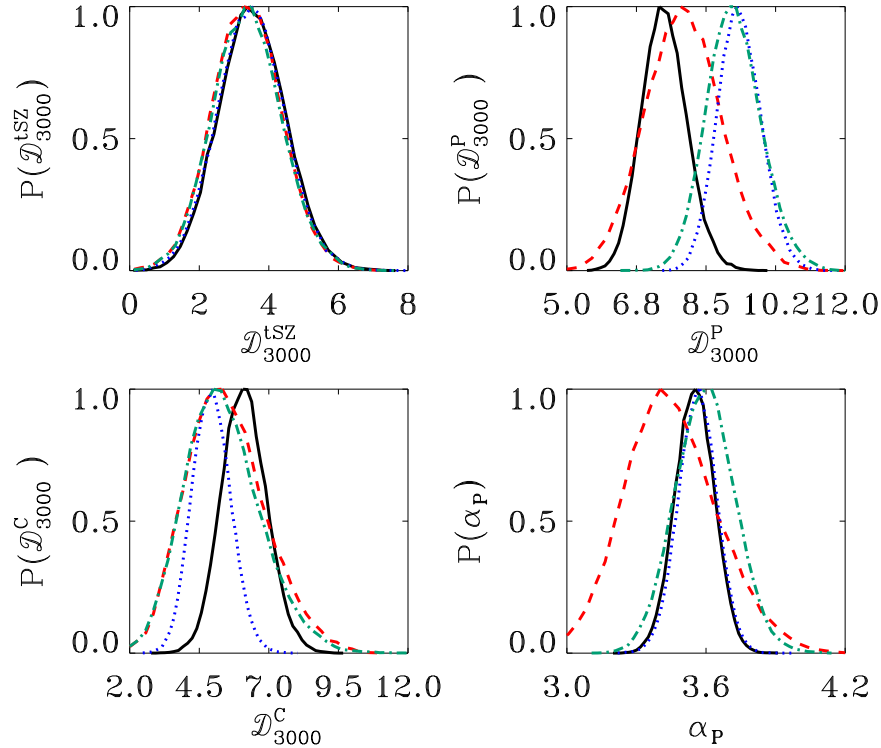
Figure 6.9 1D likelihood plots of model parameters for different DSFG clustering treatments. Clockwise from top left: the 1D likelihood curves for the amplitudes of the tSZ effect, Poisson DSFG amplitude, Poisson DSFG spectral index and clustered DSFG amplitude. Four cases are plotted for each parameter: The **black solid line** indicates the baseline model, where $\alpha_c = \alpha_p$ and the power-law clustered template is used. The **red dashed line** indicates the case where α_c is a free parameter and the power-law clustered template is used. The **blue dotted line** indicates the case where $\alpha_c = \alpha_p$ and the linear-theory clustered template is used. The **blue-green dot-dash line** indicates the case where α_c and α_p are independent and the linear-theory clustered template is used. Using the power-law clustered template tends to reduce the power in the Poisson component compared to the linear-theory template. This is expected as the power-law shape has more power at high-ℓ than the linear-theory template and the Poisson component also increases with ℓ ($D_\ell \propto \ell^2$). Including an additional free parameter (α_c) tends to increase the uncertainty on DSFG-related parameters but not on tSZ.

However, it does shift some power between the Poisson and clustered DSFG terms. The angular scale dependence of the power-law model is intermediate between the linear-theory model and Poisson terms. As a result, the flatter, linear-theory model leads to more Poisson and less clustered power. At $\ell = 3000$ and $150\,\mathrm{GHz}$, the Poisson DSFG power increases by $3\,\sigma$ to $D_{3000}^p = 9.3 \pm 0.5\,\mu\mathrm{K}^2$ from $7.4 \pm 0.6\,\mu\mathrm{K}^2$. The clustered DSFG power decreases

correspondingly by $1\,\sigma$ to $D^c_{3000} = 4.9 \pm 0.7\,\mu\mathrm{K}^2$. Note that the DSFG spectral index has dropped compared to what was measured in H10 from 3.86 ± 0.23 to $\alpha_p = 3.59 \pm 0.09$. The change in spectral index is driven by the $220\,\mathrm{GHz}$ power: the Poisson power is $2\,\sigma$ lower and the clustered power is $1\,\sigma$ lower than what was measured in H10.

Free α_c & linear-theory model

Finally, we consider the case where we allow α_c as a free parameter with the linear-theory clustered DSFG template. The resulting chains include features from both the free-α_c and linear-theory cases: the Poisson power increases and tSZ power decreases, while uncertainties on the clustered amplitude and all spectral indices increase. The spectral indices of the clustered and Poisson DSFG terms do not separate as much as they do in the power-law, free-α_c chain.

Discriminating between the power-law and linear-theory models

In principle, the likelihood of a fit to the data can be used to distinguish between the power-law and linear-theory clustered DSFG templates described above. We explore this in two ways. First we consider the improvement in the best-fit log-likelihood between the models which use each template. The power-law model produces a marginally better fit to the data, with $\Delta\ln\mathcal{L} = -2$ when compared to the linear-theory model.

In addition to the choice of one template or the other, we extend the baseline model to include a second DSFG clustering component. The two DSFG clustered amplitudes, corresponding to the power-law and the linear-theory templates, are allowed to vary independently. The spectral index for all three (Poisson and two clustered) DSFG components are tied. The two-dimensional likelihood surface for the amplitudes of each template is shown in Figure 6.10. The data show a slight preference for the power-law template over the linear-theory template; however, we can not rule out the linear-theory model or a linear combination of the two with any confidence. We can expect this constraint on DSFG clustering shape to improve with future data.

6.7.4   tSZ-DSFG correlation

As discussed in Section 6.6.3, there are reasons to expect that the signal from the tSZ and the clustered DSFGs may be correlated. In order to study that correlation, we extend the model to include the correlation coefficient of these components, $\gamma(\ell)$, detailed in Section 6.6.3. We assume the correlation coefficient is constant in ℓ, thus reducing $\gamma(\ell)$ to γ. We would expect an anticorrelation at frequencies below the SZ null; however, we do not require that the correlation coefficient is negative. Instead, we set a flat prior on the correlation γ, and allow it to range from -1 to 1.
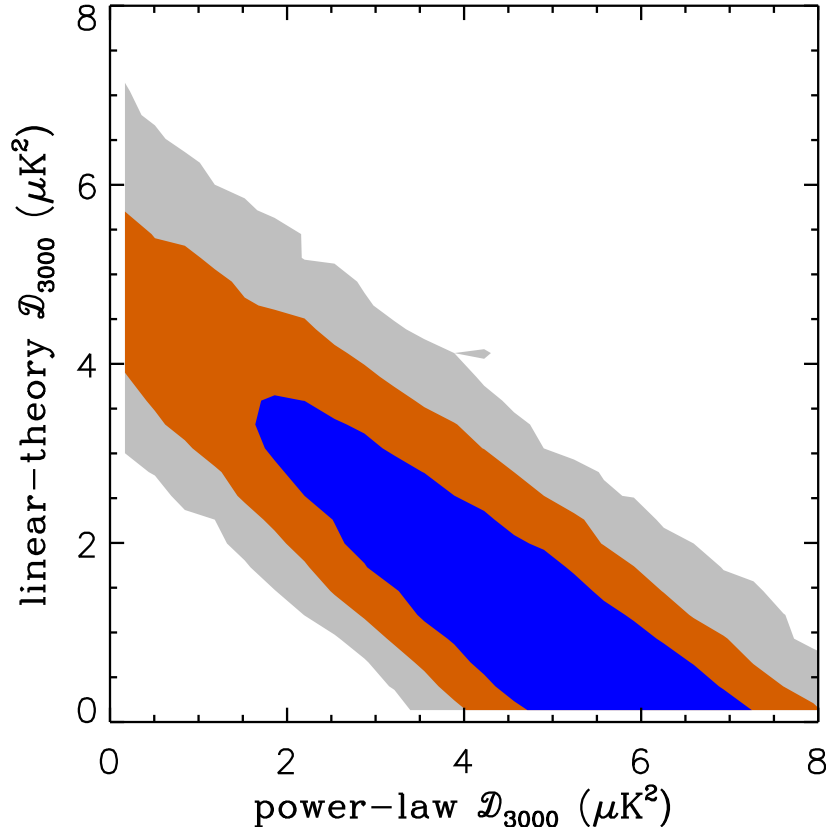
Figure 6.10 68% (**blue**), 95% (**orange**) and 99.7% (**grey**) likelihood contours for the amplitudes of clustered DSFG components for a model containing both power-law and linear-theory components with independently variable amplitudes. The power-law model is favored at the 1σ level; the data do not clearly discriminate between the power-law shape, linear-theory shape, or a linear combination of the two. The choice of clustered DSFG model has no impact on the tSZ power and we adopt the power-law template as the baseline model.

We consider the impact of introducing correlations between the tSZ and DSFGs on two chains – both allow the correlation factor to vary and one also allows the kSZ amplitude to vary. In both chains, we assume the linear-theory clustered DSFG template, because its shape is similar to the S10 tSZ template.

The results for this model without the possibility of a tSZ-DSFG correlation have been presented in Section 6.7.3. The marginalized 1d likelihood function for the tSZ-DSFG correlation factor is shown in Figure 6.11. In the fixed kSZ case, the data are consistent with zero correlation: $\gamma = 0.0\pm0.2$. When the kSZ power is allowed to vary, the data remain consistent with zero correlation, however, large anti-correlations are also possible. The 95% CL upper limit on D_{3000}^{tSZ} allowing for a tSZ-DSFG correlation is unchanged from the equivalent chain

with the correlation coefficient set to zero; marginalizing over a non-zero tSZ-DSFG correlation factor does not allow additional tSZ power. As Figure 6.12 shows, this is because kSZ power increases for larger negative correlation in order to preserve the observed power in the 150×220 bandpowers. Naively, one might expect the best fit tSZ power to increase when the possibility of a tSZ canceling correlation is taken into account; however, in practice, a negative correlation leads to less tSZ power in the best fit model. The anti-correlation reduces the predicted power in the 150×220 spectrum, and kSZ power is increased to compensate. The sum of kSZ and tSZ is well constrained by the data, so more kSZ power leads to less tSZ power. When marginalizing over the tSZ-DSFG correlation, the 95% CL on tSZ decreases slightly to $D_{3000}^{tSZ} < 4.5 \,\mu\mathrm{K}^2$, while the kSZ upper limit increases to $D_{3000}^{kSZ} < 9.7 \,\mu\mathrm{K}^2$. From this, as well as the agreement between the multi-frequency fits and the DSFG-subtracted result presented in Section 6.7.5, we conclude that the addition of a tSZ-DSFG correlation cannot explain the discrepancy between the observed tSZ power and models that predict a significantly larger tSZ contribution.

These results depend on the Poisson and clustered DSFG terms having similar spectral indices. We expect the upper limits to be substantially weakened if the two spectral indices are allowed to separate, but note that the required spectral index separation would need to be much larger than the $\alpha_p - \alpha_c \sim 0.2$ difference expected from models (H10).

6.7.5 Comparing differenced spectra results to multi-frequency fits

The main result of this work is the set of multi-frequency bandpowers. However, we also follow the treatment in L10 and consider a linear combination of the two frequency maps designed to eliminate the foreground contribution from DSFGs. Specifically, this is the power spectrum of the map m constructed from the 150 and 220 GHz maps (m_{150} and m_{220} respectively) according to

$$m = \frac{1}{1-x}(m_{150} - x\, m_{220}). \tag{6.18}$$

In L10, the subtraction coefficient x was selected by minimizing the Poisson point source power in the resultant bandpowers. We repeat this analysis for the new bandpowers and find $x = 0.312 \pm 0.06$. This is consistent with the value of $x = 0.325 \pm 0.08$ reported in L10. For complete details on the analysis, we refer the reader to that work. Given the consistency of these results, we have chosen to use $x = 0.325$ to create the 'DSFG-subtracted' bandpowers presented in Table 6.4 to enable the direct comparison of the two data sets. These two subtraction coefficients correspond to a spectral index for the DSFG population of $\alpha_p = 3.7$ and 3.6 respectively, consistent with the $\alpha_p = 3.57 \pm 0.09$ determined in multi-frequency fits. We compare the L10 bandpowers with those presented in this work in Figure 6.13, and find excellent agreement between them. Note that the two data sets are not independent since L10 analyzed one of the two fields used in this work.
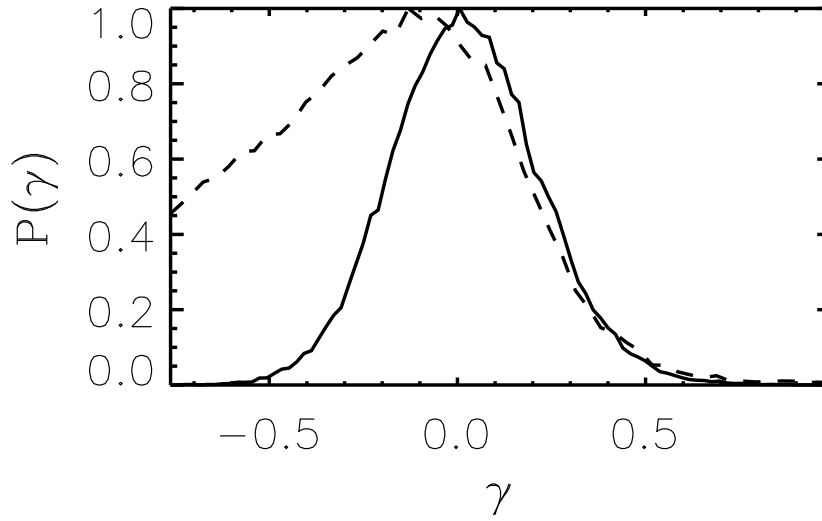
Figure 6.11 The 1D likelihood curve for the tSZ-DSFG correlation factor, γ. The linear-theory clustered DSFG template and the S10 tSZ template are assumed. The **solid line** indicates the case where the kSZ amplitude is held fixed. The data favor no correlation albeit with significant uncertainty. The **dashed line** denotes the likelihood curve when the kSZ amplitude is allowed to vary. The data remain consistent with zero correlation, but large negative correlations become possible. Essentially, the kSZ power increases to balance the lower predicted power due to anti-correlation. Because the tSZ and kSZ amplitudes are highly correlated, additional kSZ power reduces the apparent tSZ power.
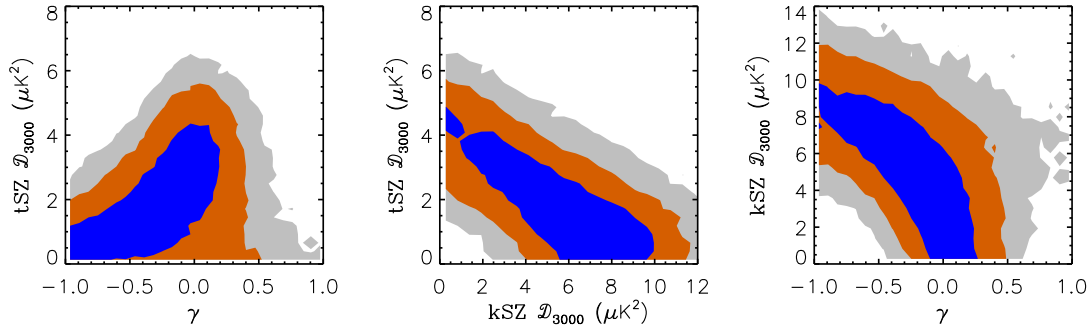

Figure 6.12 2D likelihood contours for tSZ-DSFG correlation chains in which kSZ is allowed to vary. The 68%, 95% and 99.7% likelihood contours are marked with blue, orange and gray respectively. From left to right: tSZ power vs. correlation coefficient γ; tSZ power vs. kSZ power, marginalized over γ (and foreground terms); and kSZ power vs. γ.
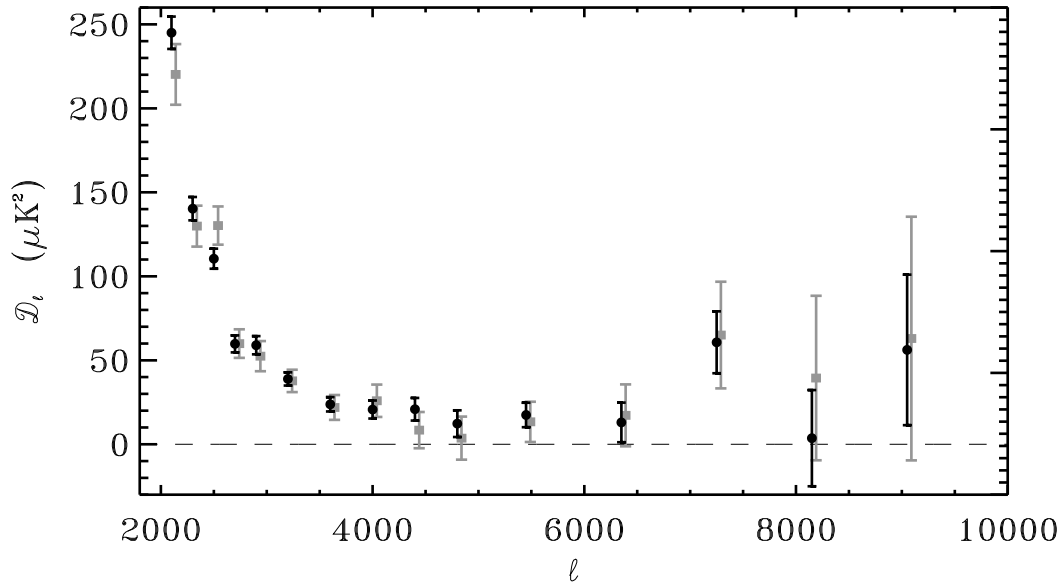
Figure 6.13 The SPT DSFG-subtracted bandpowers from this work (**black circles**) versus the DSFG-subtracted bandpowers presented in L10 (**gray squares**), an earlier reduction of one half of the 2008 data. The damping tail of the primary CMB anisotropy is apparent below $\ell = 3000$. Above $\ell = 3000$, there is a clear excess due to secondary anisotropies and residual point sources. The two datasets show excellent consistency.

This 'DSFG-subtracted' power spectrum is interesting for two reasons. First, it allows a direct comparison with the results of L10. Second, in the DSFG-subtracted bandpowers, the residual correlated DSFG power will only be significant if the frequency spectrum of DSFGs in galaxy clusters is substantially different than the spectrum of DSFGs in the field. Therefore, parameter fits to DSFG-subtracted bandpowers are independent of the assumed DSFG power spectrum shape or tSZ-DSFG correlation, and are a potentially interesting cross-check on the multi-frequency fits. However, in practice, it is worth noting that these fits constrain a similar linear combination of tSZ and kSZ, roughly given by tSZ + 0.5 kSZ. Both methods therefore result in a similarly robust detection of tSZ power independent of tSZ-DSFG correlation.

For this DSFG-subtracted case, we simplify the baseline model to include only one free parameter beyond ΛCDM: the tSZ power spectrum amplitude. We also include a Poisson point source term with a strict prior, and a fixed kSZ power spectrum. The S10 model is used for both kSZ and tSZ. The Poisson prior is identical to the point source prior described in L10 with one exception: the radio source amplitude prior has been tightened to match the 15% prior used in this work instead of the 50% log-normal prior used in L10. However,

Table 6.4 DSFG-subtracted bandpowers

ℓ range	ℓ_{eff}	$\hat{D}$ (μK^2)	σ (μK^2)
2001 - 2200	2056	245.0	9.6
2201 - 2400	2273	140.3	6.9
2401 - 2600	2471	110.5	6.0
2601 - 2800	2674	59.8	5.1
2801 - 3000	2892	59.0	5.4
3001 - 3400	3185	38.9	3.9
3401 - 3800	3581	23.8	4.3
3801 - 4200	3994	20.7	5.4
4201 - 4600	4402	20.9	6.7
4601 - 5000	4789	12.3	7.9
5001 - 5900	5449	17.4	7.3
5901 - 6800	6360	13.0	11.8
6801 - 7700	7257	60.7	18.4
7701 - 8600	8161	3.6	28.6
8601 - 9500	9063	56.2	44.8

Note. — Band multipole range and weighted value ℓ_{eff}, bandpower $\hat{D}$, and uncertainty σ for the DSFG-subtracted auto-spectrum of the SPT fields. This is the power spectrum of a linear combination of the 150 and 220 GHz maps ($(m_{150} - 0.325\,m_{220})/(1 - 0.325)$) designed to suppress the DSFG contribution. The quoted uncertainties include instrumental noise and the Gaussian sample variance of the primary CMB and the point source foregrounds. The sample variance of the SZ effect, beam uncertainty, and calibration uncertainty are not included. Beam uncertainties are shown in Figure 6.1 and calibration uncertainties are quoted in Section 6.2.2. Point sources above 6.4 mJy at 150 GHz have been masked out in this analysis, eliminating the majority of radio source power.

tests with relaxed priors show the results are insensitive to this radio uncertainty. Except for this small change in the radio prior, and the switch to WMAP7 data, these differenced spectrum fits are identical to the parameter fitting used in L10.

As shown in Figure 6.6, the resulting DSFG-subtracted tSZ amplitude agrees with both the L10 value and the multi-frequency result presented here. We measure the tSZ power at 150 GHz to be $D_{3000}^{tSZ} = 3.5 \pm 1.2\,\mu K^2$, with a fixed (S10 homogeneous) kSZ component. For the same template choices, L10 report $D_{3000}^{tSZ} = 3.2 \pm 1.6\,\mu K^2$, and the multi-frequency fit to the baseline model finds $D_{3000}^{tSZ} = 3.5 \pm 1.0\,\mu K^2$. This close agreement demonstrates the consistency of the two methods of parameter fitting, and confirms the results presented in L10.
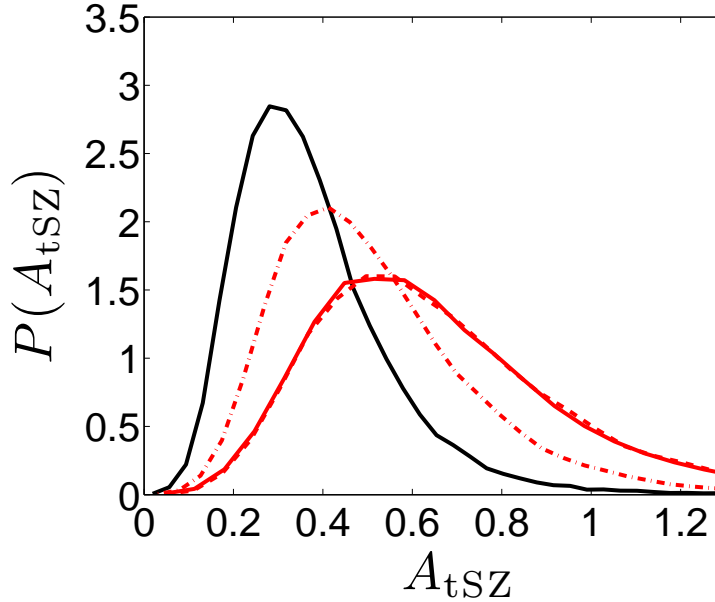
6.8   Consequences of the measured tSZ Signal

Figure 6.14 Posterior distribution of the tSZ scaling parameter A_{tSZ} (see Equation 6.19 and Table 6.6) for each of the tSZ templates. The **black line** shows the S10 prediction. The **red solid, dashed and dot-dashed lines** show the results for the Shaw, Trac, and Battaglia models, respectively. As expected, the preferred value of A_{tSZ} increases for models which predict less tSZ power. Note that a value of $A_{\text{tSZ}} = 1$ would demonstrate consistency between the predicted and observed tSZ power.

We now focus on comparing the improved measurements of the tSZ power spectrum with the predictions of recent models and simulations. We then combine measurements of the primary CMB power spectrum with the tSZ signal to obtain joint constraints on σ_8.

6.8.1   Thermal SZ amplitude

L10 found the measured amplitude of the tSZ power spectrum to be a factor of 0.42 ± 0.21 lower than that predicted by the simulations of S10 (at their fiducial cosmology). In this analysis, having doubled the survey area to 210 deg^2, we find that the amplitude of the tSZ power spectrum at $\ell = 3000$ is $D_{3000}^{tSZ} = 3.5 \pm 1.0\,\mu\text{K}^2$ at 150 GHz. This is 0.47 ± 0.13 times the S10 template.

The discrepancy suggests that either the S10 model overestimates the tSZ power, or the assumed set of cosmological parameters may be wrong. To calculate the tSZ power spectrum,

S10 combined a semi-analytic model for intra-group and cluster gas with a cosmological N-body lightcone simulation charting the matter distribution out to high redshift. The gas model assumed by S10 was calibrated by comparing it with X-ray observations of low-redshift ($z < 0.2$) clusters. However, the majority of tSZ power is contributed by groups or clusters at higher redshift (Komatsu & Seljak, 2002; Trac et al., 2011). Hence, the S10 model may substantially overpredict the contribution from higher redshift structures. Note that in Section 6.7.4, we demonstrated that the lower-than-predicted tSZ power is unlikely to be due to a spatial correlation between DSFGs and the groups and clusters that dominate the tSZ signal.

As described in Section 6.6.2, in addition to the S10 template we investigate results obtained using the templates suggested by Trac et al. (2011), Shaw et al. (2010) and Battaglia et al. (2010) (the Trac, Shaw, and Battaglia models). These three alternative models all predict substantially less power at $\ell = 3000$ than the S10 template (assuming the same cosmological parameters). For each template we run a new chain substituting the S10 template with one of the three others. The rest of the baseline model remains as described in Section 6.6.

Alternatively, the amplitude of the tSZ power spectrum is extremely sensitive to σ_8, scaling approximately as $D_\ell^{tSZ} \propto \sigma_8^{7-9}(\Omega_b h)^2$. The exact dependence on σ_8 depends on the relative contribution of groups and clusters as a function of mass and redshift to the power spectrum, and thus the astrophysics of the intra-cluster medium (Komatsu & Seljak, 2002; Shaw et al., 2010; Trac et al., 2011). All four of the templates that we consider in this work were determined assuming $\sigma_8 = 0.8$. The deficit of tSZ power measured in the SPT maps may therefore indicate a lower value of σ_8.

To correctly compare the measured tSZ power spectrum amplitude with theoretical predictions, we must rescale the template power spectra so that they are consistent with the cosmological parameters at each point in the chains. Recall that the cosmological parameters are derived solely from the joint WMAP7+QUaD+ACBAR+SPT constraints on the primary CMB power spectrum and so are not directly influenced by the amplitude of the measured tSZ power.

We define a dimensionless tSZ scaling parameter, A_{tSZ}, where

$$A_{\text{tSZ}}(\kappa_i) = \frac{D_{3000}^{tSZ}}{\Phi_{3000}^{tSZ}(\kappa_i)} \ . \tag{6.19}$$

D_{3000}^{tSZ} is the measured tSZ power at $\ell = 3000$ and $\Phi_{3000}^{tSZ}(\kappa_i)$ is the template power spectrum normalized to be consistent with the set of cosmological parameters 'κ_i' at step i in the chain. We obtain the preferred value of A_{tSZ} by combining the measurement of D_{3000}^{tSZ} with the cosmological parameter constraints provided by the primary CMB measurements.

To determine the cosmological scaling of each of the templates, we adopt the analytic model described in Shaw et al. (2010). This model uses the halo mass function of Tinker et al. (2008) to calculate the abundance of dark matter halos as a function of mass and

redshift, combined with an analytic prescription (similar to that of Bode et al., 2009) to determine the SZ signal from groups and clusters. Shaw et al. (2010) demonstrated that when the same assumptions are made about the stellar mass content and feedback processes in groups and clusters, their model almost exactly reproduces the S10 template. For the Trac and Battaglia models, we modify the astrophysical parameters of the Shaw model so that it agrees with the other models at their fiducial cosmology. Varying the input cosmological parameters thus allows us to estimate the cosmological scaling of the tSZ power spectrum for any given model.

As an indication of the relative cosmological scaling of each model at $\ell = 3000$, in Table 6.5 we give the dependence of Φ_{tSZ} on σ_8, Ω_b, and h around their fiducial values. We assume that the cosmological scaling takes the form,

$$\Phi_{3000}^{tSZ} \propto \left(\frac{\sigma_8}{0.8}\right)^{\alpha} \left(\frac{\Omega_b}{0.044}\right)^{\beta} \left(\frac{h}{0.71}\right)^{\gamma} . \tag{6.20}$$

Note that the values of α given in Table 6.5 for the S10 and Trac models agree well with those given in Trac et al. (2011). We find the templates depend only weakly on other cosmological parameters at this angular scale.

Table 6.5 tSZ Cosmological Scaling

model	α	β	γ
Sehgal	8.09	2.50	1.89
Shaw	8.34	2.81	1.73
Trac	8.34	2.90	1.81
Battaglia	8.33	2.85	1.71

Note. — α, β, and γ describe the cosmological scaling of the tSZ power spectrum for each template, as defined in Equation 6.20.

Figure 6.14 shows the posterior probability of A_{tSZ} obtained for the S10, Shaw, Trac, and Battaglia templates. The results are also given in Table 6.6. Recall that a value of $A_{tSZ} = 1$ would demonstrate that the model is consistent with the measured tSZ power, while A_{tSZ} less (greater) than 1 indicates that the model over- (under-) estimates the tSZ power spectrum amplitude. All four models display a non-Gaussian distribution with tails extending to higher values of A_{tSZ}. Therefore, in Table 6.6, we give both symmetric 68% confidence limits for both A_{tSZ} and $\ln(A_{tSZ})$ as well as the asymmetric 95% confidence limits (in brackets) for A_{tSZ}.

For the S10 template, the preferred value is $A_{tSZ} = 0.33 \pm 0.15$. The measured level of tSZ power is thus significantly less than that predicted by the S10 template. When the kSZ

amplitude is also allowed to vary, we find a slight decrease in A_{tSZ} to 0.30 ± 0.16. Note that the constraint on σ_8 obtained from the primary CMB power spectrum is 0.821 ± 0.025, which is greater than the fiducial value of 0.8 assumed by all the templates.[8] The values of A_{tSZ} are therefore less than what we would have obtained had we fixed the templates at their fiducial amplitudes.

We find that the discrepancy remains, but is reduced, for the Shaw, Trac, and Battaglia models. The Trac and Shaw templates provide the best match to the measured amplitude with $A_{\mathrm{tSZ}} = 0.59 \pm 0.25$. It is interesting to note that the total amount of tSZ power measured (D_{3000}^{tSZ} in Table 6.6) is essentially independent of the template used. This demonstrates that the differences in the *shapes* of the templates do not influence the results.

The templates that are most consistent with the observed SPT power at $\ell = 3000$ (when combined with cosmological constraints derived from the primary CMB power spectrum) are those that predict the lowest tSZ signal. The S10, Trac, and Shaw models adopt a similar approach for predicting the tSZ power spectrum. Each assumes that intra-cluster gas resides in hydrostatic equilibrium in the host dark matter halo, and include simple prescriptions to account for star formation and AGN feedback. The Trac and Shaw models – which both predict significantly less tSZ power – differ from the S10 model in two principal ways. First, following the observational constraints of Giodini et al. (2009), they assume a greater stellar mass fraction in groups and clusters. This reduces the gas density and thus the magnitude of the SZ signal from these structures. Second, the Trac and Shaw models include a significant non-thermal contribution to the total gas pressure. Hydrodynamical simulations consistently observe significant levels of nonthermal pressure in the intra-cluster medium due to bulk gas motions and turbulence (Evrard, 1990; Rasia et al., 2004; Kay et al., 2004; Dolag et al., 2005; Lau et al., 2009). In terms of the tSZ power spectrum, including a non-thermal pressure component reduces the thermal pressure required for the ICM to be in hydrostatic equilibrium, therefore reducing the predicted tSZ signal.

The Battaglia template was produced using maps constructed from a hydrodynamical simulation that included star formation and AGN feedback. While direct comparisons with the model parameters of the other three templates are difficult, Battaglia et al. (2010) found that, in simulations in which AGN feedback was not included, the tSZ power spectrum increased by 50% at the angular scales probed by SPT. If we assume the tSZ template produced from their simulations without AGN feedback we find $A_{\mathrm{tSZ}} = 0.27 \pm 0.10$ and thus a significant increase in the discrepency between the observed and predicted tSZ power. Battaglia et al. (2010) demonstrate that the inclusion of AGN feedback reduces the thermal gas pressure in the central regions of clusters by inhibiting the inflow of gas. This results in flatter radial gas pressure profiles and a suppression of tSZ power on angular scales $\ell > 2000$.

---

[8]We note that, following the upgrade to RECFAST v1.5 and in the WMAP likelihood code to v4.1, the WMAP7-alone preferred value of σ_8 is $0.811^{+0.030}_{-0.031}$ as given in Appendix B of Larson et al. (2011).

6.8.2 σ_8 **Constraints**

Table 6.6 tSZ Constraints

model	D_{3000}^{tSZ} (μK^2)	$A_{\rm tSZ}$	$\ln(A_{\rm tSZ})$	σ_8
Sehgal	3.5 ± 1.0	$0.33 \pm 0.15 \left(^{+0.40}_{-0.23}\right)$	-1.14 ± 0.45	0.771 ± 0.013
Sehgal, free kSZ	3.3 ± 1.3	$0.30 \pm 0.16 \left(^{+0.39}_{-0.30}\right)$	-1.27 ± 0.47	0.772 ± 0.013
Shaw	3.6 ± 1.0	$0.58 \pm 0.27 \left(^{+0.67}_{-0.40}\right)$	-0.54 ± 0.40	0.799 ± 0.014
Trac	3.6 ± 1.0	$0.59 \pm 0.25 \left(^{+0.72}_{-0.41}\right)$	-0.53 ± 0.45	0.802 ± 0.013
Battaglia	3.5 ± 0.9	$0.45 \pm 0.20 \left(^{+0.53}_{-0.31}\right)$	-0.79 ± 0.44	0.786 ± 0.014

Note. — Measured tSZ power and inferred σ_8 constraints for different tSZ and kSZ model assumptions. Note that the posterior distribution of $A_{\rm tSZ}$ is non-Gaussian (see Figure 6.14). To account for this we give both the 68% and asymmetric 95% (in brackets) confidence intervals. We also give the median and 68% confidence interval for $\ln(A_{\rm tSZ})$. For D_{3000}^{tSZ} and σ_8 we quote only the 68% confidence interval. The σ_8 constraints do not account for model uncertainty. All results assume the homogeneous reionization kSZ template given in S10. In the 'free kSZ' case the amplitude of this template is allowed to vary, otherwise it is held fixed at $2.05\,\mu$K^2.

To obtain joint constraints on σ_8 from both the primary CMB anisotropies and the tSZ amplitude we must determine the probability of observing the measured value of $A_{\rm tSZ}$ for a given set of cosmological parameters. In the absence of cosmic variance – and assuming the predicted tSZ template to be perfectly accurate – the constraint on σ_8 would be given by its distribution at $A_{\rm tSZ} = 1$ for each of the models. However, in practice, the expected sample variance of the tSZ signal is non-negligible. Based on the hydrodynamical simulations of Shaw et al. (2009), L10 assumed the sample variance at $\ell = 3000$ to be a lognormal distribution of mean 0 and width $\sigma_{\ln(A_{\rm tSZ})} = 0.12$. The survey area analyzed here is twice that of L10 and thus we reduce the width of this distribution by a factor of $\sqrt{2}$. For each of the four tSZ templates, we construct new chains to include this prior by importance sampling. We address the issue of theoretical uncertainty in the tSZ templates later in this section.

The black contours in Figure 6.15 show the 68% and 95% confidence limits in the $\sigma_8 - A_{\rm tSZ}$ plane for the S10 model before applying the prior on $A_{\rm tSZ}$. In this case, the constraint on σ_8 is derived entirely from the primary CMB power and is not influenced by the measured tSZ signal. The combined WMAP7+ACBAR+QUaD+SPT constraints on the primary CMB yield $\sigma_8 = 0.821 \pm 0.025$. The shapes of the contours reflect the dependence of $A_{\rm tSZ}$ on σ_8; higher values of σ_8 predict more tSZ power and require a lower tSZ scaling parameter, whereas lower values of σ_8 suggest a tSZ amplitude closer to that predicted by the S10 template.
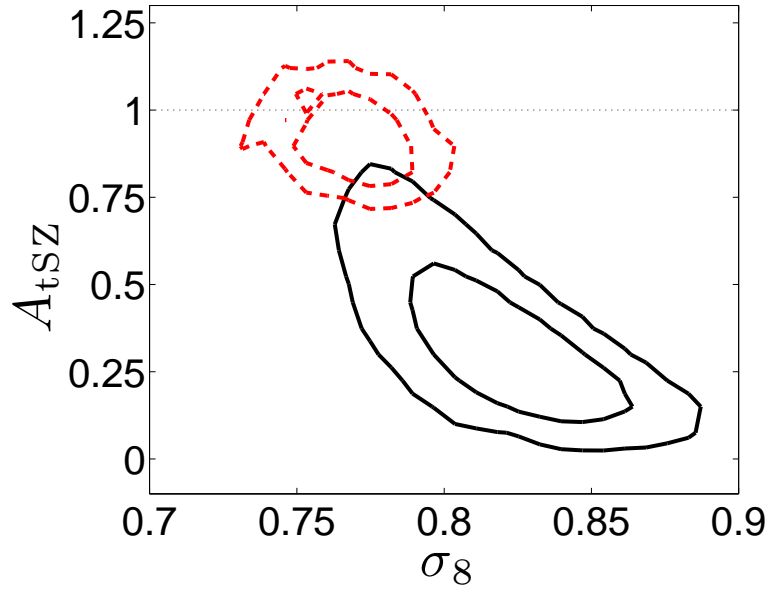
Figure 6.15 2D likelihood contours at 68% and 95% confidence for σ_8 vs. the tSZ scaling parameter A_{tSZ} (see Eqn. 6.19). **Red, dashed contours** show results having resampled the chains applying a lognormal prior to A_{tSZ} centered at $\ln(A_{\text{tSZ}}) = 0$ and of width $\sigma_{\ln(A_{\text{tSZ}})} = 0.085$. This prior is chosen to reflect the expected sample variance for the observed sky area (see text). **Black contours** show the results without this prior. All results are for the baseline model (S10 tSZ model and fixed homogeneous kSZ).

The dashed red contours in Figure 6.15 represent the joint 68% and 95% confidence limits on σ_8 and A_{tSZ} for the S10 template having resampled the chain to include the prior on A_{tSZ}. The 1D σ_8 constraints for all four templates are shown in Figure 6.16 and Table 6.6. For the S10 template the preferred value of σ_8 is 0.771 ± 0.013.[9] The Trac, Shaw, and Battaglia models all prefer higher values of σ_8. The Trac template – the most consistent with the measured tSZ amplitude – gives $\sigma_8 = 0.802 \pm 0.013$. This represents nearly a factor of two improvement in the statistical constraint on σ_8 compared to that obtained from the primary CMB alone.

It is clear from Table 6.6 that the four templates produce a spread in the preferred value of σ_8 that is larger than the statistical uncertainty on any of the individual results. This spread reflects the range in amplitude of the tSZ templates (at a fixed value of σ_8) due to the differences in the thermal pressure profiles of groups and clusters in the underlying models

---

[9]During the analysis for this work we discovered that the joint primary CMB-tSZ constraint on σ_8 in Lueker et al. (2010) erroneously assumed the S10 model was created using $\sigma_8 = 0.77$ instead of the correct value of $\sigma_8 = 0.8$. The constraints on σ_8 should therefore have been 0.767 ± 0.018 (assuming no theory uncertainty, see Section 6.4 in Lueker et al., 2010) and 0.778 ± 0.022 (assuming a 50% theory uncertainty).

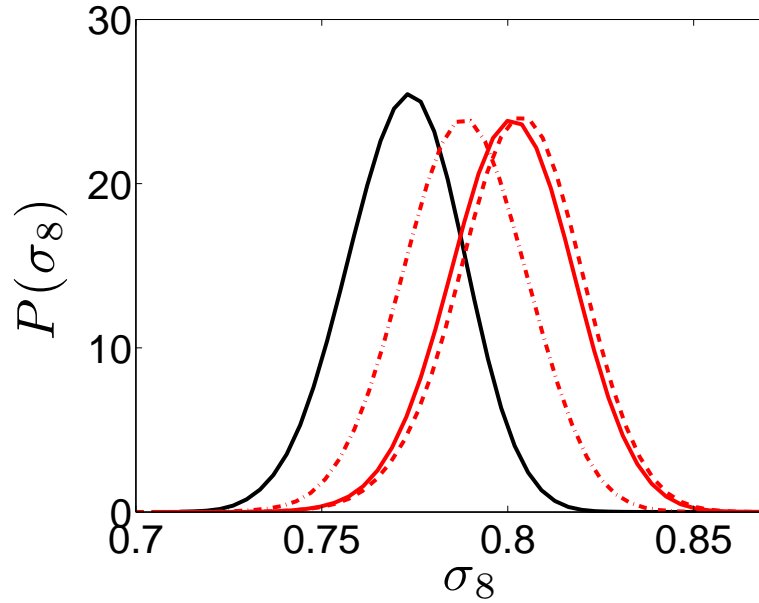Figure 6.16 σ_8 constraints for the S10 (**black line**), Shaw (**red, solid line**), Trac (**red, dashed line**) and Battaglia (**red, dot-dashed line**) models. No model uncertainty has been included.

and simulations. The dominant uncertainty on the tSZ-derived σ_8 constraint is thus the *astrophysical* uncertainty on the predicted tSZ amplitude rather than the statistical error on the measurement of D_{3000}^{tSZ}. Accounting for this uncertainty will clearly degrade the constraint on σ_8.

To produce a constraint on σ_8 that accounts for the range in amplitude of the tSZ templates we must add an additional theory uncertainty to the prior on A_{tSZ}. Assuming the Trac template – which is the most consistent with the measured tSZ signal – we find that a 50% theory uncertainty on $\ln(A_{\mathrm{tSZ}})$ is sufficient to encompass the other three templates. As the sample variance is insignificant compared to the theory uncertainty, the new prior on A_{tSZ} is effectively a lognormal distribution of width $\sigma_{\ln(A_{\mathrm{tSZ}})} = 0.5$. With this additional uncertainty, the revised constraint on σ_8 for the Trac template is 0.812 ± 0.022. The astrophysical uncertainty clearly degrades the constraint significantly – it now represents only a small reduction of the statistical uncertainty of the primary CMB-only result.

It is clear that, while the amplitude of the tSZ power spectrum is extremely sensitive to the value of σ_8, the constraints that can obtained on this parameter are limited by the accuracy with which we can predict the tSZ power spectrum amplitude for a given cosmological model. The principal difficulty in producing precise predictions is that groups and clusters spanning a wide range of mass and redshift contribute to the power spectrum at the angular scales being probed by SPT. For instance, Trac et al. (2011) find that 50% of

the power in their nonthermal20 template is due to objects at $z \geq 0.65$. Similarly, they find that 50% of the power comes from objects of mass less than $2 \times 10^{14} h^{-1} M_\odot$. To date, both these regimes have been poorly studied by targeted X-ray and SZ observations. It is therefore difficult to test current models and simulations of the tSZ power spectrum sufficiently well to produce precise predictions. X-ray and SZ observations of groups and high redshift clusters will provide constraints on models and simulations that should improve estimates of the tSZ power spectrum and thus allow tighter constraints on σ_8 from measurements of this signal (Sun et al., 2011). Alternatively, better constraints on cosmological parameters and improved measurements of the tSZ power spectrum will continue to shed new light on the relevant astrophysics in low mass and high redshift clusters.

6.9   Discussion

We have presented the CMB temperature anisotropy power spectrum from the complete $210 \deg^2$ of sky observed by SPT in the 2008 season. Bandpowers from observations at 150 and 220 GHz are shown in Table 6.1. The bandpowers correspond to angular scales, $\ell > 2000$, where secondary anisotropies and foreground contributions are significant. We also present bandpowers that have been spectrally differenced to remove the power contributed by dusty sources, following the method described in the first SPT power spectrum release (L10).

We perform multi-frequency model fits to the $\ell > 2000$ bandpowers to constrain secondary CMB anisotropies and foreground signals. The minimal extension to the six-parameter lensed ΛCDM primary CMB spectrum that we consider consists of four free parameters: the amplitudes of the tSZ spectrum, Poisson and clustered DSFG terms, and the spectral index of the DSFG sources. The addition of these four parameters improves the likelihood of the best-fit model by $\Delta \ln \mathcal{L} = -3980$. This baseline model also includes a fixed kSZ contribution and a tight prior on radio sources. We explore the effect of modifying this model by allowing additional model parameters to vary. In particular, we free the amplitude of the kSZ and the clustered DSFG spectral index. However, we do not find that these additional free parameters improve the quality of fits to the data.

With these data, the amplitudes of the two SZ components are largely degenerate. The data primarily constrain a linear combination of tSZ and kSZ, with the result $D_{3000}^{tSZ} + 0.5 \, D_{3000}^{kSZ} = 4.5 \pm 1.0 \, \mu\text{K}^2$. For the baseline model with the kSZ power spectrum fixed to that expected for homogeneous reionization, we constrain the amplitude of the tSZ power at $\ell = 3000$ to be $D_{3000}^{tSZ} = 3.5 \pm 1.0 \, \mu\text{K}^2$. We test the dependence of the measured power on the specific tSZ model power spectrum and find that with the present data, the result is insensitive to the model shape for several recently published models. We also find that the measured tSZ power is insensitive to the modeling assumptions for the DSFG and radio foregrounds. We derive upper limits on secondary anisotropy power when the kSZ amplitude is allowed to vary. At 95% CL, we find $D_{3000}^{tSZ} < 5.3 \, \mu\text{K}^2$ and $D_{3000}^{kSZ} < 6.5 \, \mu\text{K}^2$. The corresponding limit on the total SZ power is $D_{3000}^{tSZ} + 0.5 \, D_{3000}^{kSZ} < 6.2 \, \mu\text{K}^2$ at the 95% CL.

We compare the measured amplitude of the tSZ power spectrum with the predictions of recent models and simulations. L10 found less tSZ power than the Sehgal et al. (2010, S10) model predicts; the results in this paper increase the significance of that claim. We find that, for the cosmological parameters preferred by the primary CMB power spectrum, the simulations of S10 overpredict the tSZ power spectrum amplitude, with an observed-to-predicted ratio of $A_{\mathrm{tSZ}} = 0.33 \pm 0.15$. The more recent models of Shaw et al. (2010) and Trac et al. (2011) are less discrepant, but still overestimate the tSZ signal. For example, the 'nonthermal20' model of Trac et al. (2011) gives $A_{\mathrm{tSZ}} = 0.59 \pm 0.25$. All three of these models assume that intra-cluster gas resides in hydrostatic equilibrium in the host dark matter gravitational potential, and include prescriptions to account for star formation and AGN feedback. The Trac et al. (2011) and Shaw et al. (2010) models also include a significant non-thermal contribution to the total gas pressure, which results in a lower tSZ signal. For the cosmological hydrodynamical simulations including star formation and AGN feedback of Battaglia et al. (2010), we find $A_{\mathrm{tSZ}} = 0.45 \pm 0.20$. If instead we adopt the tSZ template derived from their simulations that do not include star formation and AGN feedback we find $A_{\mathrm{tSZ}} = 0.27 \pm 0.10$ and thus a larger discrepancy between the measured and predicted signal.

We allow for a correlation between the tSZ and DSFG components in the model to investigate whether such a correlation could be responsible for the measurement of lower than expected tSZ power. With the kSZ amplitude fixed, marginalizing over the tSZ-DSFG correlation coefficient has no significant effect on the resulting tSZ power. When the kSZ power and tSZ-DSFG correlation are both free to vary, the fits actually prefer a larger kSZ power and slightly reduced tSZ power. We also note that if tSZ-DSFG correlation did significantly affect the measured tSZ power, one would expect a difference between the result of the multi-frequency fits that assume no tSZ-DSFG correlation and fits to the differenced bandpowers, which should be largely free of DSFG signal. Instead, both analyses find the same tSZ power. We therefore conclude that correlation between the tSZ and DSFG components cannot be used to reconcile the measured tSZ power with model predictions, at least when operating under the reasonable assumption that the Poisson and clustered DSFG spectral indices are similar.

We also investigate combining the measured tSZ amplitude with CMB data to obtain joint constraints on σ_8. We find that, if we assume that the template predictions are perfectly accurate, the statistical uncertainty is reduced by as much as a factor of two compared to the primary CMB-only constraints. The resulting values of σ_8 range from 0.771 ± 0.013 for the S10 model to 0.802 ± 0.013 for the Trac et al. (2011) predictions. If we assume that the predicted amplitude is uncertain at 50% in order to account for the range of model predictions, the tSZ measurement adds little additional information, and the constraint degrades to $\sigma_8 = 0.812 \pm 0.022$. Current modeling uncertainties prevent the use of the tSZ power spectrum as a tool for precision cosmology, however, precise measurements of the tSZ power spectrum can provide new information about cluster physics in the poorly studied regimes of low mass and high redshift.

In addition to the constraints on SZ power and σ_8, these data allow us to place con-

straints on foreground components. The measured bandpowers are consistent with a simple foreground model consisting of clustered DSFGs with a single spectral index and an unclustered distribution of radio sources (with a strong prior from radio source count models). Using this model, we find the spectral index of the DSFGs is $\alpha = 3.58 \pm 0.09$. The Poisson amplitude is $D^p_{3000} = 7.4 \pm 0.6 \, \mu\mathrm{K}^2$ and the clustered amplitude is $D^c_{3000} = 6.1 \pm 0.8 \, \mu\mathrm{K}^2$. We explore a number of variations on this simple DSFG model and, in general, find these variations have little impact on the SZ constraints. By comparing fits using alternate models of the clustered DSFG power spectrum, we find the data show a slight preference for the power-law model over the linear-theory model used in H10.

We find a Poisson DSFG spectral index of $\alpha_p = 3.58 \pm 0.09$. Although the Poisson spectral index is well-constrained and fairly robust to changes in the model, the amplitude of the Poisson power changes by $4\,\sigma$ as we change the shape of the clustered template. The Poisson power estimates are therefore dominated by this modeling uncertainty, and any analysis of these results needs to take that uncertainty into account. The constraint on the clustering spectral index has improved from 3.8 ± 1.3 reported in H10 to $\alpha_c = 3.47 \pm 0.34$. This spectral index is sensitive to the shape of the clustered DSFG template: with the power-law template, we find $\alpha_c = 3.79 \pm 0.37$. In either case, the data are consistent with identical indices for both the Poisson and clustering DSFG contributions to the power spectrum.

In 2009, the SPT receiver was refurbished to add sensitivity at 95 GHz. Since then, we have mapped an additional $1300 \, \mathrm{deg}^2$ to depths of 42, 18, and 85 μK-arcmin at 95, 150, and 220 GHz respectively. These data will break the tSZ/kSZ degeneracy present in the current data and facilitate the separation of the SZ components. Improved measurements of the tSZ power spectrum will provide new insight to the cluster astrophysics relevant in the poorly understood regimes of low mass and high redshift. We also expect these data to provide new constraints on the kSZ power spectrum, which have the potential to illuminate the epoch of reionization.

Chapter 7

Conclusion

This dissertation, like the graduate study it represents, is something of a patchwork covering several quite different topics. There are few opportunities in contemporary physics for a graduate student to receive hands on experience in most of the major aspects of a program which also generates interesting science results. I am grateful to have taken part in one. However, it makes an attempt to summarize the work rather complicated. Rather than a tedious list, certain to bore the reader, it seems more useful to close with a few personal reflections on the design choices we made when building the instrument, comments regarding the ongoing SPT science program, and finally a few thoughts on the future of large arrays of cryogenic photon detectors.

Looking back over old presentations from my first few months working on SPT, it is clear that we all underestimated the difficulties involved in scaling from single pixels tested in the lab to a production array with automated, multiplexed readout. In particular, there is a huge difference between a fab process which yields working dies and the production of entire wafer-scale devices. The most obvious example is the XeF_2 release of spiderwebs. Our initial single pixel recipe was robust, repeatable, and easy to apply, and it always worked on individual devices. It almost always worked for APEX-SZ size arrays. But, getting it to work on SPT arrays required at least half a year of R&D and lead to the destruction of many viable wafers very late in production.

Although rarely articulated at the time, the SPT design can be characterized by three very basic choices. First, we chose to produce as large an array on a single wafer as possible. In principle, this is an entirely sound strategy. In practice, it's difficult to obtain enough information on yield to justify that strategy in a quantitative way. Although others in the collaboration would likely disagree, I believe that we were too ambitious in choosing the scale the SPT wedge. Producing working devices over a region with half the area of an SPT wedge would have allowed us to avoid several of the pitfalls we encountered, and would likely have lead to a more uniform final array with fewer production wafers. The cost, of course, is in loss of focal plane area; however, it's important not to compare that yield to a 100% complete array delivered on the same schedule, but to a more realistic estimate. The current

design sacrifices roughly 20% of usable focal plane area to mounting hardware. Were we to double that area (making the least-savvy possible choices), we'd still lose only 2/3 as many detectors as we currently lose due to both fabrication yield and the 7/8 fMUX requirement. It is unfortunate that one can rarely accurately estimate yield before committing to a particular design.

The second choice we made was to attempt to incorporate real time laboratory feedback into the fab process in order to adjust parameters, with the goal of making every wafer a good wafer. The alternative strategy is to assume that process parameters will always scatter by a factor of a few and simultaneously process a batch of units with a designed scatter in parameters. Looking back on the process, it's not clear to me whether or not we made the right decision. We certainly processed to completion and tested far more wafers than have been fielded, by at least a factor of five. In hindsight, if each batch of wafers spanned a range of design G values, it seems likely we would have done at least as well or better than we did. On the other hand, the rapid feedback and testing regimen did allow us to spot a number of problems without ruining whole batches of wafers. One thing is clear, though: the naive model in which testing allows one to converge over time on precision parameters was thoroughly unrealistic. At least in a fast-paced academic facility like the Berkeley Microlab, the timescale over which fab processes change is comparable to the timescale over which cryogenic testing can occur.

The third choice was to always strive to produce field-able detectors whenever possible. Rather than designing test devices to explore a particular parameter, we chose always to incorporate design changes into full wafers. This strategy is hard to criticize, both because of the time constraints involved, and because of the fickle tendency of processes which work perfectly on sample dies to fail on large arrays. In the end, I suspect that strategy had a lot to do with the ultimately successful detector campaign.

The South Pole Telescope and receiver have been quite successful. As of late 2011, the program is weeks from completing observations prior to the installation of a new polarization sensitive receiver, SPTPol. The final survey includes a contiguous region of 2500 square degrees mapped to a depth of $18\,\mu\mathrm{K} - \mathrm{arcmin}$ in the $150\,\mathrm{GHz}$ band, as well as a 100 square degree patch mapped to $\sqrt{2}$ times that depth. SPT analysis is ongoing; however, several results have already been published in addition to the high-ℓ power spectrum results discussed here. Keisler et al. (2011) have analyzed 800 square degrees at $150\,\mathrm{GHz}$, producing the most precise measure of the damping tail over a range of ℓ down to roughly 900. Though the constraints on ΛCDM cosmology aren't significantly better than can be obtained from WMAP, QUaD, and ACBAR, the new result does significantly improve constraints on several extension parameters, including the running of the spectral index and the tensor/scalar ratio, r. The results favor models with a slightly lower than expected damping tail, preferring (at the 1σ level) either a large helium abundance than derived from BBN results or a larger number of relativistic species. Future SPT data sets, as well as the imminent release of the Planck satellite power spectrum, will determine whether this feature is significant. Ongoing work includes the analysis of the high-ℓ, multi-band power spectrum from the first two years

of SPT data, and the statistical detection of lensing in SPT maps. Future plans include both the power spectrum of the full survey, and an accepted proposal which will map the 100 square degree deep SPT field with higher frequency bands from the HERSCHEL/SPIRE instrument, which should allow for a significant detection of the kSZ.

Cluster results from SPT include the first blind SZ cluster detection (Staniszewski et al., 2009), pointed cluster observations and maps of the outer regions of massive catalog clusters (Plagge et al., 2010), and confirmation of massive nearby clusters detected by the Planck satellite (Story et al., 2011). Massive, high redshift clusters are particularly interesting, as the existence of even a few such clusters can be used to constrain cosmological parameters. SPT has twice discovered the most massive known cluster at $z \geq 1$(Brodwin et al., 2010; Foley et al., 2011), and has produced a complete catalog of the most massive clusters from the full survey region (including 26 clusters with $M \geq 9.8 \times 10^{14} h_{70}^{-1} \ M_\odot$). (Williamson et al., 2011) The results are all consistent with concordance ΛCDM cosmology, though the most massive catalog cluster, and $M_{200} = 1.3 \pm 0.2 \times 10^{15} h_{70}^{-1} \ M_\odot$) cluster at $z = 1.18$, is expected to be quite rare, with only a 7% chance of finding a similar or more massive object in the full SPT survey.

I suspect most people would agree that the principal science goal of the SPT project was, from the outset, the generation of a complete, mass-limited catalog of clusters and the determination of cosmological parameters such as the dark energy equation of state. To an outside observer, the results so far might seem discouraging. Five years since first light, the collaboration has published a single catalog with a cosmological analysis, containing only 21 clusters. The derived cosmological constraints, $\sigma_8 = 0.81 \pm 0.09$ and $w = 1.07 \pm 0.29$ for a wCDM cosmology with WMAP-5 priors, are a significant improvement on the result using only CMB data. However; they're a factor of two worse than the best current constraints, derived from a similar analysis of an X-ray selected sample by Vikhlinin et al. (2009) and discussed in chapter 1.

Why bother, then, with SPT and with SZ cluster surveys? The answer is that despite being nearly finished with the SZ survey, we've only begun to make use of the SPT dataset. There are two factors which limit the precision of the previous SPT cluster cosmology result: sample size, and the precision with which the scaling relation between integrated SZ flux (or, equivalently, detection Signal to noise) and cluster mass is known. The first of these problems will essentially solve itself; even with the lag imposed by the need for optical redshifts, SPT already has more than 240 optically confirmed clusters from the first three years of survey data. The second is more tricky. Even for the initial 21 cluster sample, the assumed mass uncertainty slightly dominates over the statistical error. In recent years, a major mass-calibration campaign has been underway which aims to improve our knowledge of the scaling relation using targeted X-ray followup of SPT clusters, Weak lensing observations in the optical using Magellan and HST, and dynamical mass estimates from Gemini and VLT. Based on projections from the 2010 followup sample, we expect a total of approximately 440 clusters detected with a signal to noise ratio of $5\,\sigma$, corresponding to a 5% false detection rate. With the use of multi-band cluster detection algorithms, the sample properties should

be somewhat improved compared to those reported in (Vanderlinde et al., 2010), which estimate 100% complete down to a mass limit of $M_{200} = 3 \times 10^{14} h_{70}^{-1}$ $M_{\odot}$ at $z = 0.6$, and improving by 20% by $z = 1.0$ If we can improve the current uncalibrated $\sim 25\%$ scaling relation uncertainty with a plausible 5% uncertainty on the mean and a 10% uncertainty on redshift evolution of the scaling relation, simulations indicatae that we can achieve a 1% and 5% uncertainty on σ_8 and w, respectively. This is comparable to, but entirely independent of, the constraint on w from supernovae and BAO results. While still shy of the several thousands of clusters and few percent constraints on w that were projected at the time SPT (and ACT) were proposed, when the best estimates of σ_8 were around 0.9, cluster cosmology still has a role to play as the best non-geometric constraint on dark energy available.

Of course, SPT does not exist in a vacuum. One can ask what impact current and future instruments will have on our data-set and near term science goals. So far, we've been rather fortunate, with a significant and apparently sustained sensitivity and mapping speed advantage over our direct competitor, ACT. That may change in the near future, when the ACT collaboration deploys a significantly upgraded receiver with a new array of polarization sensitive detectors.

The most obvious near-term CMB instrument with the potential to dramatically impact SPT is the Planck satellite. This CMB mapping satellite successfully launched two years ago, has already released a catalog of SZ-detected galaxy clusters, and is expected to release CMB power spectra within the next year. As a cluster survey, Planck's data set will complement but not challenge ground based instruments. At very low redshifts, the Planck mass threshold is slightly lower than SPT; however, their mass limit falls off much more quickly with redshift due to their larger beam size. Thus, the Planck cluster catalog will be largely confined to extremely massive nearby clusters.(Planck Collaboration, 2011) When it comes to the CMB power spectrum, though, the story is different. With full sky coverage and two years of continuous integration, Planck will produce the most sensitive temperature power spectrum at $\ell \lesssim 2000$, and the best constraints on the primary anisotropy and damping tail for the foreseeable future. Based on a rough projection using Planck design specifications and extrapolating from the power spectrum results shown here, we expect that power spectrum derived from the full SPT data set will be more sensitive than Planck at around $\ell \geq 2000$. While this means the recent SPT results at the scale of the CMB damping tail are likely to be rather short lived, there's plenty of room left for SPT (and ground based power spectrum science) at smaller scales. For SZ and foreground science, the overlap in both spatial and frequency between the two data sets, combined with the precise dipole power calibration available to Planck, will allow for an exquisitely calibrated high-ℓ spectrum, while a joint analysis that uses high-ℓ SPT data to constrain foregrounds can potentially improve constraints on parameters which affect the CMB primary spectrum and damping tail. (Millea et al., 2011)

In the slightly more distant future, the Dark Energy Survey is expected to begin observing this year. This blind optical survey will map a superset of the SPT field in the optical and near IR.(The Dark Energy Survey Collaboration, 2005) In addition to several other

science goals, DES will allow for instant photometric followup of the entire SPT cluster catalog, extending to low significance candidates, and enabling joint SZ-optical detection strategies. An even more distant, less certain, but very exciting instrument for cluster science is the eRosita satellite imager, an all-sky survey instrument currently scheduled to launch in 2013.(Predehl et al., 2010) Based upon projections from the eRosita team, the project will produce a massive catalog of clusters, with all-sky coverage and a mass threshold below that of SPT out to a redshift of nearly 1.0. If the program is successful, blind SZ surveys will be competitive only at the very highest redshifts.

None the less, there are still plenty of opportunities for cryogenic detectors for millimeter and sub-millimeter astronomy. A number of monolithic, multiplexed TES arrays at millimeter wavelengths are currently in production or in the field, including the list mentioned in Chapter 3, most of these targeting ground based CMB polarization or sub-mm astronomy. Compared to ten years ago, when the field consisted of individually assembled devices (and the groundbreaking, but only partially-monolithic Bolocam) and plans for larger arrays, both array fabrication and multiplexed readout are now approaching maturity. At mm wavelengths and on the ground, both the Berkeley/McGill fMUX and time division systems are able to read out a Nyquist sampled focal plane area with a tolerable heat load and a cost which is a small fraction of a full instrument budget. Despite several delays and under-performing first-light arrays within the community, its clear that few-kilo-pixel-arrays of multiplexed TESes is entering the realm of established technology. Among the new generation of instruments is SPTPol, a new camera for SPT designed primarily for CMB polarization studies.

There are three areas where there is still a need for dramatic improvements in detector array technology: space missions, where weight and energy costs make the current crop of multiplexed readout hardware infeasible, sub-mm and THz instruments, where a fully filled focal plane may contain tens or hundreds of kilopixels, and multi-chroic and spectroscopic instruments at all frequencies, which may require several to hundreds of times as many detectors as pixels. A number of schemes have been devised to scale current multiplexing factors by another few orders of magnitude, though none have yet been implemented on science instruments. Among these are several code division multiplexing schemes which efficiently utilizes the bandwidth available in a time-division-like system (Irwin et al., 2011), and dynamic active nulling applied to the fMUX system, which can dramatically reduce the gain-bandwidth requirements on the SQUID feeback loop and extend the current fMUX architecture to as many as a few hundred pixels. More exotic possibilities, such as two-stage multiplexing using microwave resonators are being designed, but haven't been demonstrated in real applications yet. Another new technology which has has the potential to enable mega-pixel arrays is the microwave kinetic inductance detector (MKID), which is intrinsically frequency domain multiplexed and very easy to fabricate. Current MKID implementations are limited by first stage amplifier noise, with a similarly optimized system delivering an NEP which is around T_{amp}/T_c of an equivalent TES device. For a commercial HEMT with $T_{amp} \sim 4$ K, MKIDS aren't particularly competitive with mK TESes. In applications where

the signal-to-photon-noise is significantly higher, such as sub-mm and THz cameras and for narrow band spectroscopic applications, MKIDs are a viable alternative. The first MKID instruments are now being fielded, and engineering data looks promising, though they clearly represent a less mature technology. When it comes to mm-wavelength cameras, though, really convincing alternatives to TES sensors are hard to find.

Bibliography

Afsar, M. N., & Chi, H. 1994, Internat. J. Infrared and Millimeter Waves, 15, 1181

Aihara, H., et al. 2011, ApJ Supplement Series, 193, 29

Allen, S. W., Rapetti, D. A., Schmidt, R. W., Ebeling, H., Morris, R. G., & Fabian, A. C. 2007, MNRAS, 383, 879

Arnaud, M., Pratt, G. W., Piffaretti, R., Boehringer, H., Croston, J. H., & Pointecouteau, E. 2009, ArXiv e-prints, 0910.1234

Aubin, F., et al. 2010, in SPIE Conf. Series, Vol. 7741

Battaglia, N., Bond, J. R., Pfrommer, C., Sievers, J. L., & Sijacki, D. 2010, ApJ, 725, 91

Battistelli, E. S., et al. 2008, Journal of Low Temp. Phys., 151, 908

Bode, P., Ostriker, J. P., & Vikhlinin, A. 2009, ApJ, 700, 989

Bond, J. R., et al. 2005, ApJ, 626, 12

Bowman, J. D., Morales, M. F., & Hewitt, J. N. 2006, ApJ, 638, 20

Brodwin, M., et al. 2010, ApJ, 721, 90

Brown, M. L., et al. 2009, ApJ, 705, 978

Bussmann, R. S., Holzapfel, W. L., & Kuo, C. L. 2005, ApJ, 622, 1343

Carlstrom, J. E., et al. 2011, PASP, 123, 568

Carlstrom, J. E., Holder, G. P., & Reese, E. D. 2002, ARA&A, 40, 643

Carroll, S. M., Press, W. H., & Turner, E. L. 1992, ARA&A, 30, 499

Cavaliere, A., & Fusco-Femiano, R. 1976, A&A, 49, 137

Chamberlin, R. A. 2001, J. Geophys. Res. Atmospheres, 106 (D17), 20101

Chervenak, J. a., Irwin, K. D., Grossman, E. N., Martinis, J. M., Reintsema, C. D., & Huber, M. E. 1999, Appl. Phys. Lett., 74, 4043

Clarke, J. 1968, Le Journal de Physique Colloques, 29, C2

Cooray, A., & Sheth, R. 2002, Physics Reports, 372, 1

Crill, B. P., et al. 2008, in SPIE Conf. Series, Vol. 7010

Croft, R. a. C., Weinberg, D. H., Katz, N., & Hernquist, L. 1998, ApJ, 495, 44

Das, S., et al. 2011, ApJ, 729, 62

Davis, M., Efstathiou, G., Frenk, C. S., & White, S. D. M. 1985, ApJ, 292, 371

Davis, M., & Peebles, P. J. E. 1983, ApJ, 267, 465

Dawson, K. S., Holzapfel, W. L., Carlstrom, J. E., Joy, M., & LaRoque, S. J. 2006, ApJ, 647, 13

Dawson, K. S., Holzapfel, W. L., Carlstrom, J. E., Joy, M., LaRoque, S. J., Miller, A. D., & Nagai, D. 2002, ApJ, 581, 86

de Zotti, G., Ricci, R., Mesa, D., Silva, L., Mazzotta, P., Toffolatti, L., & González-Nuevo, J. 2005, A&A, 431, 893

Dodelson, S. 2003, Modern Cosmology (Academic Press)

Dolag, K., Vazza, F., Brunetti, G., & Tormen, G. 2005, MNRAS, 364, 753

Draine, B. T., & Lee, H. M. 1984, ApJ, 285, 89

Dunkley, J., et al. 2011, ApJ, 739, 52

Dunne, L., Eales, S., Edmunds, M., Ivison, R., Alexander, P., & Clements, D. L. 2000, MNRAS, 315, 115

Duzer, T., & Turner, C. 1999, Principles of superconductive devices and circuits (Prentice Hall)

Evrard, A. E. 1990, ApJ, 363, 349

Finkbeiner, D. P., Davis, M., & Schlegel, D. J. 1999, ApJ, 524, 867

Fixsen, D. J., Cheng, E. S., Gales, J. M., Mather, J. C., Shafer, R. A., & Wright, E. L. 1996, ApJ, 473, 576

Foley, R. J., et al. 2011, ApJ, 731, 86

Friedman, R. B., et al. 2009, ApJ, 700, L187

Fu, L., et al. 2008, A&A, 479, 9

Giavalisco, M., Steidel, C. C., Adelberger, K. L., Dickinson, M. E., Pettini, M., & Kellogg, M. 1998, ApJ, 503, 543

Gildemeister, J. M., Lee, A. T., & Richards, P. L. 2001, Applied Optics, 40, 6229

Gildenmeister, J. M. 2000, PhD thesis, University of California, Berkeley

Giodini, S., et al. 2009, ApJ, 703, 982

Gordon, M. A. 1995, A&A, 301, 853

Grann, E. B., Moharam, M. G., & Pommet, D. a. 1994, Journal of the Optical Society of America A, 11, 2695

Haig, D. J., et al. 2004, in SPIE Conf. Series, ed. C. M. Bradford, P. A. R. Ade, J. E. Aguirre, J. J. Bock, M. Dragovan, L. Duband, L. Earle, J. Glenn, H. Matsuhara, B. J. Naylor, H. T. Nguyen, M. Yun, & J. Zmuidzinas, Vol. 5498, 78–94

Hall, N. R., et al. 2010, ApJ, 718, 632

Hamilton, A. J. S., Kumar, P., Lu, E., & Matthews, A. 1991, The Astrophysical Journal, 374, L1

Hanany, S., et al. 2000, ApJ, 545, L5

Harrison, E. R. 1970, Phys. Rev. D, 1, 2726

Hicken, M., Wood-Vasey, W. M., Blondin, S., Challis, P., Jha, S., Kelly, P. L., Rest, A., & Kirshner, R. P. 2009, ApJ, 700, 1097

Hivon, E., Górski, K. M., Netterfield, C. B., Crill, B. P., Prunet, S., & Hansen, F. 2002, ApJ, 567, 2

Ho, S., et al. 2010, in Bulletin of the American Astronomical Society, Vol. 42, American Astronomical Society Meeting Abstracts #215, #370.06–+

Hoekstra, H., et al. 2006, ApJ, 647, 116

Holland, W. S., et al. 1999, MNRAS, 303, 659

Hu, W., & Jain, B. 2004, Phys. Rev. D, 70

Hwang, T., Popa, D., Sin, J., Stephanou, H. E., & Leonard, E. M. 2004, BCB wafer bonding for microfluidics, Vol. 5342 (SPIE), 182–191

Irwin, K. 2002, Physica C: Superconductivity, 368, 203

Irwin, K., & Hilton, G. 2005, in Topics in Applied Physics, Vol. 99, Cryogenic Particle Detection, ed. C. Enss (Springer Berlin / Heidelberg), 81–97

Irwin, K. D., et al. 2011, ArXiv e-prints, 1110.1608

Irwin, K. D., Hilton, G. C., Wollman, D. a., & Martinis, J. M. 1998, Journal of Applied Physics, 83, 3978

Itoh, N., Kohyama, Y., & Nozawa, S. 1998, ApJ, 502, 7

Jethava, N., Ullom, J. N., Irwin, K. D., Doriese, W. B., Beall, J. A., Hilton, G. C., Vale, L. R., & Zink, B. 2009, in AIP Conf. Series, Vol. 1185, 31–33

Jing, Y. P., & Suto, Y. 2000, ApJ, 529, L69

Johnston, D. E., et al. 2007, ArXiv e-prints, 0709.1159

Kaiser, N. 1984, ApJ, 284, L9

Kaiser, N. 1998, ApJ, 498, 26

Kay, S. T., Thomas, P. A., Jenkins, A., & Pearce, F. R. 2004, MNRAS, 355, 1091

Keisler, R., et al. 2011, ApJ, in press, arXiv:1105.3182

Knox, L. 1999, Phys. Rev. D, 60, 103516

Komatsu, E., & Kitayama, T. 1999, ApJ, 526, L1

Komatsu, E., & Seljak, U. 2001, MNRAS, 327, 1353

Komatsu, E., & Seljak, U. 2002, MNRAS, 336, 1256

Komatsu, E., et al. 2011, ApJ Supplement Series, 192, 18

Komatsu, E., et al. 2011, ApJS, 192, 18

Lacey, C., & Cole, S. 1993, Royal Astronomical Society, 262, 627

Lagache, G., Bavouzet, N., Fernandez-Conde, N., Ponthieu, N., Rodet, T., Dole, H., Miville-Deschênes, M.-A., & Puget, J.-L. 2007, ApJ, 665, L89

Lane, A. P. 1998, in ASP Conf. Ser. 141, Vol. 141, Astrophysics from Antarctica, ed. G. Novak & R. H. Landsberg (San Francisco: ASP), 289

Lanting, T. M. 2006, PhD thesis, University of California, Berkeley

Lanting, T. M., et al. 2006, Nuclear Instruments and Methods in Physics Research A, 559, 793

——. 2005, Applied Physics Letters, 86, 2511

Larson, D., et al. 2011, ApJS, 192, 16

Lau, E. T., Kravtsov, A. V., & Nagai, D. 2009, ApJ, 705, 1129

Lee, A. T., et al. 2003, in Millimeter and Submillimeter Detectors for Astronomy. Edited by Phillips, Thomas G.; Zmuidzinas, Jonas. Proceedings of the SPIE, Volume 4855, pp. 129-135 (2003)., ed. T. G. Phillips & J. Zmuidzinas, 129–135

Lee, A. T., Richards, P. L., Nam, S. W., Cabrera, B., & Irwin, K. D. 1996, Appl. Phys. Lett., 69, 1801

Lewis, A., & Bridle, S. 2002, Phys. Rev., D66, 103511

Lewis, A., & Bridle, S. 2002, Phys. Rev. D, 66, 103511

Lindeman, M. 2000, PhD thesis, University of California, Davis

Linder, E. V., & Jenkins, A. 2003, MNRAS, 346, 573

Longair, M. S. 2008, Galaxy Formation (Springer-Verlag)

Lueker, M. 2010, PhD thesis, University of California, Berkeley

Lueker, M., et al. 2009, IEEE Transactions on Applied Superconductivity, 19, 496

——. 2010, ApJ, 719, 1045

Marriage, T. A., et al. 2011, ApJ, 731, 100

Martinez, V. J., & Saar, E. 2002, Statistics of the Galaxy Distribution (CRC Press)

Mason, B. S., et al. 2003, ApJ, 591, 540

Mather, J. C. 1982, Applied Optics, 21, 1125

McMahon, J. J., et al. 2009, in American Institute of Physics Conference Series, Vol. 1185, American Institute of Physics Conference Series, ed. B. Young, B. Cabrera, & A. Miller, 511–514

Mehl, J. J. 2009, PhD thesis, University of California, Berkeley

Melchiorri, A., et al. 2000, ApJ, 536, L63

Millea, M., Doré, O., Dudley, J., Holder, G., Knox, L., Shaw, L., Song, Y., & Zahn, O. 2011, Submitted to ApJ, arXiv:1102.5195

Moore, B., Governato, F., Quinn, T., Stadel, J., & Lake, G. 1998, ApJ, 499, L5+

Nagai, D., Kravtsov, A. V., & Vikhlinin, A. 2007, ApJ, 668, 1

Nakamura, K., & Particle Data Group. 2010, Journal of Physics G Nuclear Physics, 37, 075021

Navarro, J. F., Frenk, C. S., & White, S. D. M. 1996, ApJ, 462, 563

——. 1997, ApJ, 490, 493

Niklaus, F., et al. 2001, Sensors and Actuators A: Physical, 92, 235

Nusser, A., & Davis, M. 1995, MNRAS, 276, 1391

——. 2011, arXiv:1101.1650

Ogburn, IV, R. W., et al. 2010, in SPIE Conf. Series, Vol. 7741

Ostriker, J. P., & Vishniac, E. T. 1986, ApJ, 306, L51

Padin, S., et al. 2008, Appl. Opt., 47, 4418

Peacock, J., & Dodds, S. 1994a, MNRAS, 267, 1020

Peacock, J. A., & Dodds, S. J. 1994b, R.A.S. MONTHLY NOTICES V.267

Peacock, J. A., & Smith, R. E. 2000, MNRAS, 318, 1144

Perlmutter, S., et al. 1999, ApJ, 517, 565

Pettini, M., Zych, B. J., Murphy, M. T., Lewis, A., & Steidel, C. C. 2008, MNRAS, 391, 1499

Piffaretti, R., Jetzer, P., Kaastra, J. S., & Tamura, T. 2005, A&A, 433, 101

Plagge, T., et al. 2010, ApJ, 716, 1118

Planck Collaboration. 2011, to appear in A&A, arXiv:1101.2024

Planck HFI Core Team, et al. 2011, ArXiv e-prints, 1101.2039

Polenta, G., Marinucci, D., Balbi, A., de Bernardis, P., Hivon, E., Masi, S., Natoli, P., & Vittorio, N. 2005, Journal of Cosmology and Astro-Particle Physics, 11, 1

Predehl, P., et al. 2010, X-ray Astronomy 2009; Present Status, Multi-Wavelength Approach and Future Perspectives, 1248, 543

Press, W. H., & Schechter, P. 1974, ApJ, 187, 425

Puers, R., & Cozma, A. 1997, Journal of micromechanics and microengineering, 7, 114

Rasia, E., Tormen, G., & Moscardini, L. 2004, MNRAS, 351, 237

Rauch, M. 1998, ARA&A, 36, 267

Reichardt, C. L., et al. 2009a, ApJ, 694, 1200

——. 2009b, ApJ, 701, 1958

Reintsema, C. D., et al. 2003, Review of Scientific Instruments, 74, 4500

Richards, P. L. 1994, Journal of Applied Physics, 76, 1

Riess, A. G., et al. 1998, The Astronomical Journal, 116, 1009

Righi, M., Hernández-Monteagudo, C., & Sunyaev, R. A. 2008, A&A, 478, 685

Ruhl, J., et al. 2004, in Proc. SPIE, Vol. 5498, Millimeter and Submillimeter Detectors for Astronomy II, ed. J. Zmuidzinas, W. S. Holland, & S. Withington (Bellingham: SPIE Optical Engineering Press), 11–29

Runyan, M. C., et al. 2003, ApJ Supplement Series, 149, 265

Sayers, J., et al. 2009, ApJ, 690, 1597

Schlegel, D., White, M., & Eisenstein, D. 2009, in Astronomy, Vol. 2010, astro2010: The Astronomy and Astrophysics Decadal Survey, 314–+

Schlegel, D. J., Finkbeiner, D. P., & Davis, M. 1998, ApJ, 500, 525

Schulz, A., & White, M. 2006, Astroparticle Physics, 25, 172

Schwan, D., et al. 2010, arXiv:1008.0342

Schwan, D., et al. 2003, New Astronomy Review, 47, 933

Scott, D., & White, M. 1999, A&A, 346, 1

Sehgal, N., Bode, P., Das, S., Hernandez-Monteagudo, C., Huffenberger, K., Lin, Y., Ostriker, J. P., & Trac, H. 2010, ApJ, 709, 920

Seljak, U. 2000, MNRAS, 318, 203

Seljak, U., & Zaldarriaga, M. 1996, Astrophys. J., 469, 437

Seo, H.-J., Dodelson, S., Marriner, J., Mcginnis, D., Stebbins, A., Stoughton, C., & Vallinotto, A. 2010, ApJ, 721, 164

Sharp, M. K., et al. 2010, ApJ, 713, 82

Shaw, L. D., Nagai, D., Bhattacharya, S., & Lau, E. T. 2010, ApJ, 725, 1452

Shaw, L. D., Zahn, O., Holder, G. P., & Doré, O. 2009, ApJ, 702, 368

Sheehy, C. D., et al. 2010, in SPIE Conf. Series, Vol. 7741

Sheth, R. K., & Tormen, G. 1999, MNRAS, 308, 119

Shirokoff, E., et al. 2009, IEEE Trans. on Appl. Supercond., 19, 517

——. 2011, ApJ, 736, 61

Sievers, J. L., et al. 2009, eprint arXiv:0901.4540

Silk, J. 1968, ApJ, 151, 459

Silva, L., Granato, G. L., Bressan, A., & Danese, L. 1998, ApJ, 509, 103

Staniszewski, Z., et al. 2009, ApJ, 701, 32

Steigman, G. 2007, Ann. Rev. Nuc. Part. Sci., 57, 463

Story, K., et al. 2011, ApJ, 735, L36+

Sun, M., Sehgal, N., Voit, G. M., Donahue, M., Jones, C., Forman, W., Vikhlinin, A., & Sarazin, C. 2011, ApJ, 727, L49+

Sun, M., Voit, G. M., Donahue, M., Jones, C., Forman, W., & Vikhlinin, A. 2009, ApJ, 693, 1142

Sunyaev, R. A., & Zeldovich, Y. B. 1970, Comments on Astrophysics and Space Physics, 2, 66

——. 1972, Comments on Astrophysics and Space Physics, 4, 173

Sunyaev, R. A., & Zel'dovich, Y. B. 1972, Comments on Astrophysics and Space Physics, 4, 173

Swetz, D. S., et al. 2010, ArXiv e-prints, 1007.0290

The Dark Energy Survey Collaboration. 2005, ArXiv Astrophysics e-prints

Tinker, J., Kravtsov, A. V., Klypin, A., Abazajian, K., Warren, M., Yepes, G., Gottlöber, S., & Holz, D. E. 2008, ApJ, 688, 709

Tinker, J., Kravtsov, A. V., Klypin, A., Abazajian, K., Warren, M., Yepes, G., Gottlöber, S., & Holz, D. E. 2008, ApJ, 688, 709

Trac, H., Bode, P., & Ostriker, J. P. 2011, ApJ, 727, 94

Tristram, M., Macías-Pérez, J. F., Renault, C., & Santos, D. 2005, MNRAS, 358, 833

Ullom, J. N., et al. 2004, Appl. Phys. Lett., 84, 4206

Vanderlinde, K., et al. 2010, ApJ, 722, 1180

Vieira, J. D., et al. 2010, ApJ, 719, 763

Viero, M. P., et al. 2009, ApJ, 707, 1766

Vikhlinin, A., Kravtsov, A., Forman, W., Jones, C., Markevitch, M., Murray, S. S., & Van Speybroeck, L. 2006, ApJ, 640, 691

Vikhlinin, A., et al. 2009, ApJ, 692, 1060

Vikhlinin, A., Markevitch, M., Murray, S. S., Jones, C., Forman, W., & Van Speybroeck, L. 2005, ApJ, 628, 655

Vishniac, E. T. 1987, ApJ, 322, 597

Weinberg, D. H., Dave, R., Katz, N., & Kollmeier, J. A. 2003, AIP Conf. Proc., 666, 157

Werthamer, N. 1963, Phys. Rev., 132, 2440

Westbrook, B., et al. 2009, in American Institute of Physics Conference Series, Vol. 1185, American Institute of Physics Conference Series, ed. B. Young, B. Cabrera, & A. Miller, 363–366

White, S. D. M., Efstathiou, G., & Frenk, C. S. 1993, Royal Astronomical Society, 262, 1023

Williamson, R., et al. 2011, ApJ, 738, 139

Yoon, K. W., et al. 2006, in Proc. SPIE, Vol. 6275, Millimeter and Submillimeter Detectors for Astronomy III, ed. J. Zmuidzinas, W. S. Holland, S. Withington, & W. D. Duncan (Bellingham: SPIE Optical Engineering Press), 6275

Yu, J., Wang, Y., Lu, J.-Q., & Gutmann, R. J. 2006, Appl. Phys. Lett., 89, 092104

Yu, J., Wang, Y., Moore, R. L., Lu, J.-Q., & Gutmann, R. J. 2007, J. Electrochem. Soc., 154, H20

Zahn, O., Mesinger, A., McQuinn, M., Trac, H., Cen, R., & Hernquist, L. E. 2011, MNRAS, 532

Zaldarriaga, M., Hui, L., & Tegmark, M. 2001, ApJ, 557, 519

Zehavi, I., et al. 2010, ArXiv e-prints, 1005.2413

Zeldovich, Y. B. 1972, MNRAS, 160, 1P